UNIVERSIDAD COMPLUTENSE DE MADRID

FACULTAD DE CIENCIAS FÍSICAS
Departamento de Física Atómica, Molecular y Nuclear

SEARCH FOR GAMMA-RAY EMISSION FROM PULSARS WITH THE MAGIC TELESCOPE: SENSITIVITY STUDIES, DATA CHECK AND DATA ANALYSIS

MEMORIA PARA OPTAR AL GRADO DE DOCTOR

PRESENTADA POR

Raquel de los Reyes López

Bajo la dirección de los doctores
José Luis Contreras González y María Victoria Fonseca González

Madrid, 2009

- **ISBN: 978-84-692-1769-6**

Search for gamma-ray emission from pulsars with the MAGIC telescope: sensitivity studies, data check and data analysis

Thesis presented

by

Raquel de los Reyes López

Department of Física Atómica, Molecular y Nuclear

for the degree of

Doctor of Philosophy

in the subject of

Physics

Thesis advisors:

Dr. Jose Luis Contreras González

Dra. María Victoria Fonseca González

Universidad Complutense de Madrid

Madrid

May 2008

Dedicada a mi padre, a mi madre, a mi hermana
y a todos vosotros que habéis estado a mi lado todo el camino.

Acknowledgments

En primer lugar debo agradecer la oportunidad que me dieron mis dos directores María Victoria Fonseca y Jose Luis Contreras de unirme al Grupo de Altas Energías para realizar el trabajo que ha dado como fin esta Tesis. Ademas les quiero agradecer su ayuda, dirección y apoyo constantes.

Thank you to E. Lorenz for his corrections to this work and his invaluable comments and suggestions.

Gracias también a Emiliano Hernandez por sus consejos y su guía desde el principio y a lo largo de todos estos años, y a Jaime Zamorano. Nunca habría empezado la tesis sin ellos.

I also would like to thank all my colleagues inside MAGIC for making my job easier by their help and support. Special thanks to Abelardo, Daniel, Daniela, Emma, Florian, Javi, Juan, Marcos, the two Markuses, Nadia, Nuria, Oscar, Pratik, Thomas, Toni, Wolfgang.... and many others. I have been very lucky to discover new friends and share with many of you all those meetings, shifts and holidays.

Thank you also to B. Rudak, O. de Jager and G. Kanbach for their help and guidance that enabled me to understand the theoretical part of the thesis work. Thank you for being so nice to me in all our meetings.

Gracias a mis compañeros de grupo (y sobre todo de despacho), por su infinita paciencia y ayuda: Adolfo, Antonio, Daniel, Emma, Fabrizio, Igor, Jose Luis, Juan Abel, Luispa, Marcos, Miguel, Pedro y otros tantos que han pasado brevemente. Todos ellos han conocido en cierta medida lo peor y mejor de mi caracter y les doy las gracias por no haberme tirado por la ventana, y sin embargo, haberme dado su amistad.

Y por último a todos vosotros que hab'eis estado ahí en los buenos y malos ratos, este trabajo no habría sido posible sin vosotros y una parte de él os corresponde:

A mi familia que me ha aconsejado y ha estado siempre a mi lado, con una paciencia infinita, adaptándose siempre a mí y a situaciones laborales insólitas.

A mis amigos: Juanjo, Paula, maría, Mila, Ana, Palo, Mariangeles, Rachel, Cecilia, Carmen, Laura, Esther(s), Ajo, Bego, Laura, Ruth ..... Gracias por escuchar, por vuestros consejos, pero sobre todo por vuestra compañía y amistad.

Abstract

Astrophysics is the branch of Astronomy (from the Greek "the laws of the stars") that studies the physics of the Universe. Nearly all our information for the study of distant cosmic objects in our Universe comes from the observation of electromagnetic waves and particles that reach the Earth. In the history of Astronomy, all the discoveries have been accompanied hand-in-hand by technological developments - sometimes to improve our perception of the Universe and at other times to open new as yet unexplored windows.

This Thesis intends to introduce the reader to one of the windows, opened in the recent past, since 1989, to the most violent phenomena of the Universe that take place at high energies and which has given rise to a new branch in Astronomy: *High Energy Astronomy*. The new window of observation has improved thanks to the development of new instrumentation, which needs calibration and monitoring tasks and which sometimes has to face up to new intrinsic difficulties.

This work is based on the ground-based telescopes used to observe the Universe at high energies, in particular the MAGIC Telescope. Specifically, this Thesis covers the MAGIC telescope monitoring, its detection capabilities, the new challenges opened up by the effect of the Earth's magnetic field at low energies and the first results for the physics of some members of a particular kind of star, called pulsars. It describes in detail the efforts to monitor the behaviour of the telescope, which has to be stable enough to guarantee a good understanding of the results. Finally, this work presents the upper limits of two of the most promising pulsar gamma-ray candidates: PSR J0205+6449 and PSR J0218+4232.

Summary

The window of Very High Energy (VHE) gamma-astronomy was opened by the Whipple Imaging Atmospheric Cherenkov Telescope (IACT) in 1989 with the first positive detection of the Crab Nebula at these energies (TeV gamma-rays). This Thesis deals with observations of VHE γ-rays from objects of the northern hemisphere using the MAGIC Telescope, located on La Palma in the Canary Islands. MAGIC is currently the largest single-mirror dish telescope worldwide, with the lowest detection threshold of all ground-based instruments in High Energy Astronomy. MAGIC detects VHE γ-rays indirectly by observing the very weak Cherenkov light emitted by extended air showers generated by VHE particles interacting with the atmosphere.

The first part of this Thesis presents the predictions for the MAGIC telescope's sensitivity by means of Monte Carlo simulations. These results include the effects of the Earth's magnetic field mainly for the threshold energy of the present Cherenkov telescopes. This particular study is quite general, thanks to the development of specific simplified simulations. Such modifications should be easily be transferred to other telescopes at future observatories, such as the proposed large Cherenkov Telescope Array (CTA).

An important part of this Thesis covers the description of the monitoring programs for the control of the data quality and telescope stability. This program also performs the first standard analysis of the data and it is accessible by all the members of the MAGIC collaboration by the next morning, giving also a preliminary hint of the signal significance for each observed source, specially important for targets of opportunity and multi-wavelength campaigns.

The last part of this Thesis concentrates on efforts to search for pulsed gamma-ray emission from two of the most representative candidates from a specific class of stellar objects: the pulsars.

The Thesis work is structured in four main sections:

- A brief overview about high energy gamma-astronomy and the theories about the physics of pulsars.

  Chapter 1 describes the history of the detectors used in gamma-ray astronomy. The description and basis of ground-based detectors are explained in more detail, specifically for the MAGIC telescope.

  Chapter 2 gives a brief introduction to the main theoretical models of pulsars and their environments. This description will be focused on the kind of pulsars whose results will be presented in this Thesis.

- A study of the capabilities of the MAGIC telescope to detect sources at low energies, including the influence of the Earth's magnetic field at those energies.

This study presents also some specific results for the canonical pulsars already detected at gamma-rays.

Chapter 3 presents a study of Monte Carlo simulation results of the telescope's sensitivity above 30 GeV and its capabilities to detect a wide range of pulsars within a reasonable amount of time.

Chapter 4 extends the previous Monte Carlo studies to take into account the effect of the Earth's magnetic field in the MAGIC telescope's sensitivity. The effect on other present and future observatories is also presented.

- A complete description of the program, which checks and monitors the MAGIC telescope in a hardware and data quality basis, developed by the author.

  This is described in detail in **Chapter 5**.

- At the end of this Thesis, the standard analysis of the MAGIC data and the results on MAGIC observation of two pulsars are described.

  Chapter 6 describes the calibration, reconstruction and cleaning processes of the MAGIC data images and the background rejection methods often applied. In particular, two kinds of analysis are explained, those used respectively to reconstruct the source position and to analyze the periodical emission characteristic of pulsar sources. The methods to calculate the corresponding upper limits in case of a non-detection in our analysis are also described.

  Chapter 7 presents the results of the analysis of the MAGIC observations from two promising candidates of each kind of pulsar: canonical (PSR J0205+4232) and millisecond (PSR J0218+4232).

Table of Contents

List Of Figures

List Of Tables

Abbreviations

ADC : Analog to Digital Converter

APD : Avalanche Photo Diode

CGRO : Compton Gamma-Ray Observatory

CORSIKA : Cosmic Ray SImulations for KAscade

C.L. : Confidence Level

CT : Cherenkov Telescope

CR : Curvature Radiation

DAQ : Data AcQuisition system

DC : Direct Currents

EAS : Extensive Air Showers

EAS-PDAS : Extensive Air Showers Particle Detector Array

EECR : Extreme Energy Cosmic Rays

FADC : Flash Analog to Digital Converter

FoV : Field of View

GRB : Gamma-Ray Burst

GPS : Global Positioning System

HE : High Energies

HEGRA : High-Energy Gamma-Ray Array

HPD : Hybrid Photo Diode

HV : High Voltage

IAC : Imaging Atmospheric Cherenkov

IACT : Imaging Atmospheric Cherenkov Telescope

ICS : Inverse Compton Scattering

IGRF : International Geomagnetic Reference Field

IM : Interstellar Medium

IPR : Individual Pixel Rate

IR : Infra-Red (wavelengths)

L1T : Level 1 of Trigger

L2T : Level 2 of Trigger

LC : Light Curve

LONS : Light Of the Night Sky

LV : Low Voltage

MAGICDC : MAGIC Data Check

MARS : Magic Analysis and Reconstruction Software

MC : Monte Carlo

MJD : Modified Julian Date

MSP : Millisecond Pulsar

OG : Outer Gap model

PC : Polar Cap model

PMT : Photo Multiplier Tube

PPF : Pair Production Front

PSF : Point Spread Function

PWN : Pulsar Wind Nebula

QE : Quantum Efficiency

QOSA : Quick On Site Analysis

RF : Random Forest

SAA : South Atlantic Anomaly

SCLF : Space-Charge Limited Flow

SED : Spectral Energy Distribution

SN : Super Nova

SNR : Super Nova Remnant

SR : Synchrotron Radiation

SSB : Solar System Barycentre

UHE : Ultra High Energies

UTC : Universal Time Coordinates

UV : Ultra-Violet wavelengths

VCSEL : Vertical Cavity Surface Emitting Laser drivers

VHE : Very High Energies

WMM : World Magnetic Model

Citations to Previously Published Work

de los Reyes López, R.; 2002, *Analysis and simulation of atmospheric Cherenkov telescope data*, **Master Thesis, U.C.M.**

2 Contributions to MAGIC internal documentation:

- delosReyes R., et al, *MAGIC data check and on-line analysis program*, MAGIC-TDAS 06-11.
- delosReyes R., et al, *Effect of earth magnetic field in the MAGIC telescope effective area for gammas*, MAGIC-TDAS 03-05.

7 Contributions to International Conferences:

- *MAGIC sensitivity for pulsed emission from gamma-ray pulsars*
  R. de los Reyes, J.L. Contreras and M.V. Fonseca
  Joint European and National Astronomical Meeting, Granada (Spain), 2004.
- *Low energy γ-ray detection ($E \leq 30GeV$): effect of Earth's magnetic field and a novel trigger technique*
  R. de los Reyes, E. de Ona-Wilhelmi and J.L. Contreras.
  19th European Cosmic Ray Symposium, Florence (Italy), 2004.
- *Physics potential and first results of the MAGIC telescope*
  E. Aliu,..... R. de los Reyes et al. (8 authors)
  14th International School of Cosmic Ray Astrophysics, Sicily (Italy), 2004.
- *Effect of the Earth's magnetic field in the sensitivity of Cherenkov telescopes*
  R. de los Reyes et al. (7 authors)
  XXIX Biennial of the Royal Spanish Society of Physics, Madrid (Spain), 2003.
- *Detectability of Gamma-Ray from Millisecond Pulsars with MAGIC*
  E. Ona-Wilhelmi, R. de los Reyes
  28th International Cosmic Ray Conference, Tsukuba (Japan), 2003.
- *MAGIC sensitivity for pulsars*
  R. de los Reyes and J.L. Contreras
  I meeting of High energy Astrophysics, Barcelona (Spain), 2002.
- *Observations of gamma-ray pulsars with the MAGIC telescope*
  R. de los Reyes et al (6 authors)
  V meeting of the Spanish Astronomy Society, Toledo (Spain), 2002.

Part I

Introduction

Chapter 1

Techniques for the detection of gamma-rays: Cherenkov telescopes

This chapter introduces gamma-ray astronomy, specifically in the 10 GeV - 100 TeV energy range. It focuses on the two main techniques that have succeeded in giving reliable source detections and spectral measurements: satellite detectors and ground-based Cherenkov telescopes.

It gives an overview of the most successful high-energy detectors, the ones working nowadays and in the near future.

1.1 The Non-Thermal Universe

Due to our need for knowledge of the Universe around us, astronomical exploration proceeds in two directions. First, towards the most distant and weakest sources which require instruments with an ever-increasing sensitivity. Second, towards sources of electromagnetic radiation at all frequencies. Technical developments have so far allowed us to observe the Universe from radio waves (few Hz $\simeq 10^{-6}$ eV) to high-energy cosmic rays (E $> 10^{19}$ eV).

Optical astronomy and astrophysics deal with thermal radiation from the Cosmos, emitted by hot or warm objects such as stars or dust, up to the range of some 10^{-2} eV (IR) to 10^{3} eV (UV). On the other hand, the latest modern cosmic-ray detectors reveal processes in the Universe that emit non-thermal radiation up to 10^{20} eV and beyond. These results have shown that the energy in non-thermal processes roughly equals the energy stored in thermal radiation or in interstellar magnetic fields, implying that such non-thermal phenomena play an important role in the evolution of the Cosmos.

The non-thermal Universe is seen through the accelerated charged particles and the emitted electromagnetic radiation over wide ranges of the electromagnetic spectrum. The accelerated charged particles reach the Earth as cosmic rays arriving uniformly distributed from all directions, loosing their directional information due

to their deflection in the random interstellar magnetic fields. Therefore, with the possible exception of the highest energies, the information from cosmic rays relates to their energy spectrum and elementary composition. Apart from the cosmic rays with extreme energies, source tracking or astronomy, is only possible with the help of neutral, stable particles like γ-rays or neutrinos which travel on straight paths across the interstellar medium. Fortunately, every source of charged cosmic rays produces these neutral messenger particles when the accelerated primary particles collide with interstellar gas or interact with radiation or magnetic fields, either in their source origin or in their paths across the Universe.

The so-called multi-messenger astronomy, combining detection from radio waves to the highest-energy γ-rays, neutrinos and even gravitational waves, will provide the tools to identify cosmic accelerators and their mechanisms during the incoming decade.

1.2 Gamma-ray astronomy instrumentation

γ-ray astronomy is usually divided into three energy ranges: high energy (HE) up to 10 GeV, very high energy (VHE) from 10 GeV to 100 TeV and ultra-high energy (UHE) above 100 TeV. Each energy range has developed its own techniques to provide the most sensitive detection: below 10 GeV observations are carried out by *satellite detectors*, while the higher energies (E > 100 GeV) are the domains of *ground-based detectors*.

Three important facts govern the techniques that are used in high-energy γ-ray astronomy:

(a) the Earth's atmosphere is opaque to high-energy photons. At sea level, the atmosphere is 1030 g/cm^2 thick, which corresponds to 28 radiation lengths; this implies that the probability that a high-energy photon incident from the zenith will reach ground level without interacting electromagnetically is $\sim 3 \times 10^{-10}$. Even at mountain altitudes, where the atmosphere is considerably thinner, the probability that a photon will survive to ground level is negligibly small. Thus, only a detector above the Earth's atmosphere, in a balloon or a satellite, can detect primary cosmic γ rays.

(b) the fluxes of high-energy γ rays from astrophysical sources are quite low and decrease rapidly with increasing energy. For example, Vela, the strongest γ-ray source in the sky, has a flux above 100 MeV of $1.3 \times 10^{-5} photons/cm^2/s$, and a differential flux that falls as $E^{-1.89}$. This implies that above a certain level of energy, a detector in a satellite will be too small to detect enough photons to be useful. A $\sim 1000 cm^{-2}$ detector in a satellite would detect approximately one photon/minute from Vela above 100 MeV and one photon every two hours above 10 GeV. The pursuit of γ-ray astronomy at TeV energies must be done with much

larger instruments than those that can currently be launched on a satellite. Thus VHE and UHE astronomers use Earth-based detectors.

(c) the flux of high-energy charged cosmic rays is much larger than the γ-ray flux. These charged particles are bent in the interstellar magnetic fields so that they form an essentially isotropic background. The cosmic-ray proton flux has been measured [154] from 10 GeV to $\sim$ 100 TeV [1] :

$$\frac{dN}{dE} = (10.57 \pm 0.30) \times 10^{-2} (\frac{E}{1\ TeV})^{-(2.76 \pm 0.02)}\ m^{-2}\ s^{-1}\ sr^{-1}\ TeV^{-1} \qquad (1.1)$$

where E is expressed in units of TeV. At these energies the cosmic-ray flux is about a factor 10^3 higher than the γ-flux, so the rejection of the large cosmic-ray background is extremely important in high-energy γ-ray astronomy.

Due to the steeply falling fluxes of γ-rays from cosmic sources with increasing energy and the limited surface area of the satellites, their sensitivity to energies above 10 GeV is limited by very low count statistics. Conversely, current ground-based detectors provide an effective collection area some orders of magnitude larger, covering the range above 100's of GeV with good sensitivity.

1.3 Satellite-based detectors

It was not until the launch of the *OSO-3 satellite*, in 1963, that γ-ray astronomy with satellites started to obtain its first results. This satellite detected γ-ray emission of 100 MeV from the galactic plane, whose flux was approximately the one expected from the interaction of cosmic rays with the galaxy interstellar gas. In the 1970's two γ-ray satellites were launched: SAS-2 in 1972 and COS-B in 1975. The *SAS-2 satellite* covered the energy range 20 MeV - 1 GeV with an effective area of 540 cm^2, the *COS-B gamma-ray detector* worked in the range between $\sim$ 2 keV - 5 GeV with an effective area around 50 cm^2 at 400 MeV and with a 2-12 keV proportional counter mounted on the side of the gamma-ray detector.

The most sensitive high-energy γ-ray telescope to date was the *EGRET instrument* on board the *Compton Gamma-Ray Observatory (CGRO)*, launched in 1991. EGRET was similar to the COS-B detector, although it was much larger with an effective area of more than 1000 cm^2 between 150 MeV and 1 GeV and worked in the 30 MeV - 30 GeV energy range, with an angular resolution from 5.5 degrees at 100 MeV, up to 0.5 degrees at 5 GeV. The principal scientific objectives of the EGRET instrument were to perform an all-sky survey of high-energy γ-ray emission and to make detailed studies of γ-ray emitting sources. Its major discoveries include not only

[1] The fit (χ^2/ndf = 0.7) is restricted to this energy range to minimize the effect of solar modulation in the cosmic rays. From 400 MeV/nucleon to 10 GeV/nucleon, the shape of the spectra is affected by the activity of the solar cycle.

the identification of blazars as intense γ-ray emitters, but also the high-energy tails of several γ-ray bursts. EGRET observations of the LMC (Large Magellanic Clouds) and SMC (Small Magellanic Clouds) were used to confirm that cosmic rays are galactic. EGRET obtained the first reasonably accurate map of the diffuse gamma-ray emission of the Milky Way and made a reliable measurement of the isotropic, presumably extragalactic diffuse emission. EGRET data were also used to confirm the Geminga source as a radio-quiet pulsar, the first detected in gamma-rays, followed by six more, including the first millisecond pulsar PSR J0218+4232.

For the detection of primary photons, satellite-based instruments together with techniques developed in experiments at particle-accelerators have to be used. Figure 1.1 illustrates their working principle. Two measurements have to be taken: the photon direction, determined by tracking detectors following conversion of the photon into an electron-positron pair; and the photon energy, usually measured by a total-absorption calorimeter.

The following methodology is used: a photon crosses the tracker producing an $e^{\pm}$ pair. The tracker records the path of the charged particles that gives information about the primary particle direction. The electromagnetic cascade (initiated by the pair $e^{\pm}$) develops in the calorimeter, which measures the integrated path length of the charged particles in the cascade, which is proportional to the energy of the primary photon. A charged-particle veto counter discriminates against the large background produced by incident-charged cosmic rays.

There are two important parameters for a gamma ray detector: the angular resolution and the effective area. A good angular resolution is important for identifying point sources of photons and for minimizing the effects of diffuse backgrounds. There are two contributions to this variable, the intrinsic angular difference in the pair-production process and the multiple Coulomb scattering angles in the converter. This part of the angular resolution can be reduced by using thinner converters, but this improvement in the angular resolution implies an increase in the energy resolution for a given detector configuration. Good energy resolution is needed to determine the energy spectrum of a source.

Another important parameter of a detector is its effective area, which is defined as the physical area of the detector convoluted with the γ-ray detection efficiency:

$$A_{eff}(E) = \frac{N}{\phi(E)T} \tag{1.2}$$

where ϕ(E) photons/m^2/s is the photon flux from a point source for a period of time T and N is the number of recorded events.

The *INTEGRAL* satellite was launched in 2002. It works in the range 20 keV - 8 MeV (SPI detector), with a field of view of 16°, a detector area of 500 cm^2 and an angular resolution of 2 degrees. Within the first year 12 new, strong high-energy galactic sources were detected, including Crab Nebula, and a total of six confirmed Gamma-Ray Bursts (GRBs). Another experiment, SWIFT (a gamma-ray

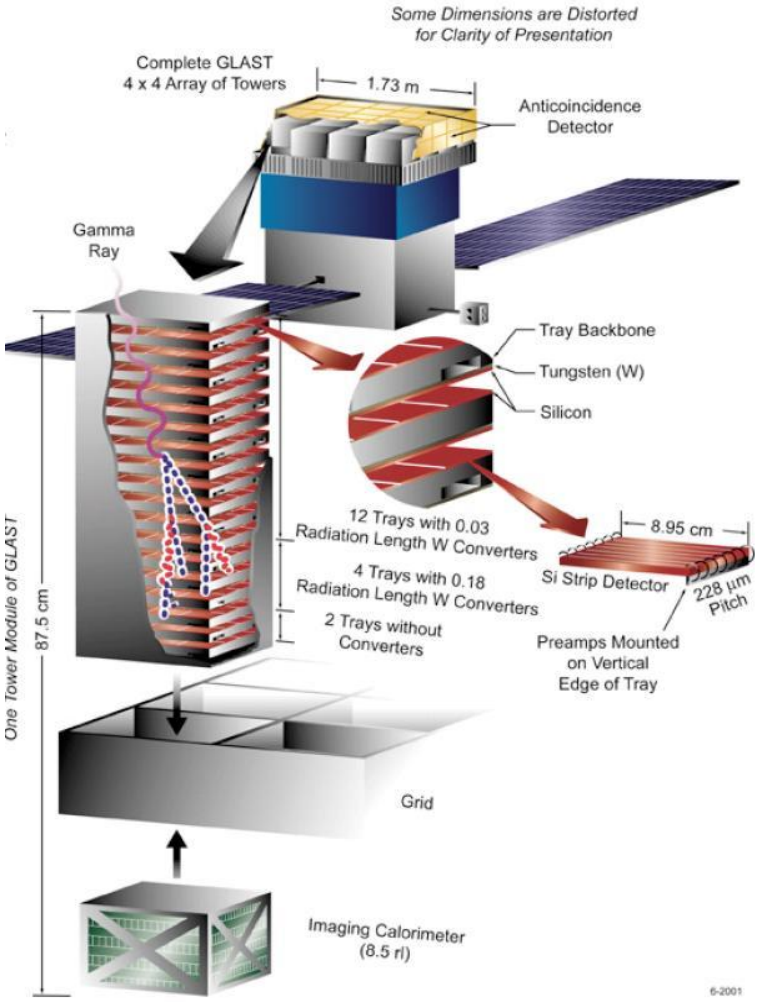

Figure 1.1: *Schematic view of GLAST (Gamma-ray Large Area Space Telescope) [180].*

burst mission) was launched in 2004. It is a multi-wavelength observatory (gamma, X-ray, UV and optical) and with its 20-75 seconds reaction time - around three times more sensitive than BATSE (CGRO) - Swift has observed more than 90 GRBs and X-ray afterglows for about 70 of them. Another satellite launched 2 years ago is AGILE (a light-weight gamma-ray imager).

γ Astronomy from space has been restricted up to now to energies below 30 GeV, due to the low photon flux at high energies and the small satellite areas, but the next generation of space detectors will hopefully overcome these limitations. Among them will be the *AMS* detector, that will be installed on board the International Space Station, with an energy range between 300 MeV and 300 GeV and with 0.5 m^2sr aperture. It is expected to have a sensitivity similar to that of EGRET. In 2008,

the *GLAST* satellite, whose sensitivity for point sources will be from 50 to 100 times better than that of EGRET, covering an energy range from 10 MeV up to 200 GeV.

Other future experiments proposed or under development are Spectrum-X-Gamma (SXG), Andromeda (a coded-aperture gamma-ray telescope) and MEGA (Medium Energy Gamma-ray Astronomy).

1.4 Ground-based detectors

For energies above 100's of GeV, the showers of secondary particles created by the interactions of the primary particles in the atmosphere are extensive enough to be detectable from ground with Earth-based γ-ray detectors. At ground level, the high-energy photons can be observed indirectly: gamma-rays striking the Earth's atmosphere interact with air molecules giving rise to a shower of secondary particles called *Extensive Air Showers* or EAS. Earth-based γ-ray astronomy instruments detect the secondary particles of the EAS and the different types of radiation associated with their interactions with the atmosphere: *Cherenkov radiation* by relativistic shower particles or isotropic *fluorescence emission* due to the atmospheric-excited nitrogen. The main limitation of these detectors is the rejection of the high background of showers initiated by charged cosmic rays and a high-energy threshold due both to atmospheric absorption and to the effect of the Earth's magnetic field on showers produced by low energy photons. On the other hand, they have the advantage of their large effective areas due to the wide extension of the EAS.

An extensive air shower can be detected by observing either the shower front of particles which reach the ground with *EAS-particle detector arrays*, or the Cherenkov radiation and fluorescence emissions produced in the shower, with *air Cherenkov/fluorescence detectors*, usually installed on mountain tops, for a lower threshold.

1.4.1 Extensive Air Showers (EAS)

On its way through outer space, cosmic radiation can interact with the interstellar medium and the sub-products of these interactions are the particles that reach the Earth's atmosphere, the so-called Cosmic Rays. They are made up of atomic nuclei, γ-rays, electron, positrons, neutrinos and other types of elementary particles. The proportion of gammas and protons that reach the atmosphere is $\sim 1\gamma$ per 10^4 protons.

EAS development

When cosmic and γ-rays enter the Earth's atmosphere they have very high energies, interacting with the atmospheric nuclei through complicated processes giving rise to a certain multiple of secondary particles which form the Extensive Air Shower or

EAS. Due to the energy loss resulting from these processes, the shower does not keep growing until it reaches the ground. Instead of growing, in every process the energy per particle is reduced so that the shower gets to a critical point where dissipation processes outweigh the creative ones and the shower begins to extinguish.

Depending on the nature of the particles, the interactions with the atmosphere can be of two types: *charged particle-matter* or *radiation-matter*. In the first case, as a result of inelastic and elastic collisions, the charged particles suffer deflections from its incident direction and at the same time, energy loss through ionization, emission of *Cherenkov radiation*, *nuclear reactions* and *bremsstrahlung*. In the second case, the loss of energy is due to *photoelectric effect* for photons at energies less than 100 keV, *Compton scattering* for photons around 1 MeV and *pair production* which begins to be important at energies above 1 MeV and becomes dominant at energies higher than 25 MeV.

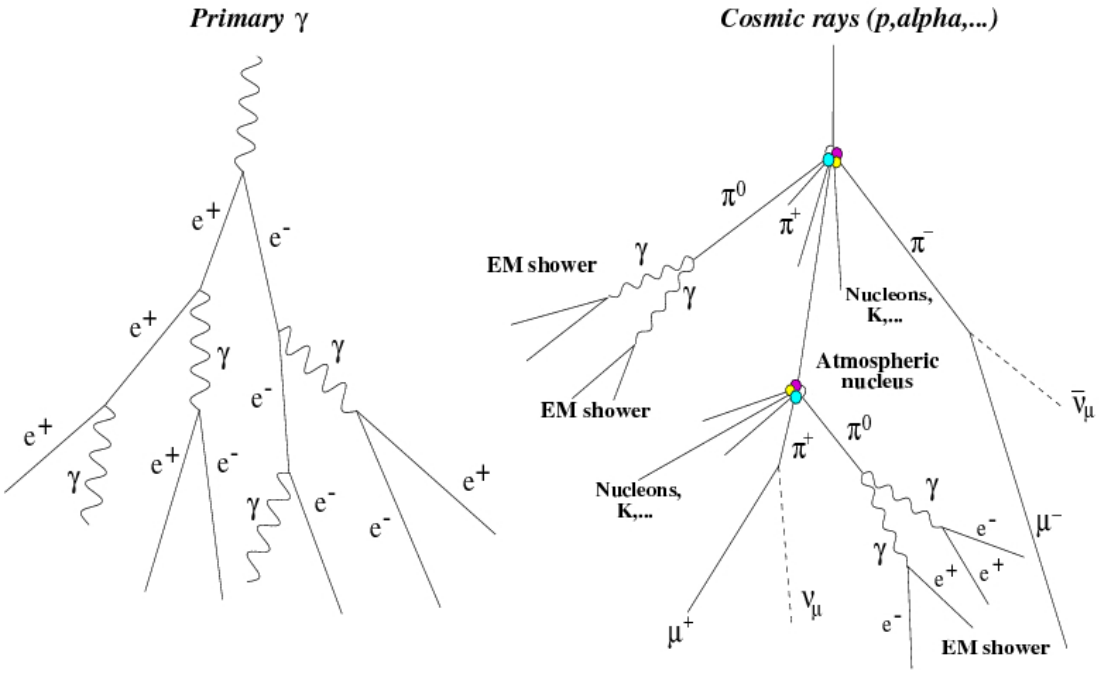

Figure 1.2: *Geometric model of extensive air shower development and the emission of Cherenkov radiation for γ-ray and cosmic ray shower [52]*

There are some differences in the development of an air shower depending on the primary particle originating the shower (fig. 1.2):

1. *Gamma-ray initiated shower*. The electromagnetic shower is the result of the combined effect of pair production ($e^{\pm}$) and bremsstrahlung emission. To have

an idea, let consider the simplified model of development of an EAS [108]. Assuming an incident photon of energy E_0 traverses a distance R before creating an electron-positron pair so, taking into account that the radiation length in the atmosphere is $\xi_0 \sim 36.7 g/cm^2$, that the probability of a photon or electron to interact is exp(-R/ξ_0)=1/2 and considering that in each interaction the energy is equally divided between $e^{\pm}$ and γ's, then at distance nR into the shower, there will be created then 2^n particles, each with an average energy $\frac{E_0}{2^n}$. The resulting electromagnetic cascade grows nearly exponentially as it propagates through the atmosphere until the average energy of the particle drops below the critical energy E_c ($\sim 81 MeV$ per particle). At this critical energy, the energy loss by ionization, via atomic collisions, becomes dominant rather than by bremsstrahlung emission, thus the energy is lost from the shower and the number of particles in the EAS decreases as the shower continues to propagate, halting the cascade. For γ-rays, the critical energy corresponds to a point where Compton scattering begins to be more important than pair production. In this model, the maximum penetration depth in the atmosphere (maximum of longitudinal development of the shower) is $X_{max} = \xi_0 ln \frac{E_0}{E_c}$, and the total number of photons and electrons at this point is $N_{max} = \frac{E_0}{E_c}$.

A better approximation for the number of particles ($e^{\pm}$) produced in a shower as a function of the primary energy and atmospheric depth, is given by Greisen's equation (1.3) [82]

$$N_e(t) = \frac{0.31}{\sqrt{ln(E_0/E_c)}} \cdot exp[(1 - 1.5 \cdot lns) \cdot t] \tag{1.3}$$

where $s = \frac{3t}{t+2ln(E_0/E_c)}$ is known as the *age parameter* that indicates the degree of development of the shower (s=0 the first interaction, s=1 the maximum development of the shower and s=2 where the shower begins to extinguish)(fig. 1.3). $t = \frac{X_{air}}{X_0} \cdot exp(-H/H_0)$ is the atmospheric depth in terms of radiation length, where the bremsstrahlung radiation length $X_0 = 37 g/cm^2$, the column height of air at ground $X_{air} = 1013 g/cm^2$ and the scale height of the atmospheric pressure $H_0 = 7.3\ km$.

In an electromagnetic shower, the particles are ultra-relativistic and the dominant physical processes are sharply peaked forward. Consequently, the cascade arrives at the ground in a thin front only a few meters thick. The lateral extent of a shower is due primarily to multiple Coulomb scattering of the electrons and positrons and it is described by the so-called NKG function (Nishimura-Kamata-Greisen)(eq. 1.4) [142].

$$\rho(r) = \frac{N}{r_1^2}\Big(\frac{r}{r_1}\Big)^{s-2}\Big(1+\frac{r}{r_1}\Big)^{s-4.5} \frac{\Gamma(4.5-s)}{2\pi\Gamma(s)\Gamma(4.5-2s)} \tag{1.4}$$

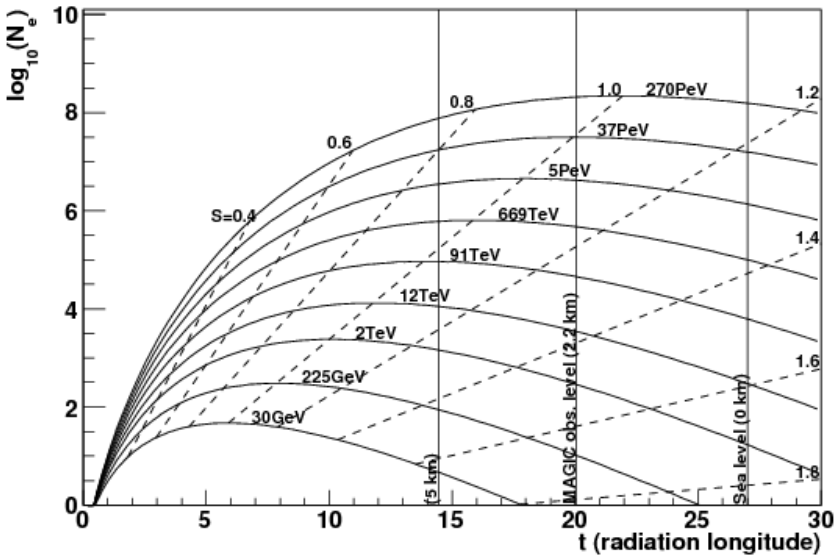

Figure 1.3: *Longitudinal development of an EAS following the Greisen's formula (eq. 1.3). The filled lines correspond to different energies of the primary γ-ray (label). The dotted lines represents the points with equal age parameter s (s=0, first interaction; s=1, max. development; s=2, shower extinction). The MAGIC observation level (2.2 km), sea level (0 km) and 5 km altitude are marked as vertical lines.*

where N is the total number of charged particles in the shower, r_1 is the Moliere multiple scattering unit. It is important to note that this function represents the average shower behaviour and that fluctuations in this behaviour can be large.

2. *Hadron initiated shower.* A larger amount of incident high-energy cosmic rays, protons and nuclei, also interact with atmospheric nuclei (N or O) high in the atmosphere producing extensive air showers of further particles (like pions $\pi^{\pm}$, π^0; kaons $K^{\pm}$ and nucleons) which in turn produce disintegrations, in which the nuclear collision length is 62 g/cm^2 for protons and smaller for heavier nuclei. The fragments of the incident nucleus and the newly created nucleons, form the so-called *hadronic core* of the shower. If the original cosmic ray has enough energy, some of its fragments could reach the ground, where some of the disintegration lifetimes are:

$$\begin{aligned} \pi^0 &\rightarrow 2\gamma & \tau &= 1.8 \times 10^{-16} s \\ \pi^{\pm} &\rightarrow \mu^{\pm} + \nu_\mu & \tau &= 2.5 \times 10^{-8} s \\ \mu^{\pm} &\rightarrow e^{\pm} + \nu_e + \nu_\mu & \tau &= 2.2 \times 10^{-6} s \end{aligned} \tag{1.5}$$

The decay of the $\pi^0 \rightarrow 2\gamma$ originates what it is called the electromagnetic component of the hadronic shower, and has the same development as a gamma-ray initiated shower.

In spite of its shorter life time, the muons with an energy of 2 GeV can reach the ground without disintegrating, representing 75% of all the secondary particles that reach the ground at sea level. The muon lateral distribution is considerably wider than that of the electromagnetic particles [83]. There are roughly 20 times more muons in a hadron-initiated EAS than in a photon-initiated EAS of the same energy.

Cherenkov radiation in EAS

In addition to shower particles, Cherenkov photons are produced in an EAS by the electrons that exceed a minimum threshold. For primary energies below 20 TeV the cascades die out in the upper atmosphere (h > 6 km) but the Cherenkov radiation, produced by charged particles travelling faster than the speed of light in air, penetrates to ground level where it might be collected.

The *Cherenkov effect* involves radiation emitted by the medium under the action of the field of the particle moving in it with a velocity higher than the velocity of the light in the medium. In the case $v > c/n$, all the molecules around the particles get an instant dipole except for the region ahead of the moving particle, because the particle travels faster than the electromagnetic waves emitted by the particle. Thus a net polarization of the medium is produced along the particle track, which consequently radiates brief electromagnetic pulses. For these pulses to be coherent, the particles have to travel from A to B in the same time that the light travels from A to C (fig. 1.4), which can be geometrically expressed as the Cherenkov angle at which the radiation can take place:

$$\cos\Theta = \frac{1}{\beta \cdot n(\lambda)} = \frac{c_{medium}}{v_{part}} < 1 \tag{1.6}$$

To get coherence, the following conditions must be fulfilled: First, that the length l of the track of the particle in the medium should be large compared with the wavelength λ of the radiation, otherwise diffraction effects will become dominant. Second, the differences in the times for particles to traverse successive distances λ should be small compared with the period $\frac{\lambda}{c}$ of the emitted light.

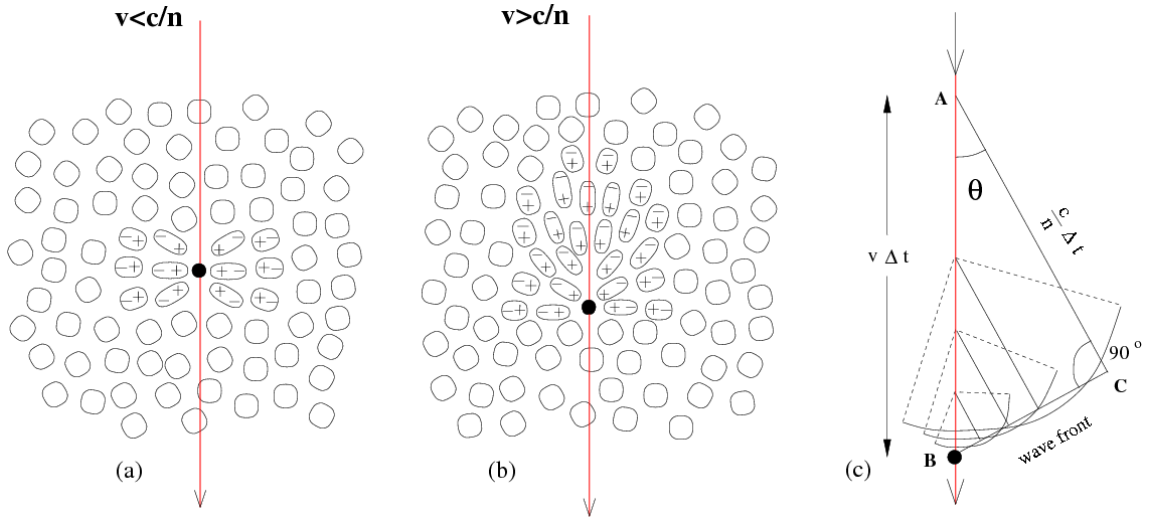

Figure 1.4: *The polarization set up in a dielectric when a charged particle passes through. (a)Low velocity. (b)High velocity. (c) Huygens construction to illustrate coherence and to obtain the Cherenkov angle* Θ. *[54]*

Cherenkov light is a thin front resulting in a pulse of 2-3 ns duration. The total distance travelled by all particles above the Cherenkov threshold is directly related to the energy of the primary particle, so the Cherenkov light carries with it information related to the exact point of origin of the primary γ-ray on the celestial sphere and also the energy of the primary particle.

If we express the refraction index as $n = 1 + \delta$ where $\delta << 1$, and taking the minimum angle for which the Cherenkov effect may occur ($\theta = 0$), equation 1.6 is transformed in $\beta_{max} = \frac{1}{n}$. $\gamma = \frac{1}{\sqrt{1-\beta^2}} = \frac{E}{E_0}$ (E_0=mc^2=0.511 MeV) which gives the minimum energy threshold (E_{th}) of a charged particle to emit Cherenkov radiation [142]:

$$E_{th} \simeq \frac{E_0}{\sqrt{2\delta}} \tag{1.7}$$

The angle of maximum emission of Cherenkov light with respect to the particle direction varies with height as well as in the energy threshold, and corresponds to $\beta = 1$ (v = c):

$$\cos\Theta_{max} = \frac{1}{n} \simeq 1 - \delta \quad ; \quad \cos\Theta_{max} \sim 1 - \frac{\theta^2}{2} << 1$$
$$\Rightarrow \quad \Theta_{max} \simeq \sqrt{2\delta} \simeq \frac{E_0}{E_{th}} \tag{1.8}$$

in both limits, the refraction index can be approximated by an exponential atmosphere, $\delta = \delta_0 \cdot exp(-h/H_0)$ where $\delta_0 = 2.9 \times 10^{-4}$ and $H_0 = 7.1 - 7.5$ km.

Through equations 1.3 (with s=1) and 1.8 one can establish analytically the maximum Cherenkov angle at the EAS maximum as a function of the energy of the primary particle (E) (fig. 1.5) for different zenith angles of observation. Figure 1.6 shows the impact parameter of Cherenkov light emitted at the point of maximum development of the EAS (s=1) for different energies of the primary particle and different zenith angles.

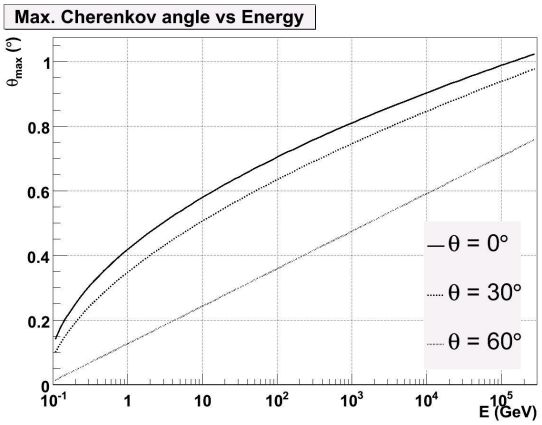

Figure 1.5: *Maximum Cherenkov angle of light emitted at the maximum of the EAS development (s=1) as a function of the energy of the primary particle for different zenith angles (0°, 30° and 60°).*

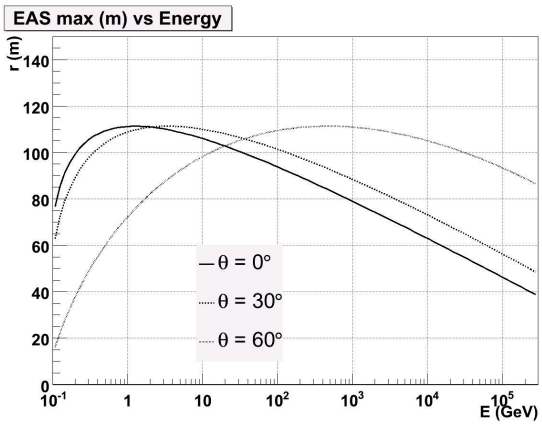

Figure 1.6: *Impact parameter of light emitted at the point of maximum of the EAS development (s=1) as a function of the energy of the primary particle for different zenith angles (0°, 30° and 60°).*

Both figures consider only the longitudinal development of the EAS. Figure 1.5 shows that the maximum Cherenkov angle (similar to the dist parameter of the image) increases with the energy of the EAS primary particle while it decreases with the zenith angle of observation. The opposite happens with the impact parameter corresponding to the maximum development of the EAS (fig. 1.6). This impact parameter is an approximation of the EAS hump because the plot does not consider the lateral distribution of the shower. In real Monte Carlo (MC) simulations the shower hump will be larger than the one shown in figure 1.6. However, the behaviour with the energy and the zenith angle of observation will be the one shown in the figure: the impact parameter will decrease with the energy of the primary particle of the EAS while it will increase with the zenith angle.

The lateral distribution of Cherenkov light is sensitive to the longitudinal shower development. Steep lateral distributions are associated with showers that develop close to the observer, while showers developing high in the atmosphere have a broader distribution. The number of photons per meter generated by a particle of energy E

emitting Cherenkov light is given by [149]:

$$\frac{dN_p}{dl} = 2\pi\alpha Z^2 \int \frac{sin^2\theta_c(\lambda)}{\lambda^2} d\lambda \tag{1.9}$$

The net effect is a beam, which exhibits a characteristic pattern on the ground called a *Cherenkov ring*. This beam is 6° at the shower core, although Cherenkov light scattered by the atmosphere can be detected at angles as large as 25°.

Through (eq. 1.8) we can establish a relation to obtain the distance R_{core} between emitted Cherenkov photons and the particle trajectory at a certain observation height h_{obs}:

$$R_{core} = (h - h_{obs}) \cdot \tan\Theta_{max} \tag{1.10}$$

A single relativistic particle starts to radiate high in the atmosphere (altitudes around 8-10 km), with a maximum Cherenkov angle that varies between 1-1.5 degrees. Therefore, we can consider $\Theta_{max} << 1$, and the distance of the emitted Cherenkov ring at ground $R_{core} \simeq \sqrt{2\delta_0} \cdot (h - h_{obs}) \cdot exp(-h/2H_0)$.

The distance at which the maximum of the Cherenkov light pool is emitted is given by equation 1.10. In particular, for the MAGIC observation level (2200 m) R_{core} has a maximum altitude around 17 km at which most of the Cherenkov light by the particle is emitted, with a R_{core} of $\sim$ 115 m.

1.4.2 EAS detectors and techniques

As detailed in section 1.4.1, an extensive air shower can be detected from the ground by observing either the shower particles that reach the ground or the Cherenkov radiation produced in the shower. In the first case, the *particles* (electrons, muons,...) are detected by large detector arrays using scintillation counters or water tanks. In addition, hadrons are registered in compact calorimeters. Alternatively, *Cherenkov light* generated by relativistic shower particles in the atmosphere is collected with imaging or light-integrating detectors. Detectors based on the atmospheric Cherenkov technique consist usually of one or more mirrors that concentrate the Cherenkov photons onto fast optical detectors. Photomultiplier tubes (PMTs) placed in the focal plane are generally used to detect these Cherenkov photons.

Another technique to register the air showers detects the isotropic *fluorescence emission*, due to the excitation of the atmospheric nitrogen by the EAS-charged particles.

In all these cases, the properties of the EAS are used to infer information about the primary particle that initiated it.

The integral flux can be derived from the observed number of events (upper limit) above background and the detector effective area versus energy. There is some dependence of the derived integral flux on the assumed spectral shape; this dependence can be minimized by giving the integral flux above the mean energy of the detector [79].

In recent years, a new technique has been developed to detect EAS through its *radio emission*. This kind of detector measures the radio pulses produced by e^-/e^+ pairs gyrating in the Earth's magnetic field (geosynchrotron). This phenomenon will produce coherent emission at low frequencies (20-100 MHz), well detectable for showers above 100 TeV [63]. Currently the LOPES 10-antennas detect radio emission from EAS in coincidence with the KASCADE-Grande experiment (Germany). Large radio astronomy facilities such as LOFAR (LOw Frequency ARray) at the Auger site, Argentina; CODALEMA (Cosmics Detector Array Logarithmic ElectroMagnetic Antennas) at the Nanay Radio Observatory, FRance; and SKA (Square Kilometer Array), South Africa, as well as satellite-based radio receivers might be used for this type of detection in the future.

EAS-particle detector arrays

Extensive air-shower particle detector arrays (EAS-PDAs) are generally used to detect EASs produced by ultrahigh energy particles ($\gtrsim 10^{14}$ eV).

Their fluxes are expected to be small, so detection areas larger than $10^4 m^2$ are needed. However, the fact that a large number of particles reach the ground in a UHE shower (eq. 1.3) means that an EAS-PDA needs to sample only a relatively small fraction of these particles.

An EAS-PDA generally consists of a number of charged-particle detectors [2] spread over a large area within a certain medium (atmosphere, water, ice, etc). Typical arrays have from 50 to 1000 scintillation counters (with a size of $\sim 1m^2$ each) spread over an area of $10^4 - 2 \times 10^5 m^2$ (fig. 1.7). The sensitive detector area is less than 1% of the total enclosed area of the array. Table 1.1 lists the recent major extensive air-shower particle detector arrays.

In general, the arrays have the disadvantages of a higher energy threshold (> 50 TeV) and a worse background rejection (>50%) than the Cherenkov telescopes (CT) (< 200 GeV, $> 99\%$). However, they have a larger field of view ($> 45^o$ vs. $\sim 2^o$ for CT) and duty cycle ($> 90\%$ vs. 5-10% for CT).

The direction of the primary particle is reconstructed by measuring the relative times at which the individual counters in the array are struck by the shower front [1]. The angular resolution for ground-based detectors depends upon properties of the EAS and the detector:

$$\sigma_\theta = (K\sigma_t)/(N\Delta) \tag{1.11}$$

where σ_θ is the rms projected angular resolution, the constant K ~ 1, N is the number of hit detectors, σ_t is the measured rms timing width in nanoseconds as seen by each detector, and Δ is the separation (in meters) between neighbouring detectors. For example, for HEGRA EAS-PDA, the angular resolution had the form of $\sigma_\theta \propto N^{-0.87}$.

[2] Although the scintillators detect mainly charged particles, they can also detect γ-rays. For this purpose sometimes they are covered by lead shields to detect the secondary pairs ($\gamma \rightarrow e^+ e^-$)

Experiment	Location	Array area (m^2)	No. detectors	E_{peak} (TeV)	μ Det. area (m^2sr)	Event rate (s^{-1})	Years operational
CYGNUS	Los Alamos, N. Mexico 800 g/cm^2 35.9°N,106.3°W	8.6×10^4	204	50	120	5	1986-96
CASA-MIA	Dugway,Utah 870 g/cm^2 40.2°N,112.8°W	2.3×10^5	1089	110	2,500	20	1991-96
HEGRA EAS-PDA	La Palma, Canary Isl. 800 g/cm^2 28.8°N,17.7°W	4.1×10^4	257	50	150	12	1992-2002
SPASEI-II	South Pole 690 g/cm^2 90°S	1.6×10^4	120	100?		1	1987-2004
EASTOP	Gran Sasso 35.8°N, 138.5°E	10^5	35	10-10	140		1989-2000
IceTop		10^6	160	300	1	0.1	2005-
AGASA	Akeno Obs. 35.8°N, 138.5°E	10^8	111	$>10^{20}$	10^6 (*)		1993-2002
Milagrito	Jemez Mts., N. Mexico 750 g/cm^2 35.9°N,106.7°W	7.8	228	1		400	1997-98
MILAGRO		4.8×10^3	723	1			2004-
TibetI-II	Yangbajing, Tibet 606 g/cm^2 30.1°N,90.5°E	3.71×0^4	697	3		200	1990-
ARGO-YBJ		6.7×10^3		0.1			–
KASCADE	Karlsruhe, Germany	4×10^4	252	10^4-10^6	128 (*)	8 (**)	1993-2003
Grande		5×10^5	252+37				2004-

Table 1.1: *Recent major extensive air-shower particle detector arrays. The corresponding new generation currently under construction (Year operational —). [57] [16] [138] [12] [177] [176] [178] (* the acceptance of the detector is 1sr) (** total number of events)*

Figure 1.7: *Tibet I EAS-PDA at Yangbajing (Tibet). The array consists of 697 scintillation counters (white cubes) spread over a* $\sim 4 \times 10^4$ m^2 *area at 4 km a.s.l. [175]*

The energy threshold of an EAS-PDA depends upon the minimum number of counters struck to reconstruct a shower, the altitude of the array and the size and spacing of the counters. The energy threshold of an array has a lot of fluctuations (into the range 1-100 TeV) since the number of shower particles reaching the ground fluctuates greatly from shower to shower for identical primary particles, the main source of these fluctuations is the variation in the altitude and the nature of the first interaction.

An EAS-PDA does not measure the energy of the primary particle properly, the energy response has therefore to be determined with the aid of Monte Carlo simulations of air showers and the array. As with satellite-based detectors, the energy response of an array is better described by the effective area (A_{eff}). However, while the energy response of a satellite-based detector is $\frac{\Delta E}{E} \sim 50 - 100\%$, for ground-based detectors, the definition of A_{eff} includes the effects of shower fluctuations. These fluctuations affect the probability that an EAS of energy E will trigger the detector. A_{eff} is a function of zenith angle and the primary particle, but very similar to the dimensions of the array, from $10^3 m^2$ for MILAGRO or $10^4 m^2$ of HEGRA up to $10^9 m^2$ for bigger arrays.

Air fluorescence detectors

All EAS produced by the interaction of cosmic rays with the Earth's atmosphere are accompanied by isotropic emission of Ultraviolet (UV) fluorescence induced in air Nitrogen by the secondary charged particles in the EAS. The result is an isotropically diffuse optical-UV signal emitted along the EAS trajectory followed by the Cherenkov light(fig. 1.9).

This scintillation light is collected using a lens or a mirror and imaged onto a

camera located at the focal plane. The camera pixelizes the image and records the time of arrival of light and the amount of light collected at each pixel. This technique works on clear and moonless nights using very fast camera elements to record light flashes of a few microseconds in duration.

This technique was used for the first time by the *Fly's Eye* detector (1981-1993). Its successor, *High Resolution Fly's Eye (HiRES)*, was operative until 2006.

Starting in 2004, the *Pierre Auger Observatory (PAO)* experiment is unique since it is the first experiment that combines two independent methods to detect and study high-energy cosmic rays: fluorescence detectors and an array of Water Cherenkov Detectors (water tanks). This combination allows cross-calibration and reduction of systematic effects that may be intrinsic to each technique. The final observatory will consist of 1600 water tanks distributed over 3000 km^2. The energy threshold is $\sim 10^{18}$ eV. At the end of 2006, there were 1285 tanks deployed with 996 recording data and 18 of the 24 fluorescence detectors operational.

Among the next generation of atmospheric fluorescence experiments there is *ASHRA (All-sky Survey High Resolution Air-shower)* detector, currently under construction on the Hawaii Islands. It will monitor at the same time optical, fluorescence and Cherenkov radiation from EAS and transient objects with a wide FoV and high resolution. Also the *Telescope Array (TA)* in Utah has to be mentioned, with its set of multiple detectors for fluorescent light plus ground array.

Future projects are planned to observe the EAS fluorescence from the space. This is the case of the pair of satellites *OWL (Orbiting Wide-angle Light-collectors)* and *EUSO (Extreme Universe Space Observatory)* on board of the ISS (International Space Station). By observing atmospheric fluorescent light from orbit, we can get an effective detection area per solid angle of $2.3 \times 10^5 km^2 sr$. The resulting geometry factor exceeds by a factor of 30 that of any proposed Earth-based cosmic ray detector.

Solar plants

Another technique for the detection of EAS consists in the use of already existing solar power plants as non-imaging gamma-ray telescopes although nowadays no solar experiment is active any more. These solar plants consist of 100's of orientable mirrors, known as *heliostats*, each one with a reflecting surface of $\sim$40 m^2. Usually these heliostats are oriented to reflect sunlight into a concentrator located in a central tower, where water, oil, sodium or other substances are heated up to produce electricity. In the same way, the field of heliostats can be used to reflect the Cherenkov light generated in an EAS to the specially designed detectors placed in the central tower (fig. 1.8). Due to technical restrictions, it was not possible to use all the heliostats, and the typical area used to collect the Cherenkov light was $\sim$3000 m^2, equivalent to that of a Cherenkov telescope of 60 m diameter.

Four experiments were based in solar plants: *CELESTE* (the Themis solar electrical plant, in the French Pyrenees), *SOLAR2* (Riverside, University of California),

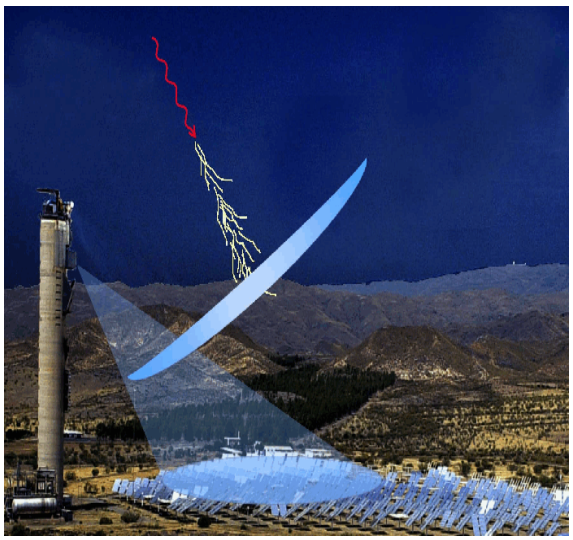

Figure 1.8: *CESA-I was used at night for the detection of the Cherenkov light produced by extensive air showers generated by cosmic gamma-rays (artistic view) [181].*

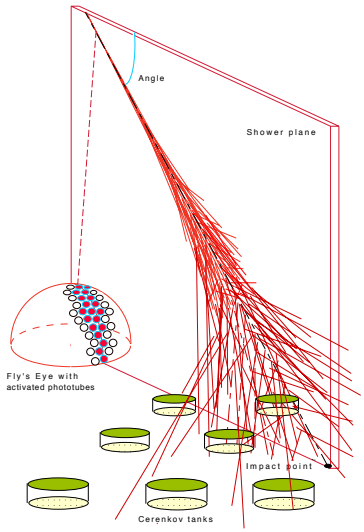

Figure 1.9: *Scheme of the Auger principle. Fluorescence detector and water tanks (EAS-PDAs), together with designed energy supplies [182].*

STACEE (at the National Solar Thermal Test Facility (NSTTF), New Mexico) and *GRAAL* (the CESA-I solar plant in Almeria, Spain). This last one was different from the other three in the fact that it used only one detector (central tower) to collect the light reflected by several heliostats, instead of having one detector for each heliostat. This had the advantage of an easier design, assembly, calibration and maintenance at the price of a worse signal-noise relation and therefore higher energy threshold.

In GRAAL, the Cherenkov light reflected by the heliostats went into concentrators located in the central tower, which focus the light onto one photo-multiplier tube (PMT). Winston cones, each with an angular acceptance of 10 degrees, were used as concentrators of Cherenkov light into a single PMT. When the signal produced in several PMTs were compatible with the expected signal for a shower (trigger condition), the time traces were recorded on magnetic tapes for later analysis. The GRAAL detector had an effective area of 12000 m^2 for γ-rays, an energy threshold of 250 GeV for γ-ray at zenith angle of 30 degrees. It observed the Crab pulsar for about 64 hours getting an excess of 4.5 σ in the central region [14].

Imaging atmospheric Cherenkov telescopes

An imaging atmospheric Cherenkov telescope (IACT) consists of a parabolic reflector and a camera placed on its focal plane. Usually the reflector surface is a tessellated mirror made out of smaller spherical mirrors with a radius that gives the

best image quality, this mount being called Cotton-Davis. The mirror is supported by a frame structure placed on an azimuthal or equatorial mount. Cherenkov telescopes differ from the optical ones in the large field of view required and in the extremely fast detector optics which rules out present CCD detectors and ungated image intensifiers. Usually the reflector of an imaging telescope provides a typical optical resolution of 0.1-0.2 degrees within a field of view of 2°-3° in diameter.

Telescope	ϕ (° ’ “)	**Mirror** (m^2)	**No. tel.**	**No. pixels**	**Pixel** (°)	E_{th} (GeV)	**FoV** (°)
VERITAS	31 40 51 N	78	4	499	0.15	100	3.5
CANGAROO-III	31 05 56 S	78	4	427	0.17	100	3.4
MAGIC	28 45 34 N	236	1	577	0.1-0.2	80	3.8
HESS	23 16 18 S	108	4	960	0.16	100	5

Table 1.2: *Summary of the characteristic parameters of some Cherenkov telescopes presently operative. [168] [171] [172] [173]*

A Cherenkov telescope uses a pointing-sensitive light detector in its focal plane to provide images of Cherenkov light showers. Several factors limit the amount of Cherenkov light collected by the detector, the first one being the energy of the primary particle. The second effect is the refractive index of the atmosphere which decreases with the height in the atmosphere and is inversely proportional to the light emitted. Therefore, at higher altitudes, fewer particles are above the Cherenkov emission energy threshold so the amount of light emitted is lower. Other factors that influence the light detection efficiency the atmospheric absorption (15% of the light emitted in an EAS), mirror reflectivity (around 90% for aluminium mirrors from 300 nm) and the quantum efficiency of the photomultipliers (QE), being around 20%, depending on the wavelength, for good photomultipliers. Taking into account all of these factors, only a small fraction of the total Cherenkov light emitted in an EAS in the direction of the mirror is converted into signal.

For example, a Cherenkov telescope with a mirror diameter of around 10 m ($\sim 100m^2$ area) means that only 0.1% of the Cherenkov light of a pool $\sim 10^5 m^2$ is collected. The area needed to provide the necessary minimum signal for detecting a shower of energy E_0 is:

$$N(ph/m^2) \cdot A_{mirror} \cdot M_{ph.e./ph.} \geq \text{minimum signal} \tag{1.12}$$

where $N(ph/m^2)$ is the average number of photons provided by a gamma shower of energy E_0 up to the impact parameter ~ 125 m; A_{mirror} is the mirror area; $M_{ph.e./ph.}$ is the Cherenkov photon conversion factor that takes into account all the factors listed above and minimum signal is the minimum number of photoelectrons needed to reconstruct a reliable image. In order to have a good image to parameterize reliably

for a given pixel size of 0.25°, the minimum signal $\sim 60-100$ *pheisnecessary.*. Once the $M_{ph.e./ph.}(\sim 12\%$ for HEGRA telescope) and A_{mirror} of the Cherenkov telescope is obtained, one can estimate its energy threshold can be estimated.

The Imaging Atmospheric Cherenkov (IAC) technique consists of obtaining an image of the atmospheric shower by collecting the Cherenkov photons spread on the ground.

Figure 1.10 shows how the Cherenkov light emitted in a cascade at different altitudes is seen as a set of rings at observation level. The light from all these Cherenkov rings is reflected by the telescope forming an image in the camera.

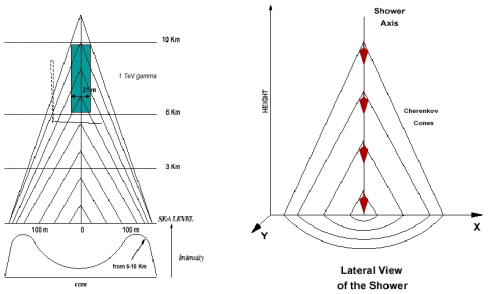

Figure 1.10: *Geometric model of emission of Cherenkov radiation for γ-ray and hadron showers. The stippled region encloses the main emission region for production of Cherenkov light from γ-ray showers. The intensity profiles on the ground reflect the peaking in the Cherenkov lateral distribution for γ-ray. [54]*

If the track is not parallel to the optical axis of the mirror, the image is offset by an amount corresponding to the angle of incidence of the particle. Defining $D(\phi)$ as the intersection of the azimuthal plane emanating from the track at an angle ϕ with the mirror:

$$D(\phi) = \begin{cases} 2R\sqrt{1-(\rho/R)^2\sin^2(\phi)} & \rho/R > 1 \\ R[\sqrt{1-(\rho/R)^2\sin^2(\phi)} + (\rho/R)\cos\phi] & \rho/R \leq 1 \end{cases}$$

where ρ is the impact parameter of the particle, and R is the radius of the mirror. If $\rho/R \leq 1$, all azimuth angles are allowed and full circles can be observed. If $\rho/R > 1$, only arcs of maximum angular extent equal to $2\phi_{max}$ can form in the focal plane.

The image shower is understood as a geometrical projection of the shower into a detector. Therefore, by this mechanism, in the camera, several images of "arcs" corresponding to the tracks of the particles of the shower (fig. 1.11) are formed. Taking into account several factors that contribute to the broadening of the image, like the mirror aberrations and the finite pixel size of the camera, the shower image can be explained as a superposition of the images of the Cherenkov rings of a cascade [148].

Depending on the nature of the primary particle initiating the shower, the development of the cascade is different as is the image formed in the camera. Therefore,

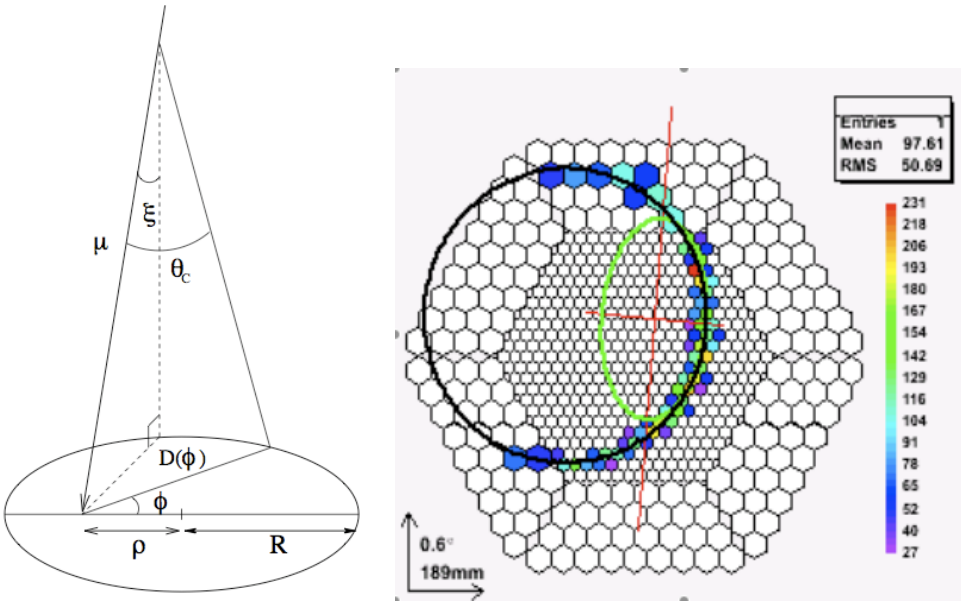

Figure 1.11: *(Left) Geometry of the problem. (Right) Image example of a muon shower taken with the MAGIC telescope. [75]*

it is necessary to develop a technique to parameterize these images in order to distinguish between gamma and hadron initiated showers. This process begins with some form of parameterization of shower images based on either a -second moments-approach (the so-called *Hillas parameters*) [91] or on some form of semi-analytical fitting of shower images. Given the essentially elliptical nature of the shower images, it was natural that the parameterization of images was originally performed in terms of a moment analysis of the recorded pixel signal amplitudes.

The zero-order momentum gives the image amount of light, the 1st-order momenta give the image gravity centre, the 2nd-order momenta give the shape and direction of the ellipse and the 3rd-order momenta give the image asymmetry.

The ellipse parameters can be classified as *shape parameters* which characterize the size and shape of the image:

- Size: total integrated light content of the shower
- Conc$n$: Ratio between the sum of light of the first n pixels with higher signal and the sum of light for all pixels in the image.
- Length: The rms spread of light along the major axis of the image. It carries information of the longitudinal development of the shower.
- Width: The rms spread of light along the minor axis of the image. It carries information of the lateral development of the shower.

- Leakage: Ratio between the number of photons in the 2 outer rings of pixels and the total amount of photons for all pixels in the image.
- M3Long: Asymmetry of the light distribution (third moment) along major axis. It is positive when the image is pointing towards the source position in the camera.
- Asym: Distance from highest pixel to centre, projected onto major axis.

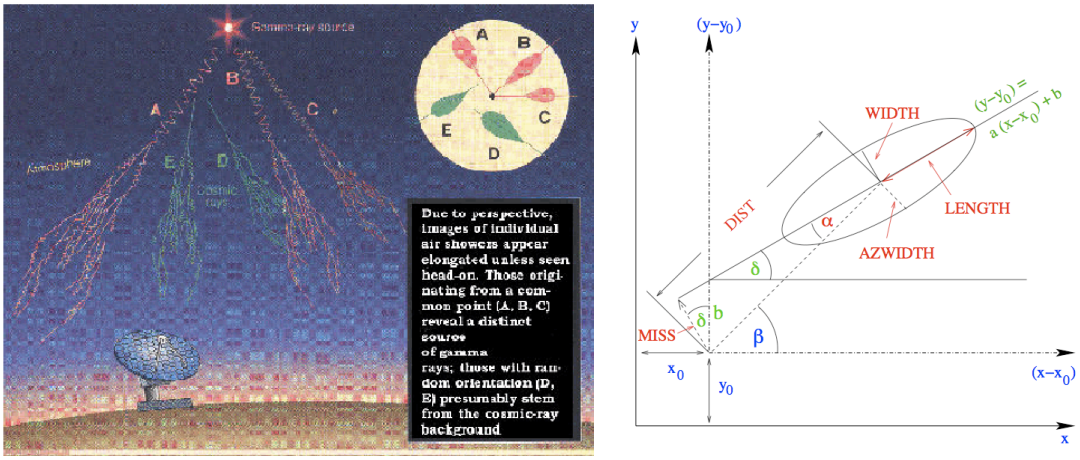

Figure 1.12: *(Left) Diagram of the formation of images depending on the nature of the primary particle initiating the shower [52]. (Right) Image parameters: an ellipse is drawn to represent a shower image. The most important Hillas parameters are displayed. Point* (x_0,y_0) *represents the centre of the camera [156].*

and *orientation parameters*:

- Alpha: Is the angle between the major axis of the image and the radius drawn from the position of the source in the camera to the centre of the image. It is related to the angle between the shower axis and the axis of the telescope.
- Distance: The distance from the centroid of the image to the centre of the field of view of the camera. It gives information about the impact parameter of the shower regarding the CT.
- Miss: The perpendicular distance between the major axis of the image and the position of the source in the camera.
- Azwidth: The rms spread light perpendicular to the line connecting the centroid of the image to the position of the source in the camera. This is a measure of both the shape and orientation of the image.

These crude elliptical images of the Cherenkov light pool are very useful (section 1.4.1) since a very efficient technique to reject the large cosmic-ray background, named the *Atmospheric Cherenkov Imaging Technique* [52], was developed. When dealing with this technique one has to fight against two difficulties: the light of the night sky (LONS) and the shower background produced by the cosmic rays from which gamma showers have to be picked out. The amplitude fluctuations of detected LONS determine the threshold of a detector. The energy threshold for a single dish is defined as the shower energy which provides a minimum given signal/noise ratio during a given measuring time. Thus, the energy threshold scales with the mirror surface area and the light collection efficiency as:

$$E_{th} \propto \frac{1}{\sqrt{A_{mirror} \cdot LCE}} \tag{1.13}$$

where the light collection efficiency (LCE) is given by the product of several terms $LCE = R \times LG \times QE \times CE$, where R is the reflectivity of the mirrors, LG (if used) denotes the light guide efficiency, QE is the quantum efficiency and CE is the collection efficiency of the used photosensors. Therefore, to lower the energy threshold for a single-dish Cherenkov observatory, the mirror area and the LCE of the photosensors have to be enlarged.

In the case of an array of Cherenkov telescopes, the energy threshold increases with the number of telescopes in coincidence as well as the sensitivity [101]. For this purpose, Monte Carlo studies are needed to calculate the optimum number of telescopes and their configuration to reach the lowest threshold.

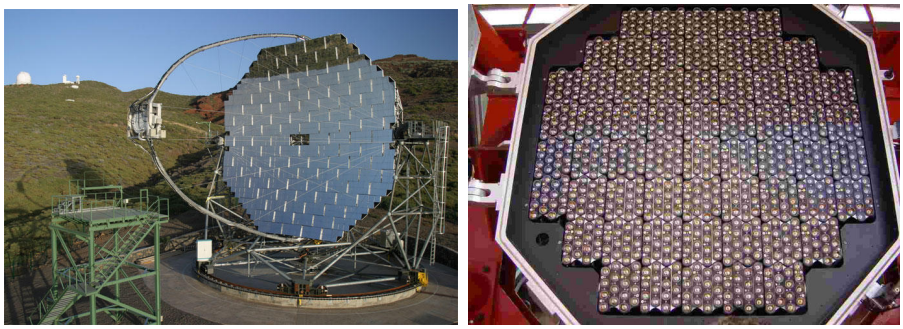

Figure 1.13: *(Left) Cherenkov telescope (MAGIC) at h = 2.2 km. Mirrors of 1 m^2 are situated over a reflector of 17 m diameter [173]. (Right) Camera of a CT (HESS telescope array). It consists of 960 pixels (0.16°) on a 5° FoV [172].*

The camera is the most important element of the telescope and decisive for the improvement of the telescope's sensitivity. Usually the camera is made out of photomultipliers tubes accompanied by fast signal-processing electronics. The number of pixels in a camera and its angular size determine the minimum angular resolution

that can be achieved by the telescope and its field of view (FoV). Because the signal is fast - the total light pool passes through the detector in only a few nanoseconds -and weak, once the light has been detected in a phototube, fast electronics and amplifiers are used to record the gamma-ray events. This short time window of the Cherenkov light pool from a γ-ray is taken to reduce the background light.

Once we have reconstructed and selected our gamma-ray candidate images, the final step in the IAC technique is the analysis, through the Hillas parameters [91] (section 1.4.1). The details of the MAGIC telescope analysis will be explained in chapter 6.

Today, the Imaging Atmospheric Cherenkov Telescopes (IACTs) have become the most sensitive technique for the observation of TeV γ-rays. This is due to the large effective collection area, which yields background suppression factors about 10^4 times larger than the current satellite experiments, and the development of the atmospheric Cherenkov imaging technique. This has led to significant advances in γ-ray detection sensitivity in the energy range from 60 GeV to 50 TeV.

Table 1.2 shows a summary of the Cherenkov telescopes currently operative in the Northern and Southern hemispheres with their main design characteristics.

The MAGIC telescope is a continuation of the work that started in 1985 with the HEGRA detectors. Its aim is to exploit all presently available technologies in order to obtain a Cherenkov telescope with an energy threshold close to 10 GeV, a sensitivity orders of magnitude larger ($> 10^3$) than EGRET sensitivity in the overlapping energy range. To reach such a low energy threshold, MAGIC has a parabolic mirror of 17 m diameter and a camera formed by 577 high efficiency photodetectors.

Besides the single dish configuration, IACT can operate as an array of Cherenkov telescopes operating in coincidence - the so-called *stereoscopic technique*. This technique consists in observing the atmospheric showers simultaneously with several telescopes yielding an improved angular resolution and better spectral reconstruction of the primary particle. This is the case of the current and incoming projects like CANGAROO-III (Australia), MAGIC-II located at La Palma (Canary Islands), HESS-II (High Energy Stereoscopic System) in Namibia, VERITAS (Very Energetic Radiation Imaging Telescope Array System) in Arizona (EEUU) and MACE (Major Atmospheric Cherenkov Telescope Experiment) located in India.

For ground-based telescopes, there is no technical barrier to improve the flux sensitivity and to reduce the energy threshold further. In principle, a telescope can be built with an energy threshold as low as 10 GeV. A new generation of telescopes with improved sensitivity has the promise of providing interesting measurements of fundamental phenomena in physics and astrophysics. Among them is the *CTA (Cherenkov Telescope Array)*, a project that will work as an open observatory for the full astrophysics community. CTA will be a factor 10 times more sensitive than any existing instrument and will provide the deepest ever insight into the non-thermal high-energy Universe, with an expected energy threshold of 10 GeV. With its large detection area and large number of telescopes ($\sim$ 100 telescopes), CTA will have a

temporal resolution ($\sim sub-minute$) and angular resolution ($\sim arc-minute$) that are currently inaccessible [179].

1.5 The MAGIC telescope

The MAGIC telescope consists of a set of integrated subsystems, structures and facilities. Figure 1.14 shows the overall design of MAGIC and its basic elements at the telescope site [20] [33] [74] [124]:

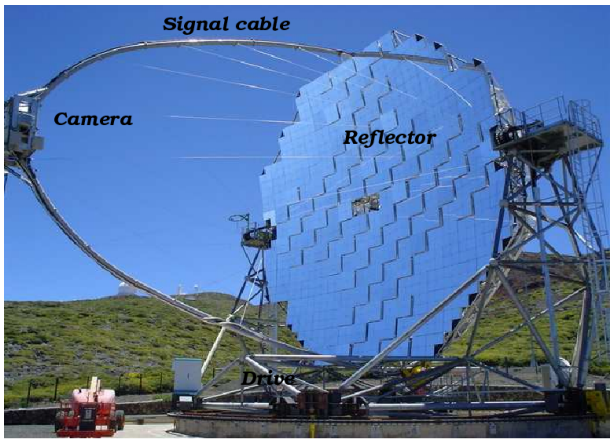

Figure 1.14: *The MAGIC Telescope at Roque de los Muchachos (La Palma, Canary). The reflector has a diameter of 17 meters [173].*

- A concrete foundation with a circular rail of $\sim$ 20 m diameter and a central support axis.
- The azimuth undercarriage with 6 bogeys, two of them equipped motors for the azimuth rotation.
- A 3-layer tubular space frame supporting the tessellated reflector of 236 m^2.
- The altitude drive ring sector and the zenithal drive motor.
- The camera support frame fixed with cables to the declination axis tubs and space frame reinforcement ring.
- The fine granularity photo-sensor camera.
- Auxiliary equipment for the telescope operation mounted on the structure.

The facility comprises also of a control room in a nearby building containing the data acquisition system, the camera power supplies and calibration box, the trigger system, the weather station, the GPS-time module, all the subsystems and network computing system and various auxiliary elements needed for safety, backup, etc.

1.5.1 The drive system

The MAGIC telescope is an Alt-Az mount with a pointing and tracking system. This drive system is designed to be powerful enough to move a weight of 64 tons performing very fast slews of $\sim 90^o/10$s, while also track a source at angular velocities less than $\sim 90^o/6$h [33]. For fast slewing, digitally controlled servo motors are used which allow for smooth and fast accelerations. The frequency converters measure the current motor position with a rotary 14-bit shaft encoder on the telescope axis (two at the elevation axis and one at the azimuth one) at a rate of 1kHz. This configuration gives an accuracy in the telescope position better than 0.02^o and is able to track a source with even higher precision. The two shaft encoders in the elevation angle check for possible torsion on the telescope dish caused by the reflector weight.

Applying a bending correction algorithm, tracking can be done with a precision better than 1.5 arcmin ($\sim 1/5$ of a camera PMT diameter). For higher precision and cross checks, a star guider system has also been installed. The star guider measures the telescope pointing position by constantly looping over the differences between stellar positions determined by a CCD image and those recorded in standard star catalogues. Depending on the number of stars in the source FoV, a total tracking precision better than 15 arcsec (0.25 arcmin) can be achieved.

1.5.2 The reflector

The main mirror support dish consists of a three-layer space frame made from carbon fiber-epoxy tubes, which makes the frame rigid and 1/3 lighter than a similar steel design. The light frame allows the telescope to slide faster ($\sim 9^o s^{-1}$) than any other existing telescope.

The frame deformation can be held below 3.5 mm with respect to the nominal curvature at any position for a combined frame and mirror weight of less than 9 tons. It also guarantees wind resistance up to more than 165 km/h and stability in case of complete ice cover up to 3 cm thick.

MAGIC has a 17 m $\emptyset$ octagonal shape tessellated f/D=1 reflector. It consists of 964 square tiles measuring 49.5×49.5 cm^2 each. The general curvature of the reflector provides a parabolic mirror surface area of ~ 236 m^2, whereas the shape of the individual mirror tiles is spherical [20].

The basic mirror elements are lightweight sandwich aluminium panels with internal heating to prevent dew and ice deposits. Although the mount is rigid, the 17 meters diameter of space frame may cause some deformation during tracking. These

small deformations are corrected by an active control system (AMC) similar to the one used in large optical telescopes. The AMC works on lightweight panels of 4 pre-adjusted mirror elements that are adjusted by two steeping motors. A laser pointer attached to the panel sends light in the direction of the panel itself and a video-camera records the position of the light spot on the casing of the camera. This is the first time that this system has been used in IACTs and keeps the telescope focal point spread function to $\sim$ 14 mm $\emptyset$.

1.5.3 The camera

The Cherenkov light from the γ-shower is reflected by the mirrors and projected onto a $0.85m^2$ camera where the conversion of the light signal to electric signal takes place by means of photo-sensors. Nevertheless, the electric signal is not digitized here. In order to minimize the camera weight, size and heat dissipation, the trigger and readout electronics is not located in the camera of the telescope, but in the counting house on the ground. Instead of heavier coaxial cables, low-weight optical fibers are used to transmit the photo-sensors signal to the counting house, in order to provide noise immunity and to minimize the time dispersion of the signals.

The camera has a field of view (FoV) of $\sim$3.8^o $\emptyset$ and is divided in two parts. The inner part of the camera, from the centre up to a radius of 1.25^o, is equipped with 397 high QE (Quantum Efficiency) pixels of 0.1^o FoV, whereas the outer part is composed of 180 pixels of 0.2^o FoV each. This outer part extends from 1.25^o up to a radius of 1.8^o [44]. This design takes into account that low energy shower images ($<$ 100 GeV) are rather compact and rather close to the camera centre, demanding fine pixelization of the camera in the central region. On the other hand, high-energy showers are more extended (up to 1.5^o - 2^o) because they reach further down in the atmosphere, hence requiring the camera to be large enough to contain the whole image of the γ-shower.

For the light sensors three options were envisaged in the beginning: classical photomultipliers (PMTs), hybrid photomultipliers (HPDs) with higher quantum efficiency, and avalanche photo diodes (APDs) as a possible option for the future. In the first phase of the MAGIC telescope, the camera has been equipped with bialkali photo-cathode PMTs. New compact hemispherical 6-dynodes PMTs [3] from Electron Tubes 9116A (25 mm $\emptyset$) as inner pixel, and ET9116B (38 mm $\emptyset$) as outer pixel are used. The 5th and 6th dynode voltage is stabilized with two independent active loads (360 V and 175V) respectively. The photocathode quantum efficiency is enhanced up to $\sim$ 28% and extended to the UV by a diffuse coating of the surface, using a wavelength shifter [125].

The QE peaking between 300 and 450 nm is well matched with the UV peaking of the Cherenkov light (λ = 260-680 nm, peaking at $\sim$ 320 nm) [58]. In addition, the

[3]MAGIC uses low gain 6 Dynode PMTs to prevent degradation damage in case of bright night sky light, moon shine or accidental light from bypassing cars that can damage high gain PMT. To make up for the low gain low noise, fast-AC-coupled preamplifiers are used.

contribution of the light of night sky (LONS) in the UV is rather low.

Even in case of a dense PMT package, a 50% active area fraction is the most that can be achieved. Specially shaped hollow light funnels of hexagonal entrance are used in MAGIC in order to achieve a higher light collection. These light funnels provide nearly 100% light collection efficiency, shielding against a large angle ($> 35°$ straight light) and further small enhancement of the QE by deflecting most light trajectories passing the hemispherical cathode twice.

Figure 1.15: *Camera of the MAGIC Telescope. Area = 0.85 m^2, FoV = 3.8° [173].*

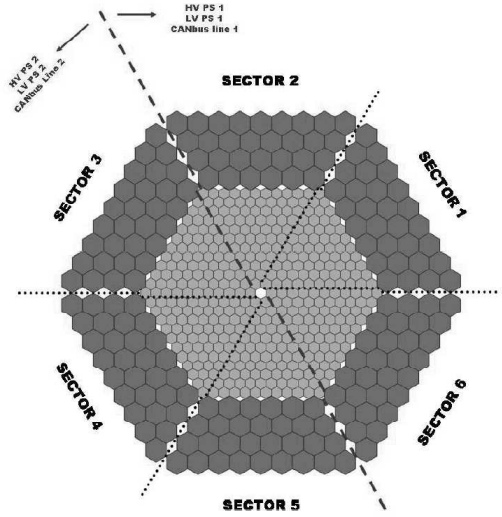

Figure 1.16: *Layouts of camera sectors. Inner part (< 1.25°) (light grey) and outer part (1.25° - 1.8°) (dark grey) [124] .*

A window of 2 mm-thick UV transmitting plexiglass in the camera front protects and seals hermetically all the electronic sensors and camera elements from environmental conditions (like humidity, dust, etc.). The reflectivity of the plexiglass mean that 92% of the total focused light arrives at the light catchers or directly to the PMTs.

The whole camera is refrigerated using a water-based cooling system. This system has sensors and actuators controlled via a PLC (Programmable Logical Controller) which monitor and control the temperature and humidity inside the camera [59]. This allows the autonomous control of the conditions during the data-taking to minimize the temperature-dependent fluctuations of some readout chain devices and to protect the camera hardware from extreme conditions.

1.5.4 The data acquisition system (DAQ)

Specific features of the MAGIC camera electronic chain (Fig. 1.17) are the use for a fast-low noise transimpedance amplifier, analogue signal transfer through the 162m optical cable and digitalization by Flash Analogue to Digital Converters (FADC).

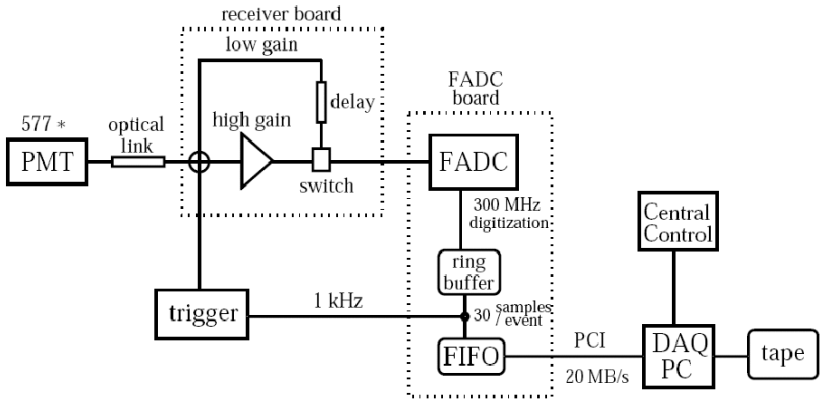

Figure 1.17: *The MAGIC camera readout electronic chain [74].*

In the first step, the signals of each pixel are fed through an AC-coupled, ultra-fast and low-noise voltage pre-amplifier at the PMT base in order to prevent damage by the LONS and give MAGIC the capability to work in the presence of moonlight - which increases the normal rate easily up to a factor of 30 [102]. In the case of MAGIC, in order to keep the PMT current flow produced by the LONS at level $\sim 1\mu A$, the PMT gain should not exceed 2-3$\times 10^4$. In order to drive the optical analogue glass fibre system, the signal needs further amplification, compensating for the low PMT gain, therefore the PMTs are followed by a fast $\sim$1 GHz bandwidth transimpedance amplifier with a gain of 7-10, providing a single photoelectron with an amplitude of 0.5-1 mV.

The Cherenkov light flashes, particularly those from γ-showers, are very "sharp" in time (usually with FWHM values of $<$ 1-2 ns). Depending on the photosensor and the preamplifier configuration, the electronics signal will be somewhat widened. Nevertheless, the pulse width time can still be reconstructed nearly to the above-mentioned precision. In order to make full use of this low-spread, such that a fast coincidence time for the trigger can be achieved, it is necessary to use very fast optical readout elements to avoid any signal distortion during its transportation to the trigger unit; for this purpose, optical analogue fibre are preferred over coaxial cables. The amplified analogue signal is transmitted over 162 m long optical fibres using Vertical Cavity Surface Emitting Laser diodes (VCSELs, $\lambda = 850$ nm [126]). When the signal reaches the counting house, photodiodes on the receiver boards transform the optical pulses back to electrical pulses. Then the signal can be processed by the trigger logic and FADC system. One part of the signal is fed to a discriminator and used for the

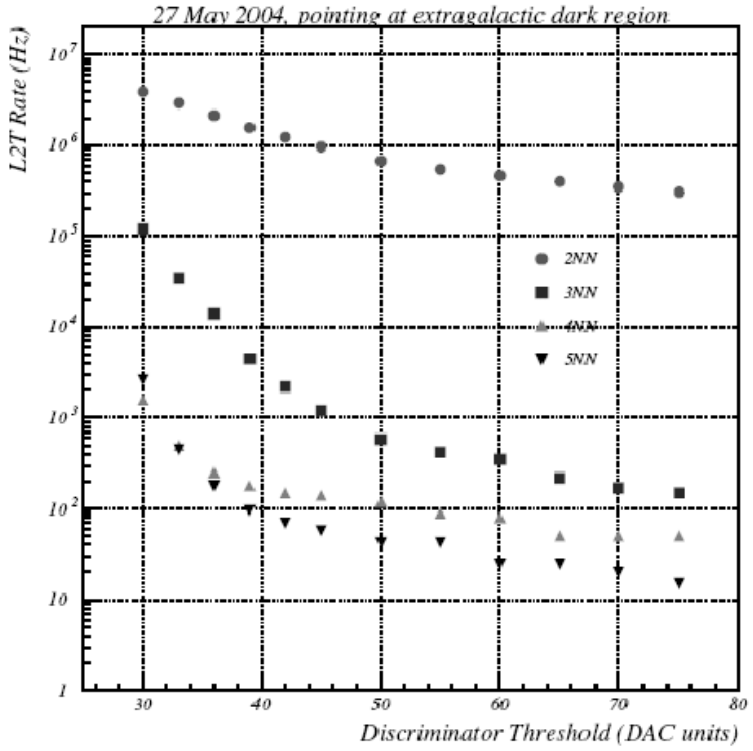

Figure 1.18: *Dependence of the telescope trigger rate (Hz) with the discriminator threshold, which is proportional in first order to the telescope energy threshold [13].*

first-level trigger decision and the other part is again split into an amplified "high gain" (HG) branch and a 50 ns delayed "low gain" (LG) branch, to increase the dynamical range and then sent to the ADC. A discriminator is a device that responds only to input signals with a pulse height greater than a certain threshold value (in arbitrary DAQ units, $\sim$ 2.32 ADC counts $\sim$ 0.30 phe in integrated charge). If the criteria is satisfied, the discriminator responds by using a standard logic signal, if not, no signal is transmitted. The discriminator threshold can be set independently for each channel in order to diminish the influence of bright stars in the camera field of view.

If the signal exceeds the discriminator, a logic signal is emitted and sent to the input of a coincidence unit which provides an output signal if N out of M inputs are coincident in time. In this case, the trigger signal opens the gates for the ADC's, latches the rubidium clock bit pattern and generates a computer interrupt to start the readout cycle.

Because of the expected rate of data collection in an extreme situation of a γ-ray burst or an AGN-flare and because of the high camera pixelization, the readout and trigger system of the camera is divided into 19 overlapping sectors (trigger macrocells)

of $\sim$ 37 pixels each (fig. 1.19).

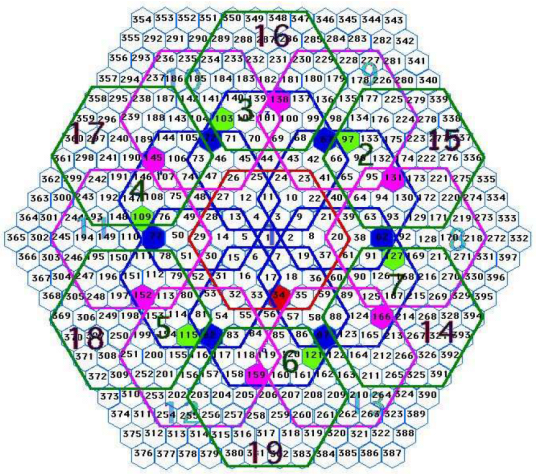

Figure 1.19: *Scheme of the trigger zone. It is divided into 19 overlapping macrocells which consists of $\sim$37 pixels each. It defines the camera trigger radius ($<0.8^{o}$) [124].*

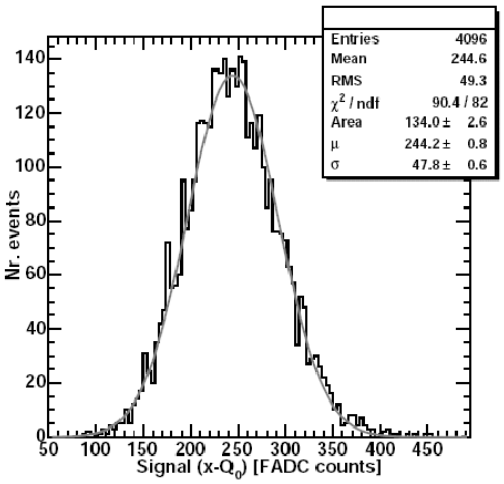

Figure 1.20: *Example of a typical calibration pulse. Distribution of FADC counts recorded by 577 pixels [72].*

The trigger system is expected to reject accidental coincidences (accidental trigger rate) due to LONS, moonlight and bright stars, allowing a reduction of the discriminator thresholds, and therefore a lower energy threshold. Since for normal operations a data flow of at most $\sim$ 1 kHz is allowed, in the original design it was planned to install several trigger levels. Each level would give a different trigger rate, reducing it by using requests in timing and topology. Currently only one based on topology logic is used. The important question is set how to the optimal values to avoid the accidental coincidences successfully, but without suppressing too many γ-ray events, especially at low energies. The first-level trigger (L1T) applies tight time coincidences and a simple next-neighbour logic within a trigger area. Low energy γ-showers develop higher in the atmosphere and close to the camera centre, therefore the telescope works only with those pixels which are within 0.8^{o} radius from the camera centre, defining the "camera trigger radius"(fig. 1.19). The light of the night sky is a very steep function of the trigger threshold (fig. 1.18) and may saturate the readout system. In order to reduce the random coincidence rate, the discriminator pulse width can be reduced by taking a first-level trigger width $\leq$ 5 ns and also by reducing the number of next-neighbour combinations making use of the topology of images from γ-showers in the camera. A second level trigger (L2T), not yet working, is expected to apply a more sophisticated logic to decrease the trigger rate processed by the DAQ. It will be used to perform a rough estimation of the γ-ray energy by looking

at the number of pixels over the discriminator threshold and by to apply topological constraints on the event images defining different trigger types according to this estimated energy [46]. In addition the L2T accepts trigger signals coming from pedestal and calibration events.

When the trigger condition is fulfilled, the fast analog signals have to be digitized. The low gain (LG) signal is combined with the high gain signal using a GaAs fast switch. The combined signal is stretched to $\sim$ 6 ns FWHM (so that the pulse amplitude can be measured at more than 3 points) and digitized. In order to keep the timing information from the camera, 300 MHz 8-bit FADCs are used for the digitalization process. The use of a FADC-based DAQ instead of a classical gated ADC allows a dead time of less than 1 μs by storing the information in an intermediate 32 kBytes long ring buffer during the 2-level trigger decision. Since the signal has been stretched, the 3.3 ns time slices allow for an effective timing resolution below 1 ns. After the trigger decision, the position of the signal in the ring buffer is determined and 15 high/low gain samples for each pixel are written into a 512 kBytes FiFo (First In First Out) buffer at a rate $<$ 80 MBytes/s.

The data are saved to a RAID0 disk system at a rate $<$ 20 MBytes/s that collects up to 800 GBytes per night.

1.6 Astronomy at gamma-ray energies with the MAGIC telescope

The MAGIC (Major Atmospheric Gamma Imaging Cherenkov) telescope is a 17 m diameter Imaging Atmospheric Cherenkov Telescope (IACT) working at the Roque de los Muchachos observatory in the Canary island of La Palma ($28.8^{o}N, 17.9^{o}W$) since the beginning of 2002. The main goal of the experiment in its first phase was to reach an energy threshold as low as $\sim$30 GeV with a sensitivity higher than any other detector currently working, whereas currently a $\sim$ 60 GeV threshold has been reached.

As seen in this chapter, the satellite detectors have good statistics up to 10 GeV (HE range) while the ground-based detectors are better for energies larger than $\sim$ 300 GeV (VHE range). A gap has remained between 10 GeV and 300 GeV which we intend to investigate for the first time with the MAGIC telescope. The sensitivity of the MAGIC Telescope in the unexplored band, will touch fundamental problems in astrophysics, cosmology and particle physics.

What follows are hypotheses about why it is important to cover this energy region and what might happen in this gap of energy:

- Active Galactic Nuclei (AGN): Below 10 GeV EGRET observed more than 60 blazars, but the energy gap needs to be covered and the telescope sensitivity needs to be improved to complete our knowledge of the γ-ray spectra in blazars.

An understanding of the γ-ray emission is essential to develop a complete physical picture of AGNs, because the observed radiated power for some sources is completely dominated by the γ-ray emission component.

- Cosmological Structure Formation and Diffuse Background radiation: The visible Universe in high-energy photons is limited by pair production on the cosmological low-energy diffuse background photons. Increasing the γ-ray energy results in a decreasing γ-ray horizon. Conversely, by triggering at γ-ray energies lower than current IACTs can observe ($z \simeq 0.1$), a much larger fraction of the Hubble volume ($z \simeq 3 - 5$) and thus a much larger source population can be accessed.

- High-Energy Counterparts of Gamma-Ray Bursts: The low inertia of the MAGIC Telescope will allow rapid positioning toward observation of targets of opportunity sources, typically within 30 s. The low energy threshold will also mean the observation of more distant GRBs.

- Study of Supernova Remnants: Shell-type Supernova Remnants (SNRs) should be the dominant sources of cosmic rays in the galaxy and, if the shell is interacting with a molecular cloud, the π^0 decay products should be visible. The expected synchrotron cut-off at millimetre wavelengths should produce a similar cut-off in the MAGIC Telescope range above 10 GeV. The MAGIC Telescope could therefore observe a two component γ-ray spectrum, which should allow us to decouple the leptonic and hadronic components in SNRs shells.

- Gamma-Ray Pulsars: No pulsed emission from pulsars has yet been detected by ground-based IACTs above $\sim$ 250 GeV. The polar cap model for pulsed emission explains this fact by a predicted sharp cut-off in the γ-ray spectra above a few GeV due to absorption in the strong magnetic field of the pulsar magnetosphere. Detailed phase-resolved modelling, however, shows that we expect the bridging emission between the two pulses to have harder spectra. This prediction was recently confirmed by phase-resolved spectroscopy of the Crab, Vela and Geminga pulsars [65] and provides for a very low threshold IACT like the MAGIC Telescope, with the unique opportunity to get answers on the emission regions for the highest energy γ-rays from the neutron star magnetosphere. However, other models predict cut-off in the pulsar spectra at energies of 100's of GeV.

- Search for a Cold Dark Matter Candidate: The dark matter in the Universe may take the form of the lightest super-symmetric particle. In most astrophysical models of the dark halo of our Galaxy, these particles would cluster in the centre of the Galaxy where even a minute rate of dark matter annihilation would produce a γ-ray annihilation line and a γ-ray continuum detectable with IACTs at energies around 100 GeV.

- Diffuse Galactic Emission: The diffuse emission above a few GeV is dominated by the inverse Compton component of galactic electrons on these soft photons. The expected flux above 10 GeV should then be larger than previous estimates for the π^0 component alone. It is therefore important for the MAGIC Telescope to scan the galactic plane at various declinations. Since the starlight photon fields are relatively well known, we can hope to infer the cosmic electron spectrum at galactic distances, as opposed to direct local measurements of the electron component of cosmic rays.

Therefore MAGIC will help to clarify many of the currently big unknowns shared by astronomy and cosmology, namely the formation and evolution of cosmic structure. Gamma-ray astronomy may contribute to the solution of the problem by measuring γ-ray turnover energies in the spectra of AGNs and GRBs and by searching for a γ-ray annihilation line from the region around the centre of the Galaxy.

In addition, the high discovery potential for γ-ray pulsars provided by phase-resolved spectroscopy may open a new window to the study of pulsar magnetospheres.

Chapter 2

Gamma-ray emission from pulsars

This Chapter will describe briefly the main theories about the mechanisms and origin of the high-energy photons emitted by pulsars and their surroundings. This overview is a summary of several theoretical works that have been carried out since the last century to explain the emission from the pulsar-PWN systems. Since the analysis performed in this Thesis will concern canonical and millisecond pulsars, this summary will be focused on these two kinds of pulsars, mentioning very briefly the other populations. Each kind of pulsar is associated with a different environment, surrounded or not by a nebula: isolated or within a binary system, respectively. Depending on the origin of the emitted photons, the emission mechanisms will have different physical phenomena. This will result in a different nature of detected emission, that will be pulsed or non-pulsed.

2.1 Introduction

The discovery of the first radio pulsar PSR B1919+21, in 1967, was followed by a further large-scale search for radio pulsars, which brought a lot more detections. Nowadays, the catalogues of radio pulsars account for more than 1700 objects: 170 of them are millisecond pulsars, 131 are in binary systems and 129 pulsars are detected in 24 globular clusters. More 60 of those radio pulsars have been seen in X-rays but only 7 of them, plus 3 more pulsars at low significance, have been recently detected at high energies ($E_\gamma \geq 30$ MeV) with EGRET [97].

It is generally accepted that pulsars are produced from massive progenitors (giant stars) with masses of $M \geq 8M_\odot$ and typical radii $R_0 \simeq 10^{11}$ cm, collapsing at the end of their evolution to neutron stars in supernova explosion, which ejected the outer envelope forming a supernova remnant (SNR).

There are different populations of pulsars according to their rotational properties (fig. 2.1). Among them, the two main populations already detected at high energies are the *canonical* or *normal pulsars* with a period P$\approx$ 1s and a period derivative $\dot{P}$

$\approx 10^{-15}$ s/s and the so-called *millisecond pulsars*, characterized by P $\sim$ 1.5 - 30 ms and $\dot{P} \leq 10^{-19}$ s/s.

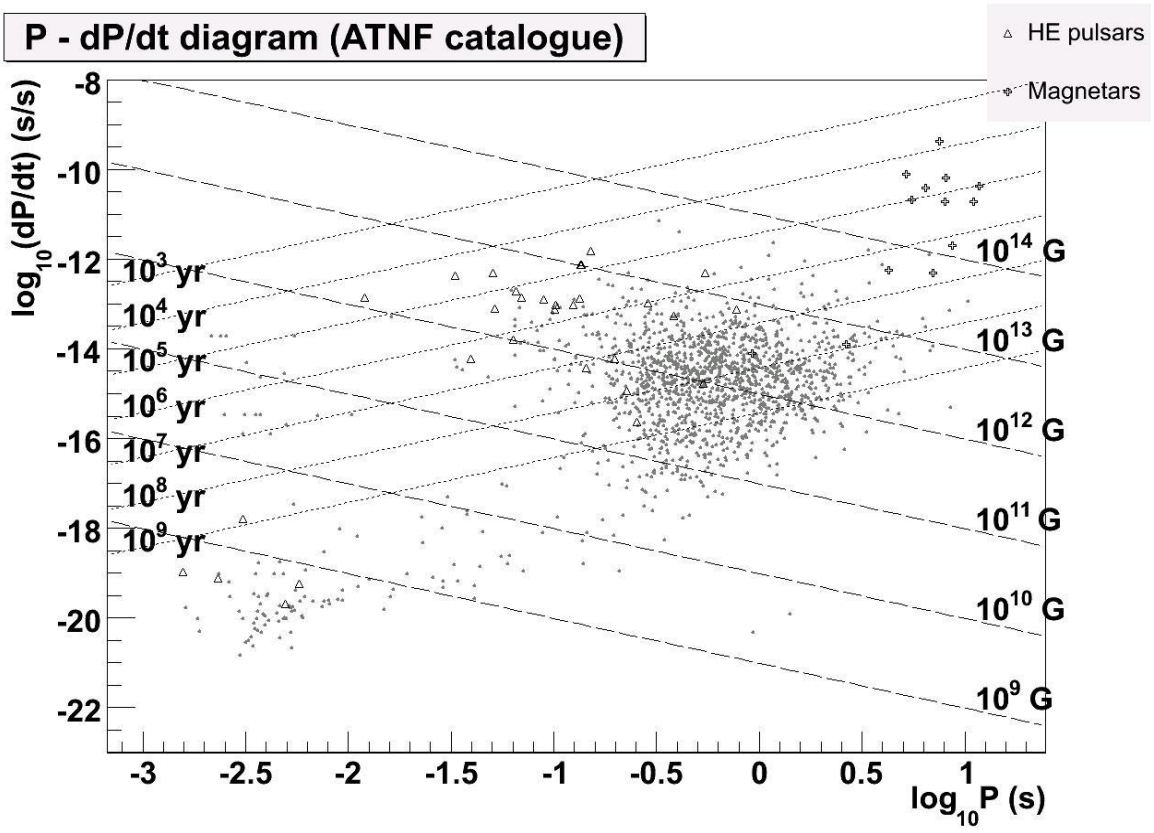

Figure 2.1: *P-$\dot{P}$ diagram from the ATNF pulsar catalogue. Two populations of pulsars can be clearly seen: canonical (up on the right) and the millisecond (bottom on the left). HE pulsars are marked as triangles. The crosses correspond to magnetars.*

The radiation emitted by these systems is explained by different physical processes and can be generally seen in many wavelengths (fig. 2.2). Some pulsars, like Geminga (PSR J0633+1746), appear to be radio-quiet, although it has been recently discovered that they are simply faint at radio wavelengths, emitting mostly at high energies (X-ray and γ-ray), i.e. the wavelengths where they were discovered.

When the radiation emitted by the pulsar interacts with the remnant material from the supernova (SNR) and/or from the material from the interstellar medium (IM), a so-called pulsar wind nebulae (PWN) is formed.

Seven pulsars show clear evidence for γ-ray pulsed emission above 5 GeV (fig. 2.8). Spectral energy distributions (SED) of γ-ray emission from the high-energy pulsars peak in the hard X-ray or γ-ray range and show a break at GeV/TeV energies (energy cut off), which is an established distinctive feature of the pulsar γ-ray emission by means of which the different pulsar models can be discriminated. From these seven

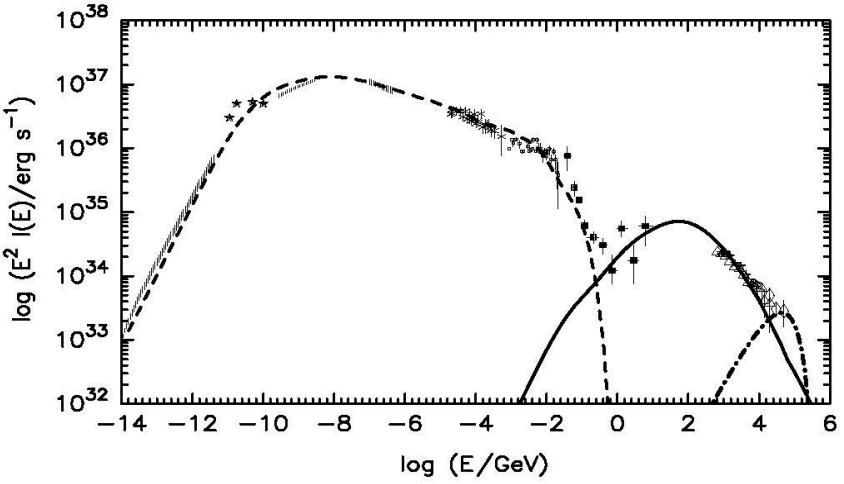

Figure 2.2: *Multi-wavelength spectrum of the Crab Nebula from radio (few GHz) to high energies (10^3 TeV) [24].*

γ-ray pulsars, only Crab Nebula [10] (E> 60 GeV), Vela [6] (E> 550 GeV) and PSR B1706-44 [36] (E> 300 GeV) are well-established sources of DC GeV-TeV γ-ray emission. This non-pulsed flux emission might be associated with the X-ray synchrotron nebula around the pulsar.

However, the spectral behaviour of both the pulsed and non-pulsed components of high energy γ-rays within the energy range from 10 GeV up to hundreds of GeV remains unknown. Spectral measurements over this energy range will severely constrain the physics of particle injection and acceleration in a pulsar magnetosphere and within the surrounding PWN and IM.

Up to now, several more or less successful theoretical models have been developed to describe the present observed pulsar data from radio to γ-rays. This chapter will summarize the main ones.

2.2 Pulsars: origin and evolution

A pulsar is the result of the collapse of a massive star ($M > 8M_\odot$) in a supernovae type II. The collapse of the star leaves a residual core of 1.4 - 2.5 $M_\odot$, in a state more compact than a white dwarf. In this state, the pressure and the densities become sufficiently big that the relativistic electrons produce inverse β-decay process ($p + e^- \rightarrow n + \nu_e$) producing large fluxes of neutrons and neutrinos. Without electrical repulsion, the neutrons gather up to densities $\sim 10^{14}$ g cm^{-3}, stopping the gravitational collapse.

The magnetic flux and angular momentum conservation during the neutron star formation process lead to the high magnetic fields and low rotational periods typical

of pulsars (P $\sim$ 0.1-10s and B $\sim 10^{12}$ G).

In the case of *binary systems*, the more massive star (the one with shorter main sequence lifetime) will explode as a SN II as described before. The explosion gives a birth velocity to the neutron star. Those binary systems with a high birth push produce a high-velocity isolated neutron star and an OB runaway star. The high binary disruption probability during the explosion explains, qualitatively at least why so few normal pulsars have companions.

In those few binaries that remain bound, and in which the companion is massive enough to evolve into a giant and overflow its Roche lobe, the old rotating neutron star can accrete matter from its companion, gaining angular momentum (and therefore pulsar life) at expense of the orbital angular momentum of the binary system. These neutron stars have rotational periods of few milliseconds, typical for the millisecond pulsar population.

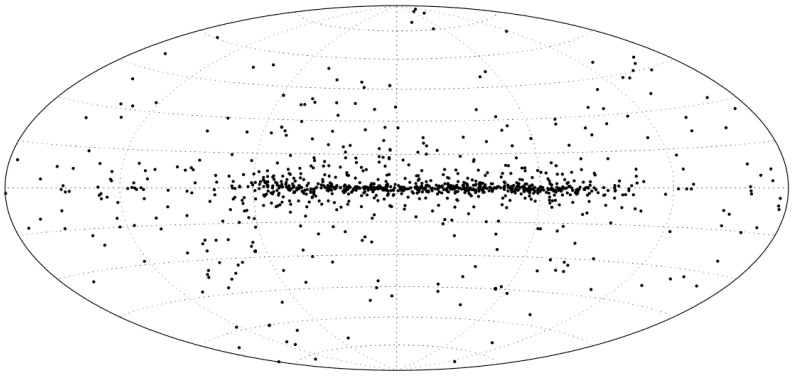

Figure 2.3: *Pulsar distribution in the Galaxy. The galactic plane is the central horizontal line (b=0°,l=[-180°,180°]). The Galactic centre (b=0°,l=0°) is the midpoint of this line. [109]*

Pulsars have long been known to have spatial velocities from 0 to over 1000 km s^{-1}, at least an order of magnitude larger than those of their main sequence progenitors, which have typical values between 10 and 50 km s^{-1}. Such large velocities can be imparted to the neutron star with slightly asymmetric SN explosions. In addition, if the neutron star progenitor was a member of a binary system before the explosion, the velocity of the binary system before the explosion can increase the birth velocity of the pulsar.

Pulsars are strongly concentrated along the Galactic plane. This indicates that pulsars are born in the disk of our Galaxy. High-velocity pulsars are born close to the Galactic plane but quickly migrate to higher Galactic altitudes (fig. 2.3). Given such a broad velocity spectrum, as much as half of all pulsars will eventually escape the gravitational potential of the Galaxy and end up in Intergalactic Space.

2.3 Pulsed emission from pulsars

Nowadays, it is believed that a pulsar is a rotating neutron star with a mass of $M \gtrsim 1.4 M_{\odot}$, a radius of $R \simeq 15$ km and a rotational period typically of order $P \simeq 1$ s or less. It was not long after the discovery of the first pulsar that observations provided convincing evidence that pulsars are magnetized rotating neutron stars, which were formed in supernova explosions.

The gamma-ray pulsations observed from these objects are particularly important as a direct signature of non-thermal processes in rotating neutron star magnetospheres.

The rotation of a neutron star possessing a magnetic field generates powerful electric fields in the space surrounding the neutron star, so the structure of the magnetosphere of the neutron star is completely dominated by electromagnetic forces. These huge induced fields are stronger than the gravitational forces, dragging charged particles out from the neutron star surface and provide all the necessary ingredients for its magnetosphere to be an extremely favourable environment for particle-photon cascades: high-energy particles, an efficient radiation process, and pair production mechanisms.

The pulsed component of the pulsar emission is a direct signature of all these non-thermal processes within the pulsar magnetosphere. All these mechanisms should describe the characteristics of pulsar physics and are the subject of the most recent observations from CGRO and will be for the future highest sensitive detectors (GLAST, MAGIC-II and HESS-II).

2.3.1 The magnetic dipole model

The simplest model considers rotating neutron stars like natural unipolar inductors with strong magnetic fields ($\geq 10^{12}$G). This magnetic dipole model explains in a very simple way how the pulsar emission is derived from the kinetic energy of a rotating neutron star.

The surface of the neutron star is formed by a plasma of charged particles. At the surface of the neutron star, the induced electric fields $\vec{E}$ ($\vec{E} = -\vec{\nabla}\Phi$) are so strong that the force on an electron (F_e) in the surface exceeds the work function (mainly due to gravitational forces) of the surface material ($F_e >> F_G$) [77]. Therefore, it is assumed that there is fully-conducting plasma surrounding the neutron star and that the generated electric fields are capable of pulling charges from a neutron star surface out of the star into the field magnetosphere (*Goldreich-Julian current*). This charged plasma will co-rotate with the star because of the strong magnetic field inside a region called the *light cylinder*. The light cylinder radius (r_L) is defined as the radius at which objects co-rotating with the pulsar would be travelling at speed of light ($r_L = c/\Omega$). In accordance with this definition, the equation of the dipole field in the neutron star is $r = const \cdot sin^2\theta = \frac{c}{\Omega} sin^2\theta$. Therefore the dipolar structure is conserved at $r < r_L$,

but breaks down at $r \geq r_L$, so one only considers the "magnetosphere" at $r < r_L$ (fig. 2.4).

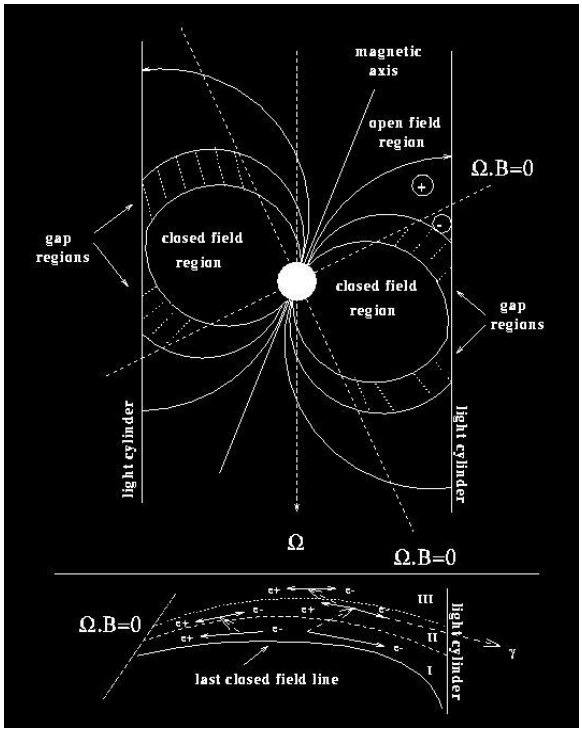

Figure 2.4: *Pulsar magnetosphere scheme. Emission regions for different models [160].*

The stellar material is assumed to be an excellent conductor (free electrons) and the co-rotating magnetosphere acts as an extension of the perfectly conducting interior. In the closed filled lines in the pulsar magnetosphere and inside the star the charged particles co-rotate with the star. This scenario implies that at the surface of the neutron star there will be an electric field satisfying ($\vec{E} + \vec{v} \wedge \vec{B} = 0$), where $\vec{\Omega}$ is the rotation velocity. Therefore the charged particles can only be accelerated along the field lines where $\vec{E} \cdot \vec{B} \neq 0$.

Assuming that the exterior region is a vacuum [136] satisfying a boundary condition for E_θ^{out} at r=R, the solution of $\nabla^2\phi = 0$ is the corresponding electrostatic potential (Φ):

$$\Phi = \frac{B_s R^5 \Omega}{6cr^3}(3cos^2\theta - 1) \tag{2.1}$$

where R is the neutron star radius and B_s is the surface magnetic field. This equation reveals that the rotation of the neutron star generates a huge external quadrupole electric field dominating the magnetosphere structure.

The regions where the filled lines close beyond the light cylinder ("open magnetosphere") receive particles that are permanently lost from the star. These regions

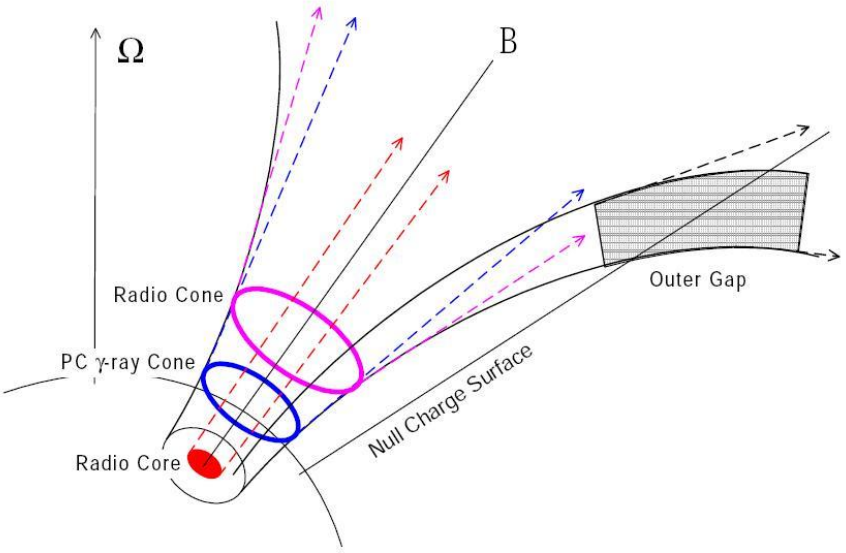

Figure 2.5: *Representation of the radio and high-energy (polar cap and outer gap) emission region. Null charge surface corresponds to* $\vec{E} \cdot \vec{B} = 0$ *[88].*

satisfy $\vec{E} \cdot \vec{B} \neq 0$. This condition implies a non-zero value of the parallel electric field component, which accelerates the charged particles along the magnetic field lines, and the vacuum solution for the region surrounding a rotating neutron star turns unstable. The locations where the plasma is pulled off, preventing it from co-rotating with the star ($\mathbf{E} \cdot \mathbf{B} \neq 0$), are thought to be located above the surface at the polar cap and along the null charge surface, $\mathbf{\Omega} \cdot \mathbf{B} = 0$, where the co-rotation charge changes sign [38]. These are the supported sites of particle acceleration and have given rise to the main bases of the two most important classes of high-energy emission models: the *polar cap* (PC) and the *outer gap* (OG) (fig. 2.4).

Huge rotational induced potential drops ($\Phi > 10^{12}$eV) are expected for pulsars and the acceleration of electrons to these energies can lead to γ-ray energies up to $E_\gamma > 10^{12}$eV as a result of a combination of processes of emission and absorption of high-energy photons in pulsar magnetospheres (fig. 2.6). Those are:

- Curvature radiation (CR), produced by an electron following a curved field line.
- Inverse Compton Scattering (ICS)
- Synchrotron Radiation (SR), produced by an electron spiralling around a field line.
- Photon-splitting ($\gamma \rightarrow \gamma + \gamma$).
- Magnetic pair creation ($\gamma \rightarrow e^{\pm}$) [62]. HE γ-rays absorbed by the magnetic field.

- Photon-photon pair creation ($\gamma + \gamma \rightarrow e^{\pm}$). High-energy photons interacting with the ambient soft photons.

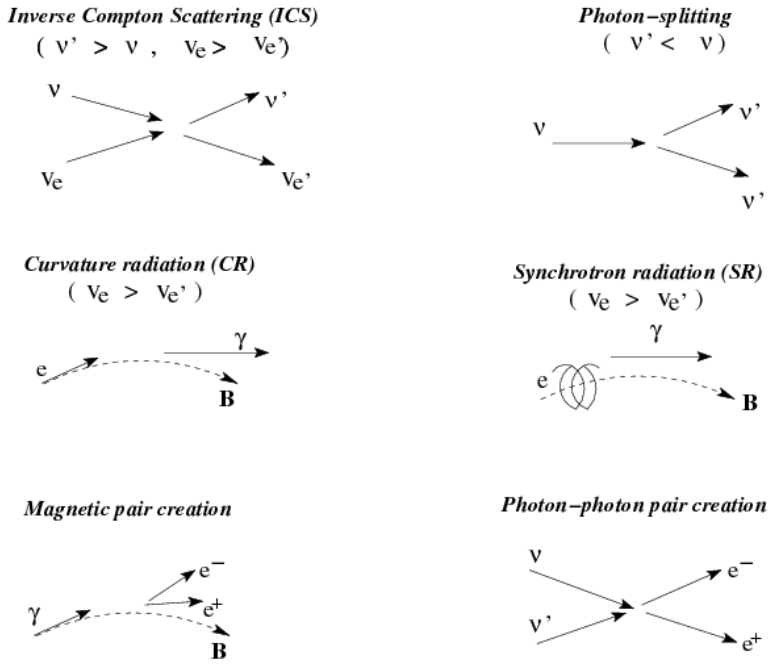

Figure 2.6: *Gamma ray production and absorption mechanisms present in the pulsar magnetospheres.*

The importance of the energetic balance among these processes is crucial to determine the optical thickness of the magnetosphere to the HE photons for each pulsar.

The magnetic dipole model explicitly demonstrates how a non-aligned rotator acts like a magnetic dipole antenna, deriving its magnetic dipole radiation from the spin-down of the pulsar, slowing it down and releasing its rotational energy ($\dot{E}$) at the rate:

$$\dot{E} = I\Omega\dot{\Omega} = 4\pi^2 I\dot{P}/P^3 \tag{2.2}$$

where $I = 10^{45} gcm^2$ is a generic moment of inertia of a pulsar.

From this assumption, one can estimate the pulsar surface magnetic field [87]:

$$B_s = \left(\frac{3\mu_0 c^3 I}{2^5\pi^3 R^6}\right)^{1/2} (P\dot{P})^{1/2} \simeq 3.2 \cdot 10^{19} (P\dot{P})^{1/2} G \tag{2.3}$$

being for a typical canonical pulsar of the order of 10^{12}G. In this model, the rotation is assumed to be sufficiently slow that non-spherical distortions due to rotation can be ignored to lowest order.

Assuming a constant magnetic field throughout the pulsar lifetime, the characteristic age of a pulsar (the so-called "spin-down age") can be determined from its rotational period and slow-down rate:

$$\tau = \frac{P}{2\dot{P}} \tag{2.4}$$

In this simple model, the photons resulting from the emission/absorption processes in pulsar magnetospheres are assumed to originate on *lighthouse beams* formed by the misalignment of the magnetic and rotational axes (α). These photons are emitted along the magnetic axis, sweeping past the observer periodically (P). Therefore, in case of double-peaked light curves, the first peak would correspond to the phase at which the observer viewpoint emerges from the interior of the hollow γ-beam, while the second peak correspond to the re-entry in the opposite side of the rim (fig. 2.7). Hence the polar cap interior is identified as the source of the inter-peak emission ($\Delta\phi$) of the phaseogram.

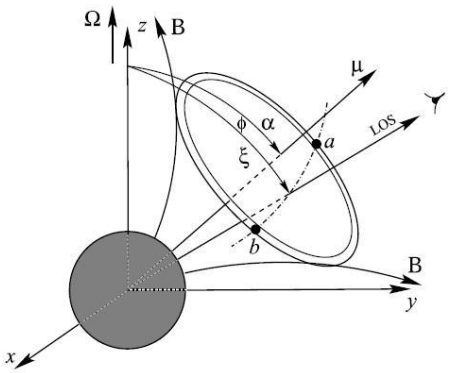

Figure 2.7: *A hollow-cone beam model. [110]*

$$\cos(\Delta\phi) = \frac{\cos\theta_\gamma - \cos\alpha\cos\chi}{\sin\alpha\sin\chi} \tag{2.5}$$

where α is the inclination angle, θ_γ is the beam angle and χ is the angle between the line of sight direction and the rotation axis (fig. 2.7).

A wide double-peaked light curve is a common feature of the high-energy emission from young canonical and millisecond pulsars. In the basic polar cap model, the observed wide double-peak profile can be explained in terms of a hollow-cone geometry from the emission region. However, either a nearly aligned or an orthogonal rotator is required because the PPF (Pair Production Front) occurs near the PC and the PC opening angle is small.

2.3.2 Polar cap based models

Early polar cap models for pulsar high energy emission [145] [136] proposed that particle acceleration and radiation occur near the neutron star surface at the magnetic poles.

The location of the γ-ray emission in the *polar cap model* lies in the "open field line" region of the pulsar magnetosphere (fig. 2.4). The area where the open field lines originate at the surface of the neutron star defines the pulsar polar cap (θ_p).

$$\theta_p \approx \left[\frac{\Omega R}{c}\right]^{1/2} << 1 \tag{2.6}$$

then the *polar cap radius* is $R_p = R \cdot \theta p$. Assuming that r=R $\sim 10^6$ cm, in the case of Crab pulsar, parameters of $\theta_p \sim 4^o$ are obtained for the angular extension of the polar cap.

The particles injected into this region from the surface of the neutron star, are accelerated through the potential drop (eq. 2.1) along the open magnetic field lines over the polar cap:

$$\Delta V = \Phi(\theta = 0) - \Phi(\theta = \theta_p) = \frac{B_s R^3 \Omega^2}{2c^2} \approx 10^{12} eV \tag{2.7}$$

With this potential drop, the $e^{\pm}$ are injected at the polar cap with Lorentz factors $\gamma \equiv E/mc^2 \sim 2 \times 10^7$.

These highly energetic primary particles above the PC are accelerated by $E_{\|}$ out along magnetic field lines producing γ-ray photons above 100 MeV through *curvature radiation* (if $\gamma_{e^-} \gtrsim 10^5$-$10^7$). The extension of the acceleration region up to several neutron star radii would increase the energy of the emitted photons and the γ-beam size, increasing therefore the spectrum energy cut off and the inter-peak phase separation ($\Delta\phi$). If the resulting curvature radiation from these particles extends to γ-ray energies $\sim$ 1 GeV, the curvature photons have a high probability of producing electron-positron pairs in the pulsar magnetosphere. This *pair production* process is the most important attenuation mechanism affecting the γ-ray emission around 500 MeV. Since the induced electric field increases the pair production rate and the pairs produced short out the E-field, the equilibrium between both processes will depend on the density of the created pairs. This density or multiplicity rises sharply with the height in the magnetosphere, shorting out abruptly the particle acceleration.

The pairs resulting from magnetic pair production will in general be created with momentum components perpendicular to the field, losing most of their energy by synchrotron radiation. These synchrotron photons seem to contribute to the total emitted spectrum mainly below 100 MeV and will be able to produce a second generation of pairs.

The synchrotron-pair production processes will continue until the synchrotron photons have not enough energy to produce any more $e^{\pm}$ pairs.

The surviving photons emitted by each radiative process (curvature and synchrotron radiation) will constitute the observable high energy radiation (X-ray and γ-ray emission) from the pulsar, while the produced pairs in the pair production front (PPF) may be the input to a coherent process which produces the radio and probably also the optical emission.

Due to the recent discovery of neutron stars with supercritical magnetic fields (for example magnetars), *photon splitting* [87] has been incorporated into the magnetosphere models. This process consists in the splitting of a single photon into two lower energy photons. Generally it becomes the dominant attenuation process above the magnetic pair creation when B $\gtrsim 2 \times 10^{13}$ G, decreasing the photon's escape energy. This process inhibits any development of electromagnetic cascades and therefore neutron stars with such high magnetic fields should not emit coherent radio emissions, defining a radio-quiet region in the P-$\dot{P}$ diagram (fig. 2.1).

In general, within the polar cap scenarios, the CR pair front limits the high-energy luminosity. The pulsar aging will decrease the surface magnetic field making it more difficult for the cascade to produce a pair production front and screen the $E_{\parallel}$. Therefore young pulsars will have thin accelerator gaps, while for old pulsars the gaps will be thicker and formed at higher altitudes, until pair fronts can no longer form and the pulsar dies as a radio pulsar. The pair production front can be related with the pulsar spin-down luminosity ($\dot{E}$), the period (P) and the surface magnetic field (B) as:

$$L_{CR} = \begin{cases} \epsilon 10^6 \dot{E}^{1/2} P^{1/14} B_{12}^{-1/7} & \dot{E} > \dot{E}_{break} \\ \epsilon \frac{3}{4} k(1-k)\dot{E} & \dot{E} < \dot{E}_{break} \end{cases} \tag{2.8}$$

where the young pulsars typically have $\dot{E} > \dot{E}_{break} = 5 \times 10^{33} P^{-1/2}$ erg s^{-1}. This relationship of the luminosity due to CR processes is only valid for pulsars with B$\lesssim 5 \times 10^{12}$ G [88].

The sharp decrease of the pair formation front for young pulsars leads the polar cap models to predict a "super-exponential" γ-ray spectra cut off, i.e., much steeper than a simple exponential as could be the case for the older pulsars.

In *polar cap models*, high-energy radiation is closely related to pair cascades at the PPF. The location of the PPF depends on the specific model for the accelerating electric field near the PC. There is a large variation among models based on the polar cap model [55]. These models have been developed to try to explain the incoming richness of spectral and temporal properties found in the new data of γ-ray pulsars.

The most recent models within the polar cap scenario assume the emission of free particles (ions) from the neutron star surface. These models are the so-called *space-charge limited flow (SCLF)* models [37] . The SCLF models assume that the surface temperature of the neutron star (T $\sim 10^5$ - 10^6 K) exceeds the ion and electron thermal emission temperatures. The $E_{\parallel}$ generated by the charge deficit from the ion flow produces large potential drops above the neuron star surface. These

larger potential drops accelerate particles ($\gamma \lesssim 10^6$) which generate inverse Compton photons (ICS) by scattering thermal X-rays from the neutron star surface [88]. Due to the low Lorentz factors required to produce pairs, an IC pair formation front will form close to the NS surface. However this IC will not be able to screen $E_{\parallel}$, helped by possible returning positrons [56]. The remnant electric field ($E_{\parallel}$) will accelerate the primary particles to a Lorentz factor high enough ($\sim 10^7$) to produce the CR (Curvature Radiation) pair production front, where there will be enough pairs to screen the short out of the acceleration region.

The previous models have assumed a magnetic field in the form of a static-like dipole, i.e. not distorted by rotational effects. This field is then approximated with axisymmetric field lines and, therefore, models cannot reproduce any strong asymmetry in the light curve.

In general, the peculiar behaviour of the light-curves reveals a complicated geometry of the pulsed emission, which is evidently not always similar to the light curves at other wavelengths. X-ray observations suggest a thermal background for some sources, where their modulation and phase behaviour are directly related with the magnetic field geometry at the neutron star surface. Recent pulsed emission observations at high energies (X-ray and γ-ray) have revealed a discrepancy in the light curves between these energies and the ones at radio wavelengths, even though they are rather similar for certain objects (like Crab) (fig. 2.8).

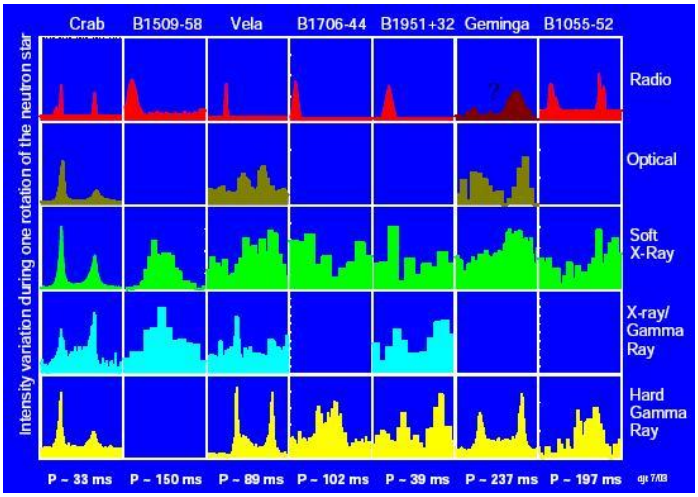

Figure 2.8: *Light curves of the 7 EGRET γ-ray pulsars at different wavelengths: from radio (top) to high energies (bottom) [147].*

This discrepancy is related to the asymmetry of the relative strength between the leading and trailing peaks with energy and the phase separation between double peaks. The already demonstrated correlation between the pulsar magnetic field and the spectral energy cut-off opens a possibility that this observed asymmetry is a

direct consequence of propagation effects due to purely rotational effects: presence of rotation-induced electric field, aberration of photon direction and decrease of the local magnetic field value under the photon's path [60]. During a pulsar rotation the line-of-sight samples various magnetic colatitudes and, therefore, the phase-averaged spectrum is composed of many spectra, each of them with different absorption through the photon path and a different position for the spectra cut-off. Therefore, these rotational effects will increase with the distance of the emitted photons from the spin axis and will be more important in the synchrotron emission region, with hardly any effect in the curvature emission.

These effects explain a leading peak being weaker than the trailing peak in the Crab light curve whereas they are not enough to explain some other EGRET light curves with the opposite behaviour (like Geminga and PSR B1706-44). These latter pulsars would need the consideration of the azimuthal properties of the pulsar magnetic field into the theoretical models.

In recent years Muslimov and Harding [118] have combined the classical polar cap model with the slot-gap model [15] in order to allow particles to accelerate up to few stellar radii, explaining the emission coming from sources with a small magnetic inclination and viewing angles, seeking the possibility of a wide hollow cone. In this scenario the pair production front curves upwards forming a narrow slot gap near the last open field line, where the $E_{\|}$ is unscreened and particles continue radiating to high altitudes along the last open field lines.

Recently there have been some fundamental developments in acceleration and emission models. Special and general relativistic effects are included and play an important role in pulsar emission, from inertial frame-dragging near the stellar surface to aberration, time-of-flight and retardation of the magnetic field near the light cylinder.

In the case of a neutron star magnetosphere filled with charges flowing along the open field lines, a qualitatively new component of the electric field is generated due to the effect of dragging of inertial frames of reference [117]. The cohesive energies are too small to support a finite electric field boundary condition at the stellar surface. Hence, one assumes the outflow of charged particles from the stellar surface, using an SCLF approximation. The alternative models rely on a large cohesive energy of atoms within the neutron star surface and imply that a vacuum gap with a huge electric potential drop near the stellar surface can be created.

All these models have been fitted in order to try to explain the most recent high-quality data in the most effective way. Numerical 3D codes are needed, capable of fast tracing the development and propagation of electromagnetic cascades in a variety of non-dipolar structures of the magnetic field. The advantage of incorporating multipolar components to the polar-cap models is that the magnetic field strength may locally be slightly lowered, thus opening windows for GeV photons to escape without magnetic attenuation; postulating high-altitude accelerators would be then unnecessary [135].

2.3.3 Millisecond pulsars

Millisecond pulsars (MSPs) are fast spinning neutron stars with small period derivative values ($\dot{P}<10^{17}$ s/s). These sources are believed to represent the final stage of low-mass X-ray binary evolution and, therefore, they are generally located in binary systems (75%) commonly accompanied by a white dwarf.

Being rather old (eq. 2.4), the millisecond pulsars do not fit the general scheme of pulsar evolution and most probably are re-accelerated by some external mechanism, such as accretion from the companion star in a binary system. Most of the radio pulsars detected so far have their rotational periods within the range from 10 ms to 10 s, whereas a few of them form a separate sample of millisecond pulsars with rotational periods in the range from 1 ms to 10 ms (fig. 2.1).

Millisecond pulsars differ from canonical ones in that they have rotational periods 1-2 orders of magnitude shorter and surface magnetic field strengths 3-4 orders of magnitude weaker ($B_s \sim 10^9$G) (eq. 2.3) that those of young pulsars. These properties make them quite different from canonical pulsars regarding γ-ray emission.

Given such low magnetic fields, their magnetosphere marginally produces pairs. The pair production will be low for CR and ICS pairs. Due to the lower multiplicity of the ICS pairs, CR will dominate the radiation from millisecond pulsars. Because, for most of them, their accelerating fields are unscreened, the cut-off energy of curvature photons due to the pair production shifts to higher energies and the maximum radiation of the millisecond pulsars should correspond to photons with energy ~ 100 GeV, with a less steep spectra near the cut-off energies.

Since millisecond pulsars have much weaker magnetic fields than normal pulsars, ICS is not important and hence is not considered here. Curvature radiation (CR) is considered first and then synchrotron radiation (SR). The synchrotron radiation spectrum is the combined emission from the whole range of altitudes from near the neutron star surface - the higher-energy portion - to near the light cylinder, forming the lower-energy portion. The critical SR energy decreases with altitude. Within the SCLF models, free emission of charged particles from the PC surface can occur because of their relatively low magnetic fields and because the work function (binding energy) is relatively small.

$$\begin{aligned} T_e &\propto Z^{4/5} B^{2/5} \\ T_i &\propto B^{0.73} \end{aligned} \tag{2.9}$$

Therefore, an additional induced electric field could occur when the local charge density is different from the co-rotation density (GJ density).

For MSPs, the hollow-cone can reproduce the wide double-peaked profile without assuming an aligned rotator.

The general relativistic effects of aberration and time of flight delays are important for millisecond pulsars (where the site of gamma-ray emission moves at relativistic speeds), and affect their light curves, especially at large inclination angles. The

combined effects of aberration and light travel delay lead to spreading of the leading peak and to piling up of photons in the trailing peak in the case of double-peak light curves. The same mechanism leads to asymmetry of single peaks in pulsar light-curves - the leading wing is broader than the trailing one [157]. Whenever the line of sight misses the outer rim of the polar cap, the observed spectra becomes soft with an apparent exponential (and not super-exponential) cut off, mimicking thus an outer-gap candidate. The millisecond gamma-ray pulsar J0218+4232 is probably a good example of such a case.

2.3.4 Outer gap model

The *outer gap* (OG) [39] models for high energy emission from pulsars are based on the existence of a vacuum gap in the outer magnetosphere which may develop between the last open field line and the null charge surface ($\Omega \cdot B = 0$) in charge-separated magnetospheres (fig. 2.4). The gaps arise because charges escaping through the light cylinder along open field lines above the null charge surface cannot be replenished from below.

The first outer gap models assumed that emission is seen from gaps associated with both magnetic poles [38]. However, most recent model versions have been more successful reproducing the observed light curves assuming emission from one pole only [133].

In this kind of model, the $e^{\pm}$ pairs are produced by photon-photon pair production. In young pulsars (Crab-like) the pairs are a result of the interaction of curvature photons (from primary particles) and non-thermal synchrotron X-ray emission from the same pairs. For older pulsars (Vela-like) the non-thermal X-ray emission is much lower and the pairs are assumed to come from the interaction of primary particle IC photons with thermal X-rays from the NS surface [159]. This thermal X-ray emission is maintained by down-ward moving accelerated pairs that heat the neutron star surface.

As in polar cap models, it becomes more difficult for older pulsars to produce the pairs required to screen the field and "close" the gap.

The high-energy spectra in both types of outer gap model have cut-offs around 10 GeV, due to the radiation-reaction cut-offs in the primary particle spectrum, which are much less sharp than the attenuation cut-offs in the polar cap model spectra. The shape of the cut-off is thus a simple exponential, dropping more gradually than in polar cap model spectra.

Outer gap models predict an emission component at TeV energies due to inverse Compton scattering by gap-accelerated particles [92]. TeV photons should escape from the outer gaps of pulsars with even strong surface fields and, therefore, this component is expected to be observable in many pulsars.

Since electron-positron pair production is thought to be a necessary ingredient for coherent radio emission, the relative geometry of the two emission regions should be

constrained from observations. In the outer gap models, the high energy emission is generally radiated in a different direction than the radio emission. Only when the line-of-sight intersects both directions does the radio pulse lead the γ-ray pulse as is observed in most γ-ray pulsars (fig. 2.8). Therefore, in these models the so-called "radio-quiet" pulsars are those pulsars whose radio emission is beamed away from us.

2.4 Steady emission from the pulsar and its surrounding

In previous sections, it has been detailed how the pulsed component arises from the pulsar magnetosphere. In this section, it will be briefly explained how the steady emission detected from the pulsar direction arises from the neutron star surface or in its vicinity and the processes responsible for such emission.

The emission coming from the neutron star surface and polar cap regions is assumed to be produced by thermal processes in the soft X-ray energy range, with no contribution at higher energies. At high energies, the main contributor to the steady emission is non-thermal. It is usually interpreted as synchrotron processes in the shock region, resulting from the interaction of a relativistic wind with a binary companion to the pulsar or the surrounding supernova remnant or interstellar medium. This last assumption suggests a correlation between the luminosity at high energies and the spin-down luminosity power ($\dot{E}$).

As it was already explained, pulsars are created during supernova explosions, ejecting the star-outermost shells into space forming the so-called supernova remnants (SNRs). For young pulsars, the supernova remnant is resolved as an extended structure, whereas for the majority of pulsars the nebula are likely to be seen much smaller, making them appear point-like. For these pulsars, the wind nebulae (the pulsar relativistic wind) interact with the interstellar medium contributing to the non-thermal steady emission component. The resulting interaction can take the form of a termination shock. In general, 2- or 3-D models are necessary to provide a detailed theoretical explanation of the emission morphology from young pulsars.

The pulsar wind nebulae (PWN) of MSPs may be older and expanding more slowly. In the case of MSPs, the non-thermal steady emission could be due to a quiescent state of the Roche lobe overflow or the shock wave resulting from the interaction between the pulsar wind and the out-flowing matter from a companion star.

2.4.1 Pulsar wind nebulae models

Young pulsars (with short periods and strong surface magnetic fields) interact in the early stage of their evolution with the surrounding SNR, injecting large amounts of relativistic particles into it. These accelerated leptons and hadrons are injected

into the nebula forming a non-thermal compact nebula called pulsar wind nebulae (PWN), which can radiate in the whole range of electromagnetic spectrum.

It is widely argued that lower energy radiation in the PWN is produced by leptons (*leptonic models*) in the magnetic field (synchrotron radiation) and the higher energy part of the spectrum is produced by leptons in the ICS (Thompson regime) of the low energy synchrotron, Microwave Background Radiation (MBR) or infrared photons (warm gas inside the nebula) [99]. The energy losses of leptons on the ICS in the Klein-Nishina regime can be safely neglected with respect to the synchrotron energy losses. Within this scenario, at the early stage of expansion of the nebula, the synchrotron energy losses of leptons dominate over the ICS and the bremsstrahlung energy losses. Therefore, most of the lepton's energy is radiated in the low-energy range. When the nebula becomes older, the energy density of the synchrotron radiation inside the nebula decreases but the energy density of the MBR remains constant. Therefore the relative importance of the ICS losses increases with respect to the synchrotron energy losses. In fact, for the PWN with the age $> 10^4$ years, the γ-rays are produced mainly by leptons scattering the MBR (not synchrotron photons). Therefore, the possible displacement of the pulsar from the place of birth has no effect on the expected level of the γ-ray flux but only on the dimensions of the γ-ray source.

While this leptonic model was successfully fitted to Crab data below ~ 10 TeV [48], reported emission up to 50 TeV [4] leads to another interpretation (*hadronic models*) for the emission at energies higher than ~ 10 TeV.

In the hadronic models, the heavy nuclei accelerated in the inner pulsar magnetosphere and injected into the nebula can release energy as a result of the acceleration of positrons, collisions with the matter of the nebula and because of adiabatic expansion of the nebula. As a result of collisions with matter, the accelerated heavy nuclei produce γ-rays ($\gtrsim 10$ TeV) via decay of neutral pions [22]. At the early stage, when the nebula is relatively dense, nuclei also fragment to lighter products due to the collisions with the matter, while the most energetic nuclei may also diffuse out of the nebula. Due to the decrease of the density and relativistic nuclei in the nebula, the contribution of γ-rays from hadronic processes is relatively less important for older nebulae. The γ-ray spectra from hadronic collisions shift to lower energies due to adiabatic energy losses of nuclei, more efficient escape of higher energy nuclei from the nebula, and lower energies of freshly injected nuclei inside the nebula by older pulsars.

In the last year the possible contribution of hadrons at the highest energies and time-dependent and 3-D radiation models for the PWN have been included in the leptonic models, taking into consideration *hadronic-leptonic (hybrid) models* [24]. Such hybrid leptonic-hadronic models also predict additional neutrinos, neutrons or charged particles which would contribute to the observed cosmic rays fluxes at the Earth's surface.

Part II

Simulations

Chapter 3

Sensitivity of MAGIC for pulsars

To study the potential of the MAGIC telescope for detecting pulsars, an MC (Monte Carlo) simulation has been carried out. The MC simulation includes the EAS processes, the detector response and the analysis procedure. This chapter will give an idea of the MAGIC telescope's capability to detect the γ-rays coming from pulsars in the energy range of 10 GeV - 30 TeV.

It will briefly explain the general characteristics of the MC simulation programs and, finally, will present the sensitivity results of the detector for the northern hemisphere EGRET pulsars.

3.1 MC simulation programs

To study the potential of the MAGIC Telescope for the observation of γ-ray pulsars, one first has to know the capability of the telescope to detect γ-showers in the energy range of 10 GeV - 30 TeV. This is done using several computing programs: the first one, CORSIKA (COsmic Ray SImulations for KAskade), simulates the EAS and Cherenkov light production in the atmosphere by a particle of a given energy, explained in section 1.4.1. There follows the Telescope simulation, that simulates the response of each part of the detector to the Cherenkov light produced in the showers, tracing the reflection of the Cherenkov photons on the reflector of the telescope, and finally simulates the formation of the images on the camera as well as the detection and processing of the signal.

3.1.1 Corsika

CORSIKA is the standard simulation program used for the simulation of EAS. It consists of a detailed Monte Carlo program to study the evolution of an EAS initiated by photons, protons, nuclei, or any other particle in the atmosphere. The program incorporates detailed routines, which simulate the transport of particles in

the atmosphere and their decays and interactions with atmospheric nuclei. It also includes a model of the atmosphere and takes into account the Earth's magnetic field. All particles are tracked through the atmosphere and the output of the program gives type, energy, location, direction and arrival times of all secondary particles that are created in an air shower and that reach a selected observation level. It is not the aim of this work to give a complete and detailed description of the physics used in CORSIKA but merely to mention the main physical considerations and how the program deals with them, placing special emphasis on Cherenkov photon production. In the simulation of an EAS, a large number of parameters have to be taken into account but the most crucial problem is that the knowledge of high-energy hadronic interactions is still incomplete.

Taking into account the main facts when simulating an EAS, the CORSIKA program can be divided into four parts [100]:

- **Hadronic interaction models and decay of unstable particles**: The distance covered by a particle before it undergoes its next interaction or decay is determined by the cross-section of the hadronic interaction as well as the density distribution of the atmosphere along this distance and the probability of a decay. The decay and interaction length are determined independently at random, and the shorter one is taken as the path length, deciding if the particle decays or interacts.

  Moreover, the hadronic interactions depend on the energy of the particle that varies along its trajectory:

  - *High-energy interactions*: For hadronic interactions of nuclei and hadrons with the air nuclei at energies $\gtrsim$ 80 GeV, at which generation of strange baryons can take place, the following models are used: VENUS (Very Energetic Nuclear Scattering, to simulate ultra relativistic heavy ion collisions) [153]; QGSJET (quark-gluon string model) [96]; DMPJET (two-component Dual Parton Model) [128]; SYBYLL (QCD minijet model) [67]; and HDPM (routines faster and adjusted to experimental data where available) [35].
  - *Low-energy interactions*: For hadronic interactions of nuclei and hadrons with the air nuclei at energies $\lesssim$80 GeV, these models are used: GHEISHA (to compute elastic and inelastic cross-sections of hadrons interacting with the air and the particle production) [64] or ISOBAR and fireball models (routines faster but simpler) [84].

  Most of the particles produced in high-energy interactions are unstable and may decay into other stable or unstable particles. Neutral pions π^o and mesons, ηs as well as resonance states, have such a short life time that interaction are negligible before they decay. Muons are prevented from penetrating the whole atmosphere

by decay only. Neutrons are treated as stable particles due to their long lifetime. For all the other unstable particles, there is a competition between interaction and decay processes and the decision to consider each process is taken when the mean free path is computed.

- **Electromagnetic interaction models**: For the simulation of interactions of electrons and photons, the EGS4 (Electron Gamma Shower System version 4) is used [121] and performs a full Monte Carlo simulation of the electromagnetic component of the showers. For electrons or positrons, it treats bremsstrahlung and multiple scattering, Bhabha and Moller scattering and annihilation. The gamma-rays may undergo Compton scattering, electron-positron production and photoelectric reactions. The photoproduction of muons pairs and the photonuclear reaction with protons and neutrons of atmospheric nuclei are also taken into account. An alternative way of treating the electromagnetic component is to use the improved form of the analytical NKG (Nishimura Kamata Greisen) formula [82]. It is faster but less accurate, and coordinates of electromagnetic particles cannot be obtained but only total electron numbers at various atmospheric depths, together with some parameters that give information about the general development of the electromagnetic component of the shower.

- **Particle tracking through the atmosphere**: For propagating particles between two interaction points, their space and time coordinates as well as their energy have to be updated, taking into account:

  - *Ionization energy loss*: When passing through the atmosphere, the charged particles ionize the medium and suffer an energy loss, which is computed along its trajectory with the Bethe-Bloch stopping power formula.
  - *Coulomb multiple scattering*: Charged particles are scattered in the electric Coulomb field of nuclei in the atmosphere. As these nuclei are generally much more massive than the scattered particles, the direction of flight might be altered, but not the energy. In CORSIKA, the process of Coulomb multiple scattering is considered for each tracking step only in the middle of the tracking distance.
  - *Deflection by the Earth's magnetic field*: Charged particles with momentum $\vec{p}$ suffer a deflection which points to the direction normal to the plane spanned by magnetic field $\vec{B}$ and $\vec{p}$.

  There are different models of atmospheres implemented in the CORSIKA program and the appropriate one is selected through the program input card. The atmosphere model in CORSIKA used in this simulations consists of 78.1% of N_2, 21.0% of O_2 and 0.9% of Ar, considering a flat atmosphere divided in 5 layers in which the density varies with the altitude.

- **Cherenkov radiation**: The Cherenkov light is produced in EAS by electrons, positrons, muons, and charged hadrons. The Cherenkov photons are considered within a wavelength band, defined in the input-card. The atmospheric absorption of the Cherenkov photons is not taken into account. The condition for Cherenkov photon production ($c/v < n$) is examined in every step of the trajectory of the charged particle, approximating the refraction index by the local density ($\rho(h)$) $n = 1 + 0.000283 \cdot \frac{\rho(h)}{\rho(0)} \quad g/cm^3$, and neglecting the wavelength dependence of n. The number N_c of photons, which are emitted per path length s at an angle θ_c is given by the expression:

$$\frac{dN_c}{ds} = 2\pi\alpha \int \frac{sin^2\theta_c}{\lambda^2} d\lambda \tag{3.1}$$

  where the integral extends over the wavelength range within which the Cherenkov detector is sensitive, α is the fine structure constant, and the angle θ_c relative to the charged particle direction is $\theta_c = arccos\frac{1}{\beta \cdot n}$.

  The emission of Cherenkov photons is treated in the following way: once the total number of emitted photons N_c have been computed for a given tracking step, it is subdivided into smaller sub-steps, such that the number of Cherenkov photons emitted per sub-step is less than a fixed predefined bunch size. In such a sub-step, all the photons are sent in a compact bunch along a straight line, defined by the emission angle θ_c and a random value for the azimuthal angle around this direction. This photon bunch is treated as a unit, rather than as a group of single Cherenkov photons treated separately, thus reducing the computational steps and time considerably. In this case, due to the low photon statistic for gammas, a bunch maximum size as 1 (table **??**) is used. Only Cherenkov photons arriving at the observation level are recorded in the output file, where - for each bunch - the number of Cherenkov photons, the x and y position coordinates at the observation level, direction cosines u and v, arrival time, and height of production above sea level are recorded.

In CORSIKA, the simulation of air showers is steered by parameters that have to be provided by the user in an input card.

3.1.2 The telescope simulation: Reflector and Camera programs

Once atmospheric showers have been generated, the next step is to simulate how the detector would record these showers. In order to simulate the detection of showers as close as possible to the real situation, two more programs are needed: *Reflector* and *Camera* programs, which can be configured using several parameters specified by their corresponding input cards. The first program takes the output file of CORSIKA and

simulates the reflector of the telescope by translating the photons from the ground to the pixelated camera. The output of this program is processed by the second one, the Camera program, finally obtaining events that fulfil several imposed conditions to the reflected events, like the trigger condition.

Reflector program

The CORSIKA program simulates neither the atmospheric extinction nor the scattering (such as Rayleigh and Mie scattering) of Cherenkov photons as they travel through the atmosphere, since they are extrapolated straight to the ground. Therefore, the first step performed by the reflector program is the simulation of these phenomena, which are going to cause a reduction of the number of Cherenkov photons which reach the ground (especially for distant or low-energy showers) and a change in their wavelength distribution.

The next step is the simulation of the reflection of the Cherenkov photons on the telescope mirror and the estimation of the impact points in the focal plane. This part includes some losses in reflectivity (taken from file *reflectivity_90.dat*) and large angle scattering. It uses the tracing technique, using the exact position and orientation of each mirror element (*magic.def* file). Realistic aberrations of the tessellated reflector of the MAGIC Telescope are included in the simulation.

This program takes as parameters an input file, where the user specifies what showers to read as well as the set-up of the telescope needed for photon detection.

Camera program

The MAGIC camera simulation program simulates the response of the photomultiplier and camera electronics to the impacting photons. For each photon that impacts each photomultiplier, the program simulates the camera electronics that includes, taking into account the effect of the QE, the trigger logic and the data acquisition system. The light of night sky also has to be taken into account. Finally, the camera files are calibrated and the cleaned images are parameterized in Hillas parameters (chapter 1). The resulting image parameters are written into an output file.

The night sky background, or light of the night sky (LONS), is one of the most important parameters to be included into the camera simulation. It is the diffuse light that arrives to the detector from the night sky. The LONS depends on the site where the telescope is located, the detector acceptance and the zenith angle. The LONS is the sum of several components: the air fluorescence, the starlight of faint stars, the airglow and, sometimes, man-made artificial light. The LONS is one of the most important factors that limit the energy threshold of atmospheric Cherenkov telescopes. It causes accidental triggers and also contaminates the γ-ray images close to the energy threshold. The LONS intensity outside the galactic plane, subtracting bright stars from the FoV, was measured for the site of the 'Roque de los Muchachos

observatory on the Canary Island of La Palma [115] to be:

$$F_{LONS} = (1.7 \pm 0.4) \times 10^{12} ph \cdot m^{-2} \cdot sr^{-1} \cdot s^{-1}$$

The essential parameters for the camera program are retrieved from a parameter file. Table **??** briefly describes the most important parameters in the simulation.

The output file has all the information of the events and has the format of a ROOT file (.root). Further details are given in section 5.0.2.

3.2 Simulation results

The complete set of programs explained in the previous section (CORSIKA, MAGIC Reflector and Camera programs) is used to estimate the sensitivity of the MAGIC Telescope by generating a set of MC simulations with the telescope response.

The main objective is to estimate the detector response expressed by the telescope effective area for gammas and proton showers as a function of the energy. The effective area can be understood as the telescope's "cross-section" for shower detection as a function of energy, which indicates the probability of observing high-energy gamma-ray pulsars with MAGIC.

In the following sections, the fraction of triggered events (trigger efficiency) and the effective area of the telescope for gammas and protons and, in particular, the expected rates for the six pulsars detected by EGRET will be computed for different zenith angles. From the MAGIC effective area and the extrapolated source spectra, the rates (respectively the number of events per second), detected by the telescope are computed. From those rates, the signal significance can be computed, determining the expected "quality" of the signal detected by the telescope.

3.2.1 MC Analysis

For the analysis of MC events, the showers simulated in the MAGIC collaboration with the CORSIKA program and the simulation programs of the MAGIC Reflector and Camera have been used. The trigger conditions used in the camera program are: threshold = 4mV (collaboration standard) per pixel and 4 pixels with topology 2 (4NN))(see table **??**)

The output of the analysis program is then processed with the same analysis program used for the real data analyzed in this Thesis. This includes a point-spread function of 1.4 cm and a 2-level image cleaning of 10 phe on core pixels and 5 phe on the boundary ones. This will give us the detection capabilities of the telescope at trigger level, before any analysis of the data.

The output file of the camera program lists the number of triggered and simulated events as a function of the energy and the impact parameter. The ratio of the triggered events and the total number of simulated events is called the trigger efficiency, P(E,r).

P(E,r) represents the fraction of detected events with primary energy E (in GeV) and impact parameter r (in meters) [1]. The integration of this expression as a function of r and δ gives the effective area S(E) [2] which determines how likely the telescope is to detect gammas and protons, as a function of the energy:

$$\begin{aligned} S_\gamma &= \int_0^{2\pi} d\phi \int_0^{\infty} P_\gamma(E,r)\cdot r\cdot dr \\ S_p &= 2\int_0^{2\pi} d\phi' \int_0^{\pi/2} sin\delta\cdot d\delta \int_0^{2\pi} d\phi \int_0^{\infty} P_p(E,r,\delta)\cdot r\cdot dr \end{aligned} \tag{3.2}$$

In the case of protons, the trigger efficiency also depends on the angle between the hadron shower incidence direction and the telescope axis (δ), and the corresponding azimuthal angle (ϕ'). Therefore, one has to integrate in these variables to cover the solid angle of generation, due to the fact that the protons come isotropically from all sky directions. In the CORSIKA program, proton showers were generated uniformly with directions forming angles between 0 and 5 degrees with respect to the telescope axis. The trigger efficiency for larger angles was found to be negligible [54]. In the case of gammas, the angle δ is zero, since the telescope points towards the point gamma source.

Folding the telescope response with the source differential flux (dN/dE) (for our studies the six pulsars detected by EGRET), the detection rate of the γ-source and protons can be calculated by a numerical integration to:

$$R_\gamma(E>E_0) = \int_{E_0}^{\infty} \frac{dN_\gamma}{dE}\cdot S_\gamma(E)\cdot dE \tag{3.3}$$

$$R_p(E>E_0) = \int_{E_0}^{\infty} \frac{dN_p}{dE\cdot d\Omega}\cdot S_p(E)\cdot dE \tag{3.4}$$

The differential fluxes taken in the simulations are:

$$\begin{aligned} \frac{dN_\gamma}{dE} &= K\cdot(\frac{E}{E_n})^{-\Gamma}\cdot exp(-(E/E_0)^b)\ \ m^{-2}\ s^{-1}\ GeV^{-1} \\ \frac{dN_p}{dE\cdot d\Omega} &= 1.94\times 10^4(\frac{E}{1\ GeV})^{-2.75}\ \ m^{-2}\ s^{-1}\ sr^{-1}\ GeV^{-1} \end{aligned} \tag{3.5}$$

where the first formula is the flux expression of the six EGRET pulsars fitted from the EGRET measurements [50], whose fitting parameters (K, E_0, b and Γ) are listed

[1] Due to the hexagonal pixels and the hexagonal structure of the camera, the trigger efficiency also has some ϕ dependence. However, this dependence is negligible and will not be considered in the simulation calculations.

[2] The effective area is measured in m^2 for γ's while, for protons is expressed in m^2·sr.

in table 3.1. This type of spectra is expected if a cut-off is caused by either pair production or, for example, synchrotron radiation of electrons with a certain maximum energy (E_0) (see chapter 2). The fitted parameters used here correspond to a super-exponential behaviour of the pulsar spectra, typical of polar cap models. Therefore, the simulation results will be the most conservative ones concerning the telescope sensitivity for pulsar studies. The second formula is the flux for protons in the VHE range [154].

Object	K($\times 10^{-4}$) ($m^{-2}s^{-1}GeV^{-1}$)	Γ	E_0 (GeV)	b
Crab	24.0	2.08	30	2.0
PSR B1951+32	3.80	1.74	40	2.0
Geminga	73.0	1.42	5.0	2.2
PSR B1706-44	20.5	2.10	40	2.0
PSR B1055-52	4.00	1.80	20	2.0
Vela	138	1.62	8.0	1.7

Table 3.1: *Gamma-ray spectral parameters above 1 GeV (as computed in [120]) used for the six EGRET-pulsar spectra.*

3.2.2 The MC data sample

The sample of MC gammas and protons (table 3.2) from the CORSIKA and Reflector programs have been generated for the MAGIC collaboration [111]. A summary with the characteristics of the simulation for each data sample is shown in table 3.2. The Monte Carlo simulation for protons has only been generated up to 30° of zenith angle due to the large computing effort needed for the proton sample generation.

	Gammas	Protons
N º (10^6)	46	29
θ (º)	0 - 60	0 - 30
E	10 GeV - 30 TeV	30 GeV - 30 TeV
r (m)	0 - 300,400	0 - 400
Γ	-2.6	-2.75

Table 3.2: *Gamma and proton MC simulated sample, where $N \equiv$ number of simulated photons, $\theta \equiv$ zenith angle, $E \equiv$ energy of the primary particle, $r \equiv$ impact parameter and $\Gamma \equiv$ spectrum slope.*

The MC sample has been divided in equally spaced bins of $\cos\theta = 0.1$ within the total zenith angle range of table 3.2. For each zenith angle bin, the generated

spectrum follows the expression $\frac{dN}{dE} = E^{-\Gamma}$, Γ being the spectrum slope, one of the simulation parameters in Corsika program. The value of the slope for protons is given by equation 3.5 whereas the slope in the case of gammas follows the Crab spectrum at HE [11].

Due to these hard slopes, the sample statistics for high energies will be small, increasing the error bars in all resulting plots.

3.2.3 Trigger efficiency

In the Camera simulation program, the trigger conditions are set to threshold =4mV and 4 Next Neighbours coincidence. These conditions will fix, together with other detector properties, the telescope trigger efficiency:

$$\begin{aligned} Trig.eff. &= P_\gamma = \frac{\#Triggered\ events}{\#Total\ events} \\ Trig.eff.error &= \Delta P_\gamma = \frac{Trig.eff. \cdot \sqrt{1 - Trig.eff.}}{\sqrt{\#Trig.\ events}} \end{aligned} \tag{3.6}$$

where the error of the trigger efficiency is computed using the expression of a binomial distribution estimator.

The trigger efficiencies for gamma and proton samples (eq. 3.6) are listed in tables 3.3 and 3.4.

θ (°)	**#Trig. evt.**	**#Total** (10^6)	P_γ (10^{-2})	ΔP_γ
0-10	37222	2.0	1.840	0.010
10-20	81330	4.5	1.800	0.010
20-30	120848	7.3	1.661	0.005
30-40	131152	10.0	1.313	0.004
40-50	115958	10.8	1.071	0.003
50-60	80153	11.8	0.681	0.002
Total	566663	46	1.221	0.002

Table 3.3: *Trigger efficiencies for* **gammas** *(P_γ) (10GeV-30TeV and 0-300 m)*

The first feature to note is that the trigger efficiency for gammas (P_γ) is much higher than for protons (P_p). This is a consequence of the lower fraction of $e^\pm$ pairs in hadronic showers. It is difficult to compare both trigger efficiencies because they are generated with different impact parameters with respect to the telescope axis and in the case of protons with a range of angles with respect to the telescope axis. Also,

θ (°)	**#Trig. evt.**	**#Total** (10^6)	P_p (10^{-4})	ΔP_p
0-10	2525	4.5	5.6	0.1
10-20	5920	11.0	5.4	0.1
20-30	7018	13.1	5.4	0.1
Total	15463	28.6	5.41	0.04

Table 3.4: *Trigger efficiencies for* **protons** *(P_p) (30GeV-30TeV and 0-400 m).*

as can be seen from table 3.4 the trigger efficiency decreases for increasing zenith angle. At the same time as the zenith angle increases, the path in the atmosphere traversed by a photon also increases (section 1.4.1) with the following consequences: first, the atmospheric absorption increases and the light density decreases; second, since the maximum of Cherenkov emission is further away from the observer, the light spreads over a bigger area, also decreasing the light density. So, as the zenith angle increases, the primary gammas have to be more energetic so that a sufficient number of photons reaches the detector and fulfils the trigger condition. This effect should decrease the telescope trigger efficiency for high zenith angles. This can be seen very clearly between 0° - 60° zenith angle, where the trigger efficiency for gammas decreases by a factor 2.7. However, for a smaller range of zenith angles (0° - 30°) the trigger efficiency hardly changes, just a factor ∼1.1 for gammas and protons.

The level of trigger efficiency is shown depending on the energy (fig. 3.1 and fig. 3.2) and the impact parameter (fig. 3.3 and fig. 3.4) for gammas and protons respectively.

For gammas, the trigger efficiency (fig. 3.1) increases with primary particle energy reaching an efficiency of 100% for primary γ-particles with energies approximately $\geq$ 1 TeV for an impact parameter of up to 300 m. At the highest energies, the behaviour is not well defined since there are not enough statistics, but it seems to tend asymptotically to 1. In the case of proton as primary particle (fig. 3.2), despite the large error bars due to the low statistics, it can be seen that the trigger efficiency reaches values up to 0.2 for 30 TeV - although an asymptotic behaviour for higher energies can not be determined.

Figure 3.3 shows the trigger efficiency for gammas versus the impact parameter for energy ranges between 10 GeV - 30 TeV. Due to the generation spectrum slope (-2.6), it is clear that our simulation results will be mostly populated by low-energy events, which have a trigger efficiency close to zero. This is the reason for the lower trigger efficiency of the figure 3.3 plateau compared to the trigger efficiency distribution versus the energy.

As explained in chapter 1, the lateral distribution of the Cherenkov shower has a maximum at an impact parameter of around 115 m, corresponding to an emission

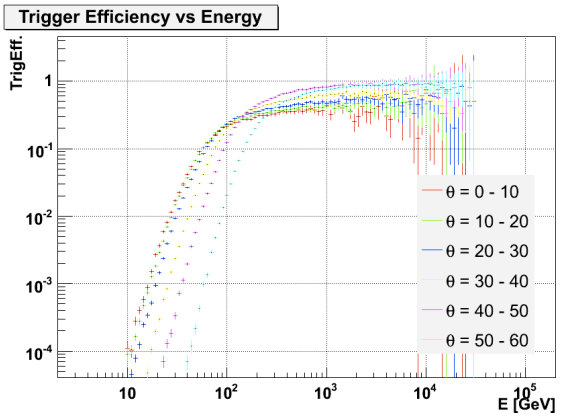

Figure 3.1: *Trigger efficiency probability versus energy for* **gammas** *between 10GeV and 30TeV at different zenith angles.*

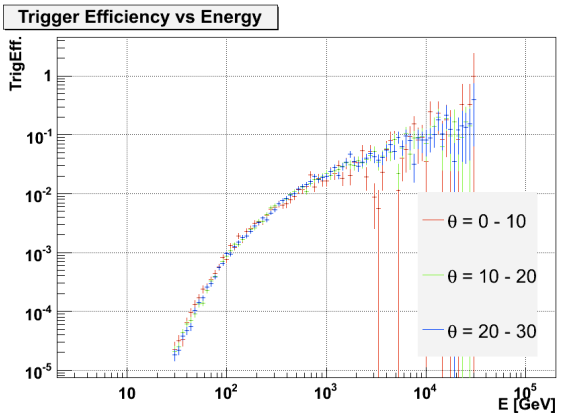

Figure 3.2: *Trigger efficiency probability versus energy for* **protons** *between 30GeV and 30TeV at different zenith angles.*

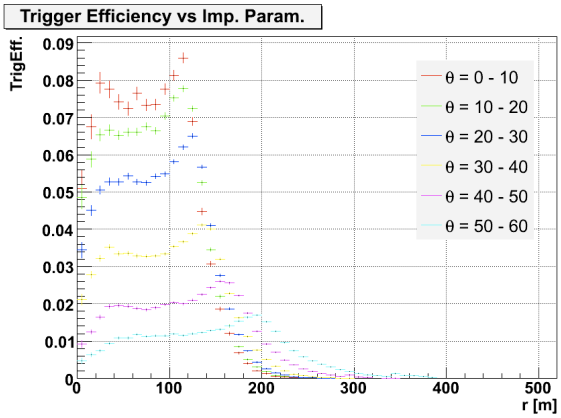

Figure 3.3: *Trigger efficiency versus impact parameter for* **gammas** *between 10GeV and 30TeV at different zenith angles.*

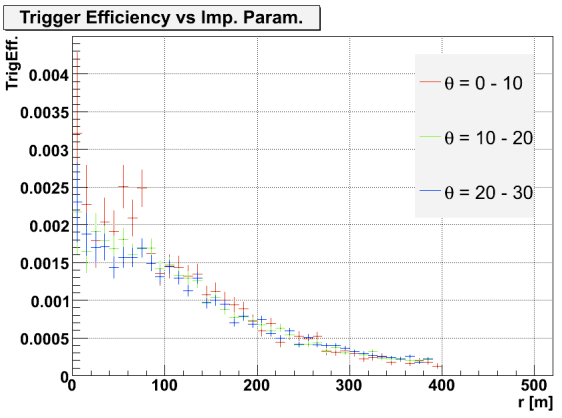

Figure 3.4: *Trigger efficiency versus impact parameter for* **protons** *between 30GeV and 30TeV at different zenith angles.*

altitude of ∼10-17 km. This point is called the "hump" and corresponds to the region where most of the Cherenkov light impacts at 125 meters on the ground. However, this region is finite and ends at an altitude of around 6 km, which corresponds to an impact parameter of around 60 m. From 60 m to the core, the trigger efficiency decreases but not down to zero, due to the contribution of the showers that develop closer to the telescope.

In the case of gammas, it can be seen that the trigger efficiency decreases with the zenith angle for all impact parameters (fig. 3.3) and mainly for low-energy events

(fig. 3.1). However, in the case of protons (fig. 3.3), it seems that the trigger efficiency is hardly dependent on the zenith angle. For all zenith angles, the trigger efficiency always decreases asymptotically to zero for high values of impact parameter. This is due to the more extended proton showers in the atmosphere (figure 1.10), which do not provide a well-defined region of maximum Cherenkov emission as in the case of gammas. When the impact parameter increases from the hump to 400 meters there is a 10 times decrease in trigger efficiency, so the trigger efficiency decreases very slowly with the impact parameter for all zenith angles. This brings us to the question of convergence of the trigger efficiency with the impact parameter [54], which should be included in the calculation of the proton rate (see section 3.2.5).

The results of figure 3.3 corroborate another effect already explained in chapter 1: the "hump" shifts from ∼110 m (for 0º zenith angle) to ∼200 m (for 60º zenith angle). This is due to the dependence of the $R_{core,max}$ on the altitude where the Cherenkov light is emitted (h) and to the change of the emission height with the observation zenith angle with $\frac{1}{cos\theta}$ (fig. 1.6).

The sum of all the contributions for all the energies are shown in figure 3.3. For the zenith angle bin between $0^o - 10^o$ (shown in fig. 3.5), one can see the flattening of the lateral distribution with the increase of the energy of the primary γ-particle. It can be inferred from fig. 1.10 that at the same time as the energy of the primary particle increases, the maximum Cherenkov light emission region develops closer to the ground. So one can see that for the energy ranges of 10-50 GeV the region of the maximum Cherenkov emission shown in figure 1.10 is very small and concentrated around the hump. In contrast, for energies above 100 GeV, there is a flattening of the impact parameter distribution between 0 and 125 meters, until reaching a constant trigger efficiency value of 1 for higher energies ($\sim$ 500 GeV). This flattening in the distribution is interpreted as an increase of the region of maximum Cherenkov light emission with increasing energies, until it reaches the ground for energies higher than hundreds of GeV.

For protons (fig. 3.6), the trigger efficiency at 10º zenith angle versus the impact parameter for different energy slices is also shown. There is a tendency of the trigger efficiency to decrease at all energies as a function of impact parameter, as observed also in plot 3.4 for the sum of these slices. The trigger efficiency increases with the energy of the primary proton.

3.2.4 The effective area

The mean trigger efficiency (eq. 3.2) is used to compute the effective area for gammas and protons for each impact parameter bin, approximating the integral to a finite sum in all impact parameter bins ($i = 0, ..., nbiny$):

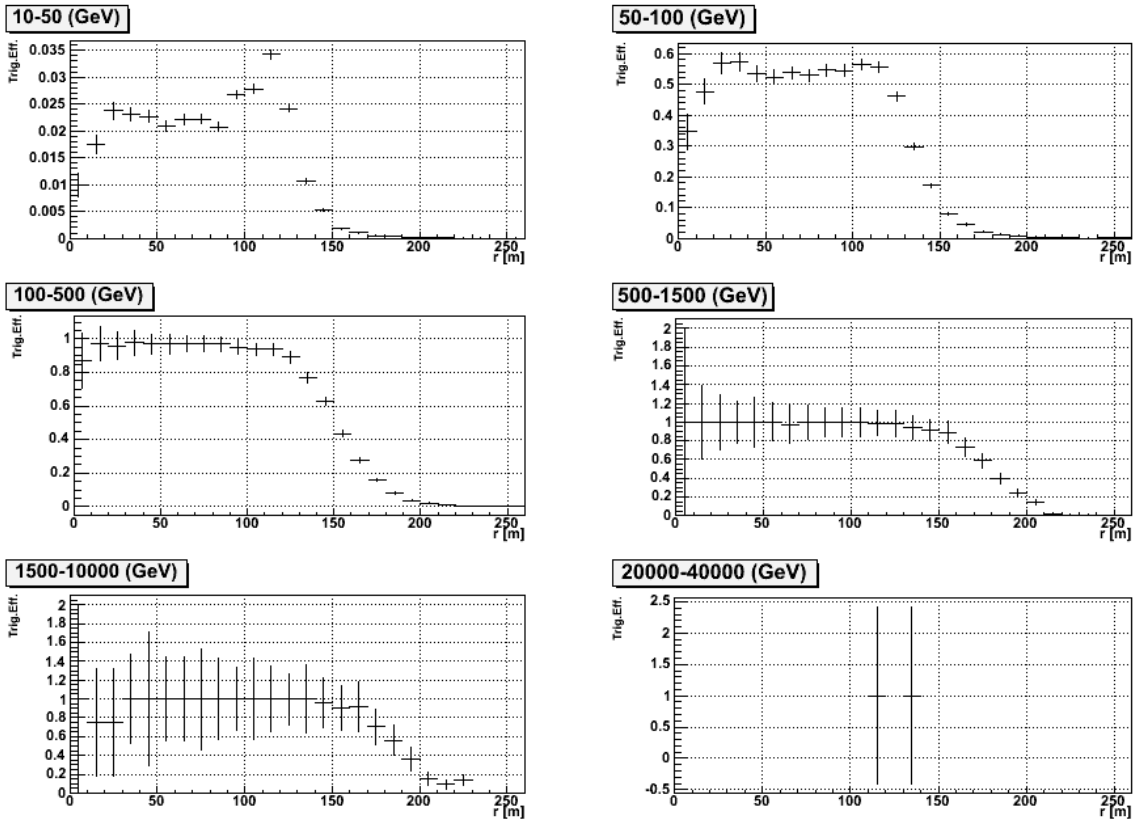

Figure 3.5: *Slices in energy of trigger efficiency for* **gammas** *between 10 GeV - 30 TeV at zenith angles between* $0^o - 10^o$. *The maximum trigger efficiency increases with the energy of the primary* γ*-ray.*

$$< P_{\gamma(p)} > = \frac{2\pi \cdot \int_0^\infty P_{\gamma(p)}(E,r) r \cdot dr}{2\pi \cdot \int_0^\infty r \cdot dr}$$

$$S_{\gamma(p)} = \pi \sum_0^{nbiny} < P_{\gamma(p)} >_i (r^2_{max} - r^2_{min})_i$$

where $< P_{\gamma(p)} >_i$ is the Monte Carlo trigger efficiency for bin i.

Because the effective area characterizes uniquely the behaviour of the telescope, it is interesting to try to parameterize it with an analytical equation (eq. 3.7). The following type of functions have been used:

$$F(E) = \frac{A \cdot E^B}{1 + (\frac{E}{C})^D} \tag{3.7}$$

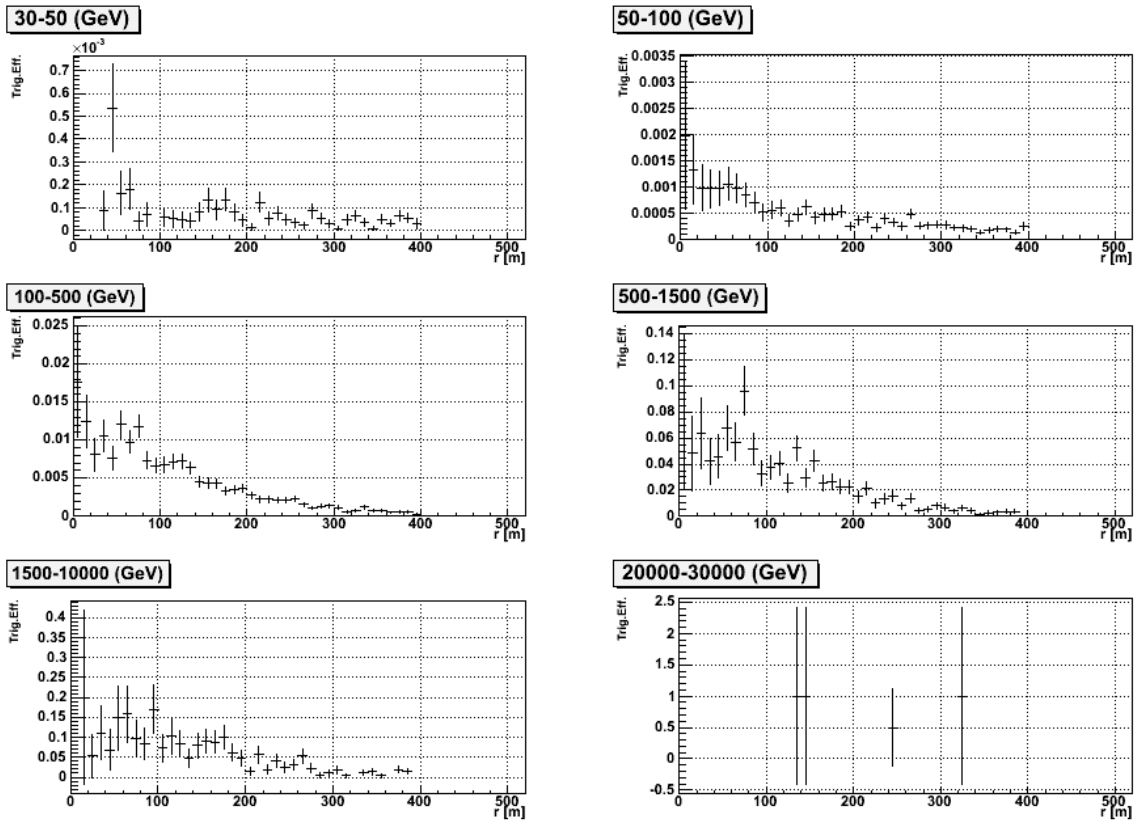

Figure 3.6: *Slices in energy of trigger efficiency for* **protons** *between 30 GeV-30 TeV at zenith angles between* $0^o - 10^o$. *The maximum trigger efficiency increases with the energy of the primary proton.*

where E is the energy of the primary particle, B is the slope at low energies, C is related with the point of change of the slope, B-D is the slope at high energies and A the global normalization.

The effective areas for gammas and protons at different zenith angles are shown in figures 3.7 and 3.8, respectively. The corresponding fit parameters for areas using equation 3.2 are listed in tables 3.5 for gammas and 3.6 for protons.

Inspecting the plots in figures 3.7 and 3.8, one can conclude that the telescope effective area depends primarily on the energy of the primary particle. To understand better the meaning of the effective area, imagine that the telescope can see any shower, of a given energy and trigger efficiency of 1, produced in the atmosphere inside a circle of this area around the telescope. For gammas (fig. 3.7), the telescope effective area has values of $\sim 10^2$ m^2 at 10 GeV, reaching at trigger level an asymptotic value of $\sim 3 \times 10^5$ m^2 for energies greater than 200 GeV. This asymptotic value corresponds to a trigger efficiency of 100% multiplied by the maximum area of impact parameter

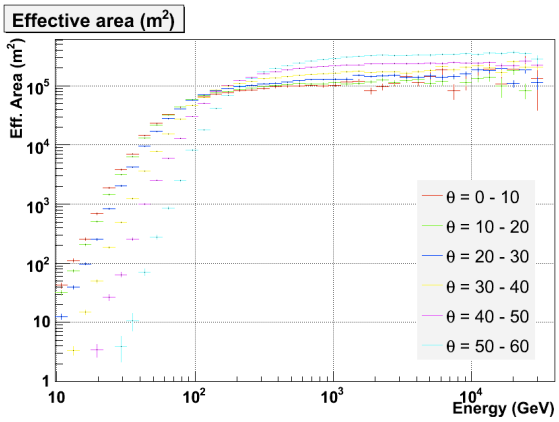

Figure 3.7: *Effective area for* **gammas** *between 10 GeV - 30 TeV at different zenith angles.*

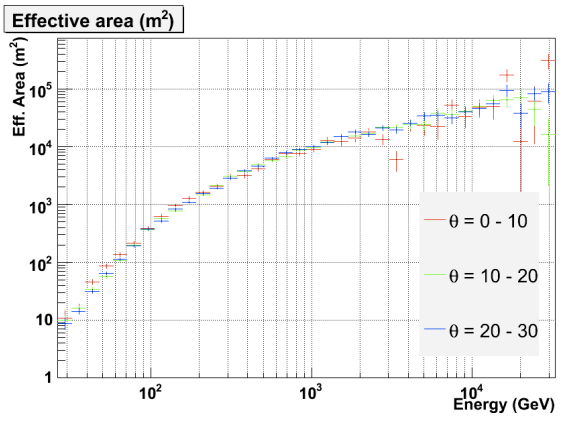

Figure 3.8: *Effective area for* **protons** *between 30 GeV - 30 TeV at different zenith angles.*

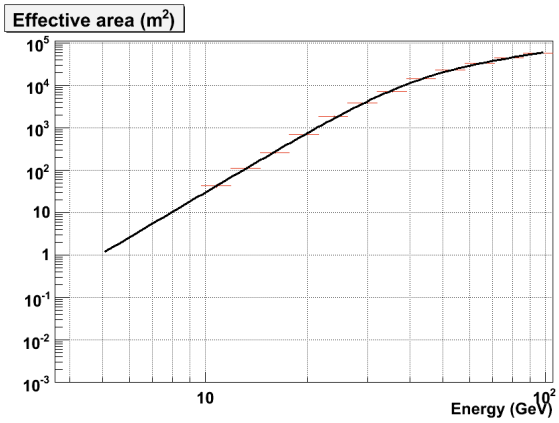

Figure 3.9: *Fit to the effective area for* **gammas** *between 10 GeV - 30 TeV at θ = 0°-10° of zenith angle. The black line corresponds to the fit function given by the parameters listed in table 3.5*

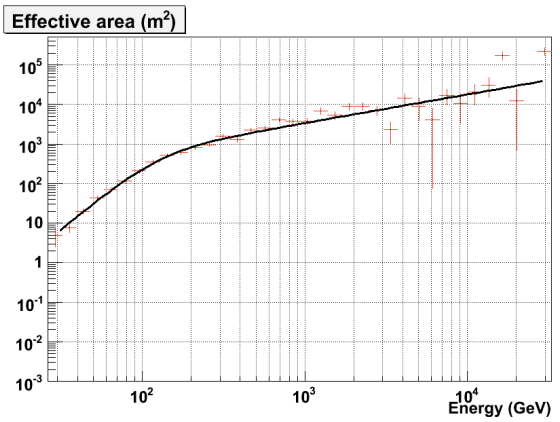

Figure 3.10: *Fit to the effective area for* **protons** *between 30 GeV - 30 TeV at θ = 0°-10° of zenith angle. The black line corresponds to the fit function given by the parameters listed in table 3.6*

($\theta = 0$: $\pi \cdot (250)^2 \sim 2 \times 10^5$ m^2). This value increases with the increase of the zenith angle, due to the larger spread of the light with high zenith angles (fig. 1.6). A higher effective area means that the telescope can see γ-showers further away, although, as can be seen in the trigger efficiency study, the increase may be high for larger zenith angles. Due to the low statistic at high energies, the histograms show quite big errors around $10^5 m^2$, in spite of logarithmic binning.

Like the trigger efficiency, the effective area for gammas shows little dependence

θ (°)	**A** $(m^2)(10^{-4})$	**B**	**C** **(GeV)**	**D**
0 - 10	5 ± 1	4.76 ± 0.08	41 ± 1	3.68 ± 0.04
10 - 20	2.6 ± 0.4	4.86 ± 0.05	43 ± 1	3.78 ± 0.03
20 - 30	0.4 ± 0.1	5.24 ± 0.06	44 ± 1	3.79 ± 0.03
30 - 40	0.005 ± 0.002	6.2 ± 0.1	45 ± 1	3.79 ± 0.06
40 - 50	(1.4±0.1)e-07	8.78 ± 0.02	35.8 ± 0.5	4.82 ± 0.03
50 - 60	(7±1)e-9	8.56 ± 0. 02	61 ± 1	4.42 ± 0.05

Table 3.5: *Fitting parameters for the effective area for* **gammas** *between 10 - 100 GeV.*

θ (°)	**A** $(m^2)(10^{-6})$	**B**	**C** **(GeV)**	**D**
0 - 10	74 ± 13	3.46 ± 0.04	135 ± 5	2.76 ± 0.04
10 - 20	770 ± 144	2.86 ± 0.04	208 ± 10	2.20 ± 0.04
20 - 30	667 ± 186	2.89 ± 0.07	198 ± 13	2.17 ± 0.05

Table 3.6: *Fitting parameters for the effective area for* **protons** *between 30 GeV - 30 TeV.*

on zenith angle for the different zenith angles, except at low energies. For energies less than 60 GeV, the difference in the effective area between 0º - 60º of zenith angle seems to increase as the energy of the primary γ-ray decreases. The increase of the effective area will yield to the rise of the energy threshold while increasing the zenith angle. This can be seen more easily in table 3.5 from the fit parameters to the expression 3.2 of the gamma's effective area for different zenith angle ranges. This table shows a decrease of the effective area for energies lower than $\sim 60\ GeV$. This decrease of the effective area is shown in the decrease of the normalization factor A and the increase of the function slope for low energies (B). In addition, a displacement towards high energies range of the "elbow" parameter (C) takes place as the zenith angle increases. This is due to the hump displacement with the energy (fig. 1.6). The low energy showers develop higher in the atmosphere. This is scaled to higher zenith angles by a factor $\frac{1}{\cos\theta}$. The effective area above this "elbow", doesn't show any clear behaviour in relation to the zenith angle. The slope B-D at high energies is nearly constant, within the fit errors, with a value around 0.2.

Figure 3.8 shows the effective area of the MAGIC Telescope for protons as a function of the energy primary proton (between 30 GeV - 30 TeV)[3]. For proton

[3]The effective area for protons is calculated over a solid angle enclosed by a cone of radius $\sim 5°$.

showers of 100 GeV and 1 TeV, the effective areas are $\sim 30\ m^2$ and $\sim 10^3 - 10^4\ m^2$ respectively. The effective area for protons is quite similar for all zenith angles. Contrary to those of the gammas, the differences in the low-energy proton effective area do not follow any trend. This can also be seen in the fit parameters in table 3.6. In theory, the EAS from more energetic protons could reach the ground, so one should have higher effective areas at high energies, but - due to the low statistics at those energies - this behaviour can't be clearly checked.

3.2.5 Thresholds and Rates

The expected rates are computed using the formula given by equation 3.3. The rate is defined as the number of gamma or proton events that trigger the MAGIC Telescope per hour for energies larger than E_0. To compute the rates a specific flux (dN/dE) (eq. 3.5) coming from a source must be chosen. In the case of gammas, the flux extrapolated from the six EGRET pulsars was chosen [50], while for protons, the proton spectrum of CR [154] was used.

Similar to the calculations of the effective area, the theoretical expressions cannot be applied and have to be substituted by numerical integrals.

The source flux does not depend on the zenith angle, therefore a decrease in the rate with the increase of the zenith angle is expected, detecting less events per hour for high zenith angles for the source and the background. The energy threshold is defined as the energy at which the highest rate is detected. The energy threshold error has been calculated as the width of the bin containing the maximum rate in the plot.

Simulated rates for pulsars

This section presents the differential and the expected integral rate for the six EGRET pulsars given by the formulae in equ. 3.5 and the parameters of table 3.1. Introducing the flux corresponding to each EGRET pulsar, the differential trigger rate (fig. 3.11), the energy thresholds and integral rates computed are listed in tables 3.7 and 3.8 respectively.

The energy threshold is inferred from figure 3.11 for each EGRET pulsar at different zenith angles, as listed in table 3.7.

Table 3.1 shows that the cut-off for the flux of the Geminga and Vela pulsars are at 5 and 8 GeV, respectively, so - at energies of that order - the flux will drop extremely steeply due to the super-exponential assumption in eq. 3.5. Geminga and Vela pulsars should have a maximum in the detected flux in the first or second bin (between 5 - 10 GeV) in the differential rate, therefore the threshold and the trigger rate are miscalculated. For the other pulsars, with a cut-off at higher energies, the threshold is expected to be between 20 - 30 GeV for all zenith angles. The simulated

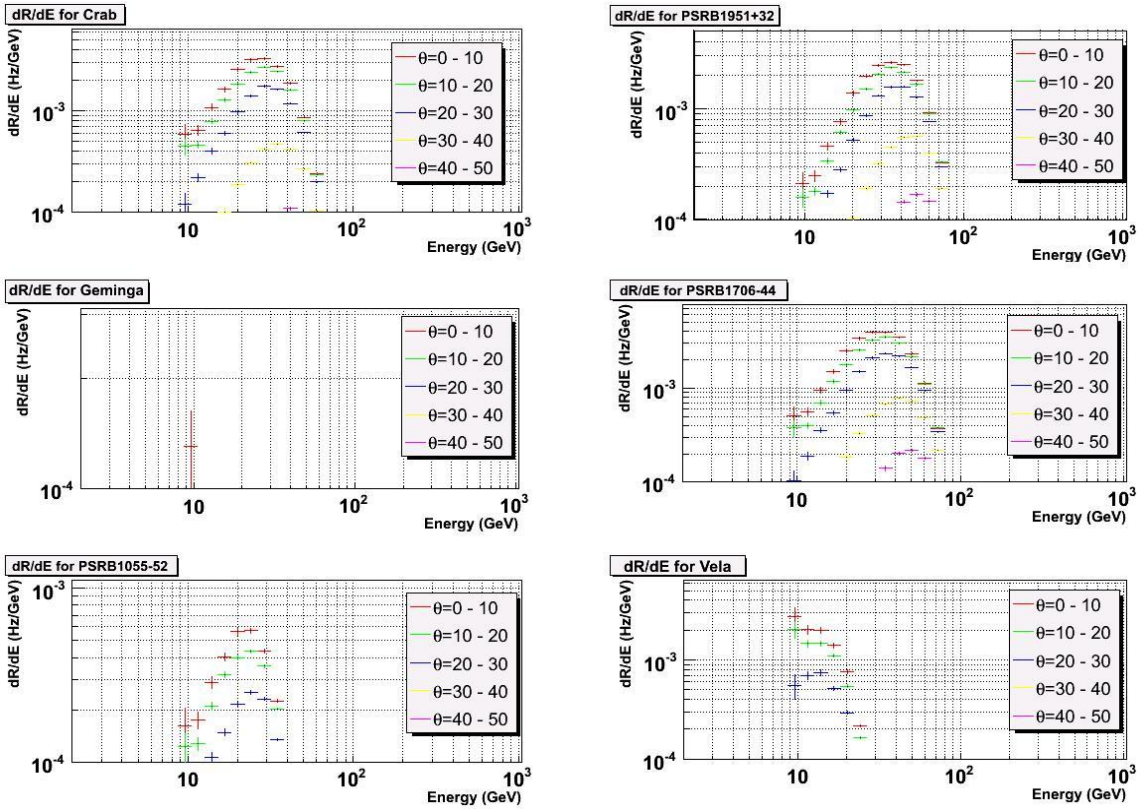

Figure 3.11: *Differential rates for the six* **EGRET pulsars** *at different zenith angles.*

	$\theta(^\circ)$					
Pulsar	**0-10**	**10-20**	**20-30**	**30-40**	**40-50**	**50-60**
Crab	24 ± 5	24 ± 5	29 ± 6	29 ± 6	36 ± 7	43 ± 9
PSR B1951+32	29 ± 6	29 ± 6	29 ± 6	43 ± 9	43 ± 9	53 ± 10
Geminga	11 ± 2	11 ± 2	11 ± 2	11 ± 2	13 ± 3	16 ± 3
PSR B1706-44	29 ± 6	29 ± 6	29 ± 6	43 ± 9	43 ± 9	53 ± 10
PSR B1055-52	20 ± 4	24 ± 5	24 ± 5	24 ± 5	24 ± 5	24 ± 5
Vela	11 ± 2	11 ± 2	11 ± 2	13 ± 3	13 ± 3	16 ± 3

Table 3.7: *Energy thresholds (GeV) for* **EGRET** *pulsars, defined as the peak of the detected differential flux.*

trigger rate (in events per hour) is shown in table 3.8 for the six EGRET pulsars at different zenith angles.

Except for the case of Geminga and Vela, table 3.8 clearly shows an increase in the trigger rate when the observation zenith angle decreases. This is due to the behaviour

	$\theta(^o)$		
Pulsar	**0-10**	**10-20**	**20-30**
Crab	9.20 ± 0.05	7.71 ± 0.03	4.95 ± 0.02
PSR B1951+32	9.76 ± 0.04	8.60 ± 0.02	6.06 ± 0.01
Geminga (10^{-4})	1.07 ± 0.05	0.79 ± 0.03	0.32 ± 0.01
PSR B1706-44	14.40 ± 0.06	12.54 ± 0.04	8.65 ± 0.02
PSR B1055-52	1.140 ± 0.01	0.906 ± 0.006	0.525 ± 0.004
Vela	1.99 ± 0.05	1.47 ± 0.03	0.70 ± 0.02
	$\theta(^o)$		
Pulsar	**30-40**	**40-50**	**50-60**
Crab	1.484 ± 0.007	0.336 ± 0.003	0.0274 ± 0.0008
PSR B1951+32	2.299 ± 0.006	0.687 ± 0.003	0.0805 ± 0.0008
Geminga (10^{-4})	0.025 ± 0.003	2.6e-4 ± 0.7e-4	4e-6 ± 1e-6
PSR B1706-44	3.13 ± 0.01	0.895 ± 0.004	0.0998 ± 0.0001
PSR B1055-52	0.122 ± 0.001	0.0190 ± 0.0004	0.0012 ± 0.00501
Vela	0.092 ± 0.004	0.0065 ± 0.0007	10e-4 ± 2e-4

Table 3.8: *Rates (Hz) (10^{-2}) for* **EGRET pulsars**.

of the effective area in relation to the zenith angle mainly at low energies.

Simulated rates for nebulae

For pulsars, the continuous component of the nebula hosting the pulsar (chapter 2) could be very important because of its contribution to the background component of the signal observed from the pulsar. In the accessible gamma energy range (60 GeV-9 TeV), the only nebula (PWN) detected at TeV energies for the 7 EGRET pulsar-PWN systems in the northern hemisphere is the Crab nebulae [11]. The gamma spectrum from the Crab nebula can be expressed between 300 MeV and 80 TeV by:

$$\frac{dN_\gamma}{dE} = 6 \times 10^{-9} \Big(\frac{E}{300\ GeV} \Big)^{-2.31 - 0.26\ log_{10}(\frac{E}{300\ GeV})} \quad m^{-2} \cdot s^{-1} \cdot GeV^{-1}$$

Expected rates for protons

The rates for protons can be computed using the second formulae in equation 3.5, which is the cosmic ray flux measured by [154]. In the case of protons, the rate expression has to be multiplied by the solid angle of generation corresponding to a cone radius of $\sim 5^o$ for the different zenith angles.

The energy threshold (in GeV) for protons is inferred from figure 3.12 at different zenith angles and is listed in table 3.10. Figure 3.13 displays the integral rates for

θ (°)	E_{th} **(GeV)**	**Rates (Hz)**
0 - 10	64 ± 13	0.6301 ± 0.0005
10 - 20	64 ± 13	0.6436 ± 0.0004
20 - 30	96 ± 19	0.6512 ± 0.0003
30 - 40	96 ± 19	0.6160 ± 0.0002
40 - 50	142± 28	0.6038 ± 0.0001
50 - 60	173± 34	0.4950 ± 0.0001

Table 3.9: *Predicted energy thresholds (GeV) and rates (Hz) for the* **Crab non-pulsed** *component.*

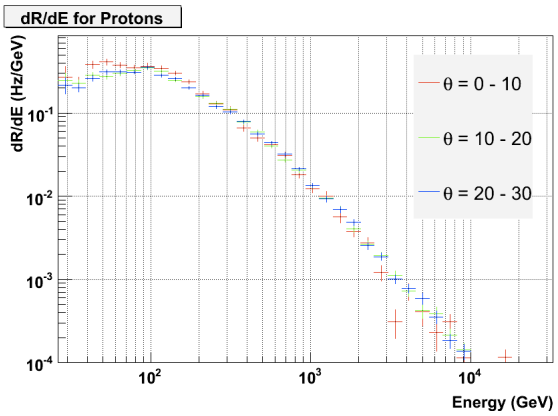

Figure 3.12: *Differential rate (Hz/GeV) for* **protons** *at different zenith angles.*

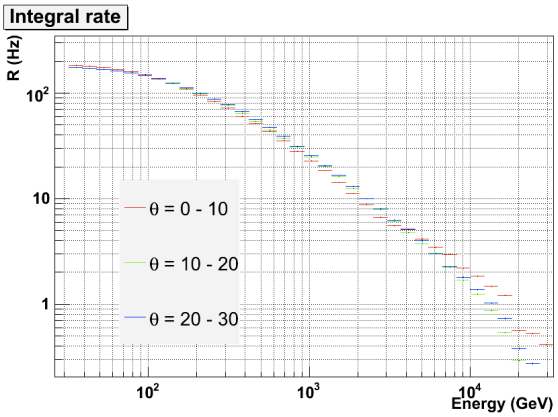

Figure 3.13: *Integral rate (Hz) for* **protons** *at different zenith angles.*

protons while the maximum values are listed in table 3.10.

θ (°)	E_{th} **(GeV)**	**Rates (Hz)**
0 - 10	53 ± 10	182.3 ± 0.5
10 - 20	96 ± 19	173.9 ± 0.3
20 - 30	96 ± 19	174.4 ± 0.3

Table 3.10: *Predicted energy thresholds (GeV) and Rates (Hz) for* **protons**.

Table 3.10 shows no dependency of the threshold and rate on the zenith angle. As explained in the previous section, this might be due to the statistics.

In the same table, it can be seen that the rate expected for protons is 10^3 times higher than the one expected for gammas, for example, coming from the Crab pulsar.

Although the trigger efficiency, and therefore the effective area for protons, is lower than that for gammas, the flux of cosmic rays (eq. 3.5) is 10^4 times larger than gammas (see chapter 1). Therefore, the background will dominate all our measurements. For this reason, it is necessary to define the "possibilities to observe" a pulsar signal submerged in the background trigger events.

Deficiency in the proton rate The simulated background rate is not realistic and is underestimated due to several factors:

- The simulations only include protons in the simulation of background, but 25% of the background rate is due to He, O, C, and light nucleus [154].
- The protons have been generated with limited ranges of the impact parameter: r = 0 - 400 m.

Therefore the background rate has to be corrected by a factor:

$$R_p = R_p(calc.) \cdot (1 + 0.25) \cdot (1 + \alpha_r) \tag{3.8}$$

where $R_p(calc.)$ is the above computed proton rate and α_r is the correction due to the simulated impact parameter range.

As previously concluded from figure 3.4, the trigger efficiency for impact parameter from zero to 400 meters decreases by a factor of 10, so one can't say that the trigger efficiency for an impact parameter higher than 400 meters is negligible. Supposing a decreasing tendency of the trigger efficiency with the impact parameter of $P_p(r) = \frac{A}{r^3+B}$, the fitting parameters to the trigger efficiency for protons (figure 3.4) for the different zenith angles are listed in table 3.11.

θ (^{o})	**A** (10^3) (m^{-3})	**B** (10^6) (m^3)	χ^2	X (%)
0 - 10	9.2 ± 0.4	4.6 ± 0.3	1.2	25
10 - 20	10.1 ± 0.3	6.0 ± 0.3	1.3	28
20 - 30	9.3 ± 0.2	7.1 ± 0.3	2.1	31

Table 3.11: *Fitted parameters for the trigger efficiency versus the impact parameter for* **protons** *between 30GeV-30TeV at different zenith angles.*

The trigger rate is computed as the integral of the fitted trigger efficiency function over the area element. The fraction of triggered proton lost when restricting the impact parameter of generation to 400 meters can be estimated by dividing the trigger rate for the bin 0-400 meters and 400-800 meters. This fraction of lost protons (X in %) is shown in the last column of table 3.11, which is expressed in percentage

of protons lost. The zenith angle with more statistics (table 3.4) is between 20-30 degrees and no other tendency has been observed of the trigger efficiency with zenith angle. Therefore one can estimate the percentage of protons lost by estimating the impact parameter of 400 meters up to 800 meters to be around 30%. In consequence, $\alpha_r \simeq 0.3$ has been used. Above 800 meters the function $\propto \frac{1}{r^3}$ does not fit the trigger efficiency. Therefore, even with this correction, the rate will be still underestimated.

Taking into account all the contributions to the proton rate not included in the MC simulations, the final proton rate is expected to be a factor ~ 1.6 larger than the predicted values in table 3.10. This correction to the proton trigger rate must be taken into account in the sensitivity studies in the next section.

3.2.6 Sensitivity study for pulsars

As was briefly commented in the introduction, the main objective of this chapter is to study the MAGIC telescope's capability to observe the seven γ-ray pulsars detected previously by EGRET. The detection of the EGRET pulsars by MAGIC is of great importance since it allows for first time the study of pulsar spectra in the range between 5-200 GeV, where the pulsar cut-off is expected even in the most conservative models. From Monte Carlo results (effective areas and rates), the chances of observing any pulsed and steady gamma source by the MAGIC Telescope can be estimated.

Initially, this section will predict the observation time required by MAGIC to detect the EGRET pulsars with a high significance under the above-listed assumption for the cut-off parameters. Secondly, the capability of MAGIC to detect pulsars with spectral parameters similar but not equal to those of EGRET will be estimated.

Signal significance

In a typical observation in γ-ray astronomy, a photon detector points in the direction of a suspected source for a certain time t_{on} and counts N_{on} photons, then turns for background measurement for a time t_{off} and counts N_{off} photons. This observation mode is also called "ON-OFF". In this observation mode, the number of background photons is included in the on-source counts and can be estimated using $N_B = \alpha N_{off}$, where $\alpha = t_{on}/t_{off}$. Therefore, the observed signal is defined in first order as the most probable number of photons contributed by the source ($N_s = N_{on} - N_B$).

For a positive observation of a source, the excess counts $N_{on} - N_B$ may not only have been caused by a statistical fluctuation in the background rate. A basic difficulty in evaluating the statistical reliability of an observational result is the fact that the background is generally not exactly known in a γ-ray astronomy experiment, but can only be inferred from the limited background counts [4]. Several experiments have used

[4] Additional uncertainties arise from atmospheric changes during the two measurements, different star light background in the ON and OFF areas and small drifts in the detector between the two

different procedures to estimate the statistical significance of their results. The most widely used is one proposed by Li & Ma [107]. Equation 17 of Li& Ma gives the estimation in the standard deviation of the observed signal N_s.

To evaluate the statistical reliability of an observational result, one estimates the probability that the observed signal was due only to the background fluctuation. Assuming in this analysis that there was no source and all the observed counts were due to the background, on-source counts N_{on} follow a Poisson distribution with variance $< N_B >$, where $< N_B >$ is the expectation of background counts in on-source time t_{on}. Therefore the variance of the signal N_s is:

$$\sigma^2(N_s) = \sigma^2(N_{on}) + \alpha^2\sigma^2(N_{off}) = (1+\alpha) < N_B >$$

If it is assumed that all the recorded photons are due to background, one can get a more accurate estimate of $< N_B >$ by using all the observed data as background (N_{on}, N_{off}):

$$< N_B >= \frac{N_{on} + N_{off}}{t_{on} + t_{off}} t_{on} = \frac{\alpha}{1+\alpha}(N_{on} - N_{off})$$

Then, the significance is:

$$N_\sigma = \frac{N_s}{\sigma(N_s)} = \frac{N_{on} - \alpha N_{off}}{\sqrt{\alpha(N_{on} + N_{off})}} \tag{3.9}$$

Supposing that the background fluctuations mainly come from background $\sigma(\mathrm{N}_s)$ = $sqrt(N_B)$, so that the On counts are perfectly known, the significance that will be used in this work will be:

$$N_\sigma = \frac{N_s}{\sqrt{N_B}} \tag{3.10}$$

where $N_s = R_\gamma \cdot t$ and $N_B = (R_{nebulae} + R_p) \cdot t$.

Observation time

From the previous Monte Carlo simulation results, the observation time needed to get a certain significance can be estimated using the expected rates extrapolated previously from the EGRET pulsars, protons and steady γ-sources. From equation 3.10:

$$N_\sigma = Q \frac{R_\gamma}{\sqrt{R_p + R_{neb}}} \sqrt{t_{obs}(s)} \tag{3.11}$$

measurements.

where R_{neb} is the rate due to the pulsar nebulae and Q is the improvement in the significance due to the γ/hadron separation. So equation 3.11 will give us the observation time needed to observe a source with rate R_γ and an analysis quality factor Q, with a background rate $(R_p + R_{neb})$ applying the corresponding correction to R_p and demanding a certain detection level (5σ) of statistical significance.

Due to the dependence on the rates, the observation time changes with the zenith angle of the observation. Therefore, it is necessary to know the celestial trajectory of the different pulsars in order to know the range of observation time needed for a certain gamma-pulsar - or even if it is observable at all from the MAGIC site. The equatorial coordinates of the EGRET pulsars are listed in table 3.12. Using the MAGIC Telescope location on La Palma ($\phi = 29^o$), one can estimate the minimum declination of a source to be visible in the La Palma sky: $\delta_* > \phi - 90^o = -61^o$. The Monte Carlo simulations only include zenith angles between 0 and 60 degrees. Therefore, reliable data are available only for these zenith angles. In addition, the energy thresholds at higher zenith angles grow very quickly, making it unrealistic to observe pulsars at higher zenith angles. The only sources that fulfil the condition $\delta_* > \phi - 60^o = -31^o$ are the Crab, PSR B1951+32 and Geminga pulsars. Although PSR B1706-44, PSR B1055-52 and Vela pulsars might be marginally visible by the MAGIC Telescope, there are no complete simulations for the behaviour of the telescope for zenith angles higher than 60^o. At these zenith angles, the expected very high thresholds make the search for pulsed emission useless.

Pulsar	α_* (^{hms})	δ_* ($^{o\prime\prime\prime}$)	θ_{min} (^{o})	t_{min} (h)	
				3σ	5σ
Crab	5 34 32	22 0 52	6.986	88	245
PSR B1951+32	19 52 58	32 52 41	3.878	78	217
Geminga	6 33 54	17 46 11	11.230	6×10^7	2×10^8
PSR B1706-44	17 9 43	-44 29 7	73.485	—	—
PSR B1055-52	10 57 59	-52 26 56	81.449	—	—
Vela	8 35 21	-45 10 36	74.177	—	—

Table 3.12: *Pulsar equatorial coordinates and minimum zenith angle reached in its trajectory by the six EGRET pulsars for the MAGIC location. Ones without a value in their minimum zenith angle are not visible with the MAGIC Telescope. The minimum hours needed to detect 3σ and 5σ signal has been computed only for the northern hemisphere pulsars.*

The visible pulsars do have zenith angles along their trajectory below 60°. In table 3.12, the column θ_{min} the minimum zenith angle along their trajectory of the three visible EGRET pulsars. The pulsars for which the column t_{min} is empty are the ones visible at high zenith angles. The zenith angle of the visible pulsars varies between θ_{min} and 90^o.

Column t_{min} of table 3.12 lists the time of observation and the γ- and proton rates at the zenith angle closer to the minimum zenith angle of the trajectory.

Detectability

From the predicted Geminga and Vela rates, it can be inferred that the spectral cut-off is determinant in the observation time. Figure 3.14 shows the estimated pulsar fluxes from EGRET data.

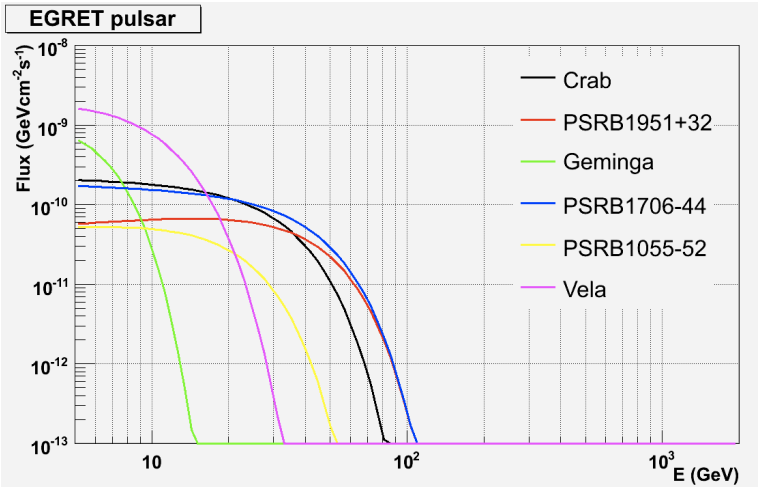

Figure 3.14: *Fluxes for EGRET pulsars fitted to equation 3.5 (table 3.1 for flux parameters).*

Because these fitted flux parameters depend on the pulsar physical characteristics (see chapter 2), it is also important to know the sensitivity of MAGIC not only in case of the spectra of the EGRET pulsars, but to those pulsars with a wider range of parameters. For this reason it is important to estimate the observation time needed by the telescope to observe pulsars with different values of K and cut-off (E_0).

To compute the observation time range for different fluxes and cut-offs, a semi-analytical formula for the effective areas was used together with the parameterized expression for pulsar flux. Figure 3.15 shows these observation time ranges for different pulsars under the assumption of Γ=2.08 (Crab), 1.74 (PSR B1951+32) and 1.42 (Geminga); and b = 2 (super-exponential spectrum at GeV energies has been assumed).

Figure 3.15 shows that there is a wide range of the flux spectrum parameters for which pulsars can be observable. This means that pulsar studies with MAGIC are likely to give good results.

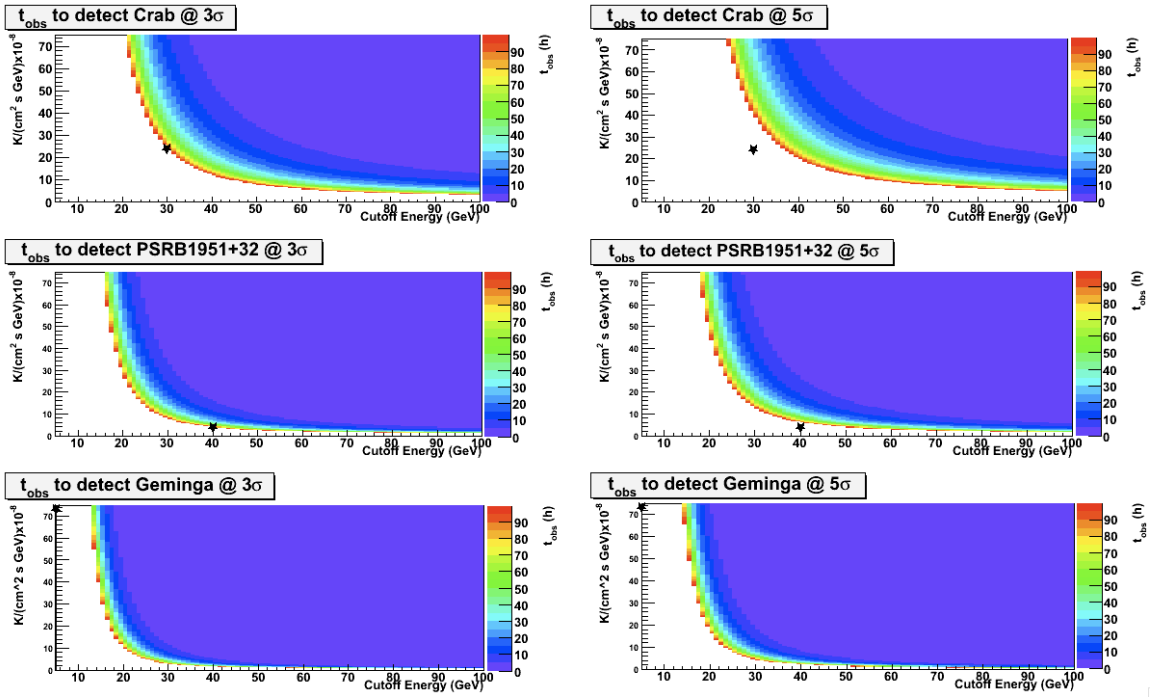

Figure 3.15: *Observation time ranges for the three "visible" EGRET pulsars and different signal detection levels (3σ left, 5σ right) for a quality factor of Q=1. K is the flux at 1 GeV and E_0 is the spectral cut-off. The star corresponds to the pulsar parameters in each diagram.*

3.3 Conclusions

From the Monte Carlo simulations of gamma and proton in this chapter, the telescope capability for detecting γ-ray sources emitting in the energy range between 10 GeV and 30 TeV have been characterized. The telescope sensitivity depends on the effective areas for gamma and proton showers.

This study shows a telescope effective area of ~ 10 m^2 for γ-showers with an energy of 15 GeV, increasing quickly up to $\sim 5\times10^4$ m^2 for E = 100 GeV. For energies above 100 GeV, the effective area increases slowly up to $\sim 10^5$ m^2 at E = 30 TeV. This telescope effective area yields to energy thresholds of 45 - 170 GeV between zenith angles of 0°-60° for the Crab nebula spectrum, which is the standard "candle" for ground-based Cherenkov telescopes. Therefore, our predictions establish that MAGIC will detect a maximum rate from Crab nebula of ~ 0.6 Hz at low observation zenith angles. MAGIC has observed the Crab Nebula for $E_{th}>$ 75 GeV at 0.2 Hz [11]. Including the analysis cuts in this MC simulation, the rate for the Crab Nebula of ~ 0.4 Hz was obtained. These real data results are better than the MC simulations presented in the chapter because a better image-cleaning and analysis cuts (Q >1)

has been used in the analysis of the real data.

It has been proven that up to 25% of the real protons collected by the telescope can be lost through the impact parameter range of the MC simulations. Therefore, it has been suggested in this chapter that the impact parameter range should be increased up to 800 meters. Taking the loss of protons into account, the simulation results for the proton rate detected by the telescope is $\sim$ 290 Hz between 0° and 30° of zenith angle. To compare with the rate of Off data, we have to include the quality cuts of our analysis (chapter 7) and the correction for the missing He and protons between 400-800 meters of impact parameter. With these corrections ($1.7R_p$) a simulated rate for Off data of $\sim$150 Hz has been obtained, which fits with the Off rates measured by the MAGIC telescope.

All these results have been applied to the specific case of pulsar sources to characterize the telescope's sensitivity at low energies with particular reference to the Northern hemisphere sources among the 7 γ-ray pulsars detected by EGRET. With the simulation results, a limit of $\sim$ 80 - 90 hours has been established for the detection with a 3σ confidence level of the Crab and PSR B1951+32 pulsed emission, for an analysis quality factor Q = 1. MAGIC has observed the Crab and PSR B1951+32 pulsars during 16 and 31 hours respectively. No pulsed emission has been detected, obtaining a significance of 1.3σ for Crab (E=60-180 GeV) [11] and 1.1σ for PSR B1951+32 at low energies [10]

At present, there are several theoretical models, which predict a large variety of fluxes coming from pulsar magnetospheres. These fluxes can be parameterized at GeV energies as a function of several parameters: the spectrum slope, the energy cut-off of the spectrum and the behaviour of the spectrum near this energy cut off (exponential or super-exponential). Using the method and parameterization of the effective areas found in this chapter, it is possible to find out and select the best MAGIC candidates among the different possible values of the flux parameters (or theoretical interpretations). The results show that the range of the flux parameters accessible with MAGIC is quite wide and quite close to the predictions from EGRET data.

Chapter 4

Effect of the Earth's magnetic field on the MAGIC Telescope's sensitivity

In this chapter the influence of the Earth's magnetic field on the performance of imaging atmospheric Cherenkov telescopes and specifically on the MAGIC Telescope's sensitivity will be evaluated. The Earth's magnetic field influences the development of extensive air showers (EAS) through their charged secondary particles (mainly by deflecting electrons and positrons), which are the responsible of the emitted Cherenkov photons. This Lorentz force spreads the Cherenkov light, resulting in a decrease in the number of photons collected by the reflector and a larger angular dispersion within the image.

As a result one expects a higher reduction of the trigger efficiency for gammas than for the background and therefore a decrease in the sensitivity of Cherenkov telescopes for γ-detection.

4.1 Earth's magnetic field

The Earth is a big spherical magnet, surrounded by its magnetic field, which carves out a hollow in the solar wind, creating a protective cavity called the magnetosphere (fig. 4.2) [161] [162]. The Earth's magnetic field is the sum of several contributions including the main (core) field, the crust (anomaly) field and the external source field (magnetosphere). These fields are superimposed on and interact with each other, but more than 90% of the field measured is generated internally by the Earth's core. This portion of the geomagnetic field is often referred to as the Main Field and dominates the field from the Earth's surface up to about four Earth radii. Beyond that, the Earth's magnetic field is affected proportionally by the solar wind interaction with the Earth's magnetosphere. The solar wind is deflected around the Earth, pulling the

terrestrial magnetic field into a long magneto-tail on the night side. Charged particles in the solar wind are deflected at the bow shock and flow along the magnetopause into the magnetic tail. These particles can be injected back toward the Earth and Sun within the plasma sheet (fig. 4.2).

The Main Field varies slowly in time and can be described by Mathematical Models such as the International Geomagnetic Reference Field (IGRF) and World Magnetic Model (WMM). Magnetic dipoles are used as a first approximation to the electric currents in the Earth's core that are assumed to reproduce the main magnetic field. The model is restricted to eccentric radial dipoles (North-South poles) at equal distances from the centre of the Earth, but with an offset regarding the geographic poles of around 11 degrees. Within this model is also included the so-called *South Atlantic Anomaly* (SAA)(fig. 4.1) [163] [164]. This anomaly is located over the South Atlantic Ocean, on the coast of Brazil. Here the shielding effect of the magnetosphere is not quite spherical but shows a dip, which can be explained by the eccentric displacement of the centre of the magnetic field from the geographical centre of the Earth (by ∼451 km) as well as by the displacement between the Earth's magnetic and geographic poles. Above this anomaly, the shielding of the Earth's magnetic field decreases, and, in turn, increasing the local flux of cosmic particles.

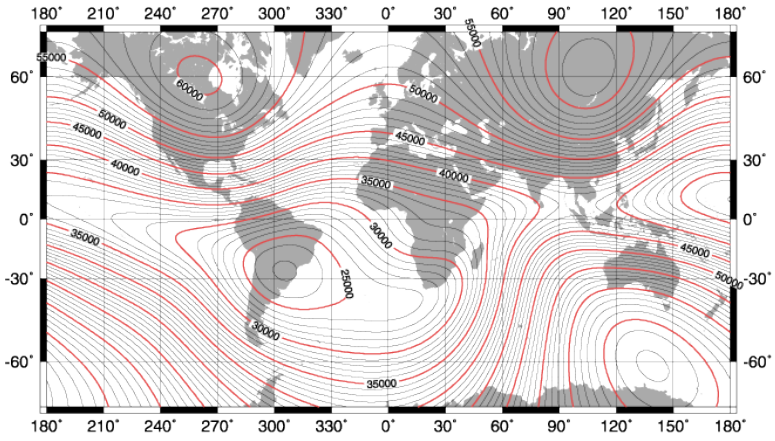

Figure 4.1: *World magnetic main field (Epoch 2000). Contour lines represent the total intensity of the main field (between 25 μT and 65 μT) at 1μT interval [161].*

At any point, the Earth's magnetic field is characterized by a direction and intensity which can be measured by the magnetic declination (D) (angle between the geographical north and magnetic north), the horizontal intensity (H) and the vertical intensity (Z) (fig. 4.4). From these three elements, all other parameters of the magnetic field can be estimated.

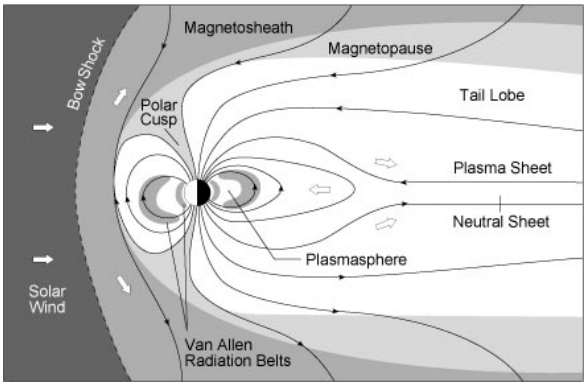

Figure 4.2: *Earth's magnetosphere. The Earth atmosphere and ionosphere (at 1.6 Earth radii), and the two Van Allen radiation belts (inner at 0.8 and outer at 3 Earth radii) lie within this magnetic cocoon. The magnetopause marks the outer boundary of the magnetosphere [161].*

4.1.1 Effect of Earth's magnetic field on cosmic radiation

Effect on charged cosmic rays: Geomagnetic cut-off

The Geomagnetic Field acts like the Earth's shield, bending the charged cosmic rays, inhibiting low-energy charged particles from cosmic rays from penetrating the atmosphere and deflecting much of the radiation away from the Earth's surface. The particle deflection is inversely proportional to the so-called particle *magnetic rigidity* ($BR_c = \frac{pc}{Ze}$, where R_c is the cyclotron radius) and to the particle's kinetic energy. It is the magnitude for characterizing the ability of a cosmic ray to penetrate the Earth's magnetic field. The minimum allowed rigidity is known as the rigidity cut-off (R_c). The rigidity cut-off can be estimated as an off-set dipole by the Stormer equation [41]:

$$R_c = \frac{59.4\ \cos^4\lambda}{r^2[1+(1-\cos^3\lambda\ \sin\theta\ \sin\phi)^{1/2}]^2}\ GV \tag{4.1}$$

which depends on the magnetic latitude (λ), the distance from dipole centre (in Earth's radius units) and the particle direction (θ,ϕ). This result is underestimated due to the Earth's shadow effect and is usually referred to as *penumbra*. The Earth's shadow effect determines an east-west asymmetry on the rigidity cut-off: trajectories of protons with enough momentum will arrive from any direction from the west, while the eastern trajectories will be allowed only if the trajectory extends up from the surface with a sufficiently vertical angle and radius to avoid projection back to the opaque Earth [137]. This expression is valid for magnetic latitudes above 20°; below this, a more appropriate expression should include the non-dipole field effects through more realistic models of the geomagnetic field. The inclusion of the penumbra effect gives an upper rigidity cut-off around 5-30% higher than R_c given by the Stormer

equation given above.

As the protons and helium nuclei are the dominant components in cosmic rays, the geomagnetic cut-off over those particles determines the spectrum of comic rays reaching the atmosphere. In both protons and heliums, the geomagnetic cut-off decreases when the magnetic latitude increases (fig. 4.1.1), whereas the opposite happens for electrons.

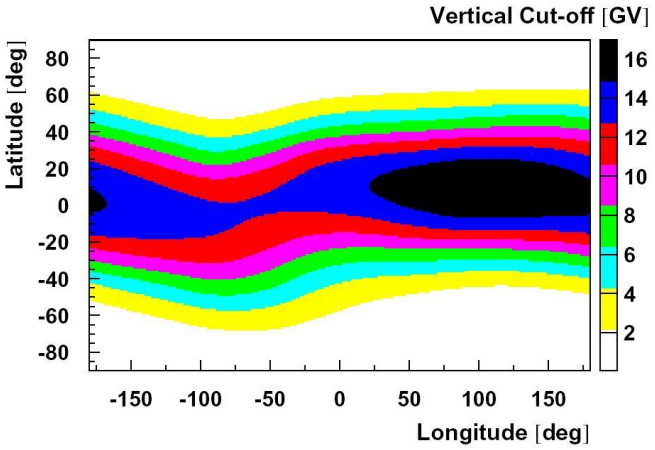

Figure 4.3: *Vertical geomagnetic cut-off for protons as a function of the terrestrial coordinates [152].*

This means that for magnetic latitudes $0^o < \theta_{mag} < 70^o$, the primary cosmic rays spectra have a cut-off at low energies between 0.3 - 7 GeV for proton/electrons [8] and between 1 - 10 GeV for helium nuclei [9]. This energy cut-off is an average over the zenith direction for certain magnetic latitude. This average deviates slightly on the longitude direction due to the East-West asymmetry.

Only the cosmic particles above the geomagnetic cut-off reach the Earth's atmosphere producing the cosmic ray EAS.

Effect on EAS development

The Earth's surrounding magnetic field exerts a Lorentz force on the secondary charged particles forming an EAS, mainly on the electron/positron pairs (electromagnetic sub-cascades) that give rise to most of the Cherenkov photons in gamma-initiated showers (see section 1). This Lorentz force depends on the zenithal (θ) and azimuthal (ϕ) angles of the gamma's shower direction (EAS momentum) and the local magnetic field intensity.

Using the CORSIKA coordinate frame $(\vec{i}, \vec{j}, \vec{k})$ (fig. 4.4), where $B_y \simeq 0$, the values H and Z of the IGRF magnetic field parameters correspond with the two CORSIKA program components B_x and B_z.

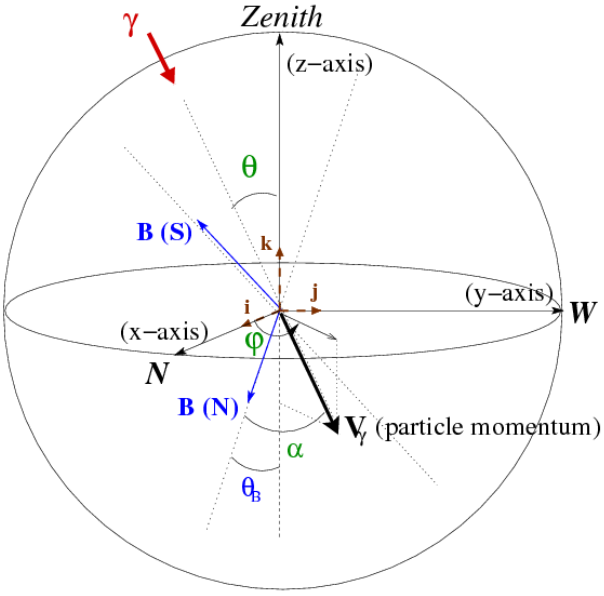

Figure 4.4: *Coordinates system of EAS momentum (V_γ) and Earth's magnetic field (B) together with the CORSIKA [100] and IGRF [161] reference frame.*

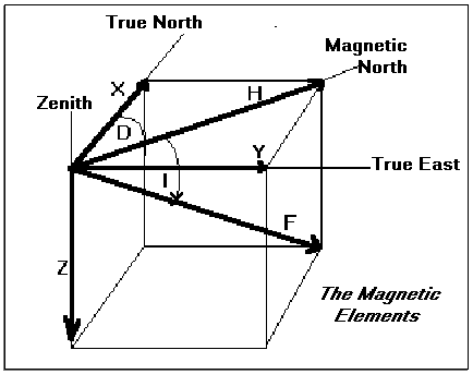

Figure 4.5: *IGRF reference frame representing the seven parameters to measure the Earth's magnetism in any place: declination (D), inclination (I), horizontal intensity (H), the north (X) and east (Y) components of the horizontal intensity, vertical intensity (Z), and total intensity (F) [161].*

$$\vec{F} =\propto q \cdot \vec{B_\perp} \propto \vec{B_\perp} = B_z \sin\theta \sin\phi\ \vec{i} + (B_x \cos\theta - B_z \sin\theta \cos\phi)\ \vec{j} + B_x \sin\theta \sin\phi\ \vec{k} \tag{4.2}$$

Fixing the γ-observatory location, the last part of equation 4.2 shows how the charged particles will be affected depending on the observing direction.

Equation 4.2 shows the behaviour of the relative Lorentz force (or perpendicular component of the magnetic field $B_\perp$), exerted on the electron/positron particles of the shower as a function of the zenith and azimuth angles of the primary particle direction [1]. The effect of the Earth's magnetic field on the EAS showers is the result of this Lorentz force which is proportional to the module of $B_\perp$ for all the telescope pointing directions above the horizon.

The results at the MAGIC telescope location (La Palma: $B_x = 30.171\ \mu T$, $B_z = 24.227\ \mu T$, $Lat. = 28.8$) are shown in figures 4.6 and 4.7 where the colour scale axis

[1]The azimuth angle at CORSIKA reference frame does not correspond to the definition of Astronomical azimuth [80], defined as the angular distance measured towards the West, from North, along the astronomical horizon. The CORSIKA definition of the azimuth angle will be the only one used in this work. According to this definition the telescope points to the opposite azimuth direction to the particle momentum direction. *N,W,S,E* are the telescope directions, which correspond to ϕ = 180°,270°,0°, 90° on the CORSIKA reference frame.

on the right represents the ratio of the $B_\perp$ for a given direction to its maximum value for the MAGIC site.

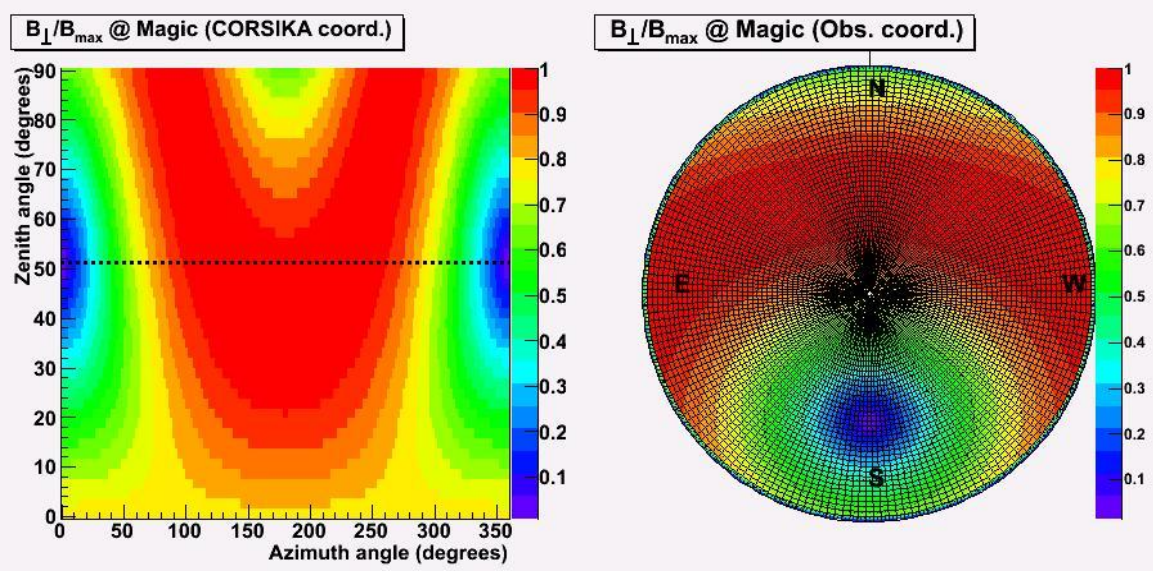

Figure 4.6: $B_\perp$ *at La Palma for* $\theta < 90^o$ *(zenith angles above the horizon) in cartesian (left) and polar (right) coordinates plots in the CORSIKA reference frame. Azimuth of 0º, 90º, 180º and 270º correspond to direction of South, East, North and West, respectively in horizontal coordinates.*

Figure 4.6 represents the module of $B_\perp$ in alt-azimuth coordinates (CORSIKA) in cartesian (left) and polar (right) coordinates. For zenith angles lower than $\sim 39^o$ the maximum effect takes place where the angle between the telescope pointing direction and the magnetic field is higher. This happens towards the geographic North (azimuth=180º) for zenith angles θ <51°, while for θ >51° the two maxima appear at both sides of the North, at the East and West directions. The minimum occurs when the telescope points to the South direction (azimuth=0º) reaching an absolute minimum at $\theta = 51^o$ to the South, since this is the zenith angle to which the magnetic field points for the La Palma location. The pointing angle of B is given by ($\Theta = \arctan B_x/B_z$)(table 4.1). When the telescope points close to the zenith ($\theta \sim 0^o$) there is no difference between the azimuth directions.

Figure 4.7 represents again the relative value of $B_\perp$ ($B_\perp/B_{max}$) but in equatorial coordinates (h,δ). Although the magnetic field changes very little along the source trajectory ($\sim$ 10%), its stronger dependency is on the declination of the source. In this way, the maximum effect takes place for sources with declination angle between [-20°<δ<20°] degrees while the minimum occurs for high declination sources ($\sim$ 80 degrees).

All these studies concern only to one specific site: that of the MAGIC teles-

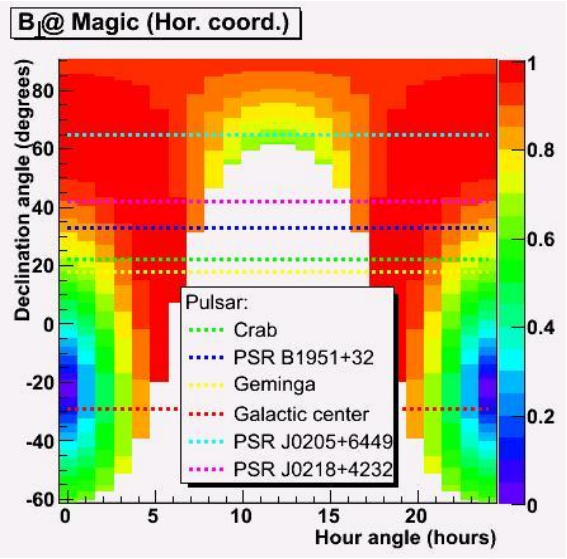

Figure 4.7: $B_\perp$ *in hour angle coordinates for* $\theta < 90^o$. *The source culmination takes place at* $h = 0^o$

cope. The values of the horizontal (B_x) and the vertical (B_z) magnetic field intensity vary with the Earth location (fig. 4.5), therefore the perpendicular component of the Lorentz force over the EAS-charged particles should change also according to the equation 4.2. For this purpose, the value of the perpendicular component of the Earth's magnetic field has been calculated for all pointing directions at different gamma observatories in different places on the Earth (fig. 4.8). Table 4.1 shows the four most important current gamma observatories and a proposed one, the CTA (Cherenkov Telescope Array) in a possible location in the Atacama desert [3], their coordinates and the values of their horizontal and vertical magnetic field components as well as the polar angle are shown in the table. These numbers have been computed using the *Geomag program* [161].

	ϕ (° ‘ “)	L (° ‘ “)	h (km)	B_x (μT)	B_z (μT)	Θ (°)
MAGIC [173]	28 45 34 N	17 52 34 W	2.2	30.161	24.245	51.2
HESS [172]	23 16 18 S	16 30 00 E	1.8	12.436	-25.872	25.7
VERITAS [167]	31 40 51.4 N	110 52 39 W	2.32	25.239	40.962	31.6
CANGAROO [170]	31 5 56 S	136 47 10 E	0.16	25.597	-51.612	26.4
CTA [174]	23 18 00 S	68 09 00 W	5.0	22.220	-7.945	70.3

Table 4.1: *Location, magnetic field components and angle for five different gamma observatories.*

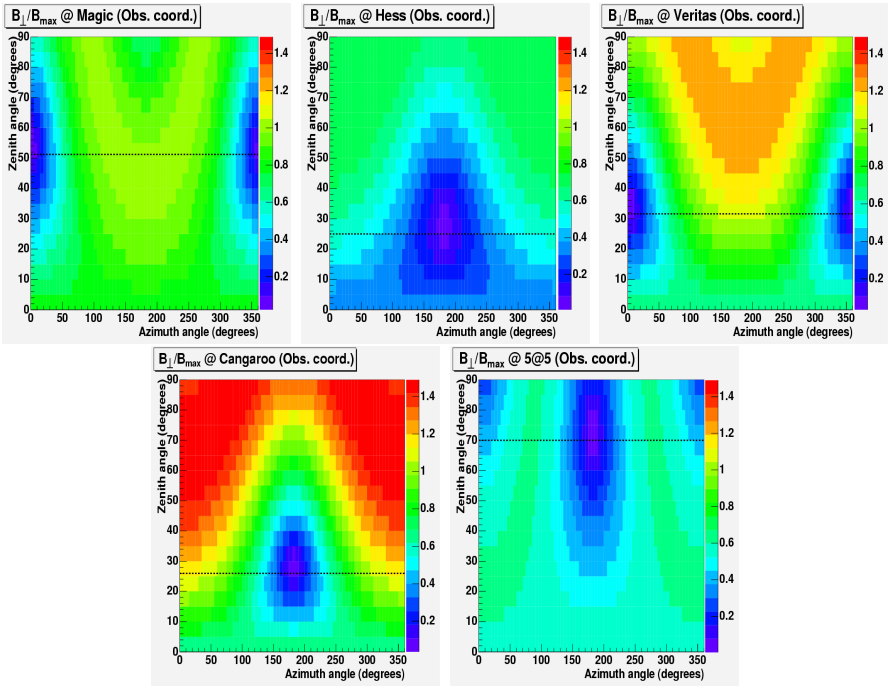

Figure 4.8: $B_\perp$ *(CORSIKA reference frame) for different observatory locations: MAGIC, HESS, VERITAS, CANGAROO and CTA for* $\theta < 90^o$*, normalized to the maximal MAGIC value. The dotted line corresponds to the zenith angle at which the effect is minimum.*

The difference in the magnetic field due to the different altitudes at any observatory location is very small. For example, the difference between MAGIC (2.5 km) and the proposed CTA (5 km) altitudes is around 0.1%.

Comparing figure 4.8 and table 4.1, it can be concluded that the minimum effect of the Earth's magnetic field occurs at the culmination of the sources in each observatory while the maximum effect, which depends on the B_z strength, takes place in those directions where the particle momentum is perpendicular to the magnetic field. Figure 4.8 shows that, in the case of VERITAS, for low zenith angles the magnetic field effect is similar to the one expected for MAGIC but for zenith angles higher than 40-50 degrees the effect increases around 30% with regard to the MAGIC site. It can be seen that the maximum value of the magnetic field takes place at Cangaroo observatory while the minimum is probably at the CTA site. The minimum effect at the Atacama dessert (Argentina) is due to the South Atlantic Anomaly (SAA), a region with the lowest local magnetic field (fig. 4.2). As a consequence of the lower value of the local magnetic field, gamma observatories close to this anomaly are expected to collect more photons into their reflectors from γ-ray showers but also an increased background due to charged particles (cosmic ray background).

For this reason, a study about the effect of the Earth's magnetic field on the telescope sensitivity is needed. Broadening our studies on the MAGIC telescope sensitivity (see chapter 3), the following simulations and the results presented in this chapter will be concentrated on the MAGIC telescope specifications [44].

4.2 The MC simulation

As a first approximation all the simulations have been performed at the CORSIKA level (version 6.19), instead of making the studies with the full MAGIC simulation. The results can give us an idea of how the magnetic field affects the effective area in the North and South direction for a wide range of different MC simulations that depend on the change in time of the telescope performance (PSF, hardware, flat fielding,etc).

The MC simulation is based on the recording of the Cherenkov photons produced by CORSIKA for each simulated event over an area of $2 \times 2\ km^2$. With this data, two different kind of plots were made. First of all, the lateral distributions averaged over several events were computed in order to understand the effect of the magnetic field on the EAS. The behaviour of the telescope was reproduced using a simple working model. To accomplish this goal the $2 \times 2\ km^2$ area was divided in squares with an area equivalent to the MAGIC reflector size ($\sim 236\ m^2$ [20]) (fig. 4.9).

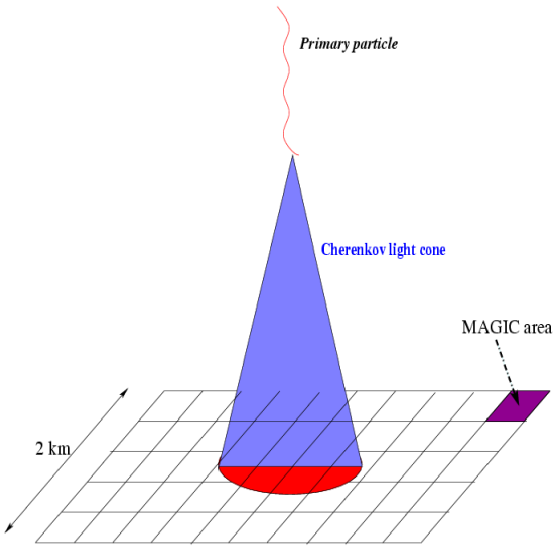

Figure 4.9: *Scheme of CORSIKA simulation area.*

At first, the trigger efficiency was computed for each distance bin and then multiplied by the bin's area. The trigger efficiency was computed as the number of squares

with a number of photons higher than the trigger condition averaged over the total number of simulated events and divided by the total number of squares. The effective area was achieved by multiplying the trigger efficiency by the area considered at ground level. The MAGIC effective areas were computed using a simplified version of the trigger features implemented in the MAGIC standard software [46].

A minimum number of Cherenkov photons, fulfilling the trigger condition to L1T without topological constraint, was required.. The standard trigger condition was a threshold of $\sim$ 15 phe/channel [44] and a multiplicity of 4 fired pixels (not including the Next Neighbour (NN) topological condition). Considering a peak QE$\sim$30% [125] and a light collection efficiency of 77% [44], $\sim$ 200 photons was set as the minimum number of Cherenkov photons to trigger the telescope at the L1T level. These photons had to fulfil an angular restriction, as only the inner part of the camera ($>$ 0.8º-1º) was used for deriving triggers. For that reason, Cherenkov photons within a trigger radius of 1º in the camera FoV had to be considered.

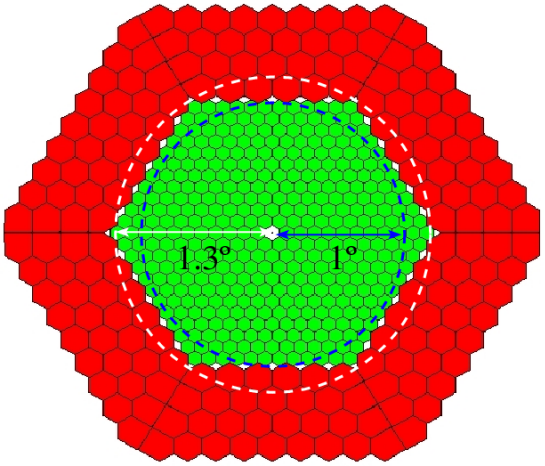

Figure 4.10: *MAGIC camera: inner part (1.3º (white)) or trigger region (<1º (blue))(green) and outer part (red).*

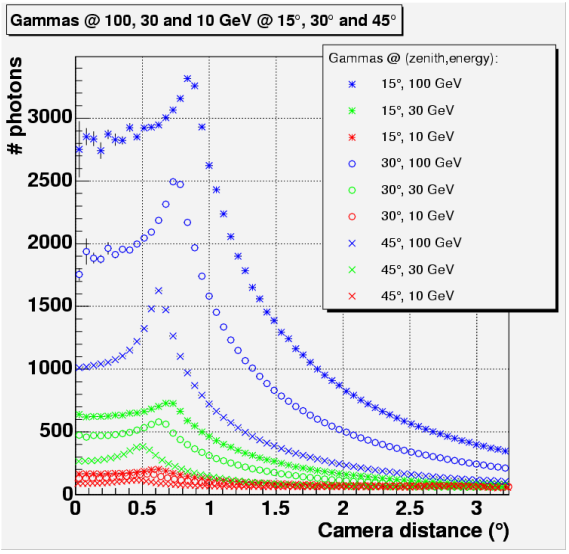

Figure 4.11: *Distribution of Cherenkov photons in the camera plane for 10 (lowest), 30 and 100 (higher) GeV and zenith angles of 15, 30 and 45 degrees.*

The distribution of photons in the camera was also computed. Figure 4.11 shows the angular distribution of Cherenkov photons in the camera plane. For increasing energies (eq. 1.3), the "hump" of the distribution moves towards the outer part of the camera (fig 1.5). Therefore, the chosen value for the trigger radius ($\leq$1º) has to be wide enough to always include the maximum of the distribution of the Cherenkov photons for the highest energies considered in our simulations (100 GeV) (fig. 4.12). This trigger region also takes into account the displacement of the "hump" of the

distribution towards the outer part of the camera when decreasing the observation zenith angle for a fixed energy of the primary γ-ray (fig. 1.6).

4.3 Magnetic field effect on Gamma showers

4.3.1 Lateral distribution for gamma showers

This section presents the results of the effect of the magnetic field on the distribution of Cherenkov light for gammas at low energies at MAGIC's site (La Palma). The $B_\perp$ plot for MAGIC site (fig. 4.6) showed that the influence of the magnetic field is minimal at the culmination of the source (South) and maximal at the North for the zenith angle corresponding to the magnetic field colatitude (Θ_B on table 4.1). For the MAGIC telescope site, the magnetic colatitude is $\sim 50^o$ so that the MC simulations will be focused on the difference between both extreme cases for zenith angles up to 45^o.

To study the magnetic field's effect on the lateral distributions of MC gamma events for different energies, zenith and azimuth angles ϕ=0º and 180º (South and North directions) were simulated. The statistics of the simulated samples are listed in table 4.2.

	Zenith angle (°)		
Energy (GeV)	15	30	45
10	10^4	10^4	10^4
30	10^4	10^4	10^4
100	10^3	10^3	10^3

Table 4.2: *Number of gamma showers generated at both azimuth angles (ϕ=180° North and ϕ=0° South) as a function of energy (GeV) and zenith angle (°).*

For each set of events, the average lateral (fig. 4.12) and ground (fig. 4.13) distributions of Cherenkov light density were computed.

Figure 4.12 shows the lateral photon distribution for gammas with energies of 10, 30 and 100 GeV (red, green and blue lines respectively) for zenith angles of 15º,30º and 45º for South (ϕ=0°) and North (ϕ=180°) directions (continuous and dotted lines respectively). The plots on the left represent the lateral distribution up to 1 km of impact parameter. The right side plots show a zoom up to 500 meters. The density of Cherenkov light decreases with the energy and the observation altitude angle for both latitude directions, as expected, but in all the cases the Cherenkov photon density is lower for gammas coming from the North than those coming from the Southerly direction. The difference between both directions depends on the energy and the zenith angle of the incoming particle, increasing with the zenith angle and

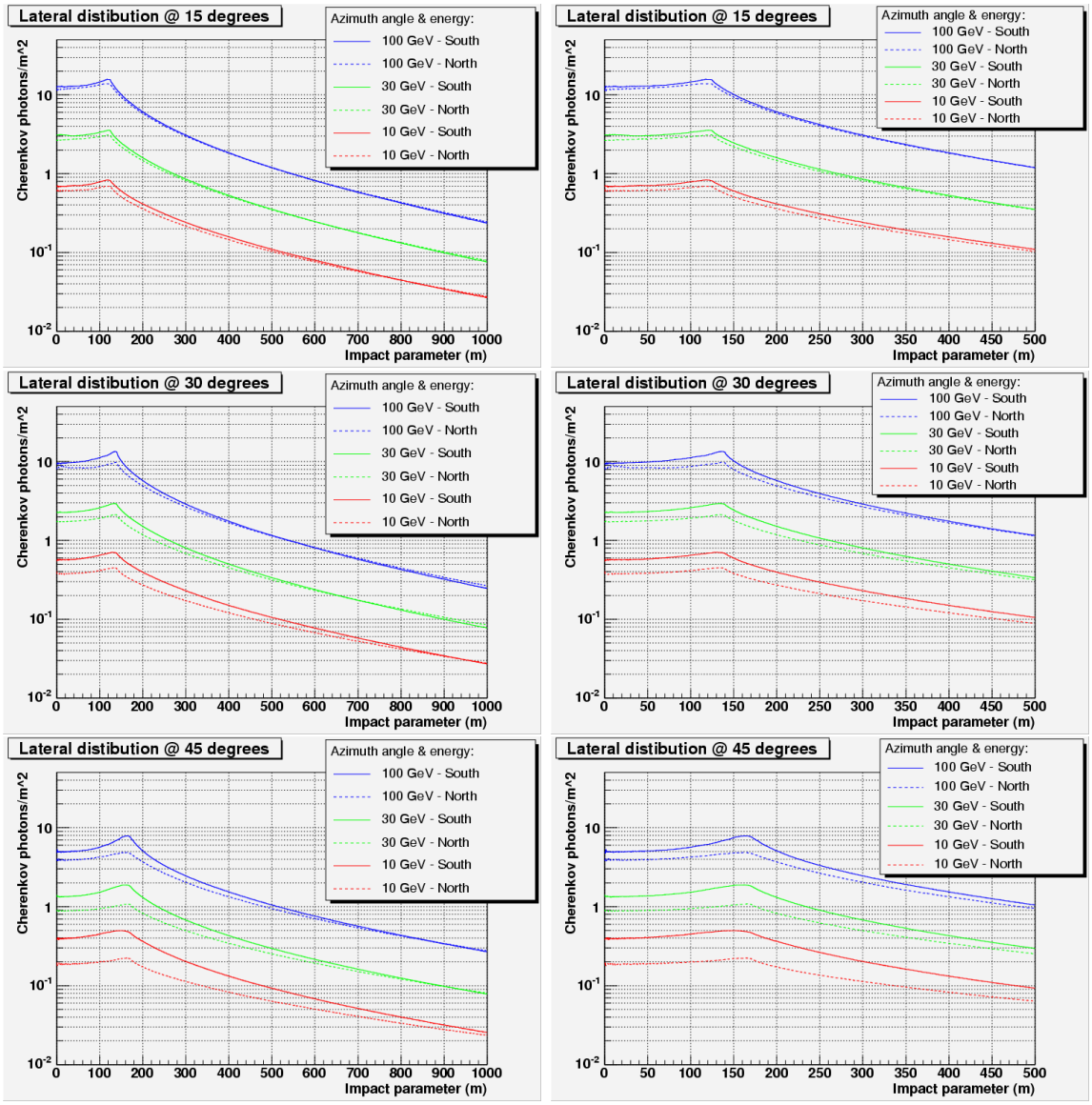

Figure 4.12: *Lateral distribution of Cherenkov photons for* **gamma** *showers of 10, 30 and 100 GeV and zenith angles of 15, 30 and 45 degrees. Plots on the right are a zoom of those on the left ones for impact parameters up to 500 meters.*

decreasing with the energy. For gamma showers at 100 GeV the difference is up to 20% at 45°, while at 15° there is almost no difference. For the lowest energy showers, those of 10 GeV, the difference increases from 10% at 15° up to 50% for zenith angles of 45°. These results are what is expected from equation 4.2, where the value of the perpendicular component depends on particle direction (or telescope

pointing direction). This dependence can be seen in more detail in figure 4.6. From these results one can expect that the maximum difference takes place for low energies around zenith angle of 51°.

As previously commented, events coming from the South have a higher density of Cherenkov light compared to events coming from the Northerly direction. The difference between the light collected at North and South directions seems to decrease with increasing impact parameters.

The loss of EAS light is due to the effect of the Earth's magnetic field in the electron-positron pairs of the gamma-showers. The Cherenkov photons spread out by the Earth's magnetic field are not recovered inside the MAGIC telescope's effective area (r $\lesssim$ 180 m). Most of the lost light at low impact parameters is spread out at impact parameters of r > 1 km.

Up to now the Earth's magnetic field effect has been verified on the integrated EAS light density with different impact parameters (fig. 4.12). Nevertheless, the effect on the shower light density is a consequence of the effect of $B_\perp$ on the EAS charged particles. The γ-ray initiated showers are pure electromagnetic showers (see chapter 1), therefore the shower lateral extension is mainly due to multiple Coulomb scattering of e^-/e^+ pairs. This process is sharply peaked forward in the EAS development and, consequently, gives rise to nearly collimated showers. Therefore, the magnetic field will also affect the shape and size of the EAS ground distribution due to its interaction with the secondary charged particles' direction.

To plot the net effect of the magnetic field on the ground distributions, specific simulations of γ-ray showers have been performed with and without B components in the MC input card. Because the CORSIKA program does not allow null values for magnetic field components, very small values have been applied ($B = 0.1\mu$T $\sim 0.3\%$ B_{MAGIC}) in the simulation for the assumption of B = 0.

The ground distribution of Cherenkov light from all the charged particles of the γ-ray shower is shown in figure 4.13. Separately the photons coming only from electrons and from positrons are shown in figures 4.14 and 4.15 respectively. The γ showers also have been simulated at energies of 10, 30 and 100 GeV, at zenith angle of 15° (on the top) and 45° (on the bottom) for different pointing directions, S(ϕ=0), E(ϕ=90), N(ϕ=180) and W(ϕ=270). The colour scale plots correspond to EAS simulated with La Palma magnetic field values and the contour lines plot are the corresponding ones without magnetic field applied. All of them are normalized to the maximum value (displayed as a label in the first plot) of the distribution in the South direction ($\phi = 0$) where the minimum effect of the magnetic field is expected.

The X and Y axes on these distributions refer to the telescope reference frame ($\vec{i}\,'$,$\vec{j}\,'$,$\vec{k}\,'$), which rotates around the z-axis (fig. 4.4) at an angle ϕ with respect to the ground reference frame ($\vec{i}$,$\vec{j}$,$\vec{k}$).

In these plots one has to distinguish between two effects: a geometrical one, due to the change of reference frame between telescope and ground, and another one, due to the real effect of the Earth's magnetic field interacting onto the EAS images.

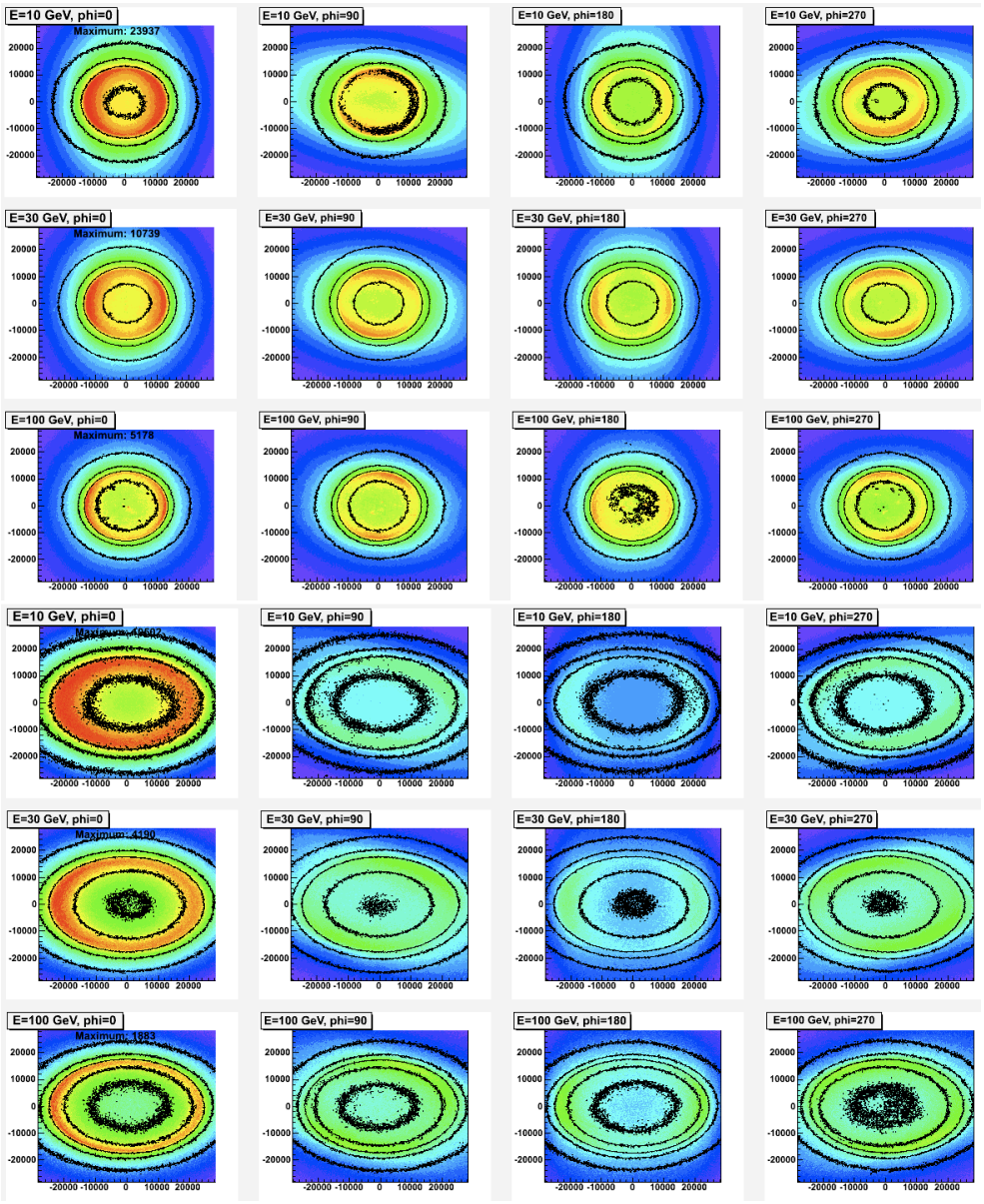

Figure 4.13: *Ground distribution of Cherenkov photons for* **gamma** *showers of 10, 30 and 100 GeV and zenith angles of 15° (upper plots) and 45° (bottom plots). Colour plots correspond to EAS simulated with B field while in the contour plots the B field is not simulated. The plots are normalized to the maximum value for showers simulated at phi=0. The X and Y axes display the impact parameters between -300 and 300 meters.*

The first effect can be clearly seen when looking at the contour plots (fig. 4.13), where no magnetic field has been applied. In these plots, the images remain very similar for different azimuth angles and energies for the same zenith angle. Comparing different distributions at zenith angles (fig. 4.13) one can see that the EAS image is enlarged along the x-axis when increase the zenith angle from 15° to 45°. This enlargement of the image produces a loss of the light collected by the telescope. This loss is significant for larger zenith angles (45°) and it is similar along the source trajectory as azimuth angle changes. This effect is due to the projection of the EAS image onto the telescope reference frame, which is the frame used for the plots of figure 4.13. If the projection were in the ground reference frame, the enlargement that is always seen along the x-axis should rotate while one moves along the azimuth pointing direction. This effect is also included in the image distortions if one includes the magnetic field into the EAS simulations, but it is no so evident.

The second effect corresponds to the distortion of the EAS images due to the Earth's magnetic field. To understand this effect it is necessary to project the component perpendicular to the magnetic field (given by equation 4.2) to the telescope reference frame ($\vec{i}\,'$,$\vec{j}\,'$,$\vec{k}\,'$). This is given by equations 4.3, which express the net effect of the Lorentz force for different azimuth directions (ϕ= 0°, 90°, 180° and 270°).

$$\vec{F} \propto -q \cdot v \cdot \begin{cases} (B_x \cos\theta - B_z \sin\theta)\ \vec{j}' & \phi = 0 \quad (S) \\ B_x \cos\theta\ \vec{i}' - B_z \sin\theta\ \vec{j}' + B_x \sin\theta\ \vec{k}' & \phi = 90 \quad (E) \\ -(B_x \cos\theta - B_z \sin\theta)\ \vec{j}' & \phi = 180 \quad (N) \\ -B_x \cos\theta\ \vec{i}' - B_z \sin\theta\ \vec{j}' - B_x \sin\theta\ \vec{k}' & \phi = 270 \quad (W) \end{cases} \tag{4.3}$$

Looking to the top plot of figure 4.13 corresponding to $\theta = 15^o$, one can only see the magnetic field effect, because the geometrical one is much less important for low zenith angles. This figure shows that the EAS images are enlarged along the x-y plane vector of the equations 4.3 for the different azimuthal angles. For azimuth angles of 0° and 180° the enlargement is along the y-axis while for azimuth angles of 270° and 90° the enlargement axis should form an angle $\tan\alpha = \pm B_z/B_x \tan\theta$ with the x-axis, respectively. Looking at figure 4.13 it seems indeed to be the case. For a zenith angle of 15°, the axis angle is around 12°, while for zenith angle of 45° it is around 40°. As well as the geometrical effect, the enlargement of the EAS images, due to the spread of the charged particles by the Earth's magnetic field, causes a loss of the light collected by the telescope. This is indicated by the colour scale plots in figure 4.13. These plots show that the amount of lost light differs for different azimuth angles because the light is spread by the magnetic field in different directions depending on the direction to which the telescope is pointing.

For EAS at 45° zenith angle (bottom plots of figure 4.13), the magnetic field and the geometrical effects are superimposed. The ratio of the maxima of light density at 45° and at 15° decreases by $\sim 50\%$. If we calculate the same ratio for EAS simulated

without a B field, the decrease is only $\sim 30\%$. This leads us to conclude that around 20% of the light lost in the telescope reflector is due to the magnetic field effect, while 30% is due to the spread of the EAS image because of the observation zenith angle.

From equation 4.3, one can see that the image enlargement caused by the magnetic field depends on the one hand on the directions to which the telescope points, while on the other hand it depends on the particle charge (q) and momentum (v) of the secondary charged particles of the EAS. The effect of the particle momentum is clearly seen in figure 4.13 on the light distributions for different energies of the primary γ-ray. The ground distribution has been simulated superimposing 10 showers. Comparing the shower images of gammas at 100 GeV with those of 10 GeV and 30 GeV, one can see that the light collected by the telescope decreases with the energy with hardly any effect on gamma showers above 100 GeV. This is because the lower momentum particles are easier to deflect (lower Larmor radius) than high energy particles.

To see how the charge dependence of equation 4.3 contributes to the change of EAS images, the ground distribution of Cherenkov light caused by the electrons (fig. 4.14) and by positrons in (fig. 4.15) have been shown. Comparing these figures and equation 4.3 one can see that the pairs e^-/e^+, which give rise to the Cherenkov photons in γ-like showers, are spread in opposite directions along the EAS image enlargement direction. It is easy to check in equation 4.3 that the light distribution for each azimuth angle in figures 4.14 and 4.15 is spread in the direction given by the unit vectors on the equation.

All these simulations have been done for two fixed zenith angles (15º and 45º) which represent only the low and high zenith angle cases. All the conclusions agree with the explanations in section 4.1, so that a higher effect is expected between North ($\phi = 180$) and South ($\phi = 0$) directions and at zenith angle closer to 50°.

4.3.2 Effective areas for gammas

The above analysis shows that the magnetic field affects the light density collected by the telescope as well as the shower image parameters in the case of imaging telescopes [151]. The next study will concentrate only on the decrease of the integrated light density and therefore on the decrease of the telescope effective area, leaving the effect on the image parameters for more complete simulations [42].

For the Northerly direction it has been shown that there is a larger loss of Cherenkov photons of up to 50% for low energies and high zenith angles compared to the South. This should result in a decrease in the trigger efficiency and also in the effective area.

In section 4.2 it was explained how to achieve roughly the effective collection area at different energies and zenith angles using a simplified simulation.

Figure 4.16 shows the effective area for North and South directions as a function of the gamma showers' energy. The relative difference on the effective area for both azimuth directions at different energies and zenith angles is shown in table 4.3.

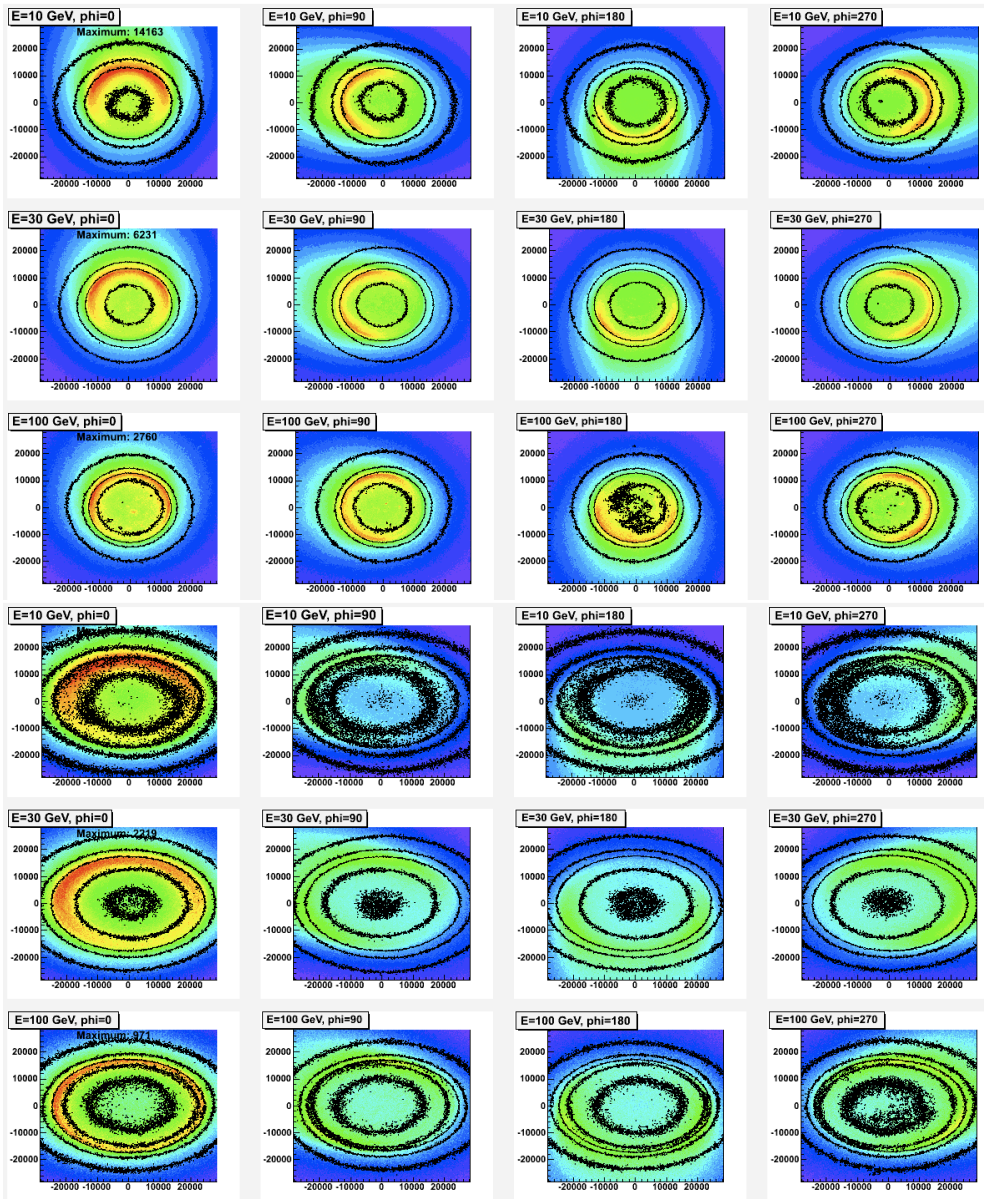

Figure 4.14: *Ground distribution of Cherenkov photons for* **gamma** *showers (***electron component***) of 10, 30 and 100 GeV and zenith angles of 15° (upper plots) and 45° (bottom plots). Colour plots correspond to EAS simulated with B field while in the contour plots the case of zero B field is simulated. The plots are normalized to the maximum value for showers simulated at phi=0. The X and Y axes display the impact parameters between -300 and 300 meters.*

Both the table and the figure confirm the results obtained for the lateral and ground

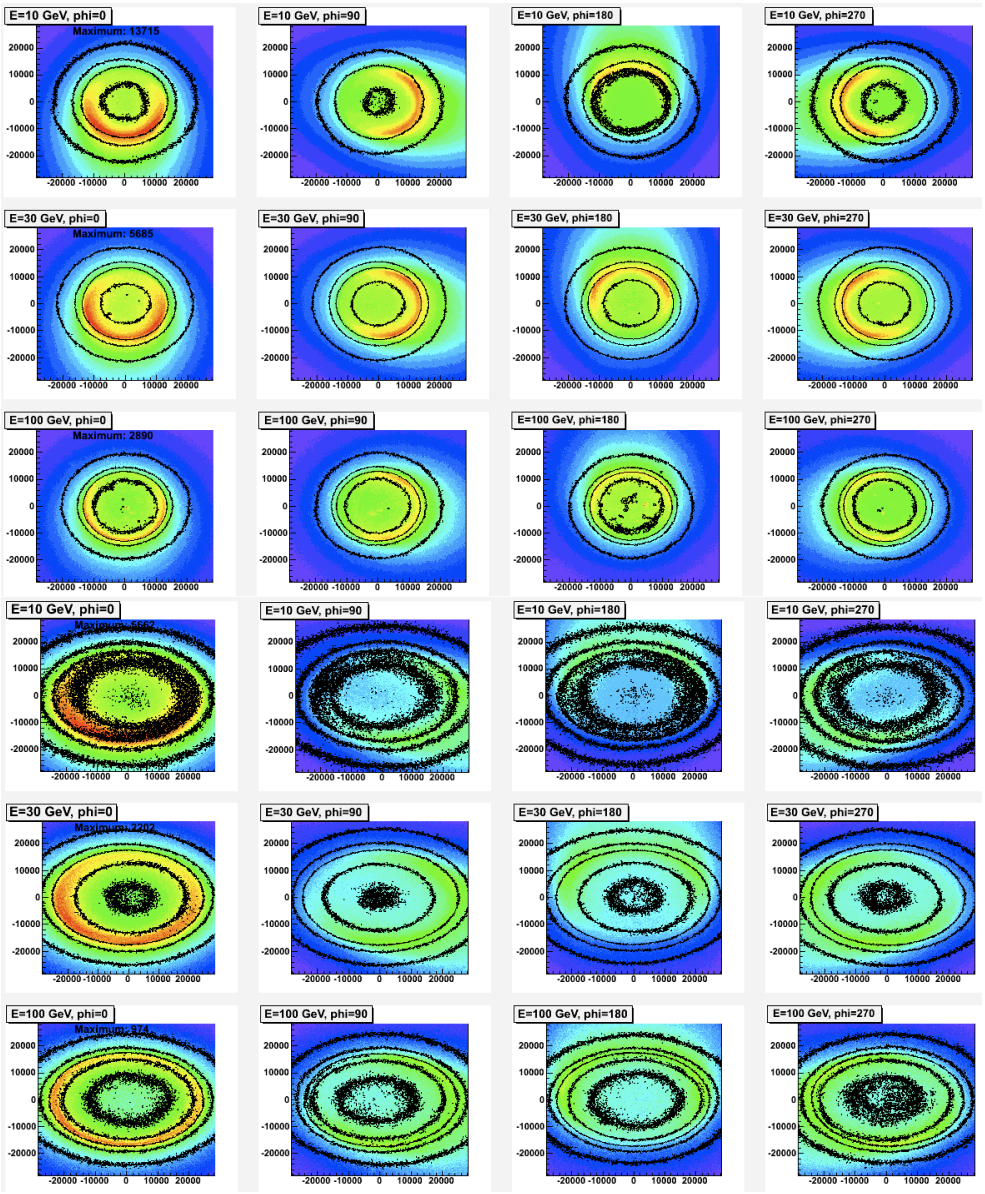

Figure 4.15: *Ground distribution of Cherenkov photons for* **gamma** *showers (***positron component***) of 10, 30 and 100 GeV and zenith angles of 15° (upper plots) and 45° (bottom plots). The colour plots correspond to EAS simulated with B field while in the contour plots the case of zero B field is simulated. The plots are normalized to the maximum value for showers simulated at phi=0. The X and Y axes display the impact parameters between -300 and 300 meters.*

distributions explained in the previous sections.

The general comments made with respect to the lateral distributions apply also

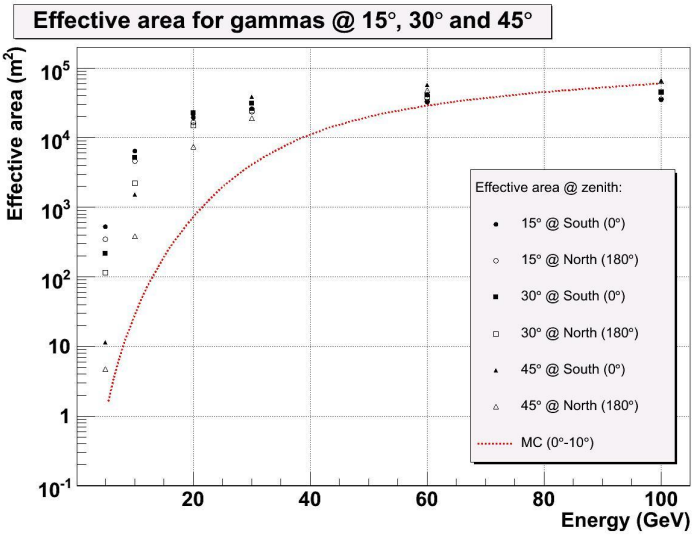

Figure 4.16: *Effective area for* **gammas** *for energies of 5, 10, 20, 30, 60 and 100 GeV at zenith angles of 15, 30 and 45 degrees. The dotted red line corresponds to the MAGIC effective area from standard MC simulations (θ= 0° - 10° and ϕ = 0°).*

to the effective areas: the effect of the magnetic field increases with the zenith angle and decreases with increasing energy.

The general shape of the curve resembles the results obtained with the full simulation (see chapter 3) and is shown in figure 4.16 as a dotted line. For energies below 60 GeV the full MC simulations seem not to fit with the simplified MC simulations in this chapter. This can be due to the bad tuning of the trigger system in the full MC simulations. The curve gives a first indication of the relative differences between North and South, but more detailed studies are required.

	15 °	30°	45°
5 GeV	30%	60%	90%
10 GeV	30%	60%	70%
20 GeV	20%	40 %	70%
30 GeV	10%	30%	70%
60 GeV	4%	5%	30%
100 GeV	∼0%	1%	10%

Table 4.3: *Relative differences in the effective area between North (empty marker of fig. 4.16) and South (filled marker of fig. 4.16) for gamma showers of energy 5, 10, 20, 30, 60 and 100 GeV and zenith angles of 15, 30 and 45 degrees.*

4.3.3 Proposed setup for future Monte Carlo simulations

Due to the fact that the effective area changes up to 90% (for low energies) with the azimuth pointing direction (table 4.3), it will be necessary to simulate more precisely Monte Carlo data at different azimuth angles and not only at different zenith angles as of the current official MC simulations. The goal in this part of the study is to find the best set of azimuth angles for these MC simulations.

In MAGIC, the Monte Carlo simulations have been done using different zenith angles which give rise to equal intervals in solid angle ($\Delta\Omega = 2\pi\Delta(\cos\theta)$) with $\Delta(\cos\theta) = 0.1$. To define the bins in azimuthal angle, one has to see how the MAGIC effective area changes with $B_\perp$ for different pointing directions. Since the magnetic field effect is larger at low energies, the effective area is shown in fig. 4.17 for 15, 30 and 45 degree zenith angle as a function of the $B_\perp$ and different azimuth angles for gamma showers of 10 GeV.

The module of $B_\perp$ is given by the expression:

$$|\vec{B_\perp}| = \{B_z^2 \sin^2\theta \sin^2\phi + (B_x \cos\theta - B_z \sin\theta \cos\phi)^2 + B_x^2 \sin^2\theta \sin^2\phi\}^{1/2} \qquad (4.4)$$

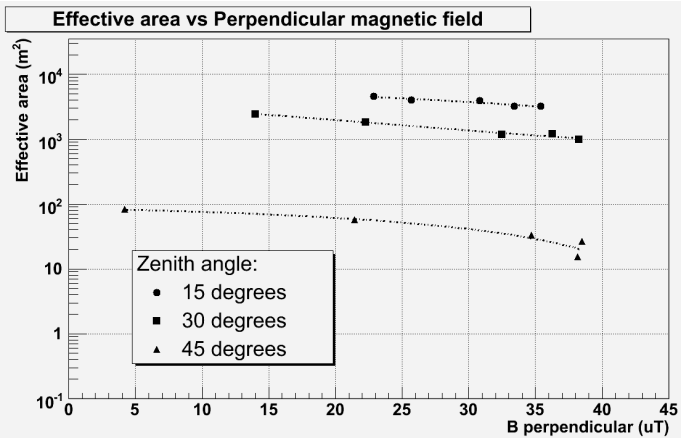

Figure 4.17: *Effective area versus the $|B_\perp|$ at La Palma for different zenith (15º, 30º and 45º) and azimuth (0º, 45º, 90º, 120º and 180º) angles for gamma showers of 10 GeV.*

Figure 4.17 shows that the effective area changes slowly with $B_\perp$ (equation 4.4) and decreases with the azimuth angle for a fixed zenith angle. The rate of change as a function of the azimuthal angle depends on the zenith angle. The largest value of the effective area corresponds to azimuth angles of $\phi = 0$ (South), while the lowest values corresponds to $\phi = 180$ (North). This can be seen also in figure 4.16 for other energies. Figure 4.17 also shows that the effect of the magnetic field has a smaller

effect for low zenith angles with hardly any change in $B_\perp$ in relation to the azimuth. All this has been already explained in section 4.1.1. Figure 4.17 shows the curves (dotted lines) of a fit to a second order polynomial to the points corresponding to the same zenith angle. The fits show that for equally spaced points in $B_\perp$ of around 11 μT, the effective area changes between 5 - 30% per step, depending on the zenith angle.

As for the case of the zenith angle bin criterion, the use of a set of azimuth angles equally spaced in $B_\perp$ for the MC simulations is proposed. For each of these generation bins in the zenith angle a number of azimuth ($B_\perp$) bins is defined, using N_{bins} = ($B_{\perp,max}$ - $B_{\perp,min}$)/($\Delta B_\perp$)$_{max}$ relation, rounded to the nearest integer. ($\Delta B_\perp$)$_{max}$ is the maximum increment in $B_\perp$, and was set to 11 μT, in order to have a reasonable number of bins in the last generated zenith angle, and at least three bins everywhere. Since the range of values of $B_\perp$ depends on the zenith angle (fig. 4.6), the number of azimuth angle bins will also depend on it. The formulae used are:

$$
\begin{aligned}
|\vec{B_\perp}|_{min} &= B_x \cos\theta - B_z \sin\theta \\
|\vec{B_\perp}|_{max} &= \begin{cases} B_x \cos\theta + B_z \sin\theta, & \theta < 38^o.7 \\ \{B_x^2 + B_z^2\}^{1/2}, & \theta > 38^o.7 \end{cases}
\end{aligned}
$$

Once the number of $B_\perp$ bins hae been calculated, the corresponding azimuth angle values are computed. The increment in $B_\perp$ is $\Delta|\vec{B_\perp}| = (B_{\perp,max} - B_{\perp,min})/N_{bins}$ and the corresponding azimuth angle for each $B_\perp$ bin is:

$$
\cos\phi = \frac{-B_z \cos\theta + \sqrt{B_x^2 + B_z^2 - |B_\perp|^2}}{B_x \sin\theta} \tag{4.5}
$$

The generation azimuth angles proposed for each zenith angle bin are listed in table 4.4. The effective area for any zenith angle can then be obtained by interpolation.

Since the values have been calculated using the expression of the Lorentz force they do not depend on the simulation details. On the other hand, they depend on the location of the telescope.

4.4 Magnetic field effect on Proton showers

4.4.1 Lateral distributions for proton showers

From gamma showers studies (section 4.3), one can conclude that $B_\perp$ affects the charged electromagnetic secondary cascades in the EAS developments, spreading the Cherenkov photons emitted, decreasing the amount of light from a shower collected by the reflector and therefore decreasing the telescope sensitivity to primary particles.

When primary protons or nuclei in general interact with the atmospheric atoms, they produce pions (π^0,π^+ and π^-). These pions are produced in approximately equal

Bin	$\theta(^\circ)$	$\Delta\lvert\vec{B_\perp}\rvert$	$\phi(^\circ)$	Bin	$\theta(^\circ)$	$\Delta\lvert\vec{B_\perp}\rvert$	$\phi(^\circ)$
0	0.00	0.0	0, 180	16	32.86	8.8	0, 41, 74, 180
1	8.11	6.8	0, 180	17	33.90	9.0	0, 41, 73, 180
2	11.48	9.6	0, 180	18	34.92	9.3	0, 40, 72, 180
3	14.07	5.9	0, 75, 180	19	35.90	9.5	0, 39, 70, 180
4	16.26	6.8	0, 73, 180	20	36.87	9.7	0, 38, 69, 180
5	18.19	7.6	0, 71, 180	21	37.81	9.9	0, 37, 68, 180
6	19.95	8.3	0, 69, 180	22	38.74	10.1	0, 36, 67, 180
7	21.57	8.9	0, 68, 180	23	39.65	10.3	0, 36, 66, 165
8	23.07	9.5	0, 66, 180	24	40.54	10.5	0, 35, 65, 160
9	24.49	10.1	0, 65, 180	25	41.41	10.7	0, 34, 64, 155
10	25.84	10.6	0, 64, 180	26	42.27	10.9	0, 33, 63, 152
11	27.13	7.4	0, 46, 80, 180	27	43.11	8.3	0, 26, 46, 72, 149
12	28.36	7.7	0, 45, 79, 180	28	43.95	8.5	0, 25, 46, 71, 146
13	29.54	8.0	0, 44, 78, 180	29	44.77	8.6	0, 24, 45, 70, 144
14	30.68	8.2	0, 43, 76, 180	30	45.57	8.7	0, 24, 44, 69, 141
15	31.79	8.5	0, 42, 75, 180	31	46.37	8.9	0, 23, 43, 68, 140

Table 4.4: *Proposed generation azimuth angle for each zenith angle bin of the Monte Carlo simulations of gamma showers for the MAGIC site.*

proportions and are the three main particles of the EAS that contribute to electromagnetic -sub-cascades (see chapter 1). The π^0 particles give rise to electromagnetic sub-cascades as in the case of γ-showers. The two charged pions (π^+ and π^-) give rise to other charged and neutral particles. The particles include many muons. When these secondary particles interact with the atmospheric atoms, several of them also produce electromagnetic sub-cascades but in smaller quantities than the π^0.

Because there are electromagnetic sub-showers and charged particles of hadronic origin, one also expects to have an effect of the Earth's magnetic field on the proton showers and therefore on the background. To estimate the effect of $B_\perp$ on the charged secondary particles of the proton showers, the same method has been used as described in the gamma section (section 4.2), generating proton showers (table 4.5) at different energies and zenith angles coming from the North (ϕ=180°) and South (ϕ=0°) directions.

The protons come isotropically from all sky directions and normally all the protons inside a cone of 5 degrees are considered as possible source of background. In order to compare the results with that of previous simulations of γ-ray showers, the proton showers have been generated coming from a point source.

Similarly, in the case of gamma showers, fig. 4.18 shows the lateral distribution of Cherenkov photons from proton showers at different energies and zenith angles for

Energy / Zenith angle	Number of events 15 °	30°	45°
30 GeV	10^4	10^4	10^4
300 GeV	10^4	10^4	10^4
3 TeV	10^2	10^2	10^2

Table 4.5: *Number of proton showers generated for each azimuth angle (North and South) as a function of energy and zenith angle.*

North and South directions. As for gamma shower simulations, the Cherenkov light density decreases with the energy and the zenith angle but decreases with the impact parameter. The curve for proton showers of 30 GeV is not as well defined as those at the other energies, due to the low amount of Cherenkov photons produced at these energies.

One of the clearest conclusions from figure 4.18 is that the difference in the light density between North and South direction is not as pronounced as in the case of gamma showers. This is better seen in the three plots on the right side, a zoom up to 500 meters of impact parameters of those on the left. At energies of 30 GeV, the density of Cherenkov photons is very low and fluctuations are important. At energies around 300 GeV and 3 TeV, the difference between North and South directions are rather small. Apparently the photon density does not depend very much on the energy or zenith angle of the primary proton.

Comparing with gamma showers (fig. 4.12), it can be seen that gamma showers of 100 GeV and proton showers of 300 GeV have approximately the same density of Cherenkov photons at low impact parameters. Apart from this, the proton showers do not show significant differences in the amount of Cherenkov photons between North and South directions, while low energy gamma shower experiments show a decrease of around 50% at zenith angles of around 45°.

These plots contain the integral of all the light for each impact parameter bin. There is hardly any effect from the perpendicular component of the magnetic field in the lateral distribution of proton showers. This is contrary to the case of gamma-showers. It could be expected that the magnetic field affects the shape of the EAS ground distribution. This effect, if existent, should be seen in the ground distributions shown in figures 4.19, 4.20 and 4.21.

As in the gamma shower section, in these figures the colour scale plots correspond to EAS simulated with La Palma magnetic field values and the contour lines plots are the corresponding ones where the magnetic field has been suppressed.

In these three figures, the ground distribution of Cherenkov photons is shown for proton showers of 30 GeV, 300 GeV and 3 TeV at zenith angles of 15° (on the top)

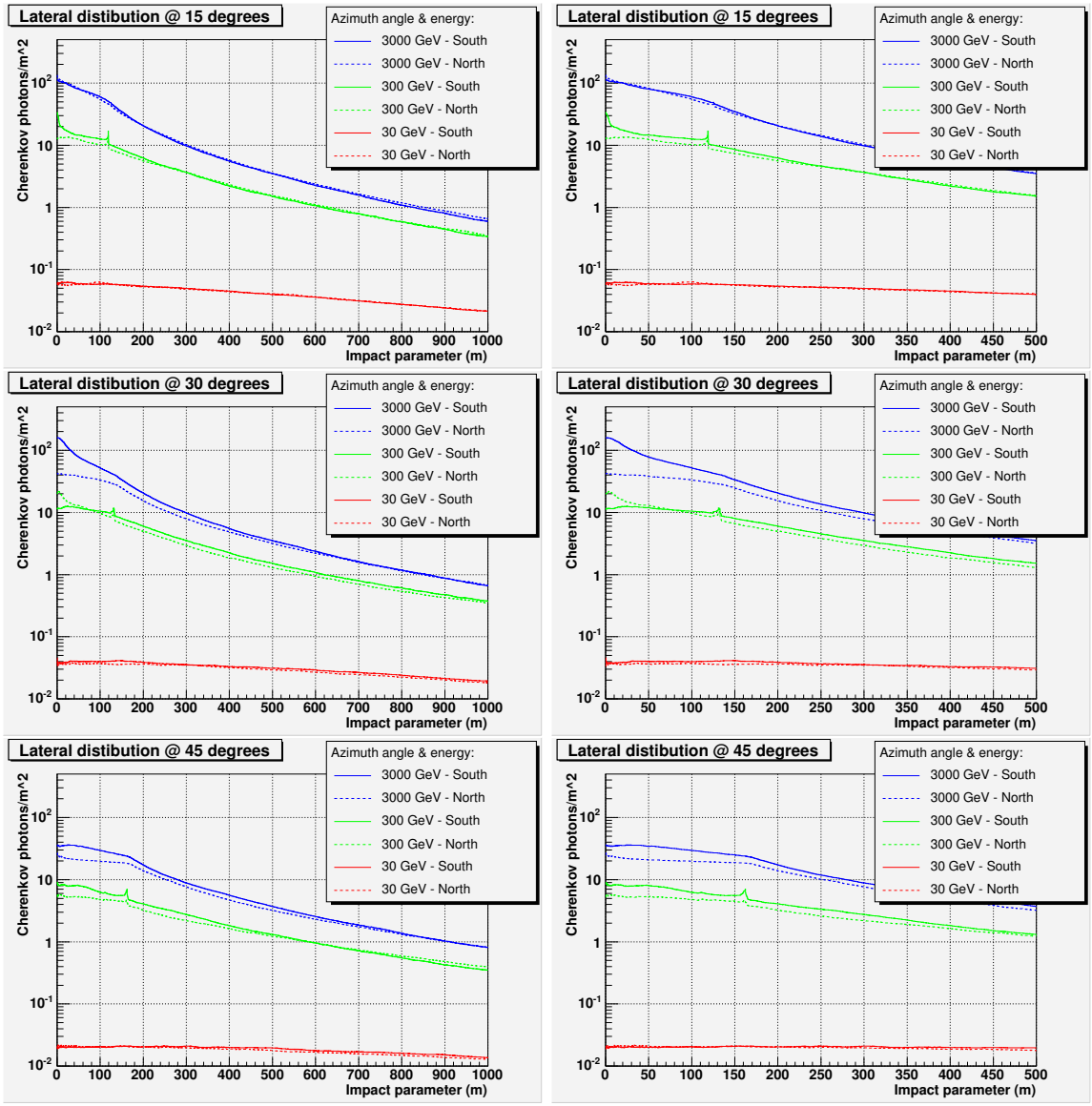

Figure 4.18: *Lateral distribution of Cherenkov photons for* **proton** *showers of 30, 300 and 3000 GeV at zenith angles of 15, 30 and 45 degrees. The plots on the right are a zoom of those on the left ones for impact parameters up to 500 meters.*

and 45º (on the bottom) for different pointing directions S(ϕ=0), E(ϕ=90), N(ϕ=180) and W(ϕ=270). All distributions are normalized to the maximum value (displayed by a label) of the distribution in the South direction ($\phi = 0$) where the minimum effect of the magnetic field is expected (fig. 4.6). Figure 4.19 shows the light distribution from all the charged particles of the proton EAS, figure 4.20 shows the light distribution

from only the secondary electrons and figure 4.21 the one from secondary positrons.

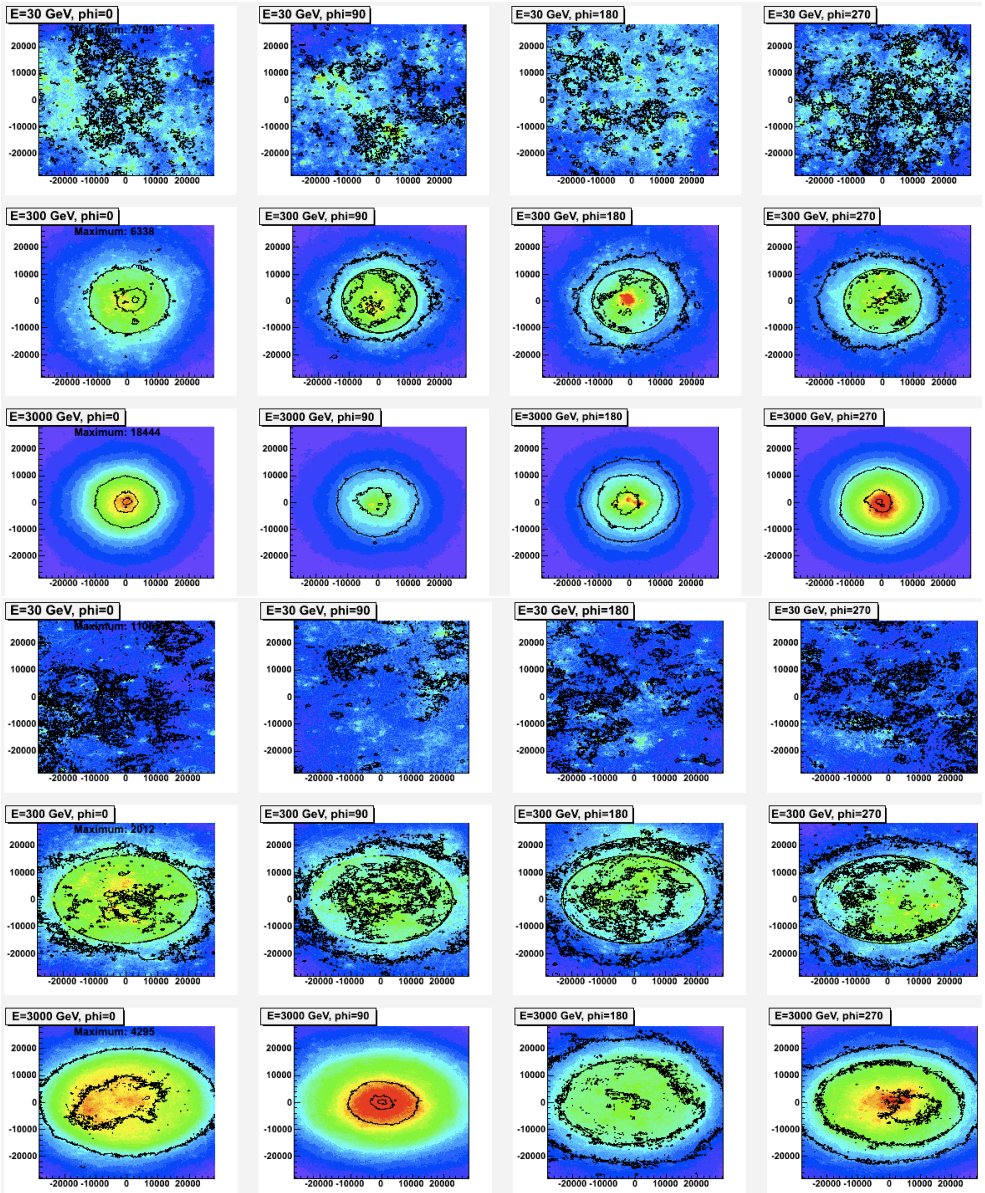

Figure 4.19: *Ground distribution of Cherenkov photons for* **proton** *showers of 30, 300 and 3000 GeV and zenith angles of 15° (upper plots) and 45° (bottom plots). The colour plots correspond to EAS simulated with B field while in the contour plots the B field is not simulated. The plots are normalized to the maximum value for showers simulated at phi=0. The X and Y axes display the impact parameters between -300 and 300 meters.*

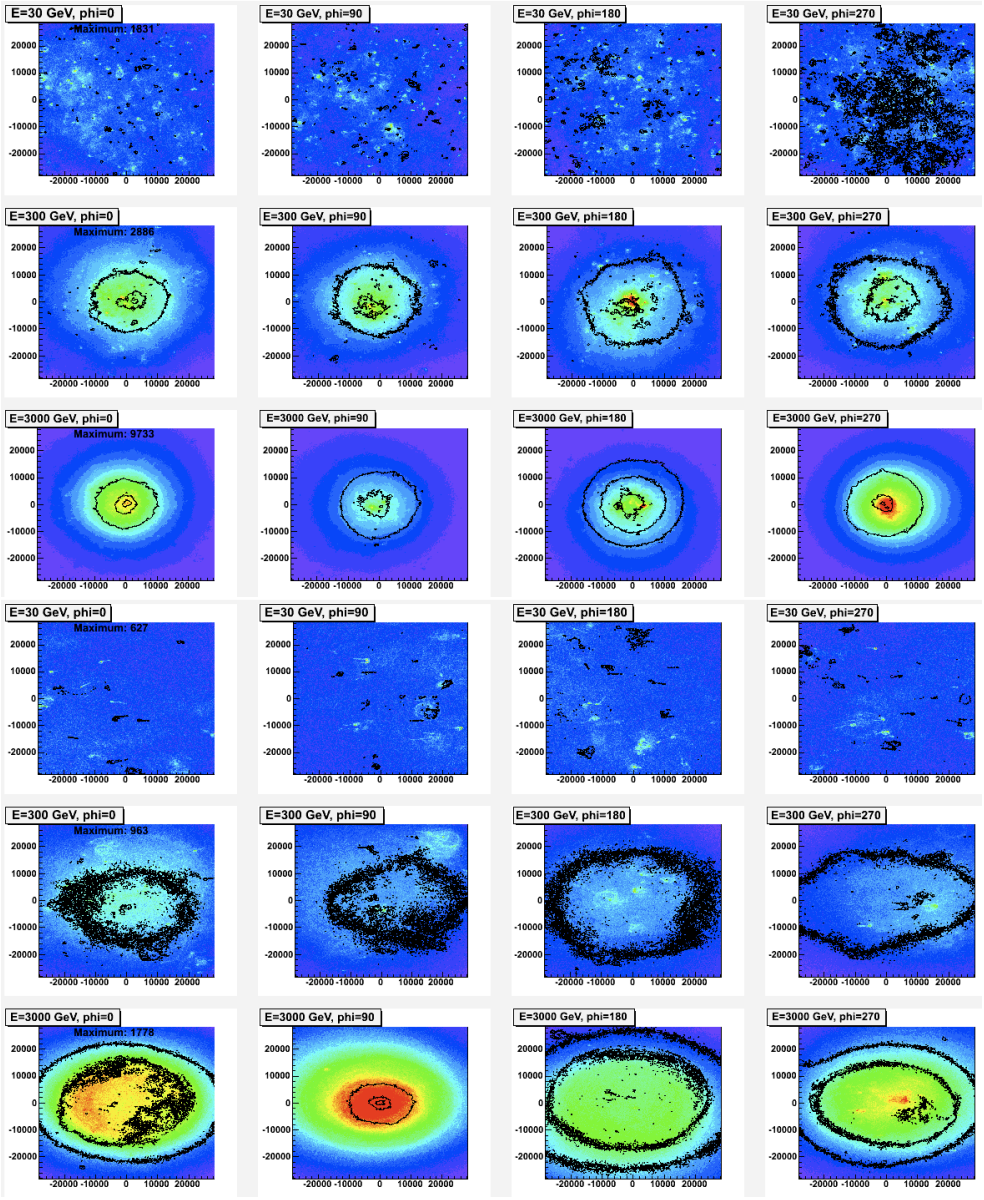

Figure 4.20: *Ground distribution of Cherenkov photons for* **proton** *showers (***electron component***) of 30, 300 and 3000 GeV and zenith angles of 15° (upper plots) and 45° (bottom plots). The colour plots correspond to EAS simulated with B field while in the contour plots the B field is not simulated. The plots are normalized to the maximum value for showers simulated at phi=0. The X and Y axes display the impact parameters between -300 and 300 meters.*

The magnetic field should have the same effect on the electromagnetic sub-

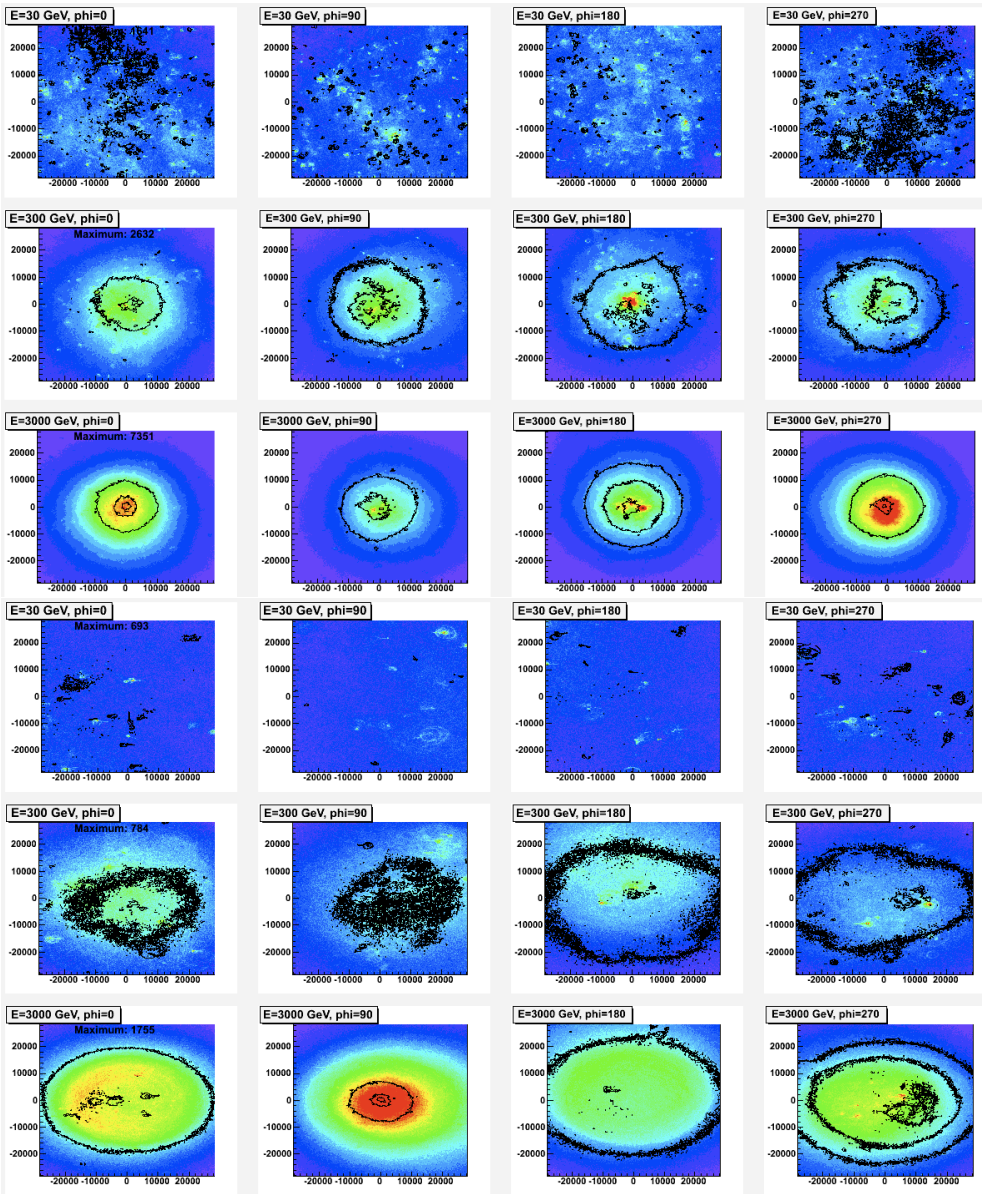

Figure 4.21: *Ground distribution of Cherenkov photons for* **proton** *showers (***positron component***) of 30, 300 and 3000 GeV and zenith angles of 15° (upper plots) and 45° (bottom plots). The colour plots correspond to EAS simulated with B field while in the contour plots the B field is not simulated. The plots are normalized to the maximum value for showers simulated at phi=0. The X and Y axes display the impact parameters between -300 and 300 meters.*

cascades from proton showers as on gamma showers. The only difference is that

in gamma showers they come from $\gamma \rightarrow e^+/e^-$ processes while in proton showers they come mainly from the initial π^0 disintegration process.

Therefore, it is expected that the upper plots (low zenith angles) in figures 4.19, 4.20 and 4.21 should not show an effect caused by the magnetic field as big as that for gamma EAS distributions. Inspecting these plots for low zenith angles, it can be seen that indeed the shape of the showers for all the pointing directions remains the same for proton energies of 300 GeV and 3 TeV. Therefore, only a slight effect from the Earth's magnetic field on the amount of light collected by the telescope is seen. This is also confirmed when comparing the ground distributions of Cherenkov photons coming only from electrons (fig. 4.20) and only from positrons (fig.4.21). Both distributions are similar with a little effect due to the magnetic field on the charged secondary particles, as it was true for gamma showers (fig. 4.14 and 4.15). For 30 GeV proton showers, it is not possible to perform any analysis due to the low statistics of Cherenkov photons.

In the case of proton showers at a zenith angle of 45°, all the images extend along the X-axis due to the projection of the shower images in the telescope reference frame, similar to the case of gamma showers. There is no dependence on the shower shape on the pointing direction (azimuth angle).

As for gamma showers, the Cherenkov light density of proton showers increases with the energy and decreases with the zenith angle. In both figures, 4.19 and 4.18, the only difference in azimuth angle is a decrease in the density of Cherenkov photons for proton showers coming from North direction. This difference is nevertheless very small. To verify whether this is due to the magnetic field effect, one should look into the ground distribution for proton showers in colour scale for the simulation without magnetic field (fig. 4.22). Because no magnetic field is included into the simulation, one does not expect to find any displacement between electrons and positrons.

This figure shows that the light distribution at ground level has the same shape and size as in the case of simulations including the magnetic field. A very small difference can be seen in the light density due to fluctuations in the shower itself: at high zenith angles (45°), for energies of 30 and 300 GeV, the light density is bigger with B than without, while it is smaller for 3 TeV.

From the analysis of the lateral and ground distributions of Cherenkov light from proton showers, one can conclude that the Earth's magnetic field has very little effect on the light density coming from proton showers.

An explanation for this apparent paradox might be found in the fact that in proton showers not only e^-/e^+ but also other charged particles (charged pions and muons) emit Cherenkov light. Therefore, figure 4.23 represents the light distributions at the ground coming from electron/positron pairs (green line) and the rest of particles, mainly muons, (blue line). Only distributions from primary protons of 300 GeV and 3 TeV, coming from the North and South directions at a zenith angle of 45°, have been shown. At these angles, a larger effect from the Earth's magnetic field is

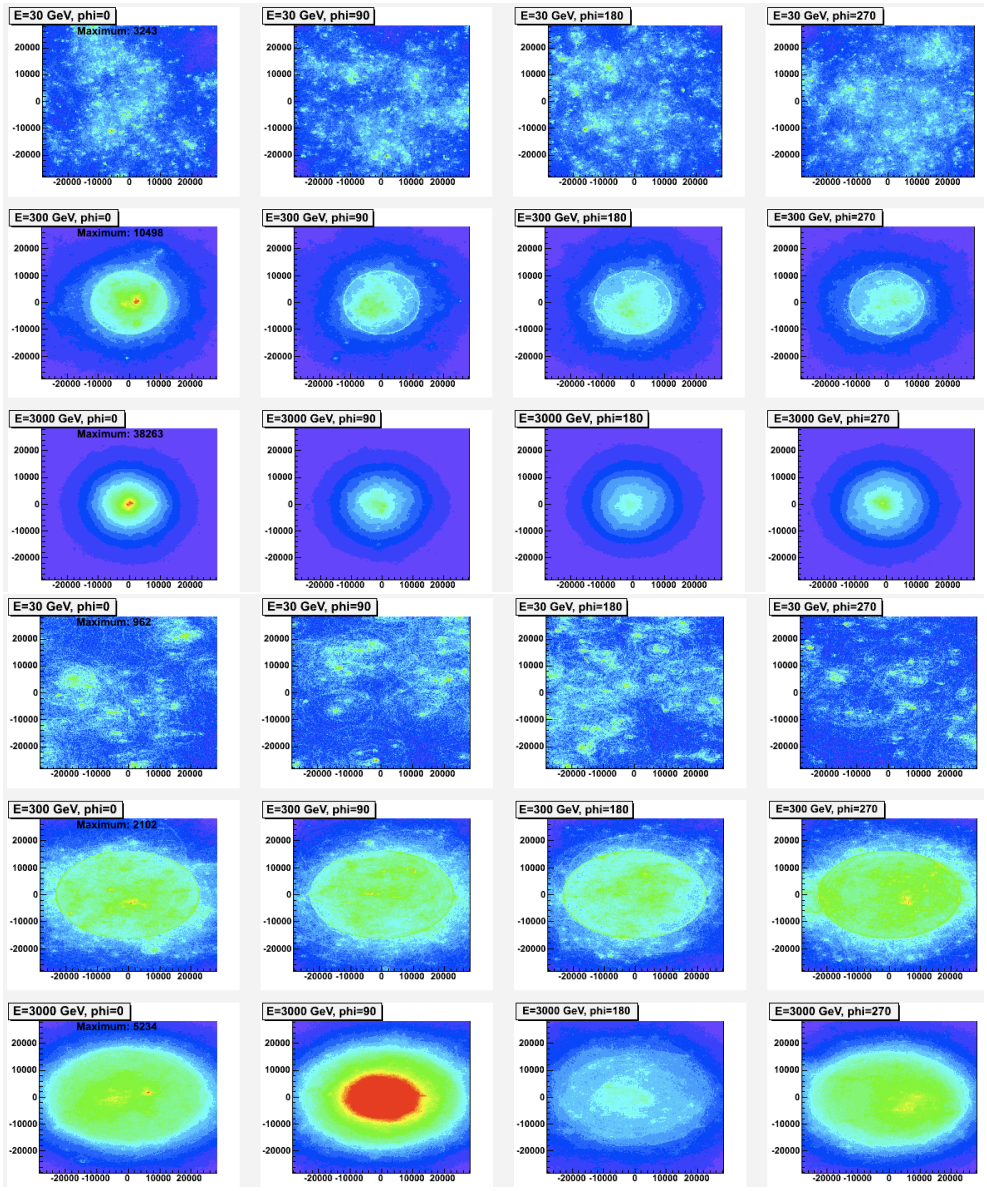

Figure 4.22: *Ground distribution of Cherenkov photons for* **proton** *showers* **without B** *of 30, 300 and 3000 GeV and zenith angles of 15° (upper plots) and 45° (bottom plots) degrees. The plots are normalized to the maximum value for showers simulated at phi=0. The X and Y axes display the impact parameters between -300 and 300 meters.*

expected, since they have larger momentum. The 30 GeV protons shower data have been excluded due to the low statistics and the large fluctuations seen previously.

These two plots show clearly that the electromagnetic cascades (e^-/e^+) (green

lines) are the main contributors to the total Cherenkov light emitted by a proton shower (∼70%), with a lower contribution of the muons and other charged particles (∼30%)

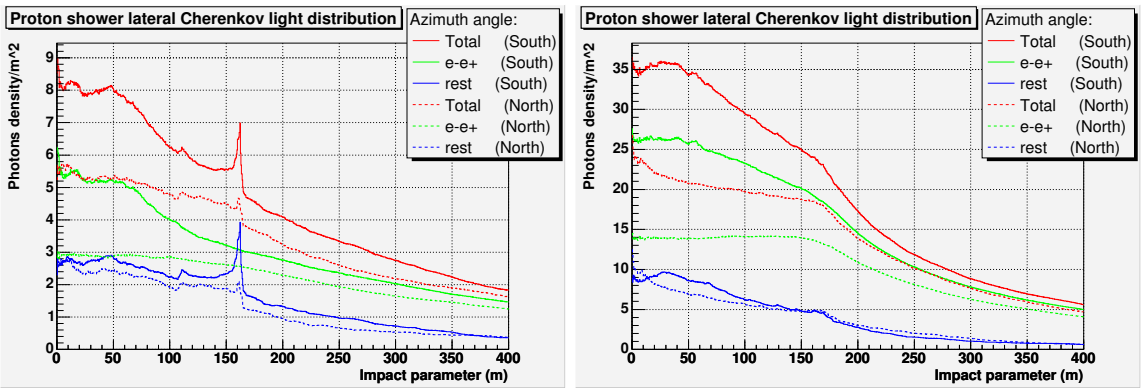

Figure 4.23: *Lateral distribution components in* **proton** *showers of 300 (left) and 3000 GeV (right) at zenith angle of 45º.*

As for γ-showers, the contributions of the electromagnetic component (e^-/e^+) to the light density differs between North and South directions. This difference is around the same order of magnitude as the difference in the total light density between both directions. Since muons have in general a higher momentum, they are less deflected. Therefore, only the electron/positron component of the proton showers is affected by the Earth's magnetic field (fig. 4.23).

As expected from the case of gamma showers, one can see that the effect of the Earth's magnetic field on proton showers depends on the amount of electron/positron pairs, although it seems that there is little effect on the total light density. This was also confirmed in the ground distributions coming from the $e^{\pm}$ component of the proton shower (fig. 4.20 and 4.21). In the ground distributions of gamma showers, the effect of the magnetic field showed up in the direction of the dispersion of each e^-/e^+ component.

In the case of proton showers, most of their Cherenkov photons come from the π^0 decay which are generated closer to the ground while the rest comes from sub-cascades of particles decays and their electron/positron pairs are widely distributed. Due to the low heights of the sub-cascades coming from π^0 particle, the magnetic field has less time to deviate them, as in the case of γ-showers. The rest of possible contributors (like kaons, muons,etc.) produce fewer electromagnetic sub-cascades and must all have high momentum to generate Cherenkov light. The high momentum of these particles will make them difficult to be affected by the magnetic field.

4.4.2 Effective areas for protons

The proton effective area is computed with the same method described in section 4.2 applied to gamma showers.

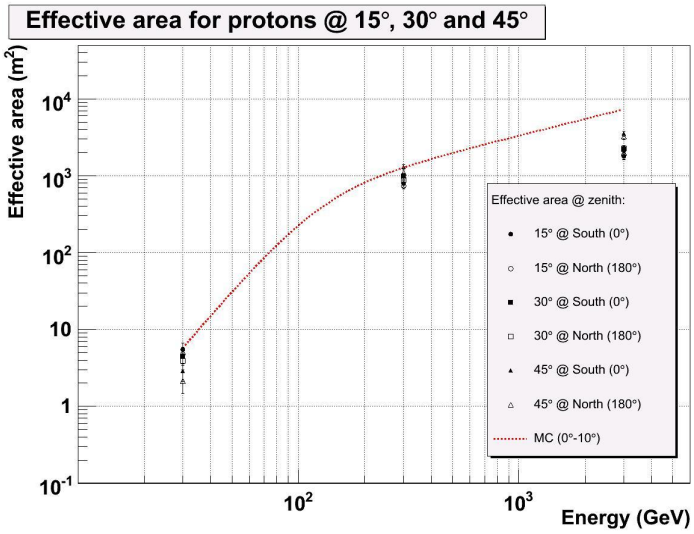

Figure 4.24: *Effective area for protons at energies of 30, 300 and 3000 GeV zenith angles of 15, 30 and 45 degrees. The dotted red line is the MAGIC effective area (θ= 0° - 10° and ϕ = 0°).*

Figure 4.24 shows that the proton effective area changes, as expected, with the energy and the zenith angle. However, it does not change noticeably with the azimuth angle $\phi = 0^o$ and $\phi = 180^o$ (South and North directions) as for γ-showers. For zenith angles of 45°, where the maximum effect is expected, the difference in the effective area for protons between North and South directions is $\sim 15\%$. The dotted red line corresponds to the MAGIC effective area for MC proton simulations with the full standard MAGIC software.

4.5 MAGIC's sensitivity for pulsars

From last sections, it can be concluded that the Earth's magnetic field has an important effect for gammas at high zenith angles ($\geq 30^o$) and low energies ($\leq$ 100 GeV), while for protons the effect is not significant. The Earth's magnetic field produces a decrease of the telescope effective area in the case of γ-rays while it hardly has any effect on the proton effective area. This result should lead us to expect a net reduction in the telescope sensitivity, making it dependent on the value of the magnetic field and the azimuthal angle. Such a result is especially important for

pulsar studies, since pulsar spectra have low cut-offs (< 50 - 100 GeV) and most of the pulsed component is assumed to arise from the energy range between 10-40 GeV.

Figures 4.16 and 4.24 show the effective area for gammas and protons (background) for the pointing directions where one expects the largest difference in the Earth's magnetic field effect. Fitting the effective areas with a function of the same kind used in the MC simulations of chapter 3 ($A_{Eff}(E) = \frac{A \cdot E^B}{1+(\frac{E}{C})^D}$), for zenith angle of 45° and azimuth of $\phi = 0°$ (South) and $\phi = 180°$ (North) and taking the pulsar spectrum from equation:

$$\frac{dN_\gamma}{dE} = K \cdot (\frac{E}{E_n})^{-\Gamma} \cdot exp(-(E/E_0)^b)$$

The expected source rate can be computed from South and North pointing directions. These rates have been estimated for the three Northern hemisphere pulsars detected by EGRET (table 4.6).

The observation time needed for a certain significance of the signal is estimated with the same assumptions made for the general Monte Carlo sensitivity studies in chapter 3 (eq. 3.10), which are made for a detection level of 3σ and a quality factor Q = 1 (trigger level):

$$N_\sigma = Q \frac{R_\gamma}{\sqrt{R_p + R_{neb}}} \sqrt{t_{obs}(s)}$$

Although the MC results of this simplified simulations do not fit at low energies with the results of the full MC simulation, the discrepancies are the same for both pointing directions (North and South). Therefore, the ratio between the observation times required for a significant detection for both directions should be more accurate.

Pulsar	θ_{culm} (°)	E_0 (GeV)	b	R (Hz) $(\phi = 0°)/(\phi = 180°)$	$t_{obs}(\phi = 180°)/t_{obs}(\phi = 0°)$
Crab	7	30	2	1.25	1.6
PSR B1951+32	4	40	2	1.22	1.5
Geminga	11	5.0	2.2	1.41	2.0

Table 4.6: *Rate and ratio of observation times to reach a 3σ detection level for the Northern hemisphere pulsars from the 7 detected by EGRET. A quality factor of Q = 1 was assumed.*

The same proton rate has been considered to estimate the observation time ratio (table 4.6) between North and South directions. As figure 4.24 shows, the proton rate can be considered the same for both pointing directions.

4.6 Conclusions and outlook

The first point to conclude is that the influence of the Earth's magnetic field in the shower development has to be taken into account depending both on the observation site and telescope threshold, varying in importance for different experiments.

The main result of this study is the fact that the Earth's magnetic field affects the EAS development of gamma showers whereas the effect is negligible for proton showers. This has a harmful consequence for the sensitivity of ground-based Cherenkov telescopes. In the simulations, the geomagnetic cut-off in the background (mainly protons [8] and electrons [45]) have also been considered. Therefore, no protons above 10 GeV have been included in this study, because charged particles below this energy do not reach the atmosphere and do not contribute as background.

The decrease of the Cherenkov telescope sensitivity with the energy threshold will have to be taken into consideration together with the telescope site for the location of future planned ground-based Cherenkov observatories.

This effect has to be also considered for future upgrades of the MAGIC telescope towards reaching a lower energy threshold, since the results have shown the great importance of the Earth's magnetic field effect for E$<$ 100 GeV.

Another important point extracted from this study is the need for another binning for the Monte Carlo simulation for gamma showers. In this study, the use of azimuth angles equally spaced in the perpendicular component of magnetic field has been proposed. In this way, corrections depending on the azimuth angle can be computed. For low energies, they might be very important.

The rough simulation results are consistent with the results presented in the previous chapter with the full Monte Carlo simulations at azimuthal angles of 0°, but only for high energies. For low energies, there is a discrepancy that could be due to a not very well tuned trigger in the full MC simulations or consider the trigger topology in the simplified MC simulations of this chapter.

Finally, this work could usefully be continued in the following directions:

- Include studies of the effect of B on the image parameters to get a more complete view of the influence of B on MAGIC results and improve the gamma/hadron separation [98] [151].

- Implement the impact of the magnetic field into studies for future upgrades of MAGIC and the next generation of Cherenkov telescopes. The simplicity of the simulation method described here makes these studies easier.

- Check the rate decrease with real data from sources with declination angles below 20°. These sources should be strong enough to reach a detection confidence level above 5σ within 1 hour. One possibility would be a flaring source.

The results of this work have been published in a MAGIC internal note (TDAS 03-05). They have been presented in the 19th European Cosmic Ray Symposium (2004) and the XXIX Biennial of the Royal Spanish Society of Physics (2003).

Part III

Analysis

Chapter 5

MAGIC Data Check and Quick On-Site Analysis programs

This Chapter is an overview of the MAGIC data check (MAGICDC) and Quick On-Site analysis (QOSA) programs. The first part contains a brief introduction to the MAGIC experiment with a detailed explanation of the telescope subsystems checked by the program. The second part describes both programs: how they work and their results. These complementary programs perform a continuous check of the telescope performance and the data quality, and a first analysis over the whole MAGIC data.

This program has been mainly developed by the Thesis Author.

5.0.1 Computing and networking

The computing system of the MAGIC telescope consists of a set of PC's that constitute an internal network connected to Internet (www.magic.iac.es) through an internal firewall [40].

The internal network consists of the subsystems PCs and the on-site analysis computers. All the computers save the subsystem data locally, sharing them through NFS access. The subsystems computers share the same operative system (OS) and software ("clones") and are connected to the internal network at 10/100 Mbytes, while the on-site analysis computers are also OS-"clones" between them but with a different OS from subsystem's computers.

All the subsystems night data needed for the analysis are copied together with the telescope raw data to a local computer that stores all the data taken. This computer is connected to the analysis computers through a 1 Gbit Ethernet connection in order to increase the speed of data access for the analysis program.

The program results are "published" in the Internet with access restricted to the MAGIC collaboration members through the MAGICDC web page at La Palma.

5.0.2 The standard analysis software MARS

The standard analysis software for MAGIC telescope data is called MARS (Magic Analysis and Reconstruction Software). It is a set of C++ (object-oriented framework) classes based on the well-known ROOT package developed in CERN. Basically it can be run inside the ROOT framework using the specific containers and tasks designed to analyze the MAGIC data or as compiled macros (MARS executables). Some of these MARS executables contain a Graphical User Interface (GUI).

ROOT is an object-oriented data analysis framework and it was agreed within the MAGIC collaboration to record the data and simulation files in a ROOT format. This root file has the structure of figure 5.1 and the information of the several "leaves" are explained in [27].

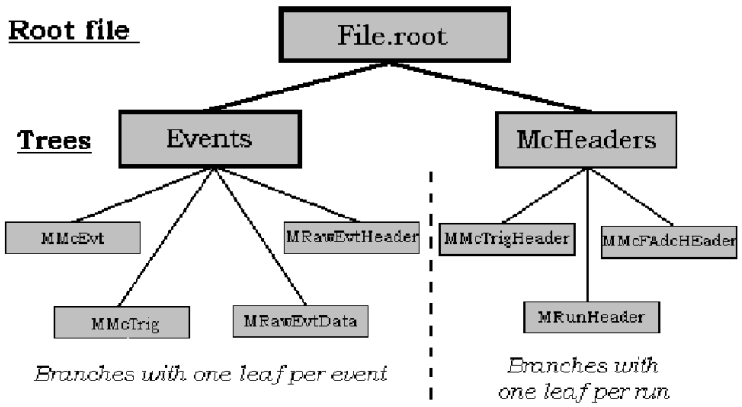

Figure 5.1: *Diagram of root_file structure [27].*

To analyze the MAGIC data in a standard way (section 5.1.5), MARS executables were used in the MAGIC telescope data check program. These executables, displayed as diamonds in figure 5.2 are the following:

- MERPP: converts the "raw" MAGIC data and ASCII format of MAGIC subsystems to ROOT package format. The output files have the ".root" extension.
- CALLISTO: calibrates the data. The calibrated files have the name-key "_Y_.root".
- SHOWPLOT: displays graphical information as Postscript file format (".ps").
- STAR: calculates the Hillas parameters. The executable output files has the name-key "_I_.root". They are so-called Star files.
- MELIBEA: applies the Random Forest matrices (section 5.1.5) to the Hillas parameters files. Its output has the name-key "_Q_.root". They are so-called Melibea files.

Most of these executables have input cards to modify the analysis parameters.

The analysis executables, Callisto, Star and Melibea, run based on sequences, where a sequence is defined as a set of data runs to analyze.

The data check and the on-site analysis programs only use the official, checked MARS release versions.

5.1 The MAGICDC: software package for the Telescope Data check

The MAGIC telescope consists of several subsystems, or telescope elements, which perform a specific task within the normal data-taking (section 1.5). The quality of the data depends on the good functioning of the telescope and therefore the performance of these subsystems. To check their behaviour and functionality, a program called MAGICDC (MAGIC Data Check) has been developed. This program runs automatically each morning after the night data-taking and extracts all the useful information about the telescope status.

The MAGICDC program consists of a set of subprograms (fig. 5.2), which carries out two main tasks: the first one is a check of the data reported by each telescope subsystem, the second one is a check of the analyzed data performing a first and quick analysis of the night data. This last feature of the program has been dubbed "On-Site Analysis".

5.1.1 Steering scripts

The telescope data check program runs in three 4-processor Intel Xeon at 3.06GHz computers (La Palma analysis computers). The MAGICDC program is managed through the Linux "cron daemon" using the standard defined linux crontab files. All the results and logs are saved into a local disc.

These crontab files launch two different jobs (C-shell scripts) (fig. 5.2):

- hal.csh: daily check and on-site analysis. The job is launched daily every 20 minutes from 9:00 a.m. to 20:00 p.m. (UTC) to look for and launch again unfinished checks or analysis jobs.

- monolith.csh: checks, for the last 7 days (default value), whether the data-check and analysis has finished properly; if it has not, the script launches the previous job (*hal.csh*) for the missing day. The number of days to review can be modified through a variable inside the program. This job is launched every day at a fixed UTC time (1:00 p.m.).

In both cron jobs *hal.csh* is launched giving as a parameter a specific date in the format "<year>_<month>_<day>" (all in numerical digits).

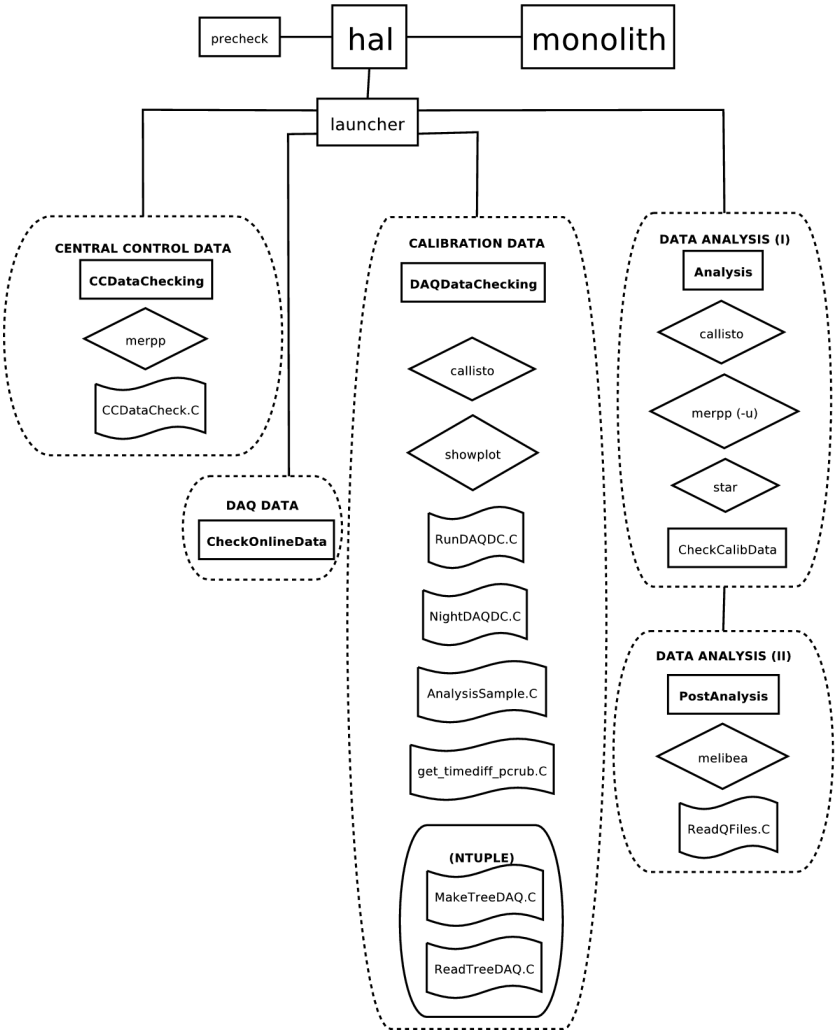

Figure 5.2: *MAGICDC program scheme.*

When the cron daemon launches the first job (hal.csh) the current date is used, while in *monolith.csh* the specified date to *hal.csh* depends on how many days you want to check.

The *hal.csh* job calls to the *precheck.csh* script which performs the following checks: if all the computers needed are switched on, if the storage directories and all the subsystem data are available and which kind of data checks should be done. This last check depends on the subsystem data available and whether any of the data check jobs has been done and finished properly. The result of the *precheck.csh* script is always an exit code. In the case of the first checks, or if all the data check jobs have finished properly, the program *hal.csh* exists with an error message (different for each exit code). For missing data check jobs or analysis, the *launcher* program is launched with the corresponding kind of data checks that should be done.

Depending on the exit code of the *precheck.csh* script, *hal.csh* calls the *launcher* script with a different set of parameters:

§1. Kind of data check: daq, cc, cal and ana (no excluding options). They can be launched all together for a complete analysis.

§2. Mode: auto, manual, plot and webpage.

§3. Day: "<year>_<month>_<day>"

The *launcher* script is the main script, which runs the check jobs for the different kinds of data (§1):

I. Central control data (cc option):*CCDataChecking* script (section5.1.2).

II. DAQ data (daq option):*CheckOnlineData* program (section 5.1.3).

III. Calibration data (cal option):*DAQDataChecking* script (section 5.1.4).

IV. Analysis data (ana option):*Analysis*, *PostAnalysis* scripts and *CheckCalibData* program (section 5.1.5).

The checking jobs mentioned above can run in different modes (§2):

- *auto*: corresponds to the mode launched by the "cron" daemon.
- *manual*: launches the data check of any day (you must specify the "Day" (§3) option).
- *plot*: only runs the executable or macros that create the plots.
- *webpage*: transfers the portable document format (.pdf) files with the result plots to the MAGIC web page at La Palma server.

An example of how the launcher program should be called:

$PROGRAM_PATH/launcher daqcccalana manual 2006_08_09

this command launches the whole data-check and analysis programs for 2006 August 9^{th}.

When all check jobs are finished, the program script sends (by e-mail) the corresponding program logs to the MAGICDC program developers and copies all the Portable Document Format (.pdf) files into the official MAGIC web page at La Palma (section 5.0.1).

The most important information shown by the MAGICDC program is checked by the MAGIC "daily-checker shift" who have to send a daily report about the MAGIC telescope status and, in case of problems, solutions should be sought by them or

the subsystems experts and be carried out by the shift workers in order to solve the problems for the next data-taking day.

All the MAGICDC program code can be found at the MAGIC repository.

The MAGICDC program is synchronized with another program that transfers the raw data to the MAGIC data centre and copies it to tape. Once the *monolith.csh* script checks the analysis of a given day and, if it finished properly, it writes an empty file into a local directory called <year>_<month>_<day>.osa-finished. If this file exists, the MAGICDC program gives its approval for the data transfer program to delete the MAGIC raw data locally at La Palma once the taping of the data has been finished successfully.

5.1.2 The central control data

The check of the central control data is, together with the DAQ data check (section 5.1.3), the first task of the data check to be carried out before any other one. This job will check the performance of all the MAGIC telescope subsystems involved in the data-taking, and will produce a first estimation of the night data quality as well.

Overview

All the subsystems are run and controlled independently by their own local programs but they allow the access (through TCP/IP protocol) to most of their functionalities and report all the useful information through the central control software of the MAGIC telescope (fig. 5.3), called *Arehucas*.

This program stores locally, at a rate of 1 Hz [43], all the subsystems reports in two different kind of ASCII files: one kind of file keeps the reports sent during the whole night, while the other kind contains the subsystems reports for each single run. In addition to these reports, specifically sent to the central control, each subsystem could have its own report, log and data check files.

CC data check job

The part of the MAGICDC program that checks these subsystems reports is called by the script *CCDataChecking*. This script joins all the night central control ASCII files, converts this joined file into a ROOT file and calls a ROOT macro, *CCDataCheck.C*, to read the root-format file and to display the corresponding subsystems report plots (section 5.1.2). These plots are classified depending on the subsystem: drive, camera and cooling, trigger, star guider, weather station and time.

The check plots of this part belong to two kinds: variable versus time, which checks the variable stability during the night of the subsystem, and variable versus any other variable to check previously known correlations between them.

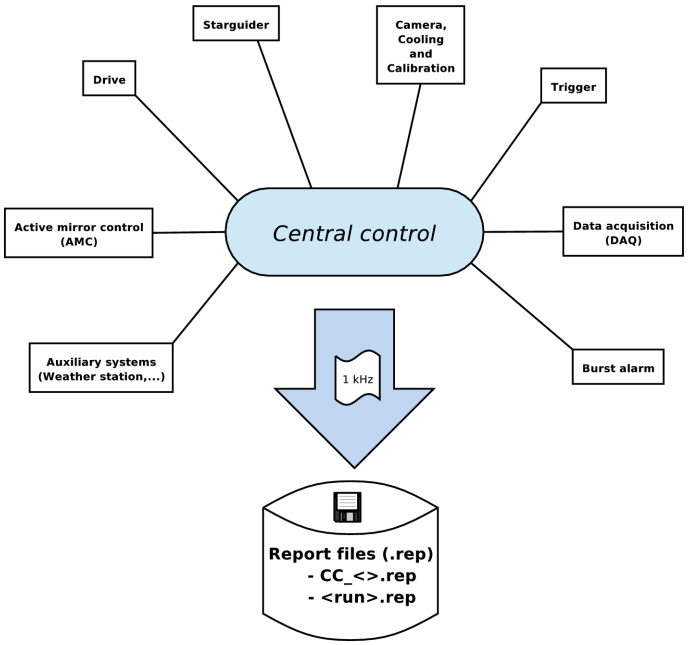

Figure 5.3: *The MAGIC subsystems scheme during normal data-taking. Each subsystem sends a report to the central control, which stores the information.*

CC data check plots

Drive checks As explained in section 1.5.1, the drive system controls the pointing and the tracking of the telescope, and it is checked through the reports sent to the central control.

The MAGICDC program checks the subsystem status during the night; the main ones are "tracking", "moving", "stopped" and "error". The tracking and the pointing of the telescope are checked, displaying the night evolution of the zenith angle of the telescope pointing position as well as the control deviation of the motors versus zenith angle of pointing position and its distribution during data-taking.

The tracking and pointing accuracy are very important for telescope pointing during the observation and for the resulting optical point spread function (PSF) of the data. For a PSF $\sim 0.1^\circ$ it is necessary to achieve a pointing accuracy $\leq 0.05^\circ$ (3 arc min).

The control deviation of the motors calculates the systematic errors in the tracking and pointing of the telescope. Three reference lines are displayed in this last histogram corresponding to the following safety limits: 1.2 (hardware limits), 0.6 (bending correction), and 0.25 (star guider correction) arc min.

Camera checks The MAGIC camera collects the light reflected by the mirrors within a field of view of $\sim 3.8^\circ$ $\emptyset$ through a set of photo-sensors and electronic sys-

tems (section 1.5.3) which form the camera subsystem: cooling, auxiliary systems, high voltages (HV), low voltages (LV), active-loads, lids, direct currents (DC) and calibration.

The MAGIC camera is fed by two external power supplies and active loads which divide the camera in two halves (A = sectors 1,2,6 and B = sector 3,4,5) (see fig. 1.16).

The Camera and Calibration program (so called *La Guagua*) controls all above noted camera elements, which reports their status to the central control as do the other MAGIC subsystems. A program routine called *Sentinel* checks the status of several camera elements to protect the camera against dangerous situations and, if necessary, prevents certain camera and calibration system operations [68]. The status of the subsystems is checked by the data-check program during the night with certain periodicity. The status, checked for each subsystem, can be:

- The HV of the PMTs: Error, Mismatch, Trip, Ramping, Off, Nominal and n/a.
- The DC of the PMTs: Error, Alarm, Hot, OK, Warm and n/a.
- The camera lids: Error, Safety Limit, Closed, Opened, Moving, Stopped and n/a.
- The cooling system: Error, Alarm, Off, OK, Temperature Warning, Condition warning and n/a.
- Sentinel: Error, All OK, Sun, Bad camera temperature/humidity, Hot camera, program control timeout and n/a.
- The LV power supply: Error, Alarm, Trip, Off, On and n/a.
- The LV power supply request: Off and On.

The *La Guagua* program also reports the values of several variables related to the different camera elements to the central control. The data-check program generates several histograms for each camera element to check its correct working through a set of reference lines:

- The high voltage (HV) settings of the power supplies and the applied direct current (DC) as function of time. This gives the night stability of the PMT HV between the cathode and the fifth dynode ($HV_{C-1}, .., HV_{4-5}$) for both camera sections A and B. The safety limits (1650 - 1750 V) are a compromise between the single photoelectron response from cathode to anode of the PMT and a low after-pulsing rate [68].
- The camera mean high voltage settings to the PMT photocathode versus time (fig. 5.4 on top).
- The trigger discriminator threshold settings as a function of time.

- The temperature and the relative humidity in the low voltage (LV) box versus time. The limits of the temperature in the LV box depends on the temperature outside but should be within 16°-26°.
- The high voltage and current versus time of the 360 V Active Load power supply of the 5th PMT dynode and anode, in addition to the independent 175V power supply of the 6th PMT dynode and anode for all the PMTs in the two camera halves A and B. The safety limits in the HV power supply (350-400 V and 170-190 V) and in the direct current (70-110 mA and 0-110 mA) are set to maintain the voltage settings (increasing the dynamic range of the phe) and a high current, even when there is a large electron multiplication.
- The time average of the HV (fig. 5.4 bottom) and threshold settings versus the pixel number as camera and histogram display.

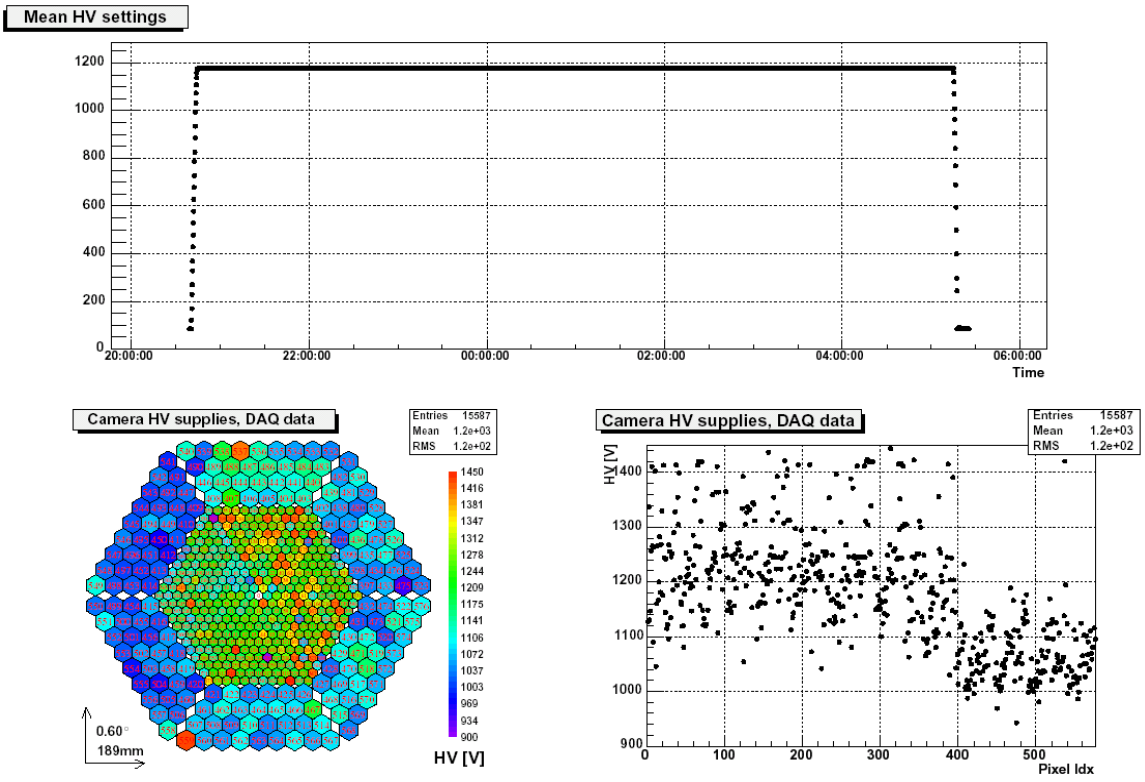

Figure 5.4: *HV settings report plots. Mean high voltage settings for the entire camera versus time (top) and time average voltage per pixel (bottom) shown both as camera (left) and histogram (right) displays.*

Another part of the camera report to the central control concerns the *cooling system* of the camera. To check its conditions, the histograms show the temperature

at the centre and the walls of the camera, the temperature of the optical drives and the cooling water deposit, as well as the relative humidity at the camera centre and walls as a function of time. The distribution of the optical drives temperature is also displayed but only during the data-taking time. The temperature at the camera centre and the optical drives (VCSELs) temperature are the most critical ones, being capable able of affecting the camera hardware and data quality. The stability of the system is tuned to temperature limits of $37^{o}\pm2^{o}$ in the camera centre [66] to guarantee the data-taking stability.

Trigger checks The MAGIC trigger system is based on a two-level programmable logic, as explained in section 1.5.4. The first level (L1T) consists of a 5 ns coincidences and a 4 next-neighbours logic. The second level (L2T) applies topological constraints for a coarse analysis [46], although is not yet operational and consists only on a trigger pre-scaler which scales the ratio of triggered events to be recorded.

To check whether this system behaves properly and the quality of the data, the MAGICDC program shows the trigger values of L1T and L2T versus time.

Due to atmospheric extinction changes with the zenith angle, the trigger rate changes also with the pointing zenith angle of the telescope. This dependence has been calibrated and fitted to the expression R_{trig} (Hz) $= 310\cdot\sqrt{\cos\theta}$ including the interleaved calibration events. This is used as the reference for checking the L2T trigger rate versus the zenith angle of pointing position. Due to the possible influence of the trigger rate by a noisy or dead pixel in the trigger logic, the night-mean (and rms) of the individual pixel rate (IPR) per pixel is also shown.

Star guider checks The star guider [33] is a subsystem consisting of a high sensitivity CCD camera which reports the pointing deviation of the telescope to the central control system. Comparing a 5 s exposure time picture of a 5° sky section with a star catalogue, the system calculates the drive system position offset with an accuracy better than 15 arcsec.

Through a bending correction algorithm, this system helps the tracking system to have a pointing precision of much less than 1 pixel size (0.1^{o} ∅), which is very important in determining the source position in the data analysis.

To check the telescope pointing stability, the MAGICDC program displays the zenith and azimuth miss-pointing and the CCD camera pixel (X and Y) that corresponds to the camera centre versus time. The maximum allowed limit for the zenith miss-pointing is 1 camera pixel (6 arcmin). The program also checks the number of correlated stars and the sky brightness from the CCD camera versus time.

Weather station checks The MAGIC telescope has its own weather station, located close to the experiment. The station data are read out every 40 seconds and the weather values are sent to a graphical display unit over the web. This web page

can be accessed publicly. As for the other subsystems, the weather station also sends a report to the central control with all the weather information.

The weather could affect the data but also the telescope's own integrity since it is not protected by a dome. To check the weather conditions, the telescope data check program displays the humidity, the temperature (fig. 5.5) and wind speed against the time, together with its corresponding safety limits of operation (humidity $< 90\%$ and wind speed $< 40 km/h$).

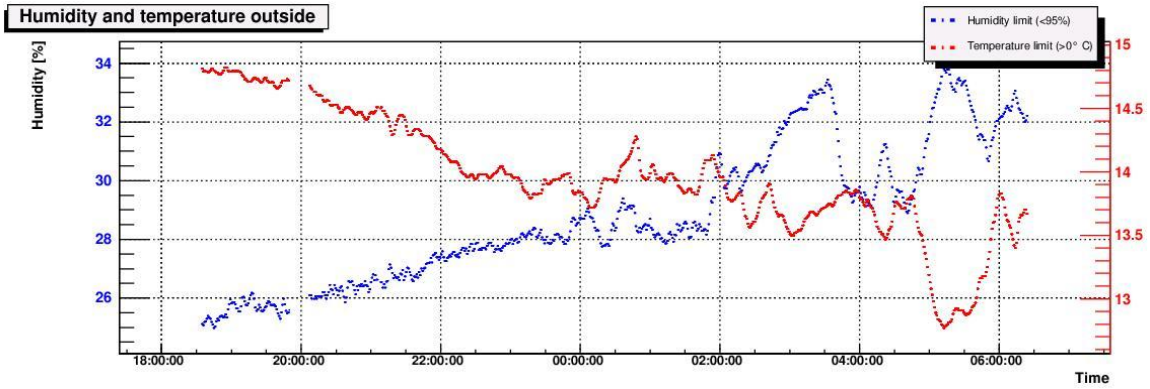

Figure 5.5: *Weather station report histograms. This plot shows the humidity (blue) and temperature (red) around the telescope versus time. The dotted lines correspond to upper limits for a safety telescope operation. Above these limits, the telescope must be parked.*

Time information checks The date and time information for a triggered event is determined on an absolute time scale, UTC (Universal Time) and added to the data in the DAQ readout process. The time stamp accuracy (200 ns) is generated by a calibrated atomic clock (Rubidium clock), a MAGIC specific module called TIC (Time Interval Counter), a HM8125 GPS Time/Frequency Standard and sub-sec NIM modules. The Rubidium-clock exhibits an unavoidable course error, which is corrected connecting the atomic clock with the GPS. The Rubidium-clock is adjusted in frequency and phase to the GPS clock pulse in a closed automatic control loop.

The MAGIC SSC (Sub-Second Counter) is based on a module which was already in use in the HEGRA experiment [113]. The CAMAC unit is adapted to a NIM cassette and provided with LVDS drivers for transmitting the information to the MAGIC DAQ system. The 5 MHz input signal is used as clock for a counter chain, composed by 3 8-bit binary counters with output registers.

Another NIM module is used to measure the difference in time between the Rubidium-clock and the GPS receiver. This information is sent to the central control as a report and is displayed by the MAGICDC program for the daily check. This difference must be always within 1.5 - 1.75 ms. In case of a larger difference, the

GPS-Rubidium clock must be synchronized manually. To check the telescope time stability the MAGICDC program displays the time difference between the GPS and the Rubidium clock versus time.

5.1.3 DAQ data

During the telescope data-taking, a DAQ subsystem performs a simple analysis of the recorded events. This analysis determines an average pedestal (from the low gain data) and the signal charge and arrival time for each event and channel. These values are sent as a report to the central control (section 5.1.2) and written to an ASCII file at the end of each run [76].

Up to now, the system reports used by *DAQOnlineDatacheck* program [1] can not be processed with the rest of the other subsystems report information. So another program has been developed which reads these (run based) ASCII files written into a local DAQ program subdirectory, joining it with the other subsystems reports (through central control report files and displaying the DAQ data check information [183].

This kind of data check is run giving the "daq" option to the *launcher* script.

A more detailed explanation about the contents of each output file and the program can be found at [183].

5.1.4 Calibration data

The next step of the data check program is to check the response of the entire light-detection and amplification chain to get the correspondence between the digitalized information and the incident number of photons from the Cherenkov light. This is done through the data calibration process, which determines the conversion factor between digitized FADC counts and incident photons, and the arrival time delay for each pixel [72].

The calibration system

The MAGIC telescope requires a precise and regular calibration system of the camera and the readout chain over a large dynamic range. This is achieved with a number of ultra-fast and powerful LED pulsers inside a pulser box located at the centre of the mirror dish. The LEDs illuminate the camera PMTs with $\sim 2\%$ non-uniformity. A pulsating mode (pulser box) is used to calibrate the detector response to Cherenkov light with 2 ns pulses, while a continuous mode is used to calibrate the response of the DC readout to background light (star and moonlight). The absolute light flux is calibrated using three so-called blind pixels [2] hosted at the camera and a

[1] Program developed by P. Liebing and J.A. Coarasa (MPI, München)

[2] The "blind" pixels have an optical attenuator in front of the PMTs such that in case of a calibration pulse flash a photoelectron is detected only in 10-30% of all triggers.

calibrated PIN diode located at 1.1 m distance from the pulser box.

For the *calibration process* two kind of runs are taken consecutively: the first one is a pedestal run, which consists of 1000 events triggered by a signal generated by the calibration box and sent to L2T. These events should contain hardly any Cherenkov pulses. The second one is a calibration run, which contains 4096 events sent by the calibration box following a number of actions predefined by a calibration script.

During the first period, the MAGIC camera data itself was used to measure the absolute number of photons/electrons generated by the light pulser by using the so-called "F-Factor" method ($N_{phe} = F^2 \cdot \mu^2/(\sigma_1^2 - \sigma_0^2)$). However, the results of this method change with the unknown degradation (QE and phe collection efficiency) of the PMTs with time (F constant) and do not take into account the transmission efficiency of the light guides.

For this reason two alternative methods are now used to calibrate the individual camera pixels with respect to the amount of photons produced in each calibration light pulse, the so-called "Blind Pixel" and "PIN-diode" methods [72] (section 5.1.4). As well as the ordinary PMTs, the blind pixels have several systematic uncertainties, like insufficient knowledge of the PMT's photoelectron collection efficiency and in particular the long term variations of the transmission coefficient of the plexiglas window due to dust. The PIN-diode provides us with an additional measurement of the absolute light flux, irrespective of these effects.

Several signal reconstruction algorithms have been studied to extract the charge and arrival time from the calibration and data runs with the highest resolution and minimum effect of the noise [72] [19]. The best extractor algorithm for low energies and timing information is the so-called "Digital Filter" [18]. This algorithm reconstructs the amplitude and time position (FADC slice) of a signal from a known pulse shape, determined basically in the signal digitalization (fig. 5.6).

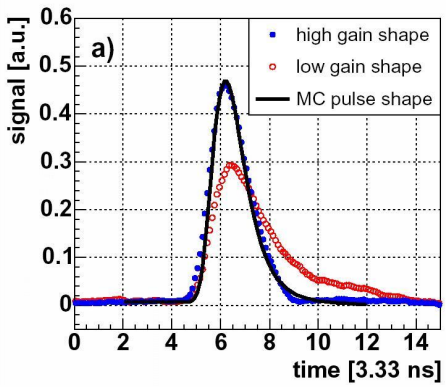

Figure 5.6: *Average normalized reconstructed high (blue) and low (red) gain pulse shapes and pulse shape (black) used by the "Digital Filter" algorithm from MC simulations [18].*

This extractor is currently the default in the corresponding MARS release version used in the data check and the on-site analysis program.

Calibration data check job

The script, which is responsible for the calibration data check, is named *DAQDataChecking* (fig. 5.2) and is called through option "cal" on the *launcher* main script. It consists of three logical parts:

I. The first task of the *DAQDataChecking* script is to define the Callisto-sequences (section 5.0.2). To do this, the script reads the central control ASCII files which contain a summary of the night data-taking. Then, a night summary ASCII file is created with the variables needed by the MAGICDC program. From this night summary ASCII file, the program extracts run information to constitute the analysis sequences (section 5.1.5).

   As explained before, to extract and check the calibration constants it is necessary to have a pedestal-calibration pair of runs. With each of these pairs, a calibration-sequence for the *Callisto* MARS executable has been defined. These calibration-sequences are different from analysis ones because no data runs are involved in their definition. *Callisto* is run on the calibration-sequence: it calculates the calibration parameters and saves them into a Root-format file (calib.root). The MARS executable then reads this file *showplot* making the calibration data check plots (see next section for a description) and saving them to a Postscript file.

   Finally, for each sequence the *RunDAQDC.C* macro is run and saves all the calibration-sequence information from pixel calibration into an ASCII file.

II. The second step is to run a set of macros to perform several other checks of all the night calibration constants calculated already (calib.root files of all sequences):

   - *NightDAQDC.C*: Displays the calibration parameters evolution versus time. It can be used to see the evolution of these values over the whole night [123]. The plots are saved to a postscript file.
   - *AnalysisSample.C*: Creates an ASCII file (samples.txt) with all the information of the night sequences. It will be used in the analysis data check (section 5.1.5).
   - *get_timediff_pcrub.C*: Calculates the time difference between the PC and the Rubidium clock for each calibration event. The results are displayed in a Postscript and in an ASCII file.

III. The final set of macros (fig. 5.2) corresponds to the manipulation of a ntuple which accumulates and stores the most relevant information about the calibra-

tion (*MakeTreeDAQ.C* macro) and then it is saved (*ReadTreeDAQ.C* macro) into a Postscript file. [53].

The calibration data check plots

As explained in the previous section, the MARS executable *showplot* creates a Postscript file with the calibration results saved in the corresponding calib.root file of a given calibration-sequence. Here follows a description of these calibration result plots.

All the reference values for the checks are extracted from a standard file (callisto.rc), within the MARS release version (defined by the calibration experts for each version of the MAGIC calibration program).

Pedestals from pedestal run The first page displays the mean and rms (from pedestal run) of the pedestal charge distribution for each pixel versus the pixel index both as a profile and as a camera display, in addition to their camera distributions. The mean and rms camera distributions are fitted to a Gaussian. In the case of the rms we distinguish between the inner and outer part of the camera (or pixels) and we sum up the number of pixels lying 4σ away from the distribution mean. Those pixels below -4σ are the so-called "dead" pixels and those above +4σ are the "noisy" pixels.

The reference values correspond to already calibrated values for pedestal runs taken with *ClosedLids* (14.6±1.7 FADC cts/slice for inner pixels), pointing to an *ExtraGalactic* (14.9±5.6 FADC cts/slice for inner pixels) and to a *Galactic* source (15.3±6.9 FADC cts/slice for inner pixels). The higher reference values of the pedestal rms for Extragalactic and Galactic sources is due to the different contribution of the NSB, which is not present when the lids are closed.

Pedestals from the signal extractor The Digital filter extractor [18] uses the pixel content for which the difference between the maximum and minimum FADC slice content is less than 40 FADC counts, as pedestal events. The extracted pedestal is updated for every 500 of these "pedestal events". As in the previous plot, the histogram of this second page displays the mean and rms of the pedestal charge distribution but from the calibration extracted signal where the pedestal has already been subtracted. Therefore, the plots are similar to those in the first page but in this case the mean pedestal is expected to be 0 (reference line) for all pixels and the camera pedestal distribution is centred at 0.

The rest of reference values are the same as in the previous histogram.

PIN Diode The third page of the calibration results file displays the PIN diode calibration charge distribution (in FADC counts) together with a Gaussian fit and its results.

The PIN-diode is located at 1.139±0.005 m from the calibration box at a viewing angle of 4°. With a 2% of LED emission uniformity, it measures the absolute light flux produced by the calibration pulses, independently of the variations of the plexiglas transmission coefficient and the uncertainties in the knowledge of the PMT QE.

The PIN-diode itself is calibrated using the photoelectrons distribution of two radioactive sources (^{241}Am and ^{133}Ba) emitting known γ-emission lines. The calibration will provide us with the conversion factors between FADC counts and number of phe. Once the PIN-diode is calibrated, the total amount of photons emitted by the light pulser can be known from the mean FADC counts collected by the PIN diode per calibration pulse extracted from the fit.

Blind pixel The forth plot shows the charge distribution (FADC counts) of the three blind pixels and a legend with the fit results.

A blind pixel consists of a PMT blinded with a light filter and a 1 cm^2 diaphragm in order to extract the single photoelectron spectra reducing the number of incident photons. The resulting number of photoelectrons during a calibration pulse is expected to follow a Poisson distribution with a mean value lower than one. The fit to this distribution yields the rms (σ_k) and the mean number of photoelectrons (ν_k) [72]. Because of the single phe response of the blind pixel, it is possible to calculate the current F-Factor constant and to compare it with the one used in the F-Factor taken from lab measurements.

Knowing the number of phe per pulse (ν), the emitted LED light spectrum provides us with an absolute calibration, computing the mean number of incident photons per pulse at the camera plane as:

$$N_p h = \frac{D_{BP}^2 \cdot \Omega}{A_{BP}} \frac{\nu}{T_{plex} \cdot QE \cdot \eta_{col}} \tag{5.1}$$

where Ω is the solid angle of a 2° LED emission cone, $A_{BP} = 1$ cm^2 is the geometrical area of the filter, $D_{BP} = 18.26 \pm 0.03$ m is the distance of the blind pixel to the diffuser plate of the calibration box, T_{plex} is the transmission coefficient of the plexiglas in front of the camera, QE is the mean quantum efficiency of the photo-cathode (including the filter) and η_{col} is the mean collection efficiency of the phe to the first dynode [72].

Currently the three blind pixels are located just outside the last outer pixel ring within the 2° camera radius and at 120° from each other.

Arrival time The fifth calibration check plots represent the distribution of mean arrival times of the calibration signal events (high gain digitized slices), defined as the FADC slice of the signal maximum, as well as its behaviour versus time (seconds). The histogram is separated into inner and outer pixels.

The reference line corresponds to the reference default values on the callisto.rc of the MARS release version used.

Calibration signal charge The sixth plot shows the distribution of the calibration signal mean charge (in FADC counts) and its behaviour versus time (seconds) for inner and outer pixels, separately.

A reference value (from callisto.rc file) with the charge of the corresponding to the expected light for the specific calibration script is displayed on it. For example, from "10 LED UV" calibration pulse (the default one), there should be 278 FADC counts for inner and 282 FADC counts for outer pixels.

Fitted charge In page number 7, the mean (in FADC counts) and rms of the fitted calibration signal charge versus camera pixel number is displayed both as a profile and as a camera display. The same page also shows the distribution of the fitted mean charge with labels with the number of "low" and "high" gain pixels and the *flat-field precision* [3], as well as the distributions of the rms (for inner and outer pixels) with the number of dead and noisy pixels. The "low" and "high" gain as well as the dead and noisy pixels are the integral between $\pm$ 4σ of the fitted distribution. The number of photoelectrons is computed by the F-factor method.

The last plot displayed in this page corresponds to the number of photoelectrons versus camera pixel number, displayed as a profile and as a camera display.

Conversion factor Page number 8 (fig. 5.7) shows for each of the calibration constants, the constant average versus pixel number in profile and camera display, and the distribution for inner and outer pixels. The three calibration constants represented are: the conversion factor from F-Factor method (mean value: 0.14 for inner and 0.4 for outer pixels), the mean quantum efficiency obtained with the F-Factor method (mean value: 0.8 for inner and 3.8 for outer pixels) and conversion factors from equivalent phes (mean value: 0.14 for inner and 0.56 for outer pixels). This last constant is the conversion factor from F-Factor method normalized to the Cherenkov shower spectrum.

The default reference values in the callisto.rc file change with the telescope performance. The values between brackets correspond to the default values in December 2005 of the three calibration constants.

Absolute times Page number 9 (fig. 5.8) shows the mean and rms values of the number of FADC slices of the signal peak of the calibration events versus the pixel number, in a profile and a camera display. It also displays the distribution of the rms for inner and outer pixels together with the number of outliers: "early" and "late" pixels (pixels at $\pm 4\sigma$ of the fitted mean of the mean arrival time per pixel)

[3]The flat-field precision is defined as the rms of the distribution fit divided by its mean and multiplied by a factor 100. A 100% flat fielding guarantees a uniform response of the entire camera PMTs.

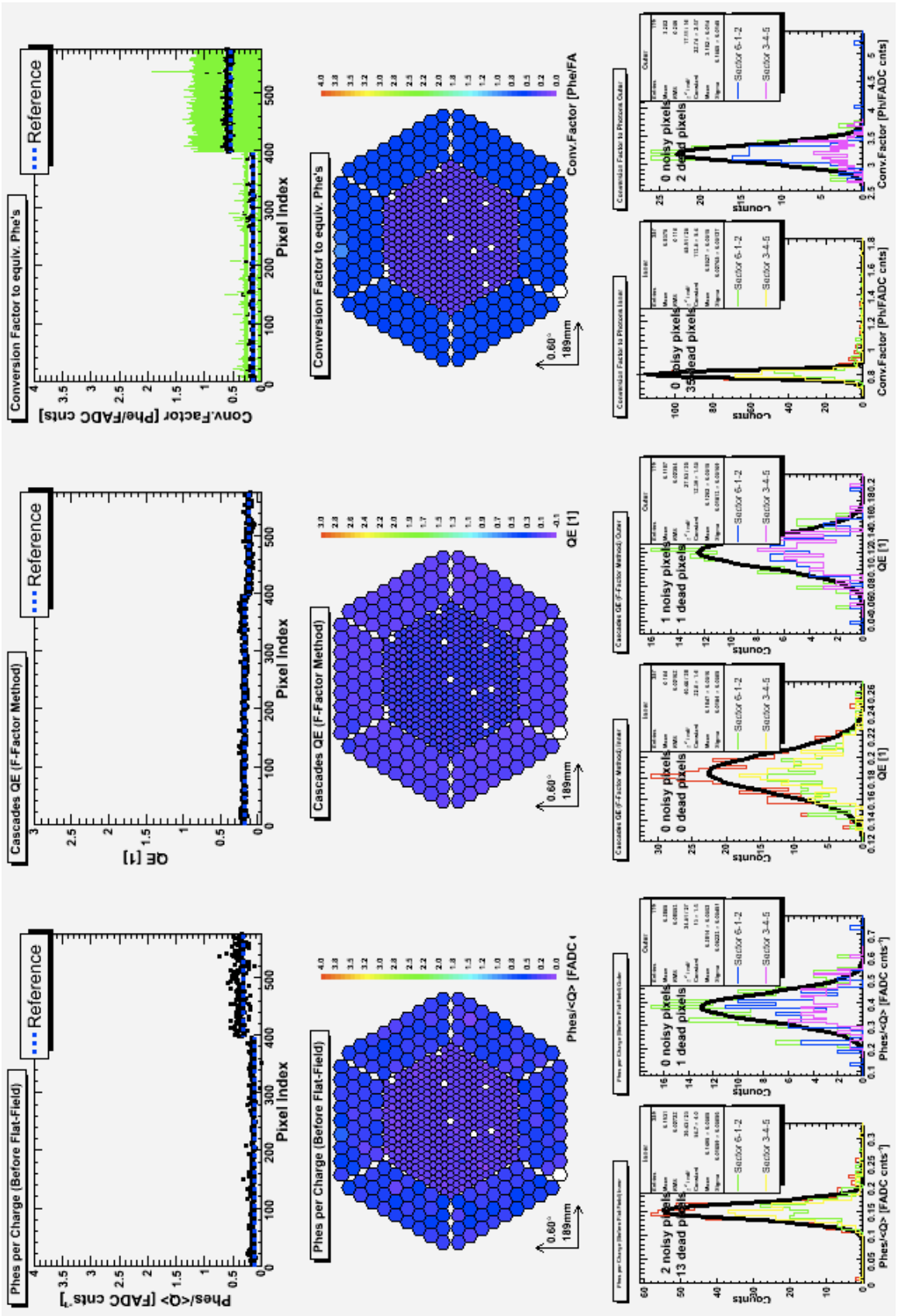

Figure 5.7: *Calibration constants. From top to bottom: the calibration constants average versus pixel index as profile and camera display, and the distribution for the following variables: number of photoelectrons per charge (phe/FADC counts), QE and conversion factor (phe/FADC counts).*

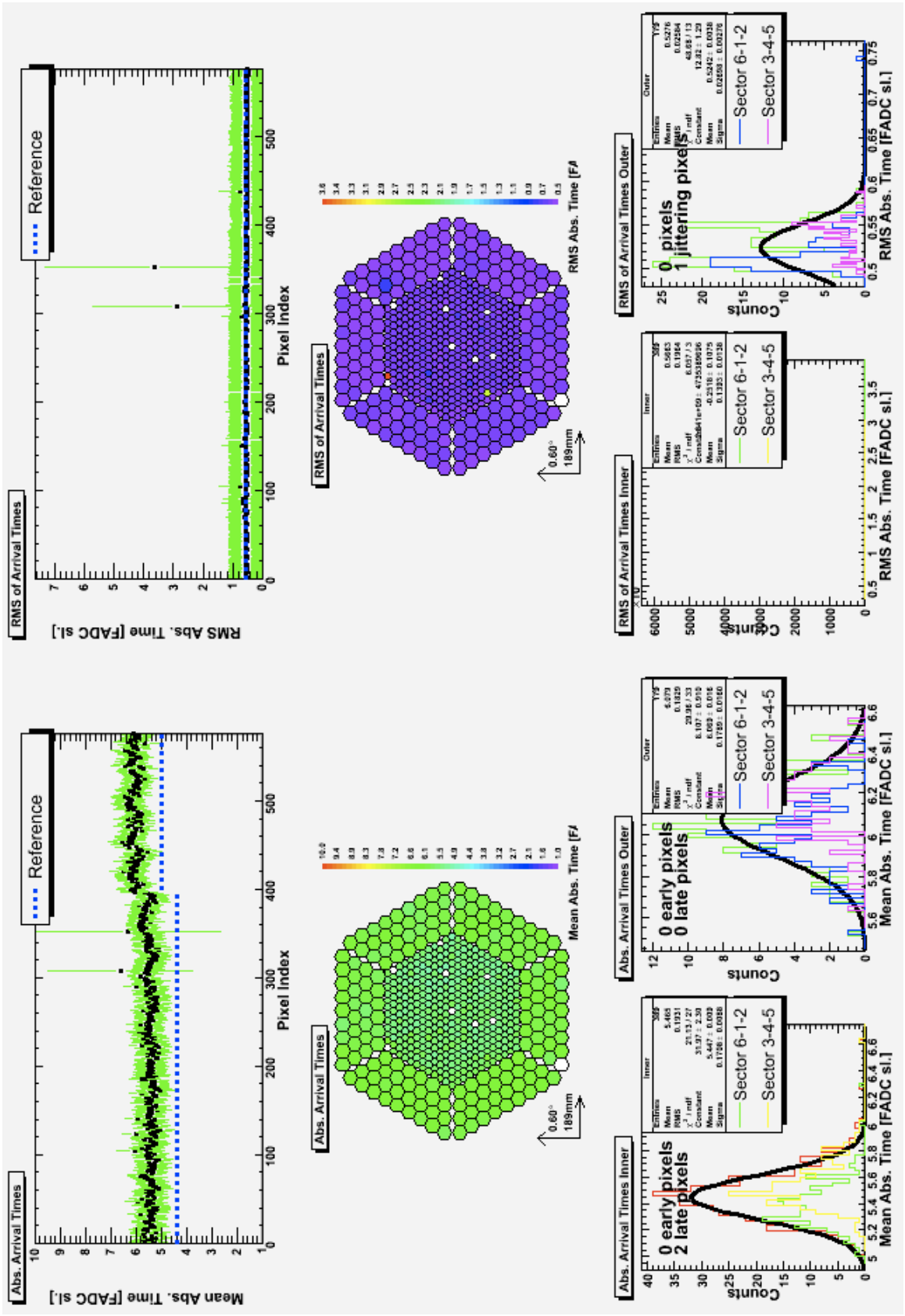

Figure 5.8: *Arrival times (FADC slice). Page displays from top to bottom: Mean and RMS of "arrival" FADC slice in profile and camera display and their distributions (for the inner and outer pixels).*

respectively, as well as "too stable" and "jittering" pixels (at $\pm 4\sigma$ of the average of the mean arrival time rms).

The typical arrival time peaks at the FADC slice 4.5±0.5 for the inner and 5.0± 0.5 for outer pixels, and their values are extracted from callisto.rc file.

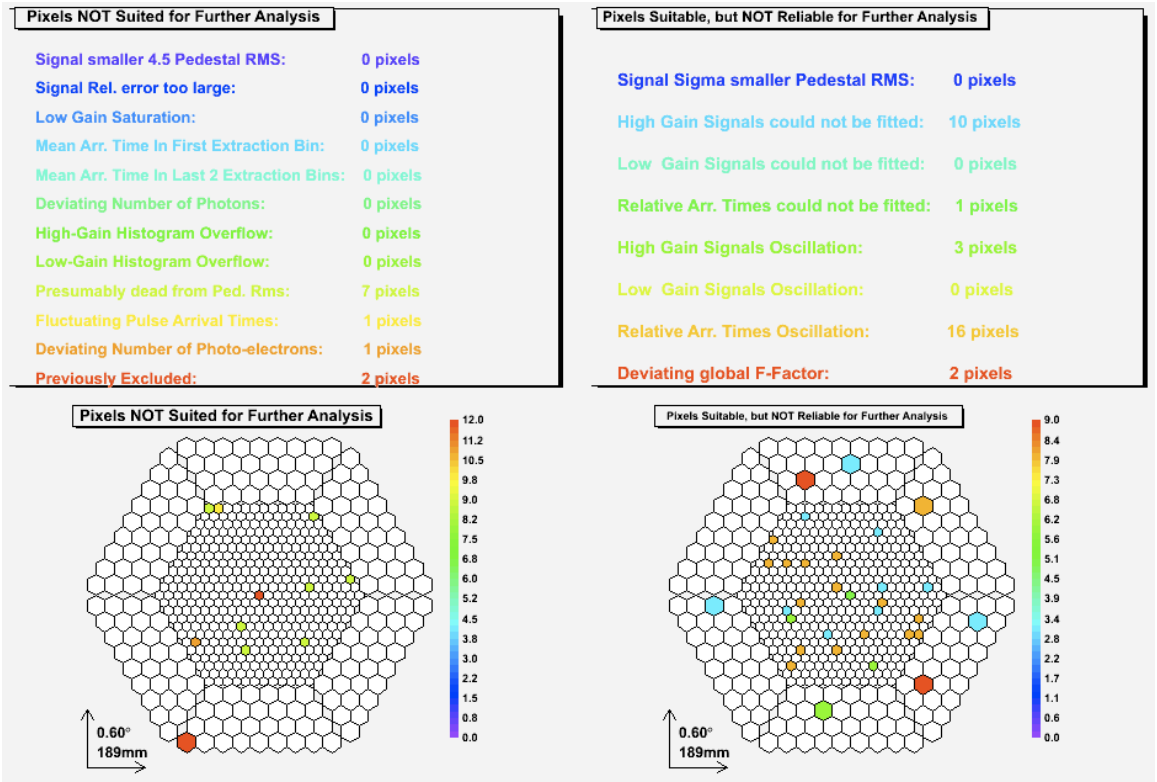

Figure 5.9: *Defective pixels. Page displays a legend with information about the calibrated defective pixels and a camera display showing the corresponding pixel by means of colour-defect criteria. On the left the "non suited pixels" and on the right the "non reliable" pixels.*

Defective pixels The tenth page (fig. 5.9) shows the defective pixels found in the calibration process. A legend is shown with the criteria (in different colours) to classify the pixels into "non suited" and "non reliable" pixels [72]. They are shown with the same colour criteria in a camera display.

The pixels marked as "non suited" are not used in the further analysis to parameterize the images, while the "non reliable" pixels will be replaced in the image cleaning analysis process by the mean signal of their surrounding neighbours.

Relative times The last page displays the mean time delay (FADC slice) and its rms per pixel in a profile and a camera display. All the relative times are calculated

with regard to pixel number 1 (hardware number = 2). The distribution of the camera mean and rms for inner and outer pixels is also shown with the number of early and late pixels, as well as the "too stable" and "jittering" pixels.

The reference of the relative arrival time for inner (-0.23±0.15 FADC cts) and for outer pixels (0.39±0.13 FADC cts) corresponds to the reference default values of the displayed variables (from the callisto.rc file).

5.1.5 Data analysis: On-site analysis

In order to have an initial idea about the quality of the nightly MAGIC data, one needs to analyze the data in a simple but robust and fast way. This is done by the so-called "on-site analysis". The on-site analysis provides the first calibrated files to the MAGIC collaboration. It will also extract calibration and analysis parameters to check the quality of the data as well as display the first analysis plots. The analysis steps are detailed figure 5.10.

The analysis process

The first step in the data analysis is to calibrate the data runs. In section 5.1.4 the extraction of the calibration parameters (mean N_{phe}, conversion factors and time delay) from a first pair of pedestal-calibration runs was explained. The signal extractor algorithm is the same for calibration and data runs and calculates the total charge and its arrival time for each pixel. The extractor algorithm subtracts the pedestal computed from the non-signal region, extracts the signal from a given sample range and finds the time of the signal maximum (section 5.1.4).

Because of observed variations in the gain of the electronic chain (specially the PMTs) at very different time scales, an external calibration trigger has been included to be able to update all the conversion factors during the data-taking, it consists of 50 Hz calibration events interleaved with normal data. Therefore, during the data-taking the calibration constants are updated within the current data file and applied to the next one. The time delay is only calculated once (using the pedestal and calibration runs) whereas the conversion factors are updated every 500 *interleaved calibration pulses* (i.e. every 10 seconds of data-taking) and the mean N_{phe} is updated every 5000 pulses.

The DAQ takes care to stop a data run every time that a predefined file size (954 MBytes) is reached. At the end of the sequence, the last updated information is saved in a "signal.root" file, which will be used, for the consecutive sequence if there are no previous calibration-pair runs. When the sequence finishes, another sequence starts with a new set of data runs, but no new calibration-pair is taken unless they are strictly necessary (calibration or trigger subsystem failure, completely different pointing position, etc.)

The second step is to clean each recorded event candidate by removing as much background noise as possible and parameterize the image using the Hillas parameters [91]. To remove the background contribution we have to reach a signal-noise compromise performing a two-step image cleaning process. The data check program uses the default image cleaning in the "star.rc" configuration file of each MARS release version (currently Standard Absolute 10-5) [155].

The third step is to classify the events γ-like or hadron-like through a γ/hadron discrimination method. The separation criteria is based in the difference in the image parameters of γ-ray and hadronic showers. The highest background rejection is achieved by using statistical learning methods (section 6.4). The standard method used in the MAGIC collaboration is the Random forest (RF) method [32]. Through this method, a hadronness parameter value is computed for each event of real data and included as another image parameter for analysis cuts. For computing time optimization reasons, the analysis data check program applies already computed RF matrices for different zenith angle ranges, because the RF training takes a lot of time, and it really depends only on the zenith angle range of the MC and Off data.

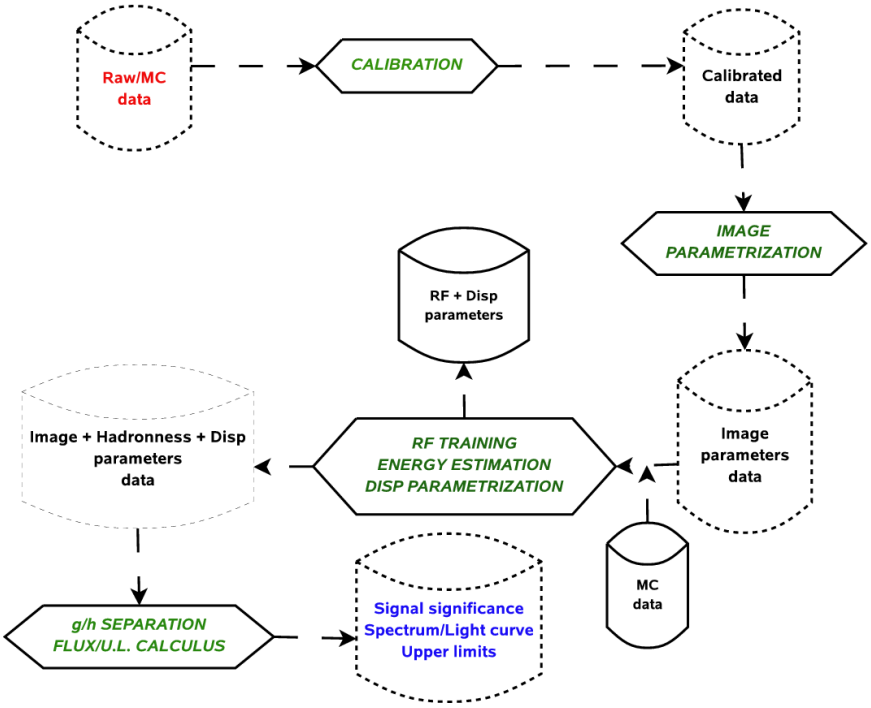

Figure 5.10: *MAGIC standard analysis scheme.*

MAGIC takes data in two different *observation modes*: On-Off and Wobble. In the first mode, the telescope points towards the source position (On) and towards a background position in the sky within the same zenith angle range and LONS level as the On data. The On and Off data are taken separately in time but within the

same telescope performance period of time. The second observation mode, "Wobble", consists of taking simultaneously the On and the Off data pointing the telescope at a region distant 0.4° to the source position. Due to the decrease of camera sensitivity with the increase of the distance from camera centre, this radius value implies a reduction of $\lesssim$40% in the observation sensitivity referred to On observation mode [127]. In both observation modes the data are analyzed in the same way by the program.

Analysis data check job

As shown in section 5.1.1, the scripts *Analysis* and *PostAnalysis* perform the analysis data check part on the MAGICDC program, calling the *launcher* with the "ana" option.

The *Analysis* script reads the night sequences information saved by the *DAQDataChecking* script into the "samples.txt" ASCII file.

An analysis sequence is constituted by a set of consecutive data runs belonging to the same source and observation mode. As explained before, for the calibration one needs the pedestal-calibration pair of runs taken inmediately before the first data run of the sequence. If this pair does not exist, the calibration parameters, updated from the last run of sequence and saved at a Root file (signal.root), are used.

For each sequence set of data runs, the *Analysis* script runs the following MARS executables: *Callisto* to calibrate the data, *Merpp* (with -update option) to include all the subsystems information into the calibrated .root files, and *Star* to calculate the image parameters. This script also launches the *CheckCalibData* script, which will be introduced in the next section 5.1.5.

Finally, the *PostAnalysis* script is launched. It will run the *Melibea* MARS executable and execute the *ReadQFiles.C* macro to display the first source results. The result plots correspond to the same source and observation mode. These plots are commented in section 5.1.5.

The log files of the *Analysis* and *PostAnalysis* scripts are saved together with the Analysis results while the PostAnalysis results are saved into a subdirectory (called Melibea) in the same parent directory.

Analyzed data check plots

At the end of the *Analysis* script, the *CheckCalibData* [4] script is launched. This script runs the *checkcalib* ROOT-compiled macro, which processes the calib.root and signal.root files produced during the calibration (section 5.1.5). These files contain the calibration constants and the last update of them. The calibration parameters used in the analysis can be checked by reading those files.

Running the data check over the calib.root files, one calculates the average of the calibration parameters for each part of the camera (inner and outer) and each

[4]Program developed by P. Liebing (MPI, München)

group of pixels (suitable and reliable) from the calibration run. Applying additional cuts [184], the quality of the calibration runs is checked and the corresponding flag is set.

All the previously calculated variables stored into ASCII files are saved also in a ntuple. The values of the ntuple are displayed in a Postscript file.

Plots of the on-site analysis results

For each source and observation mode, the results of a rough analysis are extracted in order to check the quality of the taken data and possible detection of a source.

As was pointed out in section 5.1.5, the program applies always the same standard image cleaning (Absolute 10,5) and performs the same analysis cuts (for details see chapter 6). These cuts are:

- *Basic cuts*:
  - Sparks: log10(Conc2)<(1.75-log10(Size))*0.369
  - Camera geometry: Leakage 1 < 0.1
  - 5NN trigger topology: NumCorePixels > 5
- *γ/hadron separation cuts*:
  - Analysis energy slide: Size > 300 phe
  - 0.2^o < Dist < 1.0^o
  - Dist < 1.2 + 0.3*(log10(Size) - 3)
  - Hadronness < 0.15
  - NumIslands < 3
  - Width/Length < 0.7

A very basic cut of Size > 60 phe is applied to all analysis result plots due to the basic software trigger condition (see chapter 6).

The information about the cuts is printed in the first page of each project [5] results Postscript file.

A description about the analysis results plots is given next:

Project information The first page shows information about the analysis parameters of the project: date, observation time (min), source and project names, source and telescope coordinates (right ascension and declination), mean alt-az coordinates, data runs range, cleaning method and levels, and basic and γ/hadron separation cuts (detailed before).

[5] A project consists of a set of a source plus an observation mode. In On observation mode, the project name matches with the source name. In Wobble observation mode, the project name is different for each of the wobble positions.

Hillas parameters after basic cuts The second page displays the distributions of the image parameters: Alpha (º), Width (º), Length (º), Distance (º), Conc2 and logarithm of Size (# phe in the image), before basic cuts.

Data check plots before basic cuts The third page shows the distributions versus logarithm Size (phe) of the Conc1, Width (º) and Length (º) image parameters. The distribution of Conc1 (top on the left) shows the *sparks events* [6] . The sparks events correspond to those points above the "sparks cut" red dotted line also displayed in the distribution histogram and its formulae is displayed in the information figure (first document page).

A cut of Size > 60 phe has been applied to these plots.

Image parameters before and after γ/hadron separation cuts Page number 4 shows the Hillas parameters distributions Width (º), Length (º), Dist (º) and logarithm Size (phe) before and after γ/hadron separation cuts. The alpha parameter distribution is displayed only after cuts, together with a fit and a summary of the significance of the signal referred to the camera centre. The events centre of gravity is also displayed but only after γ/hadron separation cuts.

False source plot The fifth page (fig. 5.11) displays the false source plots in sky coordinates (hour angle and declination) referred to the telescope pointing position (point 0,0 on the sky). These figures are calculated computing the significance (top-left), the number of excess (top-right) and number of ON events (bottom-right) of the alpha distribution for each sky position. The background is taken from the alpha distribution between 30°-90° while the signal is extracted with alpha $< 15°$. The distribution of significances is also displayed (bottom-left) to check that the distribution of significances in the false source plot is indeed a Gaussian centred at zero and rms ~ 1.

The maximum of the significance distribution for a detection should be at the source position in the sky. In the ON-OFF observation mode, the source is at the telescope pointing direction (the centre of the false source plot). However, in wobble observation the telescope does not point to the source so the maximum is not expected at the centre. To check a possible source detection at wobble mode, a marker (filled star) corresponding to the source sky coordinates is also displayed (fig. 5.11).

Source rate after basic cuts Page number 6 shows a display of the mean (for the first 500 events of each run for saving time) analysis rate (Hz) versus time after

[6]The *sparks events* are caused by a discharge of the high tension of the PMT's photocathode through the glass envelope to the ground via the metallic layer of the Winston cone. The resulting spark is reflected in the plexiglas illuminating the closest neighbour pixels. The sparks events will be characterized by high values of size and high values of most compact conc parameter.

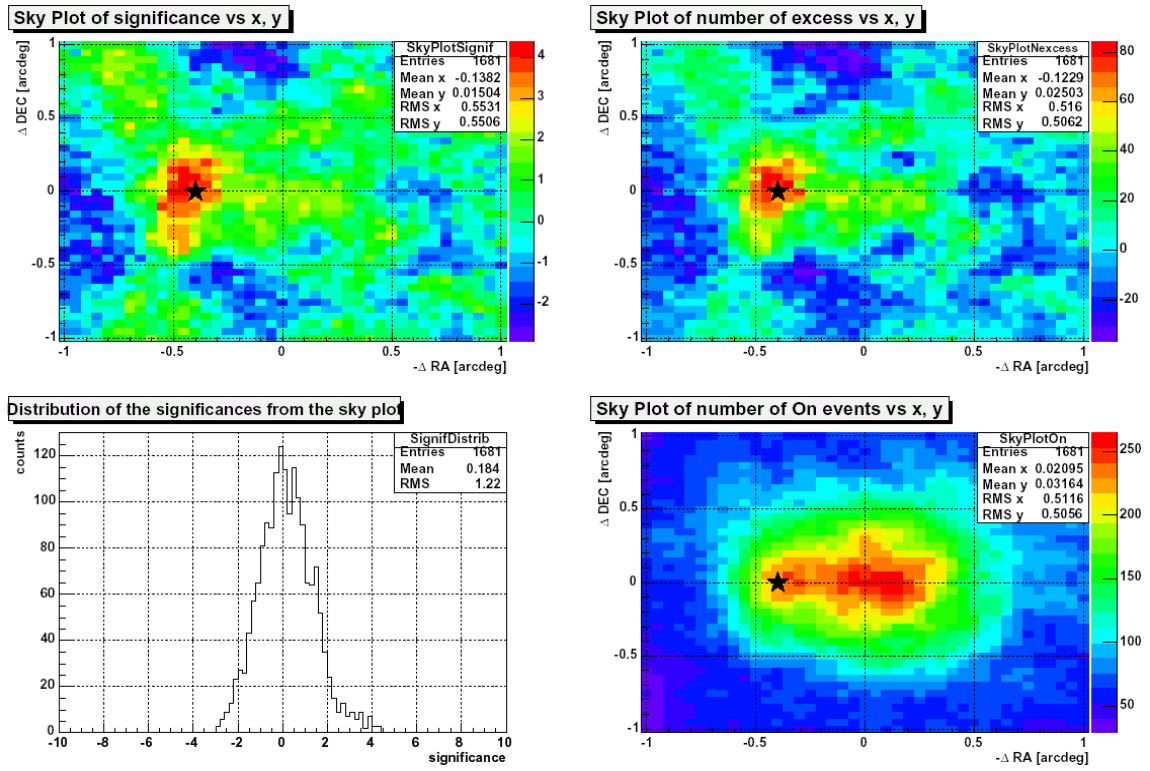

Figure 5.11: *False source plots on sky coordinates (hour angle and declination) referred to the telescope position. From top to bottom: significance versus sky point (left), number of excess events (right), significance distribution (left) and number of ON events (right). In the last plot, the star corresponds to the source position in the sky.*

basic cuts. Only the cut Size $>$ 60 phe is applied.

Camera homogeneity Page number 7 (fig. 5.12) shows a check plot of the camera homogeneity. (Top) The number of events before (red) and after (blue) cuts versus the camera angle defined as $\phi = atan2(MeanY, MeanX)$. (Bottom) The centre of gravity and the distribution of events versus camera position of the shower centre, before and after cuts, is shown.

Only the cut Size $>$ 60 phe is applied to all plots.

Muons analysis results Muons are created in great amount in cosmic ray showers. They emit Cherenkov light that hit the telescope reflector resulting in rings or arcs (for muon impact distance of $\sim$ 9 -120 m) in the MAGIC focal plane. The relative broadening for the image of these rings in the camera, compared with MC simulations can be used to calculate the telescope optical PSF with an error of $\sim$ 15% [114]. Also the reflector light efficiency can be calculated with an accuracy of $\sim$ 3% comparing

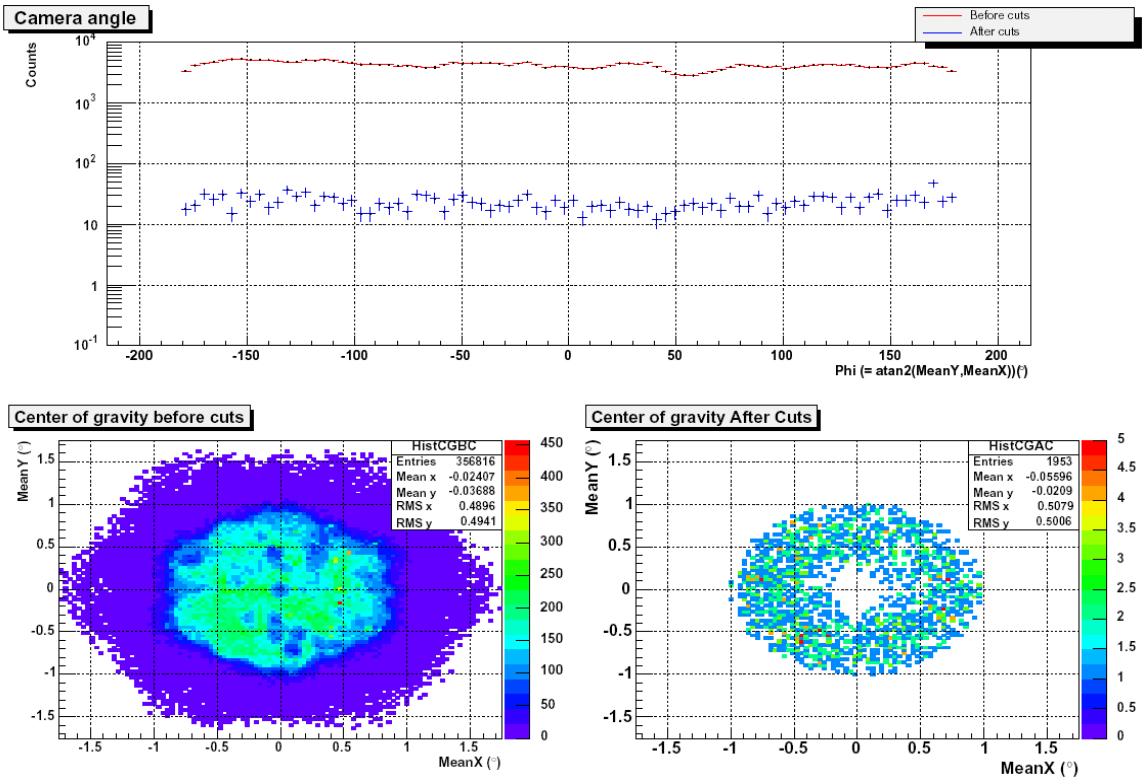

Figure 5.12: *Camera homogeneity histograms. Top: Number of events versus camera angle ϕ before (red) and after (blue) cuts. Bottom: Centre of gravity before (left) and after (right) cuts.*

the total light of muons from real data and MC simulations. The last page shows the absolute calibration of telescope characteristics through the use of muons images parameters. It displays the distributions of the radius (°) and the arc width (°) of the muon circles identified in the data. The profile of the muon size (phe) versus the muon ring radius (°) allows the calculation of the telescope collection efficiency through a fit to MC data. The profile fit of the "arc width/radius" versus the radius (°) gives an estimation of the telescope optical point spread function (PSF) [114].

5.2 QOSA: Quick Onsite Analysis

As the normal on-site analysis takes considerably more time to process a run on a single computer than the data-taking in acquiring it, a new version of the analysis program has been developed which processes the data during the data-taking dividing the task among a network of computers. This program will allow us to see the quality of the data taken during a night (in the same night or in the following night) and also to check the activity of sources as soon as possible and monitor several irregularly flaring sources to generate alerts.

5.2.1 Program description

The MAGIC Quick On-Site Analysis (QOSA) program is based on the analysis part ("on-site analysis") of the previously described MAGICDC (section 5.1.5).

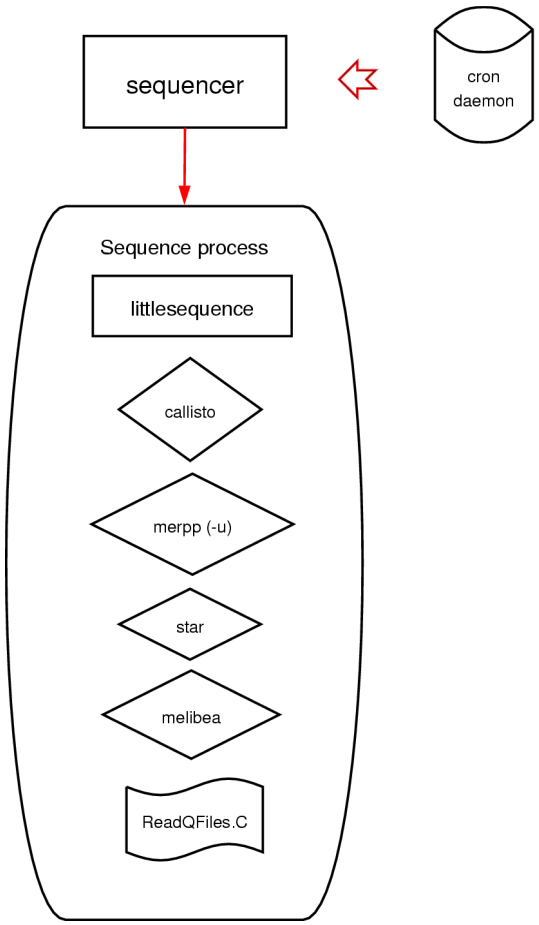

Figure 5.13: *QOSA program scheme.*

As the MAGICDC program, the QOSA program is also managed by the standard

Linux "cron" daemon running on the on-site main computer.

All the results and logs files from this program are written into the same directories as the previous version of the on-site analysis to allow the guardian scripts (sec.4 5.1.5) to check whether the analysis is complete or to fix it in the next 7 days.

While the MAGICDC program runs only in the main computer, the QOSA program is programmed to use a network of computers to compensate for the time taken by the calibration process (*Callisto*) (∼3 times slower than the data-taking time) to calibrate the data. The other parts of the analysis process (*Star*, *Melibea*,etc.) are faster than *Callisto*.

The crontab file is programmed to launch the *sequencer.csh* every 10 minutes during the MAGIC data-taking. If the analysis is not finished after the data-taking has begun, the crontab file of the guardian program (*monolith.csh*) will stop it to avoid interferences with the DAQ system.

The *sequencer.csh* script (fig. 5.13) controls all the analysis and performs all the checks that allow or forbid the data to be analyzed.

I. First of all, it sets the day of the data-taking and checks whether the "on-site analysis" has been run already. In the later case, the onsite analysis is not launched.

II. Then, it creates the night summary ASCII files from the already created central control ASCII files.

III. The next step is to create control files for the sequences of the data already taken. It is done with the same criteria as it was explained in section 5.1.5. The program will wait until the next sequence starts, or until the night finishes, to analyze the finished sequence.

IV. Once the sequence control file is created, the sequence has been already analyzed. In this case the program will not analyze the sequence. Then it checks for the last signal.root file created in case it needs it (section 5.1.5). If the sequence has to be analyzed or has not finished, then the program determines which computer is the corresponding one depending on the computer load. If the current sequence is already running in any of the computers, the sequence analysis will not be launched.

V. Once all these checks and variables set have been performed, the script launches the *littlesequence.csh* script. This script will be in charge of performing the complete sequence analysis.

The *littlesequence.csh* script (fig. 5.13) is a summary of the previously seen *Analysis* and *PostAnalysis* scripts. It calibrates the data, merges the subsystem information, extracts the image parameters, merges the standard RF matrices and displays the

analysis results in the same way described in section 5.1.5 with the same macro as the "on-site analysis" (*ReadQFiles.C*). For a description of the plots, see section 5.1.5.

Once the *littlesequence.csh* script has finished, the analysis plots are updated with the new analyzed data and transferred to the MAGIC web page.

There is an script (*killer.csh*) that can be used by the shift workers to order the *sequencer.csh* script to stop the Onsite analysis for the rest of the night. This is a safety program just in case the analysis process is interfering with the MAGIC DAQ data-taking.

5.3 Conclusions

The programs described in this chapter are currently used as the first standard reference to detect and diagnose the telescope problems. The union of both programs (MAGICDC and QOSA) allows the collaboration to know any system failure before 11:00 (UTC) and, if all telescope components worked correctly, to have a first standard analysis of the night data before 12:00 a.m (Europe local time). As a consequence the performance and up time of the telescope can be improved. The information also helps the day shift to carry out any repair or adjustments for the following night. The check results (dailycheck report) are sent to the entire collaboration.

Since its installation on January 2004, the data check program has improved gradually increasing the number of systems to check and therefore the number of resulting plots. The increase has been due to the addition of new reports to the central control, improvements in the software and, most of all, the feedback from users and those responsible for the system about known/unknown new subsystem features.

The updates on the onsite analysis program (QOSA) have led to a preliminary analysis of the night data within the next morning after the data-taking. This improvement will also enable the calibration of all the data in each collaboration institute within the next day.

The results presented in this Chapter have been published in MAGIC internal documentation (TDAS 06-11) and will be presented at VIII Meeting of the Spanish Astronomy Society (2008).

Chapter 6

MAGIC data analysis.

This chapter gives a general description of the standard MAGIC analysis chain, with emphasis on specific parts needed for the pulsar analysis. Two different kind of analysis are performed on pulsar data depending on whether the emission under consideration is pulsed or steady.

The description of the MAGIC data analysis will be divided in 3 main parts: the calibration and imaging reconstruction of the showers recorded by the telescope; the evaluation and selection of a good quality data sample; and the analysis of the final data sample. Due to the nature of the pulsar sources, a complete analysis will require two different kinds of analysis: the first to analyze the steady γ-ray radiation of the plerion and the second to concentrate only on the pulsed emission coming from the pulsar magnetosphere.

6.1 Calibration and image reconstruction

The calibration of the raw data collected by the MAGIC telescope is based on the characteristics of the light-detection and amplification chain response of the telescope. This data calibration will obtain the correspondence between the number of incident Cherenkov photons (or photoelectrons at the first dynode of the PMTs) and the digitized information recorded by the DAQ system (see chapter 5 for a more detailed description).

The calibration process determines the conversion factor from digitized FADC counts and photons converted in the PMT photocathodes as well as the arrival time delay for each pixel. As a result, the calibrated data will be given in photoelectrons (phe) per pixel. All the data used in this Thesis correspond to the image parameter files data analyzed by the On-Site analysis program, developed by the Thesis author and already described in the previous section 5.1.5.

The on-site analysis program applies the digital filter extractor for the signal

calibration and a 2-level tail-cut of 10 phe for core pixels and 5 phe for boundary pixels [1] (the so-called "Standard Absolute 10 5" image cleaning) [155]. These image-cleaning levels are independent of the background noise level (pedestal rms) and give a good agreement between On and Off observations, because the On-Off data is usually taken at different NSB conditions. This is particularly important for the sources analyzed in this Thesis. These sources were taken in MAGIC cycles I and II, where no specific Off data was taken for pulsar observations in On-Off mode (except for the Crab Nebula).

6.2 Source data quality check

The next step in the analysis after the calibration is the selection of the data sample for the source analysis. This selection is done through a data quality check, which guarantees that the data sample selected for the analysis was taken under good and stable conditions. These conditions are similar to the ones used in the MAGIC data check, although with different limits.

The quality checks select good data runs according to different data parameters, which are detailed below.

Telescope miss pointing Because a dome does not protect the telescope and the data-taking period for one source can be spread over several months, the weather conditions can change easily over time - compromising not only the telescope integrity but also the accuracy of the telescope pointing.

The first factor to take into consideration is the wind speed. The telescope design was focused on obtaining a very light structure with a low inertia moment. Therefore, the pointing can be affected by the wind and runs taken under wind speed > 15 km/h are rejected in the analysis.

To get a pointing accuracy of $\leq$2 pixel for perfect weather conditions, limits in two parameters measured by the star guider subsystem were also included: the star guider miss pointing and the minimum number of stars identified by the subsystem. The latter condition is necessary because when the star guider identifies a low number of stars, the algorithms that extract the miss pointing yields wrong values for the telescope miss pointing.

Although, I ask for a pointing accuracy of 1 pixel (6 arc min) in the pulsar analysis in the MAGIC data check, the pointing restriction is relaxed to avoid the rejection of too much data, which would make it impossible to detect the source due to the

[1] The 2-level tail-cut image cleaning selects the pixels to use for the Hillas parameters calculation. The "core" of the image is made up of pixels with more than x number of phe (in this case x=5) while the tail of the image consists of a fixed number of rings of pixels that surround the image core pixels that have a signal greater than y number of phe (in our case y=10 and rings=1). The different area between inner and outer pixels is also taken into account.

low fluxes expected from pulsars. To compensate partially for this lack of pointing accuracy, an extended source analysis (DISP analysis) is carried out in order to be able to detect sources despite some miss pointing.

Data PSF and Data-taking rate There are several factors that can affect the data point spread function (PSF) and the data-taking rate: the weather conditions, the reflector quality and signal processing problems.

The optical performance of the telescope is measured by the telescope point spread function and defines the telescope imaging resolution. The optical PSF is calculated from the width in the radial direction of the muon rings images in the camera, thus calibrating the "image" size of a punctual source in the camera. A wrong estimation of the telescope PSF will cause to obtain wrong shower image parameters concerning the size and shape of the ellipse and also the amount of light on it. The reason for changes in the PSF is that the telescope optical elements adjustments (active mirror parameters or the mirror panels themselves) change. A high humidity (>90%) is normally accompanied by formation of small water droplets (40-100 μm $\emptyset$) resulting in considerable Mie scattering losses. By imposing restrictions on the atmospheric humidity and the number of identified stars by the star guider, runs taken in the presence of low clouds or fog can be rejected.

Other problems in the DAQ or trigger system of the detector can give rise to void runs (rate = 0) or a wrong events time stamp (run time = 0). Those runs will be also rejected from the analysis

The stability of the Hillas shower image parameters and the trigger rate after image cleaning per run, for the whole data sample can show other problems with the calibration or the imaging calculation. The rejection criteria for these parameters will allow a dispersion of the Hillas parameters of less than 50% in the mean per run.

Camera and On-Off samples homogeneity Another problem that affects the quality of the data is the homogeneity of the camera response. After any change in the camera and/or the signal transmitters, the gain of each PMT is modified changing the HV settings in order to get a homogenous camera. This process is repeated from time to time, so it could happen that some of the data were taken with an inhomogeneous camera, with an increase/decrease of the rate on some parts of the camera. This will not show up in the data-taking rate but in a "false source" detection or background excess.

To detect the possibility of having this problem in our final results for each source, it is necessary to check the centre of gravity for the images and the homogeneity between the calculated Hillas parameters for the On and Off samples.

6.3 Event cleaning cuts prior to the analysis

Once all the bad runs have been removed from the data sample it is necessary to apply an event-based cleaning before the source analysis.

The events removed are those that could decrease the analysis sensitivity due to a bad performance of the telescope system. These events have to be removed before the γ/hadron separation and the energy estimation processes and before both the steady and the pulsed γ-emission analysis.

The event cleaning cuts applied in our data analysis are the same applied in the On-Site analysis:

- Camera sparks. These events are produced when a discharge from the photocathode (through the glass envelope) is reflected on the Winston cones illuminating the closest PMTs (section 5.1.5). This causes very concentrated events with different energies. This kind of event can be removed with a simple cut (black line in figure 6.2). The cut keeps all MC gamma events while rejecting only $\sim$0.5% of real data (fig. 6.1).

- Finite camera size. High-energy events with large impact parameters are not completely contained in the camera. The Hillas parameters for such kind of events cannot be properly reconstructed due to a loss of a major part of the shower image. For this reason, a new parameter (leakage) was introduced which measures the fraction of photons in the 2 outermost rings of pixels belonging to the image. In the analysis, those events with a leakage of more than 10% of the image in the outer part of the camera are rejected. About $\sim$ 1% and $\sim$ 5% of the total events for MC γs and real On-Off data respectively are affected.

6.4 γ/hadron separation

Once the data sample of star files (Hillas image parameters) is cleaned, the next step is to reject as many hadronic events as possible from the data sample while keeping as many γ events as possible. There are different methods to separate gamma-like and hadron-like events, resulting in different levels of sensitivities for the analysis:

- The so-called classical Hillas method makes use of static and dynamical cuts on the image parameters. By comparing the image parameter distribution of MC γs and recorded hadrons, cuts can be selected that keep most of the gamma events and reject as many hadrons as possible. A cut can just involve a parameter of the distribution (e.g. Dist $> 0.2^\circ$) or refer to a function of several parameters (e.g. Dist $>$ f(Size, θ,etc)). The first case deals with the so-called *Supercuts* [131] and is the simplest method used for reduction of data from Cherenkov telescopes. The second case is based on the physical development of the shower and the

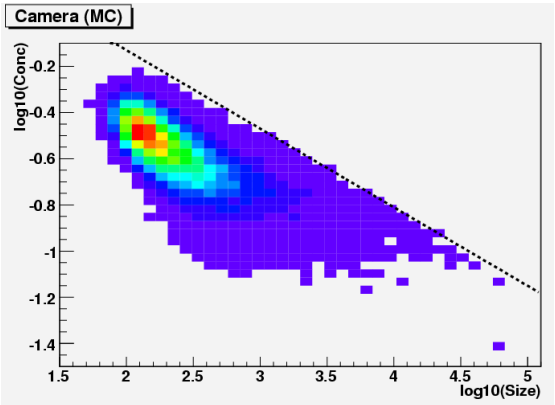

Figure 6.1: *Distribution of Size versus Concentration in MC γs data. The dotted line is the "sparks" events cut.*

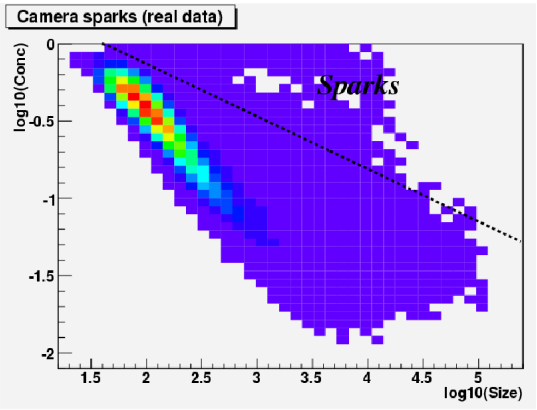

Figure 6.2: *Distribution of Size versus Concentration in real data. The sparks are those events above the "sparks" events cut.*

dependency of the shower image with the primary particle energy, the pointing zenith angle, etc.

- Multidimensional events classification. Recently new algorithms of multivariable classification (neural networks, random forest, and so on) have been developed to find differences between the γ - and hadron - induced image showers [30].

In the MAGIC analysis chain the Random forest (RF) algorithm [32] has been used for the first time as the standard γ/hadron separation method [90].

A *random forest* is made up of decision *trees* (normally 50-100). Each tree is built from a root *node*, which contains all the events (gammas and hadrons). The consecutive nodes are built from consecutive random cuts in one of the Hillas image parameters set in the program configuration file. Each cut divides the sample into nodes until one node is pure (contains only one kind of event) or the remaining events in a node are less than a certain value (typically 1-10 events). The best cut value that divides each node sample is chosen such that it minimizes the *Gini index* (fig. 6.4) of both samples after the cut. Then the Gini index measures the node purity, being 0 if there is only one kind of event in the node (gammas or hadrons) and 1 if the node contains all kind of events (gammas and hadrons). In order to guarantee the creation of a forest of independent trees, and therefore avoiding over-training, each tree of the forest is created from an independent sub sample of events from the RF training sample. Once the forest has been created, in order to classify a new event, each of the trees is followed as far as their terminal nodes. Each tree assigns to each event a probability value of being a hadron, depending on the fraction of hadrons from the root node remaining in the node where the event has being located.

The forest average of this "hadron probability" defines a new event parameter called *hadronness*. Therefore, an event with a hadronness parameter close to 0 will have a high probability of being a gamma event, while an event with a hadronness parameter close to 1 will be classified as hadron.

To decide which set of Hillas image parameters to use in the random forest training, the γ/hadron separation power of each image parameter must be measured. This is measured through the decrease of the Gini-index between nodes for each tree. By adding all the Gini-index decrease values, the separation power of each image parameter is obtained, so that those Hillas parameters with the highest decrease of the Gini index can be chosen for the configuration file (fig. 6.4).

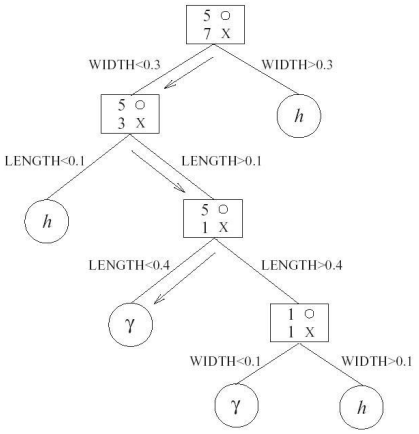

Figure 6.3: *A scheme of a possible tree in the Random forest classification of gammas and hadrons [112]. The circles and crosses represent the gammas and hadrons, respectively.*

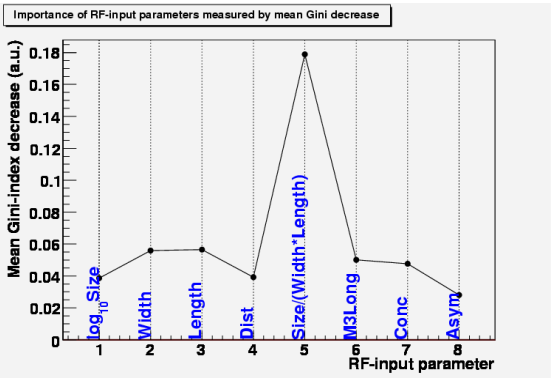

Figure 6.4: *Mean decrease of the Gini index for the image parameters used in the Random forest applied in the analysis.*

For the RF training, MC gamma events were used as the sample of gamma events and a sub sample of real Off data as hadron events, although MC hadrons events could also be used as hadron events to train the RF.

As explained previously, the Random Forest method is applied for the On-Site analysis program and also in the analysis of the sources in this Thesis as the default γ/hadron separation method. Together with the RF method, some other static and dynamical cuts will be detailed in the pulsar data analysis (see chapter 7).

Because the Hillas parameters depend slightly on the observation zenith angle and the energy of the shower, it is necessary to optimize the γ/hadron separation for each source and energy bin to be analyzed.

There are several criteria to find the hadronness cut for optimal γ/hadron separation for the analysis of our data:

- To optimize the quality factor parameter ($Q = \frac{\epsilon_\gamma}{\sqrt{\epsilon_h}}$) imposing that at least 50% of all gammas (of an independent sample) remain after cuts.

- Optimizing the signal significance of a certain γ-ray source. For this, a powerful source is needed in order to have a minimum signal for the different bins in energy. In the steady analysis in this Thesis, data from the Crab Nebula will be used as the γ sample and the corresponding Off sample for sources of our analysis as the hadron sample.

6.5 Shower energy reconstruction

Cherenkov telescopes collect the light produced by the electromagnetic component of a shower. A short of "collection cross section" is defined by the telescope's effective area (see chapter 3).

The amount of shower light collected by the telescope is described by the Hillas parameter *Size*. In first order, the energy of a primary γ-ray is proportional to the Hillas parameter Size times a function related to the Dist parameter, which is related to the impact parameter of the shower with respect to the telescope. However, the use of only Size in the shower energy estimation produces quite big errors in the shower energy reconstructed, because the energy depends on other factors, such as the shower impact parameter and the observation zenith angle (see chapter 3). In stereoscopic systems, the impact parameter is measured, so the energy of the primary gamma showers is extracted from MC simulations tables. However, in single dish telescopes, the impact parameter is not too well known, so the energy reconstruction is done through mathematical algorithms from the image parameters. Therefore, it is necessary to include other Hillas parameters (dist, width, length, etc.) with the additional information about the primary γ-ray energy in the energy reconstruction algorithm.

The most used algorithm in the previous HEGRA experiment for the analysis of single dish data (CT-1) was a semi-empirical model [103]. This method uses MC simulated γ-showers to find the relation function between the primary particle energy and several image parameters.

In this Thesis, another novel application of the Random Forest method described previously will be used. For the reconstruction of the energy shower, the method will classify the events belonging to different energy intervals instead of different kinds of events. As in the previously described classification method, it is necessary to choose a set of Hillas image parameters, which optimizes the method's efficiency. This RF method is better than the semi-empirical one because it does not assume a priori functional relationship between the primary particle energy and the set of Hillas parameters [112].

6.6 Analysis for the search of steady γ-emission

In this kind of analysis, besides the cuts already described in previous sections, a cut in the number of islands in the camera will be performed demanding it to be less than 3. Even at low energies very few MC γ-events have more than 3 islands, while hadronic events quite often have a large number of them. This cut is also important for the RF training with real Off data since, as can be seen in figure 6.5, the distribution of the number of islands is different for Monte Carlo protons and real Off data samples for values greater than 3.

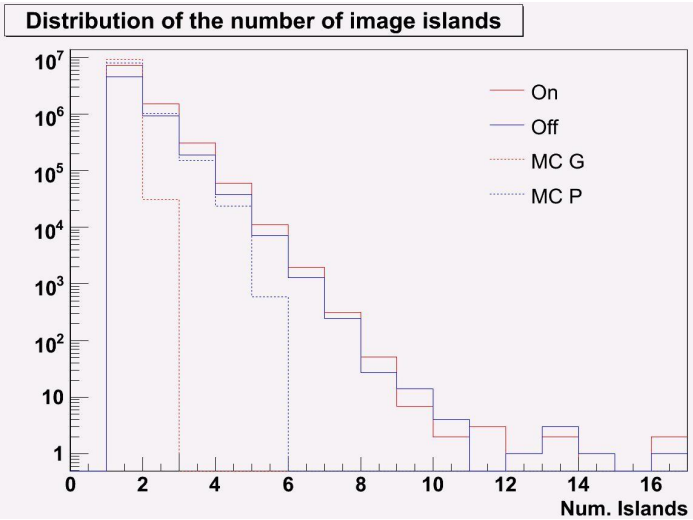

Figure 6.5: *Distribution of the number of islands in the cleaned images for MC gammas (red-dashed lines) and protons (blue-dashed lines) simulated showers. The distribution on real data (filled lines) is given for On (red) and Off (blue).*

None of these previous cuts will reject many hadron events. The strongest cut will be the hadronness parameter. To optimize the hadronness cut for each energy bin and each source, a Crab sample contemporaneous to our On and Off data will be used. The optimum hadronness cut will be chosen as the one, which yields the highest telescope sensitivity or the highest signal significance. The optimized hadronness cut will be applied to data analysis in the same way as the γ/hadron separation cut.

6.6.1 Telescope sensitivity and signal significance

The confidence level or the related significance of a candidate source is determined by the probability that an excess is due to the source and not due to statistical fluctuations on the background (not always precisely known).

In this Thesis, the calculation of the detection significance will consider a typical ON-OFF observation mode in Cherenkov telescopes. In this observation mode, the

telescope points towards the source for a certain time interval t_{on} collecting N_{on} events and then towards a dark region of the sky close to the source during a time interval of t_{off} collecting N_{off} events. The ratio between On and Off observation times is $a = t_{on}/t_{off}$[2]. Considering a weak source from where very few events are detected and using the likelihood ratio method, Li & Ma [107] evaluated how much an observation differs from the null hypothesis (all the observed counts come from the background), obtaining an expression for the observation significance:

$$N_\sigma = \sqrt{2}\left\{N_{on}\ ln\left[\frac{1+a}{a}\left(\frac{N_{on}}{N_{on}+N_{off}}\right)\right] + N_{off}\ ln\left[(1+a)\left(\frac{N_{off}}{N_{on}+N_{off}}\right)\right]\right\}^{1/2} \tag{6.1}$$

where the number of excess events is $N_s = N_{on} - a \cdot N_{off}$. In this Thesis, the significance will be obtained through two kinds of analysis: α-distribution and θ^2-distribution. The signal region will be defined through these distributions. For the α analysis distribution, all events within $|\alpha| < 10^\circ$ will be considered as well as those coming from the signal region, while the background will be determined as $35^\circ < |\alpha| < 90^\circ$ region. Therefore N_{on} and N_{off} will be the events coming from the signal region of the alpha-distribution from On and Off data, when both distributions are normalized in the dark region ($a = N_{on}(35^\circ < |\alpha| < 90^\circ)/N_{off}(35^\circ < |\alpha| < 90^\circ)$).

The sensitivity of a Cherenkov telescope for a potential γ-ray source is usually defined as the fraction (in %) of the flux of the source needed to detect a 5σ signal in 50 hours of observation:

$$S(\%) = 100 \cdot \frac{t_{obs}(h)}{50}\frac{N_s(50^h, 5\sigma)}{N_s} = 100 \cdot \sqrt{\frac{T_{obs}(h)}{2}}\sqrt{\frac{aN_{off}}{N_s}} \tag{6.2}$$

where $N_\sigma = \frac{N_s}{\sqrt{N_b}}$, $N_B = aN_{off}$ and $N_{exc} = N_{on} - aN_{off}$. Usually the source used for this definition is the Crab Nebula

6.6.2 Source position reconstruction: DISP method

The standard analysis for sources observed in On-Off mode extracts the source signal from the alpha parameter distribution because it is assumed that the source is at the centre of the camera. This is not true for observations of point-like sources with a relatively high miss-pointing or for extended sources. In the latter case, the position of the source is not known a priori, because the γ-ray emission region can be located around the pointed object with an extension exceeding that of the telescope PSF. The emission region for PWN is expected to be point-like for the MAGIC telescope. In this Thesis, a scan in the camera FoV is performed to look for possible miss-pointing and emission from the pulsar surroundings.

[2]In the analysis of this Thesis, the normalization ratio is computed through the number of events in the background region ($35^\circ < |\alpha| < 90^\circ$) of On and Off α-distributions after cuts. This ratio is equivalent to the one computed through the observation times in case of weak sources.

In this case, the arrival direction of each γ-ray event in the sky plane must be reconstructed. Because some Hillas parameters, such as Alpha and Dist, depend on the source position in the camera, one needs another method of analysis to use the shower image shape to estimate the source position for each detected shower. This new method is called DISP.

This method assumes that the source position is located along the major axis of the Hillas ellipse at a certain distance DISP from the image centre of gravity. It is based on the increase of the Hillas ellipse eccentricity with the distance between the γ-shower and the source position in the camera [69]. In the case of MAGIC, a new parameterization for DISP has been used, depending on Size, Width, Length and Leakage2. This new parameterization leads to an IACT angular resolution of 0.102 $\pm$ 0.008° above $\sim$140 GeV [59]. This improved DISP method has been implemented in the standard MAGIC analysis program. Using a sample of MC-γs, the standard program optimizes the parameters in the DISP function by minimizing the average angular distance (θ^2) between the real and the estimated source position. Because the DISP parameter has two possible solutions, head-tail shower information has been introduced through the Asym parameter.

6.7 Analysis for the search of pulsed γ-emission

This kind of analysis consists of a temporal analysis of the photons emitted by a source and checks whether they have a periodic behaviour at the pulsar rotation frequency.

The first step for this analysis is to correct the events arrival time (UTC) measured by the observatory (t_{obs}) with that in the pulsar reference frame. Neglecting second order corrections, the closest inertial reference frame to the pulsar rest frame is the solar system barycentre (SSB), so that the arrival time in the pulsar reference frame will be approximated by the barycentric arrival time (t_b) [146]. The transformation of the events time between both reference frames takes into account the following corrections:

$$t_b = t_{obs} + \frac{\vec{r}\cdot\hat{n}}{c} + \frac{(\vec{r}\cdot\hat{n})^2 - |r|^2}{2cd} - \frac{D}{\nu^2} + \Delta_{E\odot} + \Delta_{S\odot} \tag{6.3}$$

where the first two terms are the corrections from the observatory to the SSB reference frame. The third term corrects using the interstellar dispersion (D) of the pulsed radiation. The forth and fifth terms are the Einstein and Shapiro delays, respectively, due to the gravitational redshift caused by the Solar System bodies ($\Delta_{E\odot}$) and the curvature of space time near the Sun ($\Delta_{S\odot}$).

Once all the events times are referenced to the solar system barycentre, the next step is the search for a periodical signal in these events. First of all, one has to fold the events time to the pulsar phase (ϕ). This determines in which fraction of the pulsar rotation the photon was emitted by assigning a rotational phase to each event.

The phase for each event can be calculated as the number of revolutions since an initial time (T_0) until the event time (t):

$$\begin{aligned}\phi(t) &= \int_{T_0}^{t} f(t)dt = \int_{T_0}^{t} \left[\nu(T_0) + \dot{\nu}(T_0)(t-T_0) + \frac{1}{2}\ddot{\nu}(T_0)(t-T_0)^2 + \cdots\right] dt \\ &= \phi_0 + \nu(t-T_0) + \frac{1}{2}\dot{\nu}(t-T_0)^2 + \frac{1}{6}\ddot{\nu}(t-T_0)^3 + \cdots \end{aligned} \quad (6.4)$$

In the case of binary pulsars, the event barycentre time has to be corrected from the pulsar motion in the binary orbit, introducing the binary orbital parameters [29].

The Taylor derivatives of the pulsar frequency at a reference time T_0 (ν,$\dot{\nu}$,$\ddot{\nu}$,...) are the so-called pulsar *ephemeris* and describe the pulsar rotations. Depending on the pulsar activity, the ephemeris will describe with more or less accuracy the pulsar rotation along time. Some pulsars need up to second order Taylor expansion ($\ddot{\nu}$) to describe the changes in the rotation frequency over a short period of time, while the most stable rotating pulsars need a time interval of tens of years to observe any change in the frequency.

In addition, one has to take into account irregularities in the pulsar rotation. All the irregularities in the pulsar activity are classified in two groups: the first one is the so-called *timing noise* and gathers the pulsar erratic behaviour over several years observed mainly in young pulsars caused by one or more known processes. The second ones, also typical of young pulsars, are known as *glitches* and are characterized by a sudden change in the rotation speed ($\Delta\nu/\nu \sim 10^{-9} - 10^{-6}$), followed by a slow recovery of the extrapolated frequency. This slow recovery of the pulsar frequency makes it necessary to use new ephemeris after each pulsar glitch.

Therefore, for very active pulsars, ephemeris contemporaneous to the pulsar observation period will be needed. Because the pulsar rotation properties are expected to be the same at all the observation wavelengths, the ephemeris given by other experiments (radio, X-rays, optical,etc.) will be used in the analysis of each pulsar. If the available ephemerides are not contemporaneous, it is necessary to study the stability of the pulsar rotation and extrapolate which ephemeris are valid for our pulsar observation period.

The distribution of the events phase is the so-called pulsar *light curve* (LC). Once the pulsar light curve has been calculated, one has to look for a periodic signal at the pulsar frequency, performing an uniformity test over the collected photons phase (ϕ_i). The uniformity tests are based on the measurement of how much the pulsar light curve $f(\phi)$ differs from an uniform , i.e. flat, distribution (null hypothesis H_0) [47]:

$$\begin{aligned} H_0 &: f(\phi) = 1 \\ H_A &: f(\phi) = pf(\phi)_s + (1-p); \quad where\ \phi \in [0,1] \end{aligned} \quad (6.5)$$

Equation 6.5 represents the alternative hypothesis of a pulsed signal with p being the pulsed signal intensity of the light curve.

For the timing analysis of this Thesis, the timing analysis program *SearchPeriod* [112] developed inside the MAGIC analysis program (MARS) was used. For the millisecond pulsar PSR J0218+4232, the program *Tempo* [146] was used to correct the arrival time from the movement through the binary system. Among all the existing periodicity tests, the most frequently used uniformity test has been implemented in the SearchPeriod program (χ^2, Z^2 and H-test).For the timing analysis of this Thesis, both the χ^2 and H test will be used. A brief description of them will be made in the next section.

To check the MAGIC timing analysis, XMM data of an isolated pulsar (Geminga) and a pulsar embedded in a binary system (PSR J0437-4715) have been used. These results have been cross checked with the result from XMM analysis software (SAS) [3] giving matching results (fig. 6.6 to 6.9), thus confirming the accuracy of the timing program.

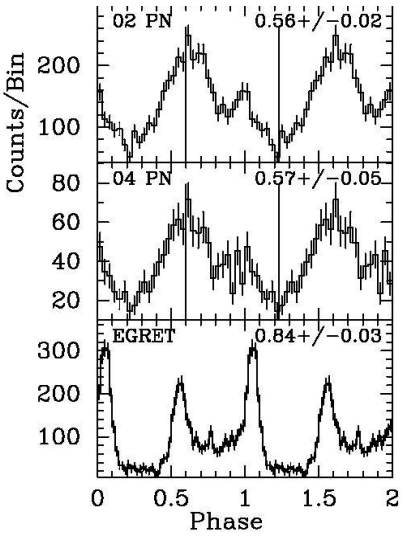

Figure 6.6: *SAS results of XMM data for the isolated pulsar (Geminga) [94] from 2002 and 2004 (two upper plots). Bottom plot is the light curve from EGRET measurements.*

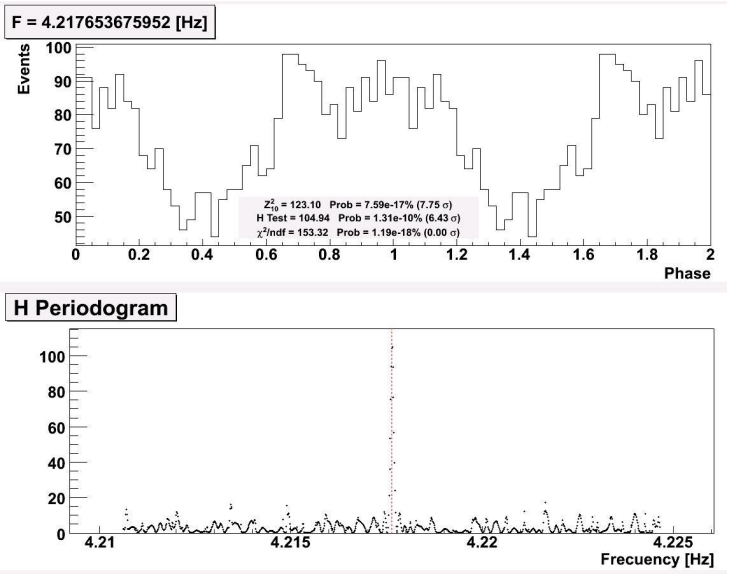

Figure 6.7: *MARS results of XMM data for the isolated pulsar (Geminga). The light curve and the corresponding folding frequency for best H-test results are shown in upper plot. The resulting best frequency is at 0.1 IFS from the ephemeris frequency in Jackson (2005). The H-test results of the frequency scan are shown in bottom plot.*

[3]Thanks to Antonio Martin-Carrillo and Aitor Ibarra (E.S.A.C.,Madrid).

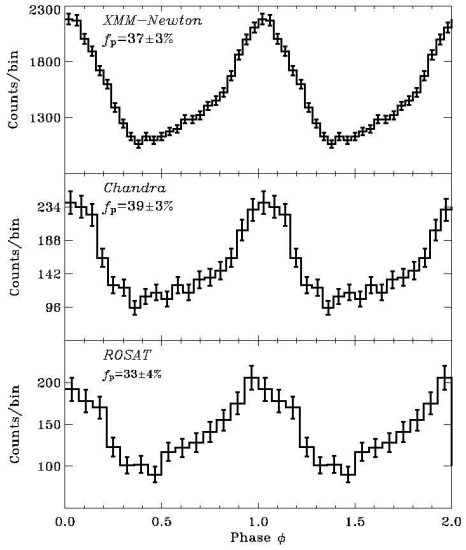

Figure 6.8: *SAS results of XMM data (upper plot) for the binary pulsar (PSR J0437-4715) [158]. The plots in the middle and the bottom correspond to the pulse profiles from Chandra and ROSAT data.*

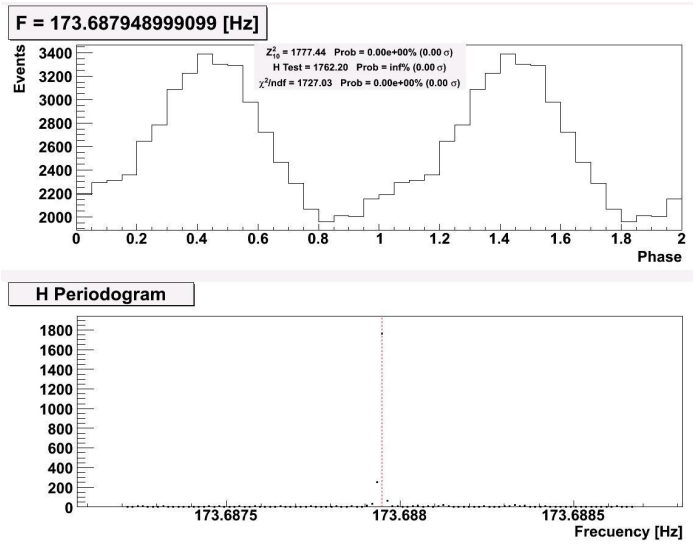

Figure 6.9: *Tempo results from XMM data for the binary pulsar (PSR J0437-4715).The light curve and the corresponding folding frequency for best H-test results are shown in upper plot. The resulting best frequency is at 0.0 IFS from the ephemeris frequency in Zavlin (2006). The H-test results of the frequency scan are shown in bottom plot.*

6.7.1 The χ^2 or Pearson test

Among all the existing tests of uniformity, the χ^2 test is the most used in optical and X-ray data timing analysis because of the large signal strengths at these wavelengths.

By definition, χ^2 is the squared deviation from the expected distribution, a uniform one in our case:

$$\chi^2 = \sum_{i=1}^{K} \frac{(x_i - \mu_i)^2}{\sigma_i^2} \quad ; \quad P(\chi,\nu) = \frac{1}{2^{\nu/2}\Gamma(\nu/2)} \int_{\chi^2}^{\infty} t^{(\nu/2-1)}\, e^{-t/2}\, dt \tag{6.6}$$

where $P(\chi,\nu)$ is the probability function for this test with $\nu = K-1$ and K being the number of bins used in the histogram.

The Pearson test is very sensitive to the number of bins, K, used in the light curve, because only large deviations from the uniform distribution will yield high values of χ^2 and, therefore, a high significance. In general, for broad peaks one should use low number of bins (K) but for light curves with narrow or multiple peaks the usage of large values of K gives better results, although the highest number of bins to use is limited by the achieved time resolution. Therefore, for strong signals with one single

narrow peak in the light curve, the Pearson test will yield a very high significance, while for sinusoidal light curves it will be less effective.

6.7.2 The H test

At high energies, pulsars are very weak sources, resulting in only a few photons per observation. All the uniformity tests are powerful for certain light curves shape while they loose sensitivity for other light curves. This makes necessary a uniformity test consistent and powerful in the detection of weak sources for which the light curve shape is unknown. A possible solution is offered by the H test.

The H test is based on the Z_m^2 test statistics, which makes a Fourier analysis of the phaseogram. Z_m^2 is defined as the sum of the squares of the first m Fourier coefficients of the folded light curve. Although, the Z_m^2 test avoids the problems of histogram creation, the power of the test for different light curves shapes depends on the number of harmonics chosen.

The H test optimizes the number of harmonics (m) of the Z_m^2 test, minimizing the error between the Fourier function and the real unknown light curve and yielding a maximized H estimator:

$$H \equiv max(Z_m^2 - 4m + 4) = Z_M^2 - 4M + 4 \tag{6.7}$$

where m is ≤ 20 because the M value is always below 20 [50]. This means that it is the most powerful uniformity test for most possible light curves shapes (fig. 6.10). Only for specific number of peaks in certain multi-modal light curves is the Z_m^2 test more powerful than the H test (fig. 6.11)

In the absence of signal, the probability distribution of the H test is an exponential. Unfortunately, for this test, no analytical function for the test probability exists, but only Monte Carlo simulation results [47].

6.7.3 Stability of the pulsar rotation

Generally, the pulsars are known as "stable rotators", losing their rotational energy only gradually by some deterministic damping mechanism. This stable behaviour will allow us to extrapolate old ephemeris to the epoch of our observations. However, irregularities in the pulsar rotation have been observed mainly in young pulsars. These irregularities affect the phase by a stochastic term $o(T)$.

One of the most common irregularities is the so-called *timing noise*. It is believed to be caused by internal oscillation inside young pulsars, causing a deviation between the observed frequency and that extrapolated from equation 6.4. In the case of the Crab pulsar, the deviation is around 12 ms for periods of 3 years. Pulsars with small $\dot{\nu}/\nu$ usually have little or no observable timing noise, that means that the next order is also very small.

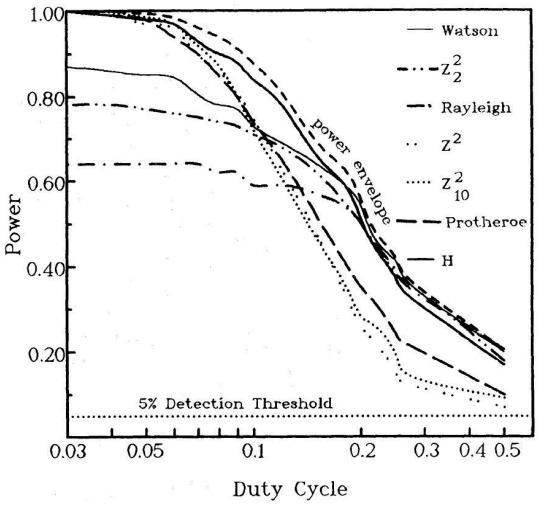

Figure 6.10: *Power curves for different uniformity tests as a function of the duty cycle of the light curve represented by a single-peaked Gaussian with 10% signal strength. The envelope curve represents an "ideal" test [47].*

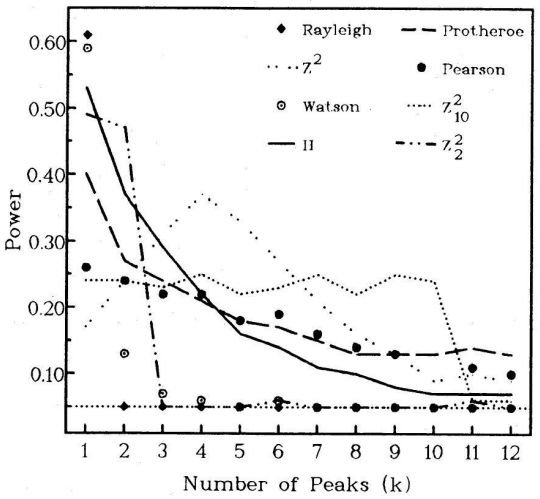

Figure 6.11: *Power curves for different uniformity tests as a function of the number of peaks (k) of the light curve f(φ)=0.312/(1+0.2cos(kφ). In this case a signal strength of 20% has been used [47].*

Another kind of irregularity is named a pulsar *glitch*. This phenomenon is caused by "star quakes" in the pulsar. Within a time interval of several years, some young pulsars experience a sudden acceleration in the rotational frequency typically of the order of $\Delta\nu/\nu \sim 10^{-8} - 10^{-6}$. Often the glitch also increases the pulsar frequency acceleration ($\propto \dot{\nu}$). After the glitch episode, the pulsar slows down gradually until it recovers the extrapolated period for that epoch.

These two phenomena can hamper the extrapolation of valid ephemeris for the observation epoch for young pulsars or even cause an error in the pulsar light curve if the change on the pulsar frequency is so large that $\Delta\phi = \Delta f \cdot T_{obs} >> 1$. None of these phenomena have been observed in millisecond pulsars, therefore they can be considered as stable ones for the timing analysis in this Thesis.

6.8 Upper limits (UL) calculation

In the case of very weak sources, the signal measured could be below or equivalent to the background fluctuations. A signal significance below 5σ will define the limit to consider a signal above fluctuations. This will be the case for the pulsars analyzed in this Thesis. For these sources, one can establish an upper limit at a certain confidence level to the flux emitted by the source for an energy interval.

The upper limits can be calculated in different ways depending on the kind of

analysis performed: for steady emission, confidence intervals are calculated using a hypothesis test. In the case of the timing analysis, the upper limits will also be calculated from uniformity tests.

The aim of this analysis will be to calculate the upper limit (N_{ul}) on the number of excess events N_{exc} through a certain statistical approach for steady and timing analysis. The flux upper limit will be given by $F_{ul} = N_{ul}/A_{eff}T_{on}$, where $\mathrm{A}_{eff}\mathrm{T}_{on}$ is the mean effective area (A_{eff}) multiplied by the effective On observation time (T_{on}) at a pre-selected energy range.

6.8.1 UL on the steady emission

There are two different statistical approaches to the calculation of the flux upper limits: *Bayesian* [81] and *Frequentist* [132].

The *Bayesian approach* is obtained using Bayes' theorem, which define the probability as the degree of belief for a proposition ($\pi(\theta)$) and infer or update this degree of belief in the light of new data (x). Bayesians assign probabilities to propositions that are uncertain:

$$p(\theta|x) = \frac{L(x|\theta)\pi(\theta)}{\int L(x|\theta'\pi(\theta')d\theta'} \quad ; \quad 1-\alpha = \int_{\theta_{lo}}^{\theta_{up}} p(\theta|x)\ d\theta \tag{6.8}$$

where $1-\alpha$ is called a *Bayesian* or *credible interval* and contains a given probability fraction. In the case of upper limits, $\theta_{lo} = 0$. The main difficulty in determining upper limits with Bayesian intervals is the uncertainty in quantifying the prior beliefs ($\pi(\theta)$).

In this Thesis, the *Frequentist approach* is used, which defines the probability of a random event as the limit of its frequencies of occurrence in a large number of trials.

The frequentist intervals are obtained through the Neyman procedure [122], which constructs the interval including the true value of the parameter with a probability greater or equal to the so-called *coverage probability*:

$$1-\alpha = \int_{x_{lo}}^{x_{up}} f(x;\theta)dx = P(x_{lo}(\theta) < x < x_{up}(\theta)) = P(\theta_{up}(x) < \theta < \theta_{lo}(x)) \tag{6.9}$$

For upper limits calculation $\theta_{lo}(x) = 0$, having a *confidence level* (CL) equal to $1-\alpha$.

The standard technique for constructing confidence intervals is the Profile likelihood, where the likelihood ratio follows a χ^2 distribution with k degrees of freedom if the null hypothesis is true ($H_0 : \pi = \pi_0$). In the case of only one parameter, k = 1.

$$\lambda(\Pi_0|X) = \frac{supL(\Pi_0, \Theta|X); \theta}{supL(\Pi, \Theta|X); \pi, \theta} \tag{6.10}$$

where $\Pi = (\pi_1, \ldots, \pi_k)$ are the parameters of interest, $X = (x_1, \ldots, x_n)$ are the independent observations and $L(\Pi, \Theta|X) = f(x_i|\Pi, \Theta)$.

This method is called the *Rolke method* [132] and generalizes the likelihood ratio test statistic for the case where there are many parameters of interest, instead of only one. This means it can be adapted to treat problems with several nuisance parameters $\Theta = (\theta_1, \ldots, \theta_l)$ which are not exactly known.

In our analysis, X will be the number of N_{on} events and N_{off} are the number of background events normalized to the On observations through $a = t_{on}/t_{off}$ or normalization in the background region of the α-distribution. Then, the number of excess events $N_{exc} = N_{on} - aN_{off}$ and the background aN_{off} will correspond to the parameters to be estimated.

6.8.2 UL on a possible pulsed emission

The upper limits to the flux of the pulsed emission can be calculated in two different ways: through the known On and Off regions of the light curve (On-Off method) or by the uniformity tests (H test).

Both methods are based in different hypothesis and have been implemented in the Magic telescope analysis software [112]. In the *On-Off* method, the upper limit is calculated by specifying the phase region in the light curve for the expected pulsed signal. This signal is assumed to be similar to the one at other wavelengths. In the second way, the number of excess events is given by the applied statistical test.

ON-OFF To calculate the upper limits for pulsed emission, the Rolke method shown for the steady emission upper limits will be applied. In this case, the number of On events (N_{on}) corresponds to the events in the phase intervals where the pulsed emission is located, while the Off events are those located in the inter-peak phase regions (fig. 6.12). As a result, the number of excess events will be $N_{exc} = N_{on} - \frac{\delta}{1-\delta}N_{off}$, where δ is the fraction of the light curve where one expects to find the pulsed emission contribution (duty cycle).

H uniformity test Another method to extract upper limits to the pulsed emission is by means of the uniformity test applied to the data. In this Thesis, the H test has been applied to extract the signal significance for the pulsed emission of the source, because of our ignorance about the pulsar light curve shape at energies above 30 GeV.

In general, the upper limit of the pulsed flux emission can be obtained using the different statistical approaches (frequentist and bayesian) but, following the same criteria for the calculation of the upper limits as in the steady case, a classic frequentist approach will be used.

Given a Z statistical test for uniformity, if Z_{obs} is the result of our uniformity test, the upper limit (x_{ul}) of $x = \delta N^{1/2}$ with a confidence level of $1 - \alpha$ can be found by solving:

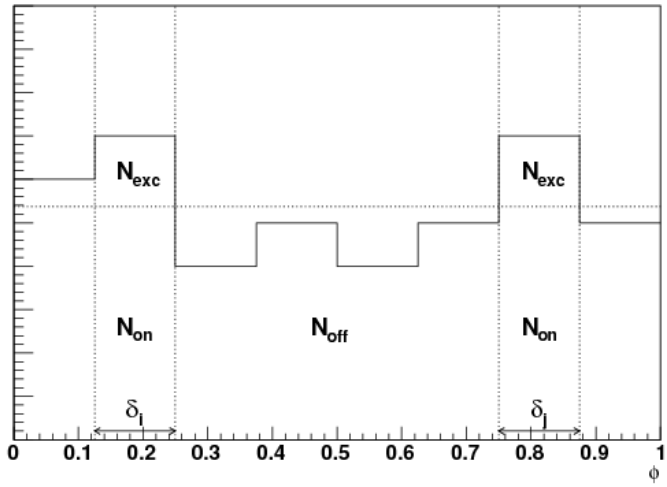

Figure 6.12: *Scheme of a double peak light curve. The number of events for On and Off region are N_{on} and N_{off} respectively. The number of excess events is given by $N_{exc} = N_{on} - \frac{\delta}{1-\delta} N_{off}$ and the fraction of light curve for pulsed emission is $\delta = \delta_i + \delta_j$*

$$\alpha = \int_0^{Z_{obs}} g(Z|x_{ul}) dZ \tag{6.11}$$

where δ is the pulsed fraction, N is the total number of photons and $g(Z|x_{ul})$ is the probability density function of the uniformity test Z, which depends on the assumed shape and strength of the signal ($x_{ul} = \delta_{ul} N^{1/2}$) [49].

Solving the last equation in the case of Z = H, a statistical test of uniformity for the upper limit on the number of excess events will be obtained for a given fraction of the light curve for the pulsed emission as well as a confidence level.

Chapter 7

Pulsars data analysis: PSR J0205+6449 and PSR J0218+4232

This Chapter shows the results of the analysis of the data taken by the MAGIC telescope from two pulsars belonging to different pulsar's populations: canonical (PSR J0205+6449) and millisecond (PSR J0218+4232) pulsars.

7.1 Introduction

Observations of pulsars and pulsar wind nebulae (PWN) have been conducted during the last two years using the MAGIC Imaging Cherenkov Telescope. In addition to the study of the nebula emission, the low energy threshold of MAGIC offers the opportunity to search for the pulsed emission from the pulsar within the nebula with very high sensitivity.

As it was described in chapter 2, the PWNs are described as the end product of a core-collapse supernova which leads a pulsating neutron star radiating its surroundings and forming the pulsar wind nebulae (also called plerion at high energies).

The selection of these two specific pulsar-PWN system as the best candidates γ-ray emitters was based on their spin-down luminosity and the probability of emission given the various models of the VHE γ-ray production above 100 GeV.

Following this selection criteria, PSR J0205+6449 is the second best candidate among the canonical pulsars after Crab, followed by the EGRET detected pulsars Geminga and PSR B1951+32. The narrow pulse profile and the hard spectrum at X-rays of the pulsed emission from PSR J0205+6449 make it a very promising target for the next generation of high energy detectors with a threshold in the GeV range.

The other source analyzed in this Thesis is PSR J0218+4232. This millisecond pulsar is of special interest because of the evidence for the first detection of pulsed γ-ray emission from a millisecond pulsar by EGRET [104]. Only 5 millisecond pulsars have been detected at high energies, mainly at soft X-rays, amongst them PSR

Canonical pulsars			Millisecond pulsars		
Pulsar (PSR)	P (ms)	E/d^2 ($\times 10^{38}$) (ergs kpc^{-2} s^{-1})	Pulsar (PSR)	P (ms)	E/d^2 ($\times 10^{34}$) (ergs kpc^{-2} s^{-1})
B0531+21	33.1	1.2	B1957+20	1.6	6.8
J0205+6449	65.7	0.026	J0613-0200	3.1	5.8
J1833-1034	61.9	0.018	B1257+12	6.2	3.2
J0633+1746	237.1	0.013	J0034-0534	1.9	3.1
B1951+32	39.5	0.006	J0751+1807	3.5	1.9
J1930+1852	136.9	0.005	J1012+5307	5.3	1.7
B0656+14	384.9	0.005	J1906+0746	144.1	1.3
J1747-2958	98.8	0.004	**J0218+4232**	2.3	0.7
B1823-13	101.5	0.002	J2019+2425	3.9	0.6
J2229+6114	51.6	0.002	B1855+09	5.4	0.6

Table 7.1: *Top ten list of the best pulsar candidates from the ATNF pulsar catalogue observable by MAGIC at observation zenith angles below 60°. The candidates list is divided between canonical (left) and millisecond (right) pulsars. PSR J0205+6449 is the second best candidate of the canonical pulsars list while PSR J0218+4232 is at the 8th position of the millisecond pulsars best candidates.*

J0218+4232.

This chapter describes the observation of the pulsar-PWN systems: PSR J0205+6449/3C 58 and PSR J0218+4232 performed with MAGIC, showing the results obtained from the pulsed and non-pulsed emissions.

7.2 Pulsar data analysis

The two pulsars analyzed in this chapter, PSR J0205+6449 and PSR J0218+4232 were targets of the MAGIC observation cycle I (2005) and II (2006), respectively.

7.2.1 Observation mode for pulsars

As it was explained in previous chapters, there are two different observation modes with the MAGIC telescope: *wobble* and *On-Off*. Both observation modes have advantages and disadvantages. The wobble mode has the advantage over the On-Off mode of producing simultaneous On and Off data. At the standard distance from the camera center in wobble observation mode of 0.4°, the telescope efficiency decreases to ∼60% [127]. The decrease of the efficiency results to a telescope sensitivity of around ∼ 80% in this observation mode and could cause an increase of the energy threshold.

Due to the weakness of the pulsar sources at GeV energy range, all the pulsar data were taken in On-Off observation mode in both MAGIC cycles (I and II). In order to have as much On data as possible all the observation time required was spent pointing to the source (On data). Therefore, there was no Off data taken specifically for each source, extracting the Off data set from no-signal source data at the same zenith angle range of each source.

7.2.2 Data quality checks

Before any analysis it is necessary to perform a cleaning of the data sample to reject data runs with bad data quality.

Because pulsars are very weak sources and the timing analysis has a higher quality factor than the steady standard analysis, the quality criteria for run rejection can be more relaxed in order to keep as much data as possible.

The first quality check is to select those runs taken with good weather conditions, with good pointing accuracy and without unusual rates after the image cleaning.

The requirements were:

- Data miss-pointing: Star guider miss-pointing < 12' and number of identified start > 20. A pointing accuracy of 1 pixel, with a clear sky.
- Weather conditions:
  - Clouds: Humidity <70 % and number of identified stars > 20. No clouds.
  - Windy: Wind speed <30 km/h. An stable pointing.
- Proper data mean rate per run: ΔRate(Hz)/<Rate> < 20% after image cleaning. All runs with a rate dispersion above 20% are rejected from the analysis.

After this first "run cleaning" of our data I applied a set of cuts to remove those events that introduce known bugs in our analysis:

- Sparks events: $log10(Size) < 1.6 - 2.93 * log10(Conc2)))$
- Camera border effect: $Leakage1 < 0.1$.
- Mismatch MC protons and real data hadrons: Number of core pixels > 4.

These "event cleaning" conditions will be included from the beginning in our data in the RF training and in the final runs for the analysis.

The image cleaning used in our analysis is "absolute standard" with Lvl1 = 10 phe and Lvl2 = 5 phe. This is considered in the following "analysis cuts" to improve the sensitivity of the telescope mainly at low energies:

- Number of Core Pixels > 5.

- Number of Islands < 3.
- $0.2 <$ Dist(°) < 0.9. Static distance cut.
- Hadronness. Optimized for each energy range with Crab Nebula data within the same zenith angle range of On data samples.

Owing to the direct dependency of the distance parameter with the energy and zenith angle (chapter 1), a conservative value of the upper limit on the static cut on distance parameter has been chosen because our analysis will be mainly focused on low energy events. Taking higher values of the dist cut like 1.1 will lead to an increase of hadron showers pointing towards the camera center due to the MAGIC camera geometry (hexagon angles). This will give rise to an increase of the events at low α values from background signal in On and Off α-distribution. This steepness in the α-distribution makes the On-Off normalization region in the α-distribution ($30°<$ α $<90°$) not very flat, introducing a systematic error in the signal extraction. This can results in "fake" signals at low energies, mainly due to the very inhomogeneous efficiency of the camera at those energies, as it will be seen in the next sections.

7.2.3 γ/hadron separation

The parameters used to train the Random Forest (RF) in the α-analysis are:

- log10(Size), Length, Width, Conc, Asym.
- $\frac{Size}{Length \cdot Width}$, $\frac{M3Long \cdot Cos\Delta\alpha}{|Cos(\Delta\alpha)|}$
- Dist

For the Disp-analysis the last parameter (Dist) is excluded from the RF parameters.

The parameters included in the Random Forest for the energy estimation are:

- log10(Size), Dist, Length, Width, Conc, Leakage1.
- $\frac{Size}{Length \cdot Width}$.
- Zenith angle (Zd).
- MC true energy (MMcEvt.fEnergy).

In the analysis of this Thesis, the Random Forest has been trained with a MC-γ subsample, applying the resulting RF matrices to a second independent subsample to estimate the energy. The estimated energy and the RF matrices have been applied to a third independent subsample for MC testing purposes in the rest of the analysis. In the RF training process a subsample of On data has been used as the hadron subsample, in order to have a data sample comparable with MC-γ in terms of zenith angle range.

7.2.4 Timing analysis

The program used in the timing analysis on this Thesis is the Mars executable *SearchPeriod*. Details of this program and the flux upper limit calculation in this Thesis have been described in chapter 6.

Due to the availability of contemporaneous ephemeris to the MAGIC observation data, the timing analysis has been restricted to the search of pulsed emission at a given rotational frequency.

The timing analysis will keep the same "event" cleaning and "analysis" cuts as in the steady emission analysis, but changing the upper limit cut on the number of core pixels to 4. The low value would lead to a decrease of the sensitivity of the steady emission analysis due to the increase of background included in the analysis. However the sensitivity of the timing analysis depends a lot on the light curve shape. Therefore, it is expected that for narrow peaked light curves (like PSR J0205+6449 and PSR J0218+4232), the increase of the signal to noise ratio, due to this relaxation in the number of core pixels cut, would increase the timing analysis sensitivity including more gammas in the analysis.

The only cut from the steady analysis not applied here is the hadronness cut, due to the unavailability of any calibration source from which optimize the hadronness cut at very low energies.

7.3 PSR J0205+6449 / SNR 3C 58

The supernova remnant 3C 58 and the pulsar PSR J0205+6449 form a "Crab-like" pulsar-PWN system. Due to its similarities with the Crab remnant, 3C 58 was identified as a pulsar wind nebulae (PWN) twenty years before its pulsar was discovered in X-rays [116] and radio wavelengths [34].

3C 58 (G130.7+3.1) was first detected by the *Einstein Observatory* [21] and associated with the remnant of the supernova recorded in A.D. 1181 (SN 1181). This association implied an age of 820 yr, although it was not unanimous and evidences of the association inconsistency (like spin-down age and the nebula expansion velocity) have accumulated in the last years [78] .

7.3.1 Source overview

The pulsar is located at RA = $02^h05^m37^s.92$ and DEC = $+64^o49'42''.8$ [139] at a distance of 3.2 kpc.

This Crab-like system seems to be 4 times older and has a spin-down luminosity ~ 0.02 times the one of Crab pulsar, although its surface magnetic field is of the same order of magnitude.

The PWN has an extension twice that of the Crab nebula and is fed by a nearly aligned rotating pulsar pointing toward us.

The pulsar PSR J0205+6449

The pulsar PSR J0205+6449 was discovered on 2000 at the center of the remnant SNR 3C 58 by the Chandra X-Ray Observatory [116], and soon confirmed in archival RXTE data [116] from 1997 observations. In 2002 it was confirmed in radio wavelengths finding extremely faint radio pulsations with the Green Bank Telescope [34].

The radio measurements [34] have revealed pulsar parameters typical of young pulsars: $\dot{E} = 2.7 \times 10^{37} erg/s$, $B = 3.6 \times 10^{12} G$ and $\tau = 5400$ yr.

The pulsed emission coming from the neutron star has different features depending on the observations energy range. PSR J0205+6449 has been detected in radio and X-rays wavelengths. The details of these detections will be described below.

Emission at radio wavelengths The observations reporting the discovery of PSR J0205+6449 in radio wavelengths were carried out by the 100 m Green Bank Telescope (GBT) at 820 MHz and 1375 MHz. The average pulse profile at both frequencies, dedispersed at DM = 141 cm^{-3} pc, consists of a single narrow pulse of width ∼0.05P (fig. 7.1), absolutely aligned with the X-ray profile. However there is no evidence at these frequencies for the existence of an interpulse with amplitude $\geq 15\%$ that of the sharp pulse, in contrast with the X-ray profiles (fig. 7.3).

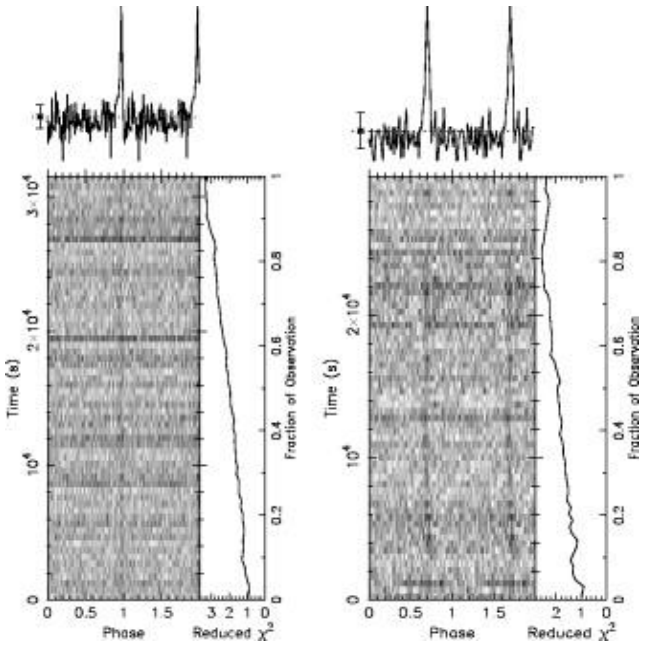

Figure 7.1: *Pulse profiles as a function of time (bottom) and summed (top) for Green Bank radio telescope (18hr). Left: Data at a center frequency of ν = 1375 MHz. Pulse FWHM of 2.3 ± 0.3 ms. Right: Data at ν = 820 MHz. Pulse FWHM = 3.8 ± 0.4 ms. Observation data between 2002 February 22nd - 23rd. [34]*

The spectral index between 800-1400 MHz is $\alpha \sim -2.1 \pm 0.6$, and the radio luminosity is $L_{1400} \sim 0.5(d/3.2\ kpc)^2\ mJy\ kpc^2$ [34].

X-ray emission The first observations of SNR 3C 58 by *Einstein* and *ROSAT X-ray* detected a compact object at the center of the remnant, although no periodic signal was detected.

After more than 20 years of searching in X-ray and radio wavelengths the *Chandra X-Ray Observatory* detected a double-peak light curve with a significance $\sim$6.7 σ. The light curve obtained with Chandra (fig. 7.2) shows a double-peak signal slightly asymmetric with the pulses separated $\sim 180^o$ in phase angle. The pulsed fraction for the folded light curve is $\sim$21%. The main pulse has the same sharp structure and width ($\sim 0.04P$) as the radio pulse, with amplitude of the interpulse $\sim$ 30% that of the main pulse.

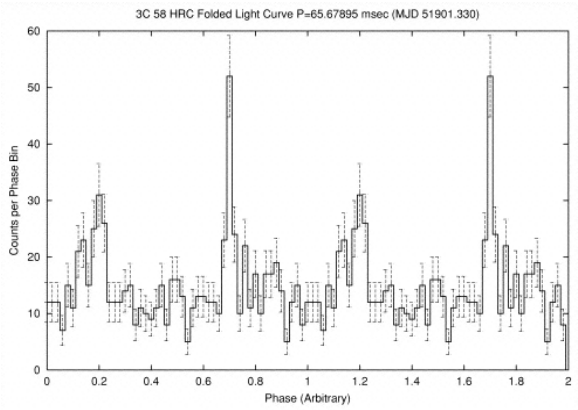

Figure 7.2: *Folded light curve for the HRC-S (Chandra) observation (0.07 - 7.29 keV) of SNR 3C 58 for the 65.67895 ms period. The best profile has a significance of* $\sim 6.7\sigma$. *Observation on 2000 December 23rd. [116]*

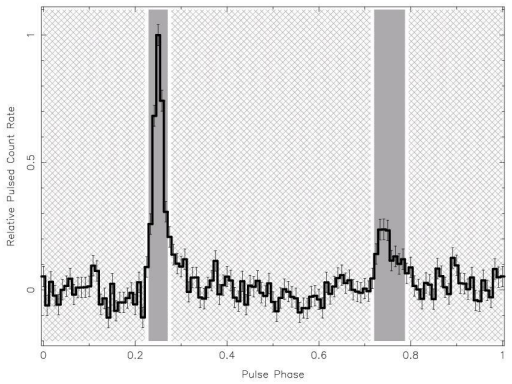

Figure 7.3: *Folded light curve from RXTE observation (2-16 keV) of SNR 3C 58 (*$\sim$ *114 hr). Observation time: MJD [52320 - 52780]. [116]*

After the Chandra detection, RXTE data from 1997 September 30th confirmed the detection at 2-60 keV energies with a significance of $\sim 11\sigma$ [116]. The pulsar timing behaviour is extremely noisy. Analyzing all the available RXTE data on 3C 58 from 2002 February to 2003 May a giant glitch ($\Delta\nu/\nu \sim 1\times10^{-6}$) [130] was discovered that occurred around 2002 October 8th (MJD 52555). The folded light curves at X-ray energies show a delay between the radio and the X-ray main pulse (fig. 7.1 and fig. 7.3) which could be explained by energy-dependent features of the emission mechanism. This differences in the emission features can be also seen between the Chandra and RXTE energy bands (0.07-7.29 keV and 2-10 keV respectively) (fig. 7.2 and fig. 7.3).

This can be seen in the measured photon indices $\Gamma = 0.84$ and $\Gamma = 1.73$ for the main pulse and the interpulse, which are difficult to reconcile with the $\Gamma = 1.73 \pm 0.07$ photon index measured with Chandra [139].

γ-ray emission The flux sensitivity of the EGRET instrument ($E > 100MeV$) to search for PSR J0205+6449 emission is $F_\gamma \sim 5 \times 10^{32} ergs^{-1}\ kpc^{-1}$ (for a typical photon index of $\Gamma = 2$ for γ-ray emitting pulsars). If the rotational power conversion efficiency to γ-rays follows the relation $\eta \propto \dot{E}^{-1/2}$, the extrapolated flux may be just below the detection threshold of EGRET.

SNR 3C 58

The pulsar in 3C 58 is the most similar one to Crab and is the second highest spin-down powered pulsar in the Galaxy. However, PSR J0205+6449 powers its PWN with ~ 15 times less energy than Crab. This leads to a radio luminosity of the remnant of ~ 10 times less than that of the Crab, while in X-rays 3C 58 is a factor ~ 2000 lower.

The large scale structure of 3C 58 is similar to that of other PWN, including the Crab Nebula, with a central region dominated by the pulsar. Figure 7.4 shows the nebula morphology at different wavelengths.

Since its discovery, further X-ray and radio observations have revealed additional details of the PWN system, like the structure spectrum of the nebula, evidence of thermal emission, etc.

The nebula expands with a velocity of ~ 900 km/s and has a column density of $N_H = (4.5 \pm 0.09) \times 10^{21}\ cm^{-2}$ [140], with no evidence of a radius dependence. The low expansion velocity of the SNR contradicts the assumption of 3C 58 being the remnant of SN 1181, suggesting on the other hand an age ~ 7000 yr [25], consistent with the spin-down age of the pulsar ($\mathrm{P}/\dot{P} = 5380$ yr).

X-ray emission Chandra observations of 3C 58 (fig. 7.4) show an extended structure perpendicular to the long axis of the nebula (east-west direction) produced by the pulsar. This structure is interpreted as a torus associated with the pulsar wind termination shock, similar to the structure observed at Crab, with a jetlike feature, of ~ 30" to the west nearly perpendicular to the inferred torus structure. The orientation of the torus allows to suppose a pulsar rotation axis tilted out 30° with the line of sight, with the eastern side beaming toward us [139].

X-ray measurements show a PWN emission dominated by a synchrotron power-law spectrum from high-energy electrons, with a faint thermal component mainly at the outer regions (fig. 7.5). The spectral index in X-ray and radio wavelengths get steeper with the distance from the nebula center as a result of the electron short lifetime, supporting the hypothesis of a pulsar powering the nebula. The spectrum steepness is gradual and similar at both wavelengths, although the X-ray emission extends up to $\sim$20" or i.e., far beyond the radio emission contour ($\sim$6').

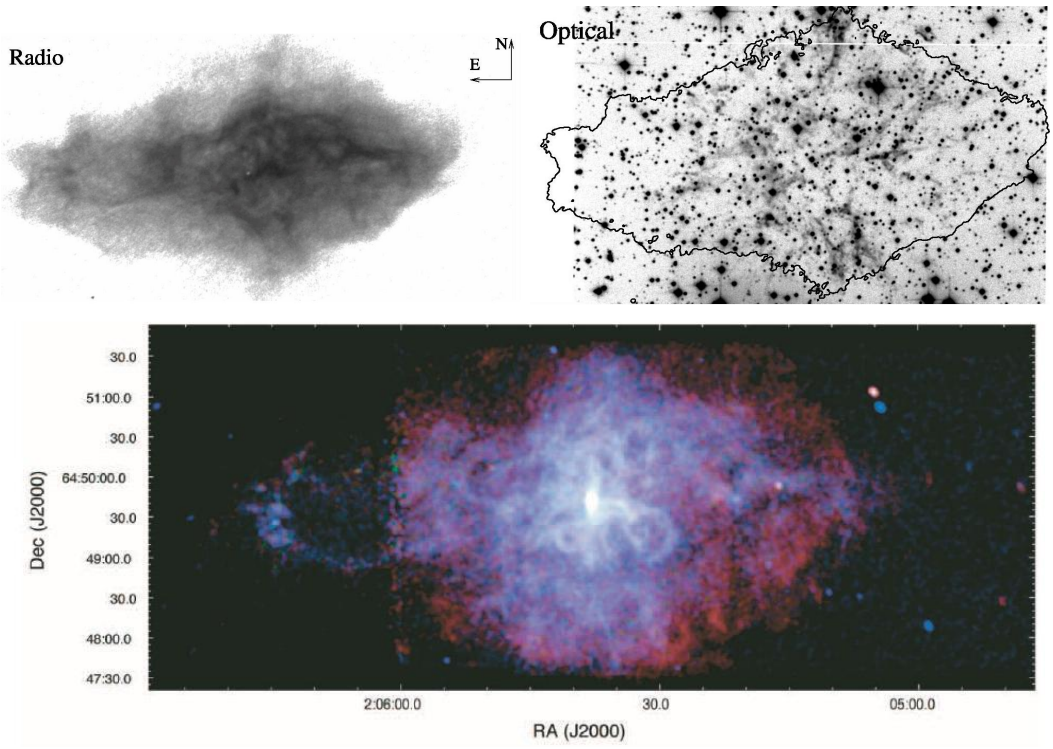

Figure 7.4: *Image of the PWN 3C 58 at different wavelengths. Top-left: VLA (radio) 1.4 GHz [25]. Top-right: Hα (optical). Contour line corresponds to radio image bounds. Bottom: Chandra (X-ray, 0.5-10 keV) [140] image ($0^h.03$,0.007°).*

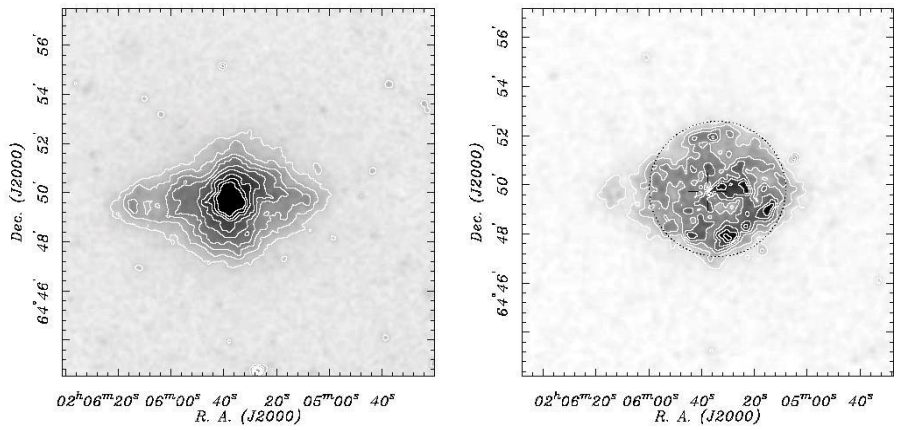

Figure 7.5: *XMM-Newton image of PWN 3C 58 (left)(1.0-2.0 keV) ($0^h.03$,0.3°)) and the thermal shell (right) image (0.5-1.0keV). Observation time ∼ 343 ks between 2002 September 11-13 [78]. The cross in the right plot corresponds to the pulsar location (27"±5" east from thermal shell center).*

Optical emission Optical observations reveal knots and filaments, also seen in X-rays and radio observations (fig. 7.4), with velocities $\sim 900 kms^{-1}$. The presence of these filaments and the high abundance of Ne and Mg indicates a disrupted toroid-shape magnetic field by the interaction of the expanding bubble and the supernova ejecta [140].

Radio emission Figure 7.4 shows the radio morphology, which resembles the observed one in X-rays, with estimated emission confinement regions for both wavelengths.

Radio polarization measurements infer a PWN magnetic field of B_{neb} $\sim 80\mu$G and support the previous hypothesis [140] for the filaments origin of a torus structured magnetic field, probably disturbed by kink instabilities. This scenario shows a synchrotron nebula expanding into the supernova ejecta at low velocities ($v_{exp} = 630 \pm 70 kms^{-1}$).

γ-ray As it was explained before, the high spin-down luminosity of the pulsar which feeds the PWN 3C 58 makes it a good candidate as TeV γ-ray source.

Guided by previous detections at VHE of similar objects, Whipple IACT collaboration included 3C 58 in a program conducted to search for galactic TeV emitters. A 4 hours observation of 3C 58 yielded only a flux upper limit $F(E > 500GeV)(99\%CL) < 1.31 \times 10^{-11} cm^{-2} s^{-1}$ [85].

7.3.2 MAGIC observations: PSR J0205+6449/3C 58

The observations of PSR J0205+6449 (3C 58) were part of the Cycle I of MAGIC observations. The data were taken between September and December of 2005 (MJD 53625.0 - 53707.0) in the On-Off observation mode. The final data sample doesn't include data taken with moon presence in order to get a more homogenous data sample.

Tables 7.2 and 7.3 show a summary of the daily On and Off data quality and the characteristics of the final data set.

The On data table 7.2 specifies, for each day: the mean PSF, the zenith angle range and mean rate after image cleaning of the data sample observed. The last two columns give the night observation time (in minutes) and the total time of night data that will be used in the analysis. The quality check reasons for rejecting part of the data of the night are indicated in the second column.

Table 7.3 summarizes the Off source data parameters. As in the On data summary, the mean zenith angle range and the mean rates after image cleaning of the sample are listed. The last two columns show the total observation time and the total observation time used in the analysis.

Because no specific Off data for this source were taken, the Off data set for the analysis was conformed retrieving a few hours of different sets of sources for which no

Date	Quality check	PSF (mm)	θ (°)	Rate a.c. (Hz)	T_{Obs} (min)	T_{Obs}^{Eff} (min)
2005 Sept 12	M	16.6	35 - 39	127 ± 37	153	141
2005 Sept 28	M	16.3	35 - 37	126 ± 4	106	49
2005 Sept 29	M	14.1	35 - 40	130 ± 1	100	91
2005 Sept 30	M	12.1	35 - 41	115 ± 3	114	98
2005 Oct 1	C	12.5	—	—	114	0
2005 Oct 2	C	12.5	—	—	49	0
2005 Oct 3	M	13.4	35 - 42	137 ± 3	117	107
2005 Oct 4	OK	13.4	35 - 41	143 ± 2	112	112
2005 Oct 5	M	12.8	35 - 42	134 ± 2	118	104
2005 Oct 6	M	11.6	35 - 42	127 ± 1	113	87
2005 Oct 7	C	12.1	—	—	84	0
2005 Oct 11	OK	12.3	36 - 39	140 ± 1	69	69
2005 Oct 25	M	15.2	35 - 45	137 ± 2	140	136
2005 Oct 26	H	13.3	36 - 42	128 ± 3	81	80
2005 Oct 29	M	15.7	35 - 42	134 ± 2	108	104
2005 Nov 1	M R	15.4	36 - 41	133 ± 1	105	68
2005 Nov 2	H R	15.5	36 - 41	129 ± 6	100	86
2005 Nov 3	H	15.1	36 - 41	130 ± 7	86	86
2005 Nov 4	M	15.1	36 - 42	130 ± 10	75	65
2005 Nov 5	R	16.8	38 - 41	138 ± 4	70	38
2005 Nov 6	M	15.1	36 - 42	132 ± 3	90	88
2005 Nov 7	OK	15.3	36 - 40	135 ± 2	71	71
2005 Nov 21	M	15.1	37 - 40	143 ± 2	44	36
2005 Nov 24	M	13.9	37 - 40	119 ± 3	18	17
2005 Nov 25	M	–	37 - 40	122 ± 6	44	40
2005 Dec 3	M	14.7	37 - 39	122 ± 2	40	36
Total		**15±3**	**35° - 45°**	**130±10**	38.7 (h)	**30.2 (h)**

Table 7.2: *PSR J0205+6449 data sample. The quality check criteria gives the reason of the data rejected for the analysis (miss-pointing (M), cloudy night (C), abnormal rates (R) or abnormal distributions of the Hillas parameters (H) and no rejection (OK). The amount of time (minutes) rejected in the analysis is given by* $T_{Obs}^{Eff} - T_{Obs}$.

hint of signal was reported. The list of sources used and data sample parameters are shown in table 7.3. To guarantee the same data taking conditions, the Off data were selected among those sequences with the same image response[1] (PSF = 15±3 mm) and pedestal RMS (P_{RMS} = 1.09±0.07) as the On data. This guarantees a spread of

[1]Optical PSF: obtained from the analysis of the spread of muon rings

Date	θ (°)	Rate a.c. (Hz)	T_{Obs} (h)	T_{Obs}^{Eff} (h)
GRS1915				
2005 Oct 4 - Nov 3	16 - 61	138 ± 20	12.7	8.9
TeV2032+42				
2005 Nov 4 - 6	32 - 41	121 ± 3	1.5	0.7
PSRJ2229+61				
2005 Aug 2 - Dec 2	31 - 38	120 ± 10	12.5	10.2
Total	16° - 61°	**120 ± 20**	37.5 (h)	**19.7 (h)**

Table 7.3: *Off data sample for PSR J0205+6449. PSF = 15 ± 3 mm, P_{RMS}(Inner pixels) = 1.09 ± 0.07.*

light forming the Hillas images of less than 20% in the PSF of the observations and a dispersion of 6% on the image noise for the whole analysis sample.

Due to a lack of data for the same high zenith angles ($\theta > 35°$) and data taking conditions as the On data, the zenith angle range for the Off data has been increased to 16°-65°. Because the Off sample will be used only for significance extraction, it has been considered more important to increase the statistic than to keep the exact range of zenith angles.

In order to keep as much Off data as possible, some data quality check criteria have been relaxed for the Off data sample for the analysis. Therefore, the Off data sample includes data with high miss-pointing and clouds as long as the total Off data rate stayed within the rate range of the On sample during the whole On data taking period (fig. 7.6).

To check whether the On and Off samples are equivalent before any γ/h separation analysis, I have compared the On and Off data rates during the observation period and the pointing zenith angles (fig. 7.6 and 7.7), the telescope miss-pointing in the observations zenith angle range (fig. 7.7,bottom), the Hillas parameters distribution (width, length, dist and size) (fig. 7.8) and the camera efficiency homogeneity (fig. 7.9)

Comparing On and Off data samples it can be seen that they match quite well and both are stable during the whole analysis data sample. This indicates that the telescope response was nearly the same during both observations, thus it is justified to use the same hadronness cut for On and Off data selection.

In the camera homogeneity plots (fig. 7.9) one can see that for high energies the camera efficiency is nearly the same for both data samples, while there is a clear mismatch between the camera response in the upper right corner during the On and Off data taking for low energies. This corresponds mainly to $\phi = 0°$ - $90°$. The reduction in efficiency in this part of the camera could lead to the detection of a "fake" signal at low energies due to a higher efficiency of On events triggered in

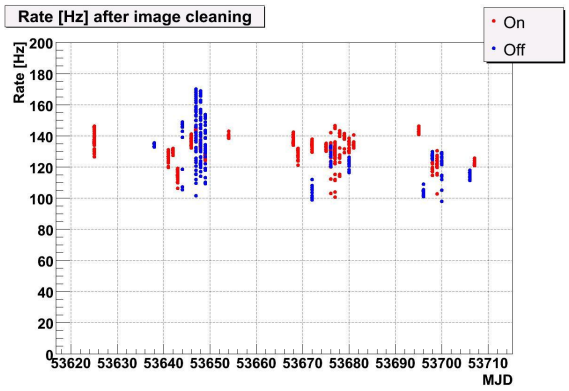

Figure 7.6: *Rates after image cleaning of the ON (red points) and OFF (blue points) data sample as a function of time (MJD). The rate stability during the On data observations is ∼20%.*

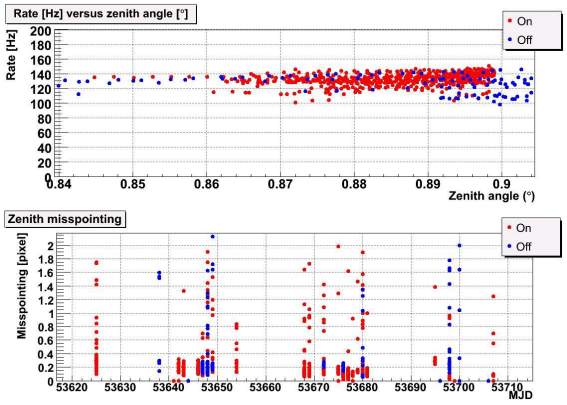

Figure 7.7: *ON (red points) and OFF (blue points) data rates after image cleaning as a function of the observation zenith angle (top) and data miss-pointing (in camera pixels) as a function of time (MJD).*

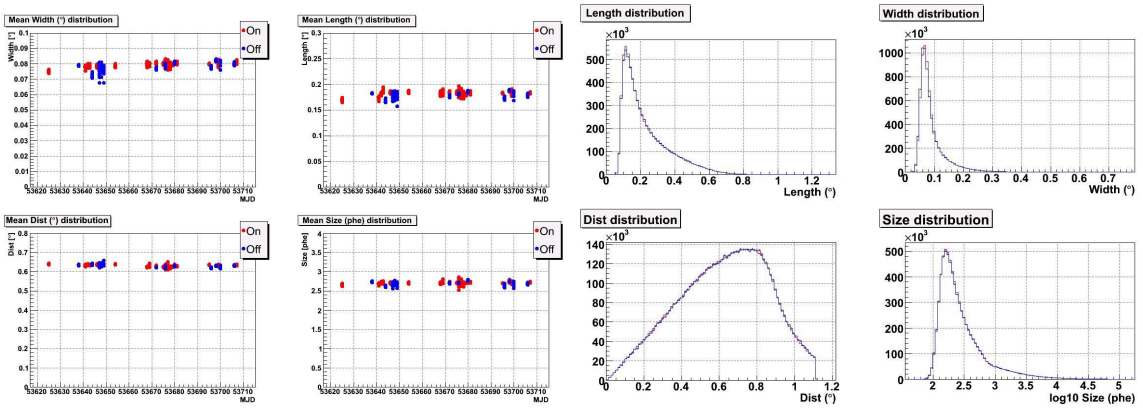

Figure 7.8: *Hillas parameters (width, length, dist, size) distribution (right) and stability (left) for On (red) and Off (blue) data applying analysis cuts and Size > 60 phe. The distributions are normalized to the same number of events.*

this area. There are several possible reasons for this inhomogeneity of the camera response. One could be a bad pixel threshold setting for some pixels. Other ones are possible defective pixels in the camera due to a variation of the pixel gain or the presence of stars in the MAGIC FoV. Figure 7.10 shows the stars present in the pulsar field of view during the observations. The ones present within the camera trigger region ($\lesssim 1°$) have a magnitude between 5.58^m - 6.52^m. Neglecting the stars contribution (fig 7.10), the only possible explanation could be a wrong camera flat fielding which can not be corrected through software. This camera response would

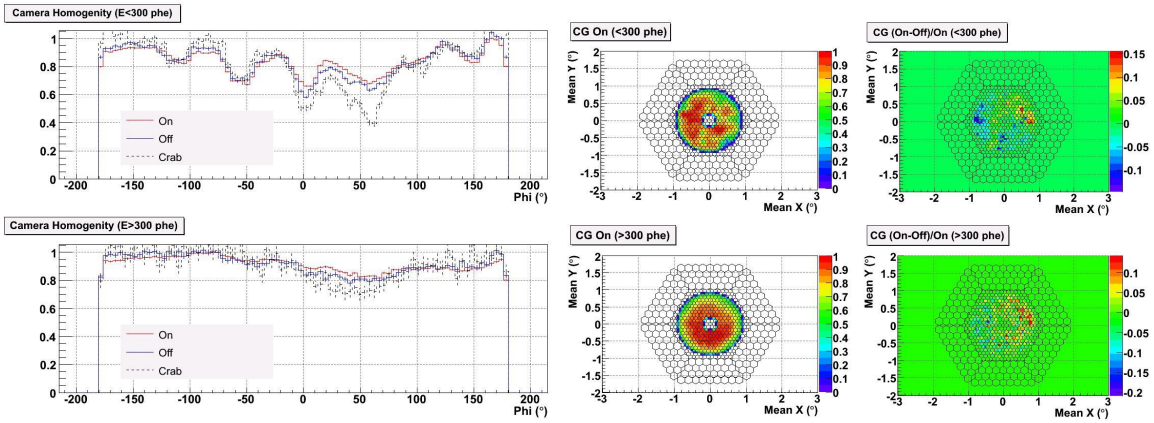

Figure 7.9: *Camera homogeneity distribution computed using the angle of the center of gravity of the events with respect to the center of the camera: angle of the events ($\phi = atan(y/x)$) (left) and 2-D distribution of the event center of gravity (right). The distributions have different energy ranges: low energies (top) (Size < 300 phe) and high energies (bottom) (Size> 300 phe). The center of gravity distributions of On and Off data sample have been normalized to the On events distribution. The point $\phi = 0°$ corresponds to (meanX,meanY) = (0.8,0) while $\phi = 90°$ to (meanX,meanY) = (0,0.8)*

have to be present in the rest of the analysis, mainly at low energies.

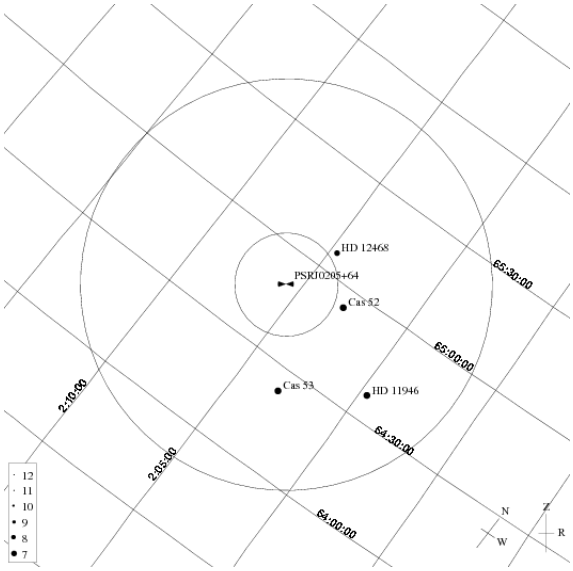

Figure 7.10: *FoV (∼2.8°) around PSR J0205+6449 from of Roque de los Muchachos observatory (La Palma) for MAGIC observation period. The eyepieces correspond to FoV of 0.5° and 2° diameter.*

Finally MC-γ are used to determine the resolution of the estimated energy of the On sample events (fig. 7.11). For the zenith angle range of this source the energy resolution is ΔE/E$\sim$23% for low energies (Size$\sim$60 - 300 phe) and ΔE/E$\sim$19% at high energies (Size>300 phe) .

The image quality is influenced also by the point spread function (PSF). The point spread function for the origin of γ-showers (PSF$_\gamma$) is calculated through a gaussian fit of the sky map for Crab Nebula (fig. 7.12). The PSF$_\gamma$ found was 0.125° $\pm$ 0.016° for zenith angles between 35°-45° during the observations period of PSR J0205+6449.

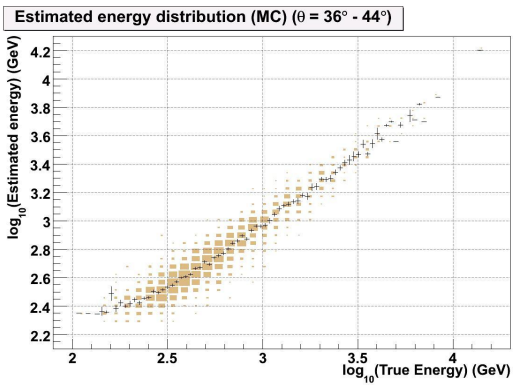

Figure 7.11: *Distribution (filled squares) of the estimated energy versus the true energy for Monte Carlo events. The distribution profile is also displayed (black). The energy resolution is ΔE$\sim$23% for Size$\sim$60 - 300 phe and ΔE$\sim$19% for Size>300 phe.*

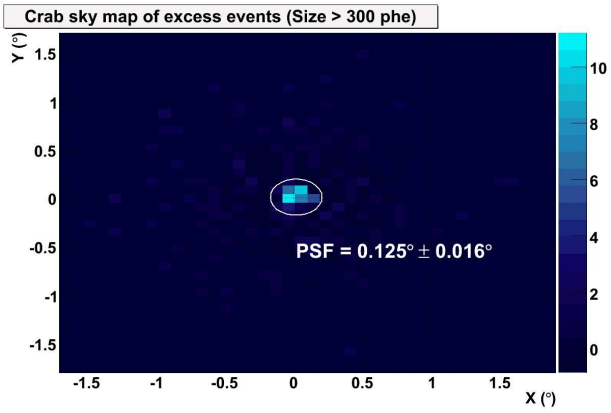

Figure 7.12: *PSF distribution from Crab data between 35°-45° zenith angles at high energies (E>220 GeV).*

7.3.3 MAGIC results: PSR J0205+6449/3C 58

Steady emission: PSR J0205+6449 and 3C 58

As shown in table 7.2, the optical point spread function of the telescope during the PSR J0205+64 (3C 58) data taking was $\sim$ 1.5$\pm$0.3 cm, so MC simulations of the telescope performance at that period with an optical PSF = 1.4 cm will be used in the analysis.

The γ/h cut optimization for this analysis is based on 40 minutes of a Crab Nebula data sample at the same zenith angle range as the On data sample. The Crab Nebula data were taken between 2005 October 6th and November 26th with a mean rate of 125 $\pm$ 25 Hz and the same optical PSF.

As explained in the chapter introduction, a subsample of On data events was used for the RF and energy estimation due to the low statistic of Off data (11 hours) between 25 and 45 degrees of zenith angle. This can be done because of the perfect match between On and Off data (fig. 7.8). The Off data were used only for the θ^2 and α analysis significance extraction and for hadronness cut optimization.

The hadronness cut for the γ/hadron separation was optimized with the Crab and Off data samples to reach the highest significance (eq. 6.1) and, therefore, the highest telescope sensitivity at each energy range.

The tail cut used in the image cleaning applied in the analysis (10 phe for core pixels and 5 phe for boundary pixels) and software trigger condition (5 NN) fixes a lower size cut in 60 phe. These cuts select MC gammas with E> 54 GeV with an $E_{th} \sim 237$ GeV for the source zenith angle range (table 7.2) in this analysis.

Table 7.4 shows, for each integral size bin, the hadronness cut value which optimizes the Crab signal using formula 17 of Li & Ma [107](σ_{17} is the corresponding significance obtained). This value of the hadronness cut will determine an analysis sensitivity (% of Crab flux) and an energy threshold (GeV) for each size (or energy) bin. The efficiency (in % of surviving events) of the hadronness cut in MC-γ and hadron (Off) samples is also shown in table 7.4.

Size (phe)	Hadr. cut	Hadr. eff. MC-γ (%)	Hadr. eff. Off (%)	E_{th} (GeV)	σ_{17} (Crab)	Sensitivity (% Crab)
> 60	0.175	19	0.1	280	13.1	2.98
> 100	0.175	20	0.1	280	13.1	2.98
> 200	0.175	34	0.2	280	13.1	2.99
> 300	0.175	51	0.3	320	13.3	2.83
> 500	0.175	71	0.3	440	11.8	3.05
> 700	0.175	78	0.3	660	10.0	3.54
> 900	0.175	83	0.2	790	7.5	4.86
> 1200	0.175	83	0.2	950	6.2	5.84
> 1600	0.225	84	0.2	1440	4.5	8.72
> 2000	0.675	97	0.7	1430	5.5	7.17
< 300	0.725	37	4.2	204	7.0	7.78

Table 7.4: *Cut efficiency table for Crab (∼40 min) and PSRJ0205+6449 Off data.*σ_{17} *corresponds to the significance extracted with eq. 17 of Li & Ma [107].*

The α-analysis The α-analysis consists in extracting the signal significance from the excess of events that point towards the camera center (α Hillas parameter).

Once the optimum hadronness cut for each energy bin (table 7.4) has been selected, it is applied to the On and Off data samples, together with the static cuts mentioned in previous sections.

These cuts will yield the best sensitivity on Crab analysis. Allowing at most a miss-pointing in the data of < 2 pixels, it is assumed that all the gamma events coming from the source will point towards the camera center. This will allow us to impose an additional cut of α<10° to select those events coming from the source in the On data sample for high energy showers. For low energy showers (60 phe < Size < 300 phe) the α-cut is increased to α<20° due to the uncertainties in the α parameters reconstruction for less elliptical images, typical of low energy events (fig. 7.13).

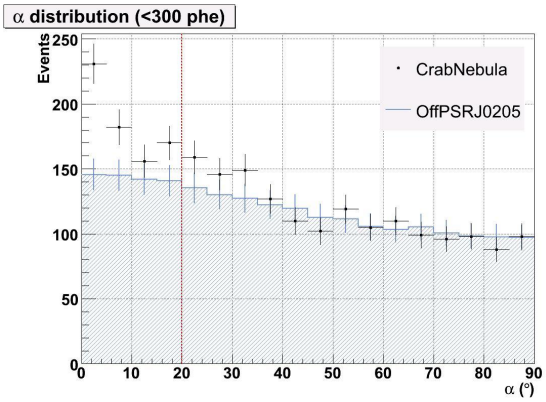

Figure 7.13: *Crab (black-points) and Off (blue-line) α distributions for Size < 300 phe. σ_{17} (40 min) $\sim$ 8.*

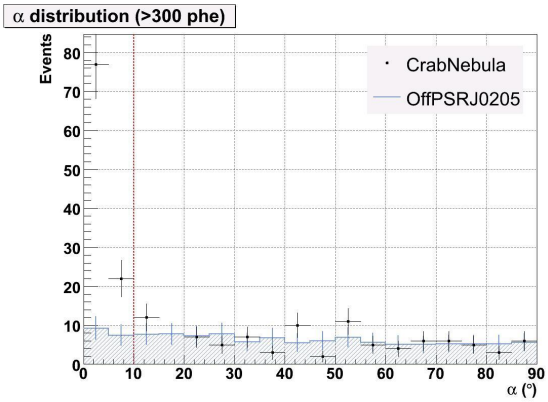

Figure 7.14: *Crab (black-points) and Off (blue-line) α distributions for Size > 300 phe.σ_{17} (40 min) $\sim$ 13.*

Checking first the hadronness cut in the Crab data sample, I obtain 8.6 $\sigma h^{-1/2}$ for low energies (Size < 300 phe) and 16.3 $\sigma h^{-1/2}$ for high energies (Size > 300 phe). The α distribution for Crab data shows a clear signal at high energies (fig. 7.14), while for low energies the excess events are more spread up to $\alpha\sim$20° (fig. 7.13).

The next step in the α-analysis is to apply the α and hadronness cut to the On and Off data sample for different integral size bins, calculating the number of excess and background events (N_{exc} and N_{bg}) to compute the significance (eq. 6.1) of the excess events (N_{on}-$N_{Off,norm}$) over the background fluctuations. The results are listed in table 7.5.

The α distribution of the On (PSR J0205+6449/3C 58) and Off data, for low and high energies (Size < 300 phe and Size > 300 phe., respectively), are displayed in figures 7.15 and 7.16. The α cut applied to each size bin is represented as a dotted line in both figures.

The α-analysis does not yield any significant signal detection for the non-pulsed emission of the PSR J0205+6449/3C 58 PWN-pulsar system.

As it was explained in chapter 6 the final result in case of no signal detection is to calculate the flux upper limits of the source according to our telescope sensitivity. The integral upper limits (table 7.5) are calculated for a 99% C.L. (3σ). Figure 7.17 displays these integral upper limits as a function of the energy.

Size (phe)	E_{th} (GeV)	E range (GeV)	N_{exc}	N_{bg}	Signif. (σ)	F_{UL} $\times 10^{-12}(cm^{-2}s^{-1})$
> 60	280	> 110	51	781 ± 34	1.0	7.7
> 300	320	> 220	40	626 ± 31	0.8	5.9
> 500	440	> 320	44	319 ± 22	1.4	4.0
> 700	660	> 440	38	171 ± 16	1.4	2.4
> 1200	950	> 710	14	73 ± 10	0.7	1.0
> 2000	1430	> 930	12	139 ± 14	-0.4	1.0

Table 7.5: *Results for the 3C 58 analysis in integral energy bins.* $T_{On}^{Eff} = 1815^m$. *The number of background events* (N_{bg}) *are normalized to the number of On events. The number of excess events are* $N_{exc} = N_{on}$-$N_{Off,norm}$.

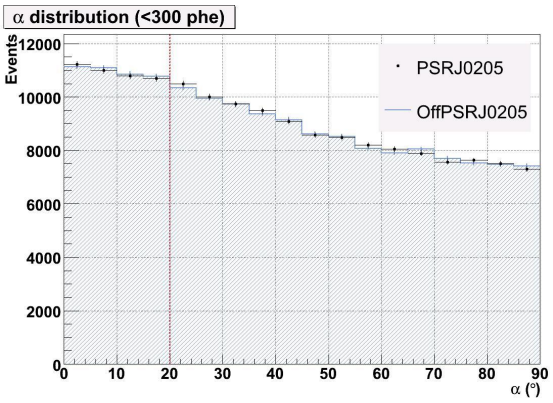

Figure 7.15: *On (black-point) and Off (blue-line)* α *distributions for Size < 300 phe (E∼80-500 GeV,* $E_{th} \sim$ *200 GeV). The red dotted line corresponds to the cut for the signal extraction area* ($\alpha < 20°$). σ_{17} *(1817 min) ∼ -0.4*

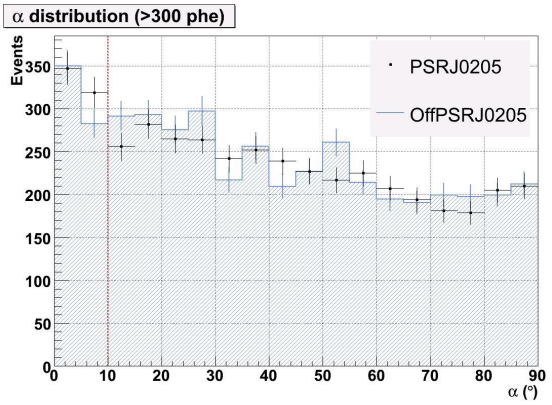

Figure 7.16: *On (black-point) and Off (blue-line)* α *distributions for Size > 300 phe (E> 220 GeV,* $E_{th}\sim$ *320 GeV). The red dotted line corresponds to the cut for the signal extraction area* ($\alpha < 10°$). σ_{17} *(1817 min) ∼ 0.8*

The upper limits are between 1%-10% of the Crab flux, more strict than the previous measurements from other γ-ray experiments (Whipple [85]) at high energies.

The Disp-analysis The α-analysis can provide the significance of the signal detection in case the source is located in the center of the camera. This analysis requires the source to be located at the camera center with a precision of $\pm$ 1 pixel. This is needed to make the α-analysis results reliable.

However, it may happen that the signal emission comes from another point in the sky than the source coordinates or that the emission is spread over a large area and,

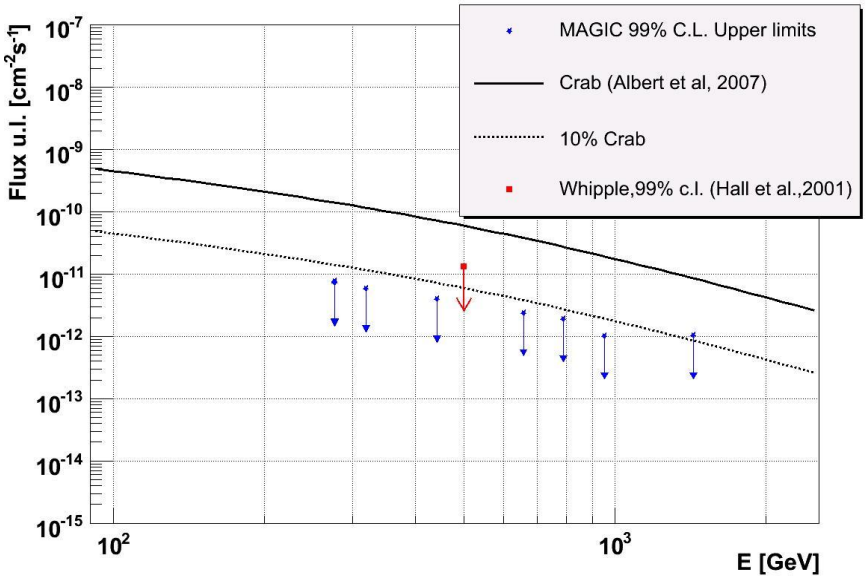

Figure 7.17: *DC Flux upper limits (99% c.l.) (table 7.5) for PSRJ0205+6449/3C 58 (blue arrows). The black lines are the different fractions of Crab flux (10% and 100%). The red filled square corresponds to the upper limit obtained from Whipple observations [85].*

therefore, the α-analysis is not valid anymore.

In case of 3C 58, the emission of the pulsar wind nebula is constrained to a region of 6' $\emptyset$ as seen from radio to X-ray wavelengths. Due to the telescope PSF$_\gamma$ ($\sim 0.125°$) 3C 58 is considered as a point-like source for MAGIC analysis.

The first argument about a possible γ-ray emission coming from another point than the source coordinates, could be true if the emission comes from the interaction of the PWN with the interstellar medium, as happens with other young pulsars like Vela [7].

To analyze this last possibility another kind of analysis than the α-distribution has to be performed. The Disp-analysis calculates the distance (θ^2) of each event to the source coordinates (camera center). This kind of analysis calculates the excess events coming from any point in the sky (see section 6.6.2).

This new analysis requires creating new Random forest matrices without any dependence in source position image parameters (Dist). As the new matrices are not equivalent to the ones used in the α-analysis, the hadronness parameters is not equivalent either. Therefore a new optimum value for the hadronness cut has to be calculated in the same way done in the α-analysis.

These new hadronness cut values, optimized for each energy bin, are shown in table 7.6.

The optimum hadronness cut obtained is applied to the Crab data sample, obtain-

Size (phe)	Hadr. cut	Hadr. eff. MC-γ (%)	Hadr. eff. Off (%)	Sensitivity (% Crab)
> 60	0.39	29	0.6	3.7
> 300	0.39	64	1.3	3.3
< 300	0.57	19	1.6	11.5

Table 7.6: *Hadronness cut efficiency table for the Disp-analysis for Crab (∼40 min) and PSRJ0205+6449 Off data.*

ing a relative decrease on the Disp-analysis sensitivity compared with the α method, at the camera center, of ∼24% for Size > 60 phe and ∼17% at high energies (Size $>$ 300 phe).

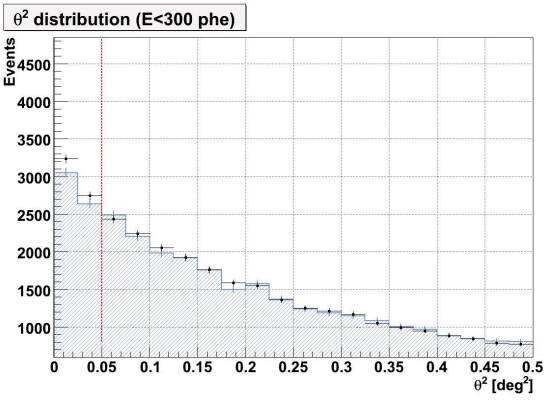

Figure 7.18: *On (black-point) and Off (blue-line) θ^2 distributions for Size<300 phe. The red dotted line correspond to θ^2<0.05° (source at the camera center).*

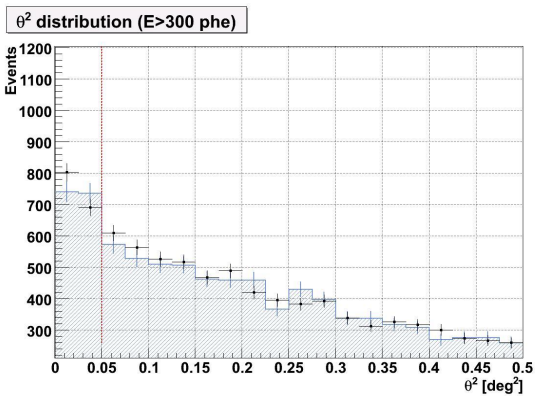

Figure 7.19: *On (black-point) and Off (blue-line) θ^2 distributions for Size>300 phe. The red dotted line correspond to θ^2<0.05° (source at the camera center).*

Figures 7.18 and 7.19 show the θ^2 distribution for the source position for Size < 300 phe and Size > 300 phe, respectively, for the hadronness cuts of table 7.6. Both figures confirm the α-analysis results of no significance emission coming from the source position.

Extending the analysis to a sky map region of 1x1 $(^\circ)^2$ around the pulsar position, figure 7.20 shows the sky map of possible excess significances for each sky position. The significance distribution (fig. 7.20 on the right) reveals no hint of a signal from point like or extended emission up to 0.5° radius from 3C 58 center position.

Search for pulsed emission: PSR J0205+6449

The analysis of the steady emission from the source PSR J0205+6445/3C 58 reveals that this source doesn't emit γ-rays for E> 110 GeV at the level of 7.7×10^{-12}

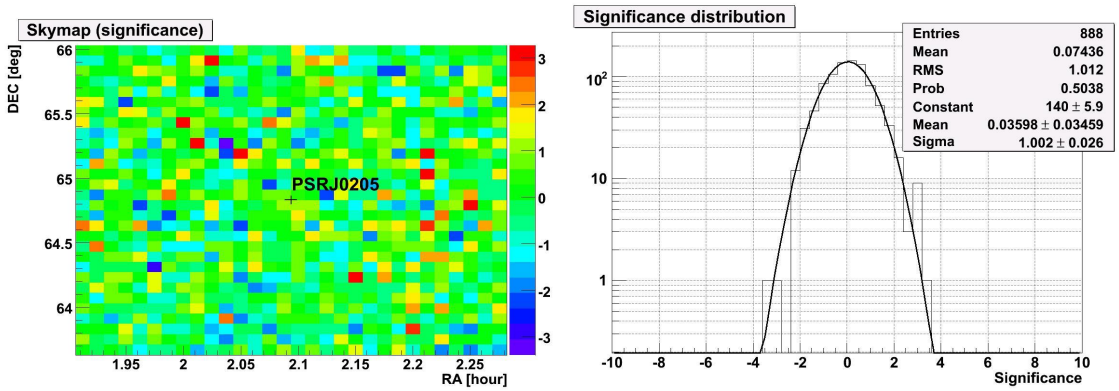

Figure 7.20: *Left: Sky map (significances) for the On search around PSR J0205+6449 for E>110 GeV. The sky map has been scaled to 3σ. The black cross marks the pulsar position. Right: Distribution of significances of the sky map.*

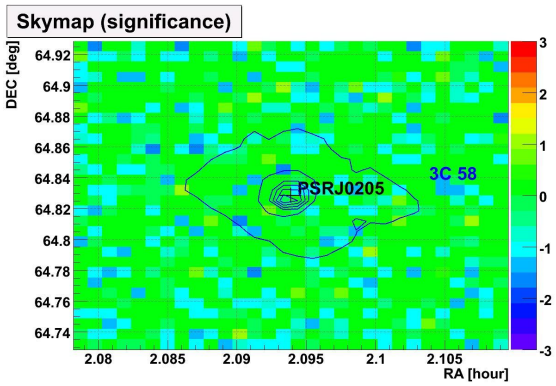

Figure 7.21: *Zoom of the sky map (significances) (fig. 7.20) for the On search around PSR J0205+6449 for E>110 GeV. The sky map has been scaled to 3σ. The black cross marks the pulsar position and the contour lines (blue lines) mark the XMM-Newton image of 3c 58 [78].*

cm^{-2} s^{-1}. This analysis includes the possible emission coming from the pulsar (PSR J0205+6449) and its pulsar wind nebula (3C 58).

As it was explained previously, the hadronness cut is not very effective separating gammas from hadrons at low energies (Size $<$ 300 phe, $E_{th} \lesssim$ 200 GeV). This is especially unfortunate in case of the signal from the pulsar itself, due to the low energies where the spectrum of pulsed emission is expected (chapter 2). The pulsed character of the pulsar signal leads to perform another kind of analysis over the On observations, data looking specifically for the pulsed emission. Such an analysis is more sensitive than the standard excess search for pulsed emission. This approach corresponds to the timing analysis described in chapter 6, where the emission coming

PSR	J0205+6449
RAJ	02:05:37.92000000
DECJ	64:49:42.8000087
F0	15.2186895772360167
F1	-4.509215381905E-11
F2	2.937386722091E-20
F3	6.415286141647E-27
PEPOCH	53682.000001
START	53617.136
FINISH	53726.402
DM	140.700000
EPHEM	DE200
CLK	UTC(NIST)

Table 7.7: *Ephemeris for PSR J0205+6449 from RXTE data [129] in Tempo 1 program format. The validity period is from 2005, September 4th to December 22^{sd}*

from the pulsar will correspond to the sought signal, and the background will be made up by the hadronic background and the emission coming from the PWN.

The Timing analysis The timing analysis software used in this Thesis is the executable *SearchPeriod* (chapter 6) within the standard analysis software for MAGIC.

As it was explained previously, PSR J0205+6449 is a very young pulsar which suffered an abrupt change in its rotation pattern (*glitch*) in 2002 October, while the latest ephemeris available for this pulsar are from 2002 March. Therefore, I need to use ephemeris closer to the observation period of the analysis data sample.

The latest data extracted from RXTE monitoring has provided us with contemporaneous ephemeris to the MAGIC observations of this Thesis. These ephemeris [2] are valid to better than 2% of the pulse phase between 2005 September and December [129]. The ephemeris used in the analysis are detailed in table 7.7.

Due to the validity of the ephemeris during all the MAGIC observations, there is no need of performing any frequency scan. The analysis uses only one value of the pulsar rotational period and the absolute phase alignment of the X-rays and Magic data will improve the significance of our analysis.

The analysis has been guided by the two main models of pulsar magnetosphere emission (chapter 2). The timing analysis has been carried out in two energy bins: E $<$ 300 GeV focussed on low energies in case all the pulsed emission follows the most conservative model (polar cap), and E $>$ 110 GeV (Size $>$ 60 phe), analyzing all the events collected by the telescope in order to include the emission extended up to TeV energies (outer gap).

[2]Thanks to S. M. Ransom (NRAO, Charlottesville).

In addition to the energy cut and the analysis cuts described in section 7.2.4 an α-parameter cut, depending on the expected wideness of the α distribution, has been applied, as it was done for the steady analysis. However, due to the lack of a low energy signal to find out the optimum hadronness cut, I have chosen a conservative hadronness cut which keeps ∼80% of the MC gammas. This conservative hadronness cut has been chosen to keep as many low energy events as possible in order to increase the statistics of pulsed emission photons in the timing analysis. Imposing this condition, for both the E>50 GeV and E<300 GeV samples, I applied an hadronness cut of 0.930 and 0.955 which will keep ∼18% (Q = 1.9) and ∼38% (Q = 1.3) of the hadrons respectively. This hadronness cut is different from the one applied in the steady analysis emission search for each energy range (table 7.4).

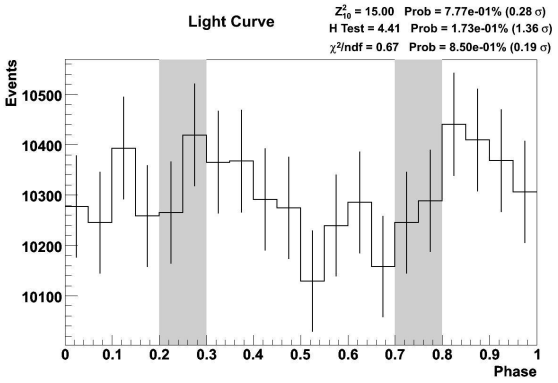

Figure 7.22: *Light curve for PSR J0205+6449 for all energies and α<10º (Hadronness<0.930 and Q∼1.9). The shadowed area corresponds to the RXTE pulse peaks [130]. Signal significance ∼ 1.4 σ from the H-test.*

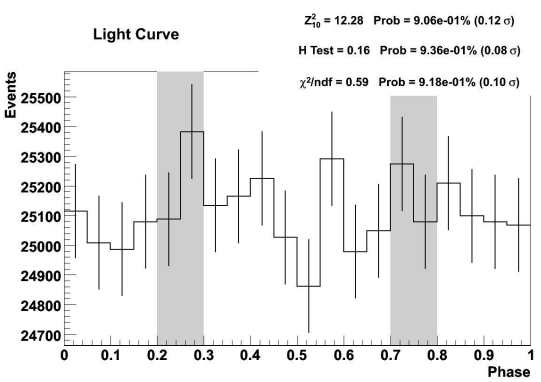

Figure 7.23: *Light curve for PSR J0205+6449 for E<300 GeV and α<20º (Hadronness<0.955 and Q∼1.3). The shadowed area corresponds to the RXTE pulse peaks [130]. 0.1σ signal significance for the H-test.*

Figures 7.23 and 7.22 show the light curves for the ephemeris frequency for the low and all energy samples, applying the analysis cuts mentioned previously. The shadowed areas correspond to the rotational phase intervals where the X-ray pulse is emitted (fig. 7.3).

The results of an uniformity H-test yields a significance signal detection of 1.4σ for E> 50 GeV and $\sim 0.1\sigma$ at low energies (E< 300 GeV). Similar results are extracted from Z^2_{10} and χ^2 uniformity tests (also shown in figures 7.23 and 7.22). Following the uniformity test results, one can conclude that no pulsed emission has been detected from PSR J0205+6449 for E>50 GeV within the MAGIC sensitivity.

The next step is to calculate upper limits on the pulsed emission for different energy ranges. These upper limits have been calculated for a 3σ confidence level using the On-Off pulsed fraction method and the results from H-test of uniformity

(chapter 6). The results are listed in detail in table 7.3.3.

		H-Test (3σ)			On-Off (Rolke 99%)
E (GeV)	E_{th} (GeV)	H-test	p	F_{UL} $\times 10^{-6}(MeVcm^{-2}s^{-1})$	F_{UL} $\times 10^{-6}(MeVcm^{-2}s^{-1})$
48 - 119	80	1.2	0.02	26.6	13.5
119 - 300	210	1.0	0.01	7.9	4.3
300 - 754	530	0.5	0.02	1.9	2.1
754 - 1893	1320	5.6	0.1	2.3	1.9
1893 - 4755	3320	11.9	0.3	3.6	1.9
4755 - 11943	8350	5.5	0.4	3.9	2.0
11943 - 30000	20970	0.1	0.5	4.6	4.0

Table 7.8: *Results for PSRJ0205+64449 analysis.* $T_{On}^{Eff} = 31^h$. *The duty cycle is taken from the RXTE light curve [130] (ϕ = 0.2-0.3 and 0.7-0.8) and "p" is the pulsed fraction obtained.*

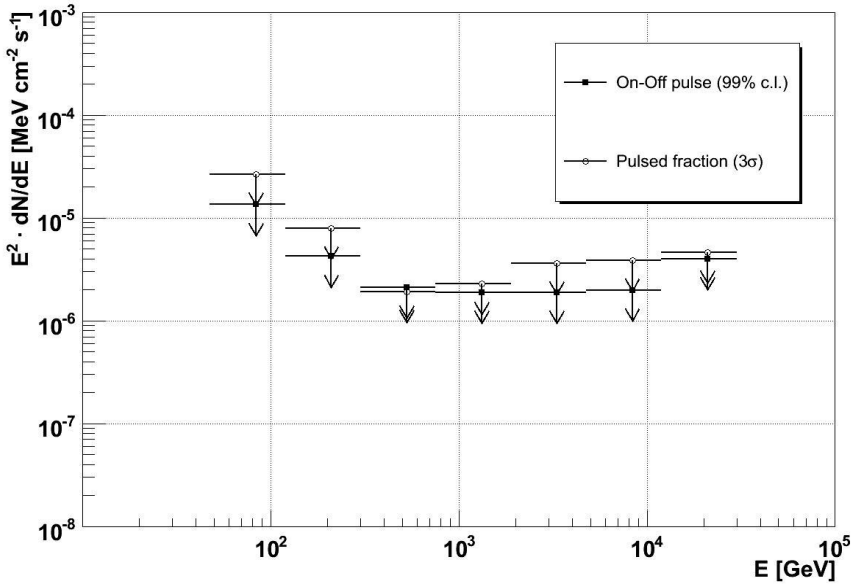

Figure 7.24: *Flux upper limits (99% c.l.) for PSRJ0205+6449 for pulsed emission ($\alpha < 10^o$). The full squares correspond to the On-Off pulse Rolke limit method and the circles to the pulsed fraction limit method (H-test). Results are shown in table 7.3.3*

Figure 7.24 shows the differential upper limits for a possible pulsed emission.

The result of the MAGIC timing analysis yielded no detection of pulsed emission coming from PSR J0205+6449 with a flux upper limit at 3σ confidence level of $F_{u.l.,3\sigma}$ (E>220 GeV) = 1.57x10^{-11} cm^{-2}s^{-1}.

7.4 PSR J0218+4232

Discovered at radio wavelengths [119], this 2.3 ms pulsar belongs to a binary system of 2 days orbital period with a low-mass ($\sim 0.2 M_\odot$) white dwarf companion.

PSR J0218+4232 is one of the three known millisecond pulsars (together with PSR B1821-24 and PSR B1937+21) with a hard spectrum and high luminosity emission in X-rays, and is the only millisecond pulsar seen at γ-ray energies [104]. This indicates a highly non-thermal origin of the high energy emission.

No pulsar wind nebulae emission has been observed at any wavelength from the direction of this source. Therefore only the search for the emission coming from the pulsar will be envisaged in this chapter.

7.4.1 Source overview

The pulsar is centred at the sky coordinates: RA= $2^h\ 18^m\ 6^s.305$ and DEC = 42° 32' 17".23 at a distance of 5.7 kpc.

Radio measurements infer a surface magnetic field strength B $\sim 4.3 \times 10^8$ G and a $\dot{E} \sim 2.5 \times 10^{35}$ erg s^{-1}, yielding a spin-down age of $\sim 4.6 \times 10^8$ yr. The column density best fit is $N_H \approx 5{\times}10^{20}$ cm^{-2}.

It is classified as a Class II millisecond pulsar in X-rays with a Crab-like pulse profile, with the high energy pulses (X-rays and γ-ray) aligned with two of the three radio pulses (fig. 7.25). This points to a magnetospheric origin of its non-thermal emission. Its high energy emission reaches up to E < 1 GeV.

It is the only Crab-like millisecond pulsar with large DC (radio and X-rays), initially explained as the emission of a possible compact nebula. However, Chandra observations [105] rejected extended emission at ∼1" diameter from the source center.

The Radio wavelengths emission VLA discovered this millisecond pulsar in 1991 in an imaging survey by the 76 m Jodrell Bank antenna.

PSR J0218+4232 is extremely luminous ($L_{1400} > 2700\ \ mJy\ kpc^2$) in giant pulses observations [95]. This GPS phenomenon has been observed in four more millisecond pulsars and in Crab

Although a first interpretation of the radio data reported a compact nebula of size < 16" (VLA beam), a review [144] of the radio polarization profiles of these observations suggested a nearly aligned rotator (8° ± 11°), with a magnetic field almost aligned with the rotation axis ($\alpha = 0°$). A broad pulse profile at radio wavelengths (fig. 7.25) supports also the aligned rotator scenario.

An angle between the line of sight and the rotation axis of $\zeta \sim 0°$ would lead to the hypothesis of a DC emission coming from the heated polar cap of the neutron star [144], keeping the observer looking continuously at the heated polar cap region. This is also consistent with X-rays observations.

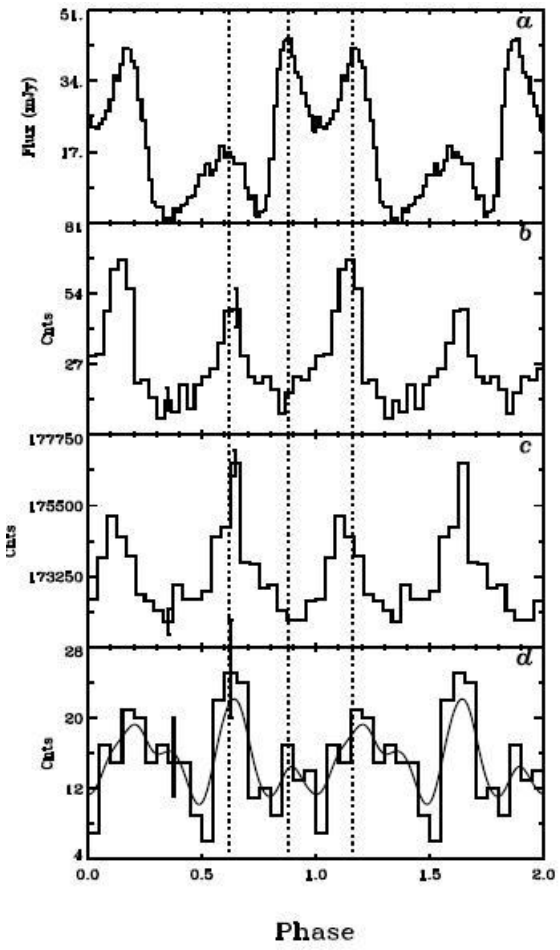

Figure 7.25: *PSR J0218+4232 light curves in absolute phase at different wavelengths: (a) VLA radio 610 MHz, (b) Chandra NRC-SI 0.08-10 KeV, (c) RXTE PCA 2-16 keV, and (d) CGRO EGRET γ-ray profile (0.1-1 GeV). The dotted lines correspond to the central phase of the 2 aligned pulses (ϕ_1=0.24 and ϕ_2=0.73) [106]*

X-ray emission At X-rays, the millisecond pulsars are divided in two classes, depending on their pulses profiles: Class I are pulsars with low luminosities and broad pulses with a soft pulsed emission with blackbody spectra, where the emission comes from the neutron star surface; and Class II, pulsars characterized by high luminosities and narrow pulses with a hard power law spectra, where the non-thermal emission is thought to come from the pulsar magnetosphere.

Pulsed and non-pulsed X-ray emission has been detected by ROSAT (0.1-2.4 keV), BeppoSAX MECS (1.6-10 keV), Chandra (0.07-7.29 keV) and XMM (0.6-12 keV) instruments (see fig. 7.27).

The non-pulsed emission at X-rays fits well to a blackbody of 0.10±0.08 km of radius. This is also consistent with emission coming from polar cap ($\theta_{pc} \sim 17°.5$)

supposing that the pulsar is a nearly aligned rotator [105].

XMM observations has found a pulse separation of ϕ=0.491±0.022 and a pulsed fraction of ∼60%. The first pulse is located in the phaseogram at ϕ_1=0.242±0.008 with a FWHM $\delta\phi_1$=0.112±0.038, while the second pulse corresponds to a phase ϕ_2=0.733±0.014 with a FWHM $\delta\phi_2$=0.121±0.056 [150]. The variations of the pulsar light curve for different energy bins yields a spectral index for pulse 1 of α_1=0.66±0.29 and α_2=0.42±0.36 for pulse 2 [150].

γ-ray emission While the number of millisecond pulsars detected in X-rays is greater than 30, PSR J0218+4232 is the only one detected at γ-ray energies. It has been detected at 3σ confidence level in the error box of the unidentified EGRET source 2EG J0220+4228/3EG J0222+4253 from 100 MeV to 1 GeV energies (fig. 7.26). For E > 1 GeV, the counterpart seems to be the AGN 3C 66A, which is also inside the error box (2σ c.l.) [104].

Supressing all the background contributions (including 3C 66A), and folding the EGRET data to radio ephemeris [119], Kuiper et al extracted a signal with $\sim 3.5\ \sigma$ detection significance [104] in the 100 MeV - 1 GeV energy range (fig. 7.25).

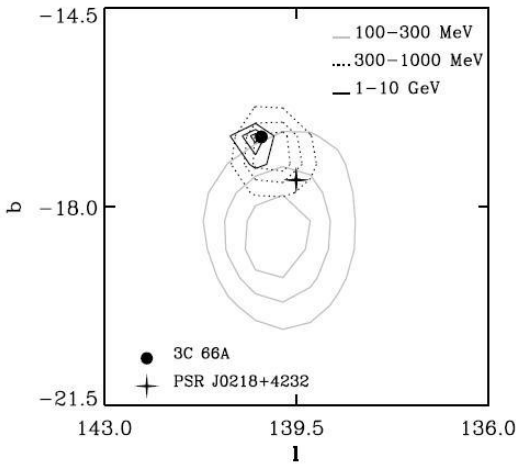

Figure 7.26: *Confidence contours (1,2 and 3σ) of the EGRET source 3EG J0222+4253 for 3 different energy bands (100-300 MeV, 300 MeV-1 GeV and 1-10 GeV). The filled circle represents the position of 3C 66A, while the cross is the PSR J0218+4232 location [104].*

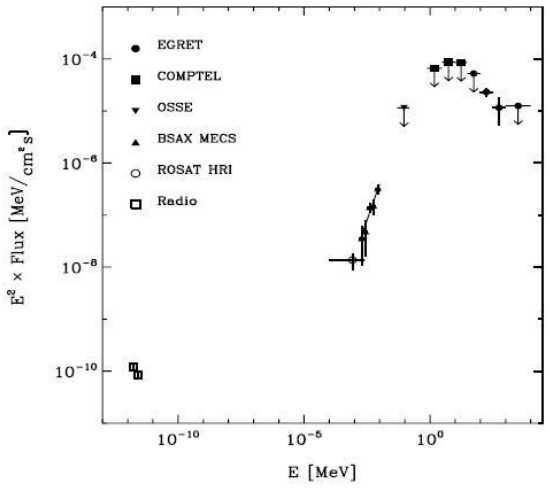

Figure 7.27: *Multi-wavelength spectrum of PSR J0218+4232 pulsed emission. The OSSE, COMPTEL and EGRET upper limits are given at 2σ c.l. [104].*

The phase alignment of the γ-ray pulses with the X-ray data increases the EGRET

significance from 3.5σ up to 4.9σ.

The pulse profile (fig. 7.25) shows an interpulse phase separation of ∼0.45 with a phase position of pulse 1 ϕ_1 ∼0.2 and ϕ_2 ∼0.65 for pulse 2, with a pulsed fraction of ∼ 0.5 [104].

Assuming $\Delta\Omega = 1$ sr as the γ-ray emission beam size, the conversion efficiency obtained of the spin-down luminosity in high energy γ-rays is around 7% for PSR J0218+4232. The spectral index between 0.1 and 1 GeV is ∼ -2.6 with an EGRET upper limit between 1-10 GeV of $(3.38\pm1.08)\times10^{-12}$ cm^{-2}s^{-1}MeV^{-1} at 2σ c.l.

7.4.2 MAGIC observations: PSR J0218+4232

The millisecond pulsar PSR J0218+4232 was observed during the Cycle II of MAGIC observations. The telescope collected in ON-OFF observation mode a total of ∼29 hours no-moon data between 2006 September and 2007 January (MJD = 53983.0 - 54115.0).

A detailed summary about the ON and OFF analysis data samples can be found in tables 7.9 and 7.10.

Since the millisecond pulsars are very weak sources, there was no request for Off observations in favour of an increase of On observation time. As in the PSR J0205+6449, for PSR J0218+4232 analysis, a set of off-axis and very faint sources compatible with our On observations in zenith angles range, PSF, data rate (after image cleaning), observation periods, and camera response (Pedestal RMS = 1.22 ± 0.07) has been used for Off data it has been used for Off data. Table 7.10 summarizes the characteristics of the Off data used in the analysis of PSR J2018+4232.

The quality check criteria for data selection (second column) is the same as in the analysis of PSR J0205+6449 and it is explained at the beginning of this chapter.

The quality checks results show a telescope performance very unstable during the observation period (large data rate fluctuations) with some days of bad weather. This will restrict the analysis to only 20.2 hours of On data from a total of ∼30 hours of observation time.

The data selection guarantees a change in the rate per run of the complete data set of less than ∼ 20% after image cleaning for the On and Off data. The mean rate per run of the data sample, together with the total observation and analysis time are shown in the last row of tables 7.9 and 7.10 for On and Off data respectively.

Analyzing the good On and Off data samples for the analysis it can be seen that On and Off data match quite well (fig. 7.28) before any hadronness cut, and that the Hillas parameters (width, length, dist and size) mean values of each run are very stable during the whole data taking period.

The rate stability requirement of $\lesssim$20% of the On and Off data samples used in the analysis are shown in figure 7.29. Although the observations zenith angle range is large, figure 7.30 (top) shows that the stability of the rates is high for its whole range.

Date	Quality check	PSF (mm)	θ (°)	Rate a.c. (Hz)	T_{Obs} (min)	T_{Obs}^{Eff} (min)
2006 Sept 4	R	17.9	—	—	2.7	0.
2006 Sept 5	R	11.0	—	—	96.0	0.
2006 Sept 6	R	11.8	—	—	40.8	0.
2006 Oct 2	R	12.7	13 - 19	145 ± 1	94.6	56.5
2006 Oct 3	OK	12.0	13 - 16	138 ± 1	36.3	36.3
2006 Oct 22	OK	13.7	12 - 31	161 ± 3	111.2	111.2
2006 Oct 23	OK	14.3	13 - 31	170 ± 3	104.8	104.8
2006 Oct 24	C R	14.0	12 - 30	162 ± 5	110.6	96.8
2006 Nov 11	OK	12.6	28 - 36	153 ± 3	14.1	14.1
2006 Nov 14	R	13.6	12 - 31	138 ± 6	240.7	194.9
2006 Nov 15	C	10.6	—	—	11.0	0.
2006 Nov 17	OK	14.3	21 - 29	159 ± 7	46.1	46.1
2006 Dec 13	R	15.4	11 - 34	150 ± 8	166.4	165.4
2006 Dec 14	R	15.2	12 - 22	172 ± 4	128.9	2.9
2006 Dec 15	R	14.7	12 - 29	160 ± 15	90.8	85.7
2007 Jan 6	OK	??	14 - 15	164 ± 11	20.7	20.7
2007 Jan 7	OK	13.7	15 - 20	140 ± 8	35.7	35.7
2007 Jan 8	R	–	—	—	0.4	0.
2007 Jan 9	R	15.3	—	—	95.5	0.
2007 Jan 10	R	14.8	13 - 30	131 ± 5	102.0	97.9
2007 Jan 11	R	14.9	14 - 31	172 ± 3	102.4	32.6
2007 Jan 15	OK	14.2	13 - 33	163 ± 5	110.3	110.3
Total		**13±2**	**11 - 38**	**150±25**	29.4 (h)	**20.2 (h)**

Table 7.9: *PSR J0218+4232 data sample. The quality check criteria gives the reason of the data rejected for the analysis: miss-pointing (M), cloudy night (C), abnormal rates (R) or abnormal distributions of the Hillas parameters (H) and OK night. The amount of time (minutes) rejected is given by* $T_{Obs}^{Eff} - T_{Obs}$.

Figure 7.30 (bottom) shows a low data miss-pointing < 2 pixels, which guarantees a good α-analysis performance.

Similarly to analysis of the previous source, figure 7.31 also reveals an inhomogeneous camera, mainly at low energies (Size < 300 phe), with decreasing efficiency up to 20% in the upper right corner of the camera ($\phi = 0°$ - $90°$). This mismatch will be considered further in the analysis conclusions, being part of the systematic error at low energies.

The presence of stars in the PSR J0218+4232 FoV (fig. 7.32) of the trigger area could fake a signal detected by a group of pixels. This hypothesis for the camera inhomogeneities can be rejected since the only source present in the field of view is

Date	θ (°)	Rate a.c. (Hz)	T_{Obs} (h)	T_{Obs}^{Eff} (h)
PSR B1951+32				
2006 Jul 5 - Sep 16	**2 - 26**	**144 ± 11**	29.7	**14.6**
3EG J2021+371				
2006 Sep 1 - Oct 23	**8 - 32**	**140 ± 10**	10.5	**3.3**
TeV 2032+42				
2006 Sep 25 - Nov 11	**28 - 43**	**147 ± 7**	14.0	**2.4**
Geminga				
2006 Nov 27 - 28	**8 - 47**	**149 ± 7**	7.5	**2.5**
Total	2° - 48°	**140 ± 20**	61.7 (h)	**22.8 (h)**

Table 7.10: *Off data sample for PSR J0218+4232. PSF = 13 ± 2 mm, P_{RMS}(Inner pixels) = 1.22 ± 0.07.*

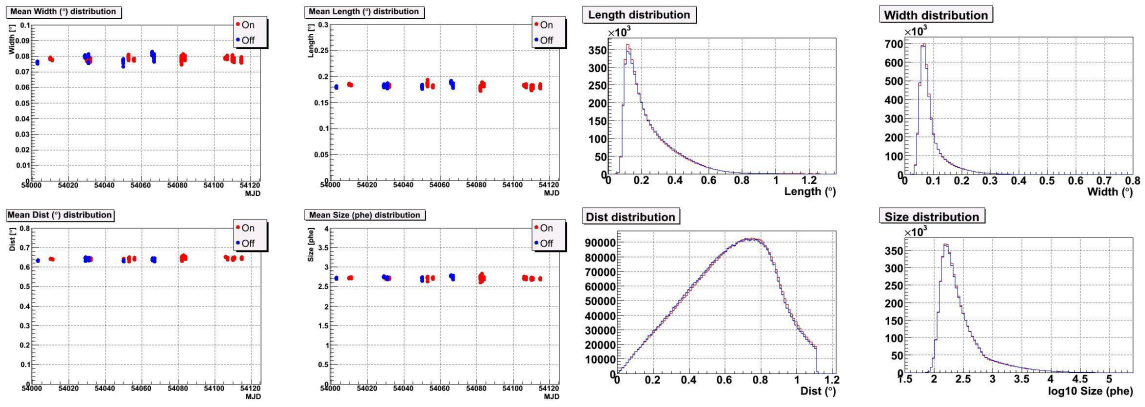

Figure 7.28: *Mean Hillas parameters (left) for each run as a function of time (MJD) and its distribution (right) for On (red) and Off (blue) data for analysis cuts (without hadronness cut) and Size > 60 phe.*

3C 66A at 0.9° from the camera center. This source is a possible γ-ray source, but very faint at optical wavelengths ($\sim$15-16^m in B-band [17]).

From MC-γ simulations at the zenith angle range of this source, one obtains a resolution of the estimated energy of ΔE$\sim$25% at low energies (60<E (GeV)< 380) and ΔE$\sim$20% at high energies (E_{th}> 200 GeV) (fig. 7.33).

For this source I used a different MC simulation compared to the one used in the analysis of the previous source, although the optical PSF of the data is similar (14 mm). This is due to changes in the telescope hardware between the observation periods of both sources.

Calculating the imaging response of the telescope for γ-showers (PSF$_\gamma$) in the

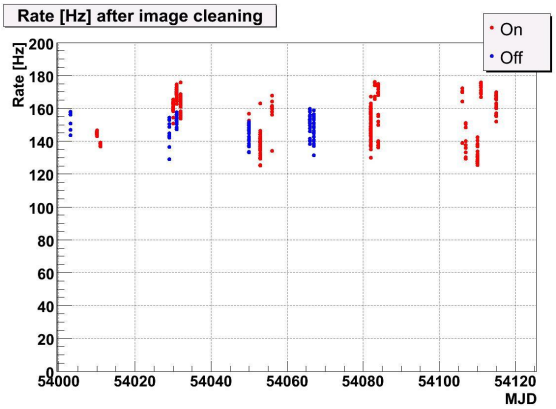

Figure 7.29: *Rates (Hz) after image cleaning of the ON (red) and Off (blue) data samples as a function of time (MJD). The run rate stability during the On data observations is ∼20% for On and Off data.*

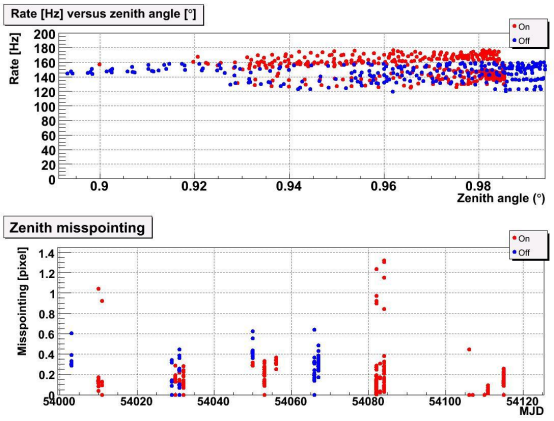

Figure 7.30: *Top: Rates (in Hz) after image cleaning of the ON (red) and Off (blue) data samples as a function of the observations zenith angle. Bottom: Miss-Pointing (pixels) of the On (red) and Off (blue) data sample as a function of time (MJD).*

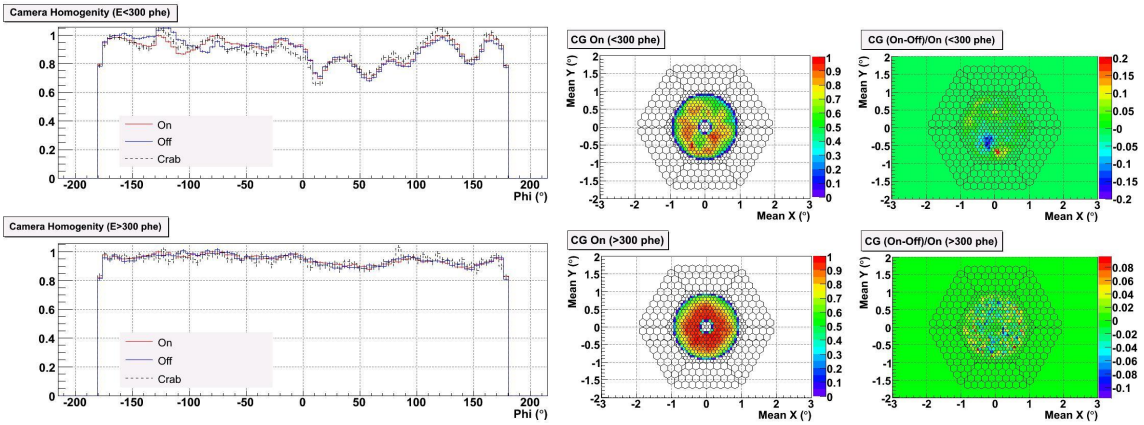

Figure 7.31: *Camera inhomogeneity for On (red) and Off (blue) data. The angle $\phi = arctan(y/x)$ distribution (left) shows the angular inhomogeneity of the camera events distribution (right) for low energies (left-top) and high energies (left-bottom).*

same way as in the previous source analysis, for PSR J0218+4232 observations the gamma PSF is found out to be $0.081° \pm 0.027°$ (fig. 7.34).

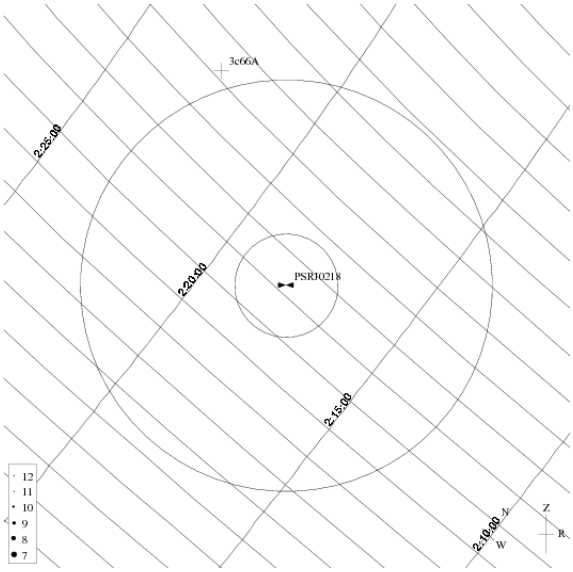

Figure 7.32: *FoV (∼2.8°) of PSR J0218+4232 from El Roque de los Muchachos observatory (La Palma) for MAGIC ON-observation period. The eyepieces correspond to FoV of 0.5° and 2° diameter.*

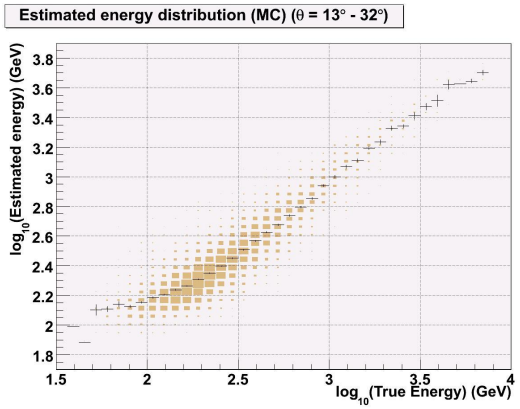

Figure 7.33: *Distribution (filled squares) of the estimated energy versus the true energy for Monte Carlo events. The distribution profile is also displayed (black).* $\frac{\Delta E}{E}$ *∼25% for Size∼60 - 300 phe and* $\frac{\Delta E}{E}$ *∼20% for Size>300 phe.*

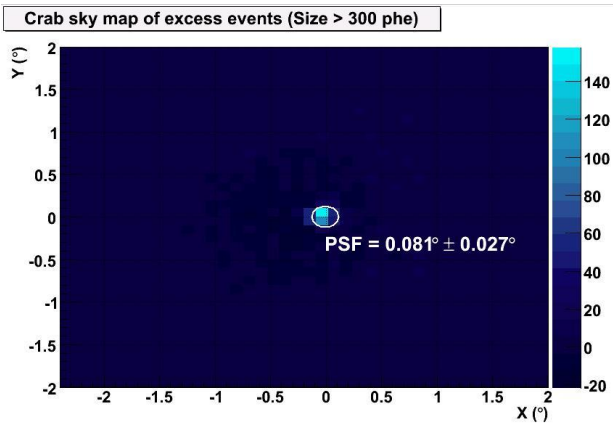

Figure 7.34: *PSF$_\gamma$ distribution from Crab data between 14°-32° of zenith angles at high energies (E>200 GeV).*

7.4.3 MAGIC results: PSR J0218+4232

Search for steady emission: PSR J0218+4232

Once the agreement of On and Off Hillas parameters and rates (fig. 7.28 and 7.29) has been confirmed, the analysis can be performed in the same way as for the previous

source: a small fraction of the On sample is used to train the Random Forest and estimate the hadronness and the energy of each event of real data. The Off data will be used for significance extraction in the α-analysis and θ^2-analysis of the pulsar emission, optimizing the hadronness cut from the significance of Crab data for each energy bin. This cut will correspond to the highest telescope sensitivity at these energies.

For the PSR J0218+4232 data analysis, a total of 2.5^h of Crab data between 2006 October 2nd and 3rd, with a mean rate of 135 $\pm$ 10 Hz and the same zenith angles as the On data, can be used.

Due to the hardware changes, the tail cut used in the image cleaning applied in the analysis (10 phe for core pixels and 5 phe for boundary pixels) and the software trigger condition (>5 NN) will select slightly different energy events than in the previous analysis. Imposing a cut in the zenith angle range of the source observation, this will select MC gammas for E> 20 GeV with an $E_{th} \sim 156$ GeV in case of a lower size cut of 60 phe before any γ/h separation cut.

A summary of the size/energy bins and their corresponding optimized hadronness cut is listed in table 7.11. For each integral size bin the optimized Crab signal (σ_{17} obtained with eq. 17 of [107]), the analysis sensitivity (% of Crab flux), the energy threshold (GeV) and the efficiency (in % of surviving events) of the hadronness cut in MC-γ and hadron (Off) samples are listed.

Size (phe)	Hadr. cut	Hadr. eff. MC-γ (%)	Hadr. eff. Off (%)	E_{th} (GeV)	σ_{17} (Crab)	Sensitivity (% Crab)
> 60	0.075	40	1.5	140	25.6	3.8
> 100	0.075	41	1.4	140	25.6	3.8
> 200	0.075	64	1.8	140	23.9	3.8
> 300	0.075	74	1.5	200	25.8	3.3
> 500	0.075	79	1.1	310	23.1	3.4
> 700	0.075	81	0.8	360	22.1	3.5
> 900	0.075	82	0.6	480	20.3	3.9
> 1200	0.075	83	0.5	590	15.6	4.9
> 1600	0.075	80	0.4	670	14.2	5.1
> 2000	0.025	65	0.1	810	11.3	5.2
< 300	0.125	33	2.6	130	8.3	10.8

Table 7.11: *Cut efficiency table for Crab (∼152 min) and PSR J0218+4232 Off data.*

The telescope sensitivity and the Crab significance measures the telescope performance during the data taking period.

The α-analysis The application of the optimum hadronness cut for each energy bin and the static cuts already mentioned in previous sections applied to the On and

Off data sample will yield the best sensitivity on the Crab α-analysis.

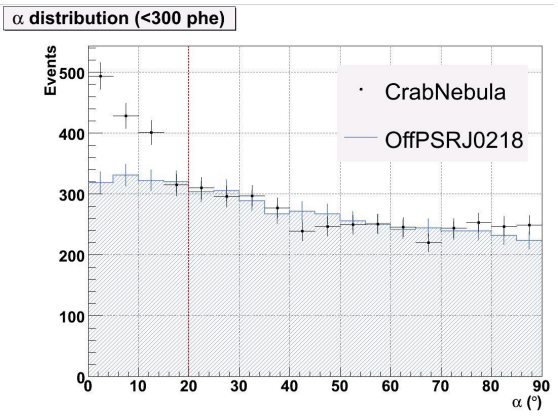

Figure 7.35: *Crab Nebula (black-points) and Off (blue-line) α distributions for Size < 300 phe (E∼60-380 GeV, E_{th} = 130 GeV). $\sigma_{17}(\alpha < 20°)(152\ min) \sim 8$.*

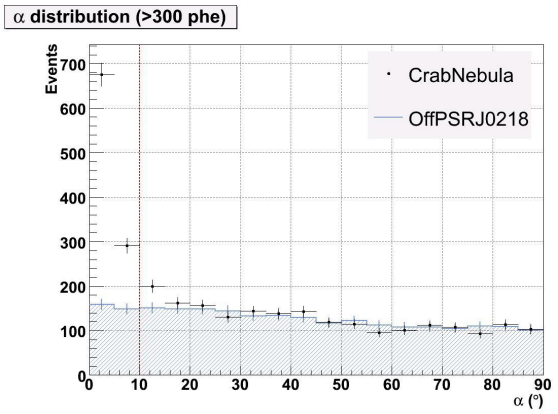

Figure 7.36: *Crab Nebula (black-points) and Off (blue-line) α distributions for Size > 300 phe (E> 130 GeV, E_{th} = 200 GeV). $\sigma_{17}(\alpha < 10°)(152\ min) \sim 26$.*

Figures 7.35 and 7.36 show the α-distribution for Crab nebula data and PSR J0218+4232 Off data. The optimum α-cut for signal extraction is α<20° for low energy bins (60 phe < Size < 300 phe) and α<10° for those energy bins involving high energy events. For 2.5 hours of Crab data the analysis yielded 16.3 $\sigma h^{-1/2}$ for high energy events (size > 300 phe) and 5.2 $\sigma h^{-1/2}$ for low energy events (size < 300 phe)

The same procedure is used to extract the excess events and the signal significance of the On data (PSR J0218+4232) after subtracting the Off data sample for different integral bins. Table 7.4.3 shows the results of the α-analysis of the source: the number of excess and background events (N_{exc} and N_{bg}) and the significance (σ_{17})(eq. 6.1) of the excess events (N_{on}-$N_{Off,norm}$) over the background fluctuations.

The α-distribution for the On and Off data can be seen on figures 7.37 and 7.38 for low (E∼60-380 GeV) and high energies (E>120 GeV) respectively.

Since no significant signal has been detected, the integral flux upper limits (in cm^{-2} s^{-1}) are calculated for each energy bin and listed in table 7.4.3. These flux upper limits are also shown in figure 7.39 as blue arrows. The red arrows correspond to the upper limits reported by other HE detectors like STACEE [31], GT-48 [143],Whipple [93] and HEGRA [2]. As flux reference lines the Crab Nebula flux (black continuous line) as measured by MAGIC [10], and as well as the 10% of Crab flux (dotted lines) are shown.

The Disp-analysis It is known that the millisecond pulsar PSR J0218+4232 doesn't have a pulsar wind nebula associated up to 1" diameter scales, which is

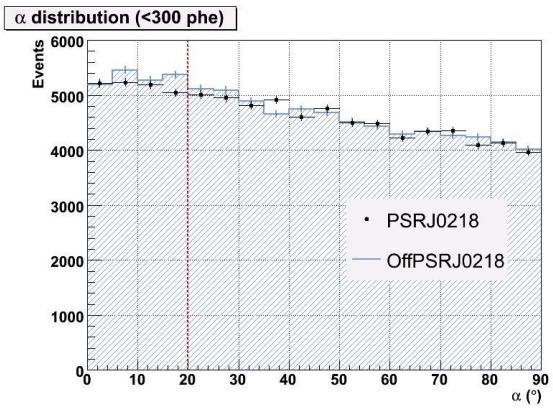

Figure 7.37: *PSR J0218+4232 (black-points) and Off (blue-line) α distributions for Size < 300 phe (E∼60-380 GeV, E_{th} = 130 GeV). The red dotted line is the used signal extraction area ($\alpha < 20°$) cut. $\sigma_{17}(\alpha < 20°)(20.2^h) \sim$ -3.*

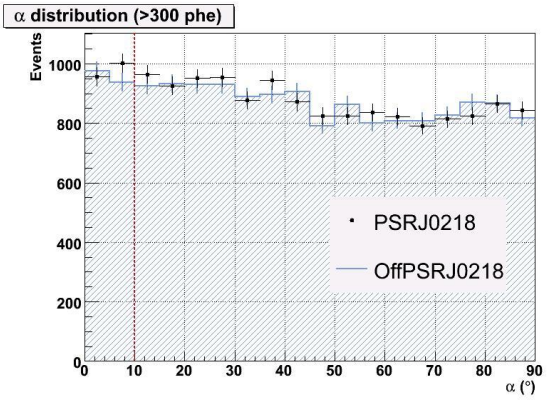

Figure 7.38: *PSR J0218+4232 (black-points) and Off (blue-line) α distributions for Size > 300 phe (E>130 GeV, E_{th} = 200 GeV). The red dotted line is the used signal extraction area cut ($\alpha < 10°$). $\sigma_{17}(\alpha < 10°)(20.2^h) \sim 1$.*

Size (phe)	E_{th} (GeV)	E range (GeV)	N_{exc}	N_{bg}	Signif. (σ)	F_{UL} $\times 10^{-12}(cm^{-2}s^{-1})$
> 60	140	> 70	49	7180 ± 100	0.4	31.7
> 300	200	> 130	122	1914 ± 52	0.8	14.6
> 500	310	> 190	-20	704 ± 32	-1.2	3.0
> 700	360	> 290	-4	357 ± 22	-0.8	2.8
> 900	480	> 310	-20	236 ± 18	-1.8	1.5
> 1200	590	> 390	12	128 ± 77	0.1	2.9
> 2000	810	> 670	9	19 ± 6	0.6	2.1

Table 7.12: *Results for PSR J0218+4232 analysis.* $T_{On}^{Eff} = 1211min$.

far smaller than our telescope PSF. However, EGRET detected contribution at high energies (E> 1 GeV) of the BL Lac 3C 66A [104] which is located at ∼0.9° from the PSR J0218+4232 position. This will determine whether this AGN could contribute to the background of the source analysis.

As in the analysis of the previous source, the Disp variable is used to calculate the signal significance of the excess events coming from the surroundings of the source position (sky map). For this new analysis, random forest (RF) matrices are created but without parameters which depend on the source position of the events on the camera.

As it has been done in the whole analysis in this Thesis, the hadronness cut is

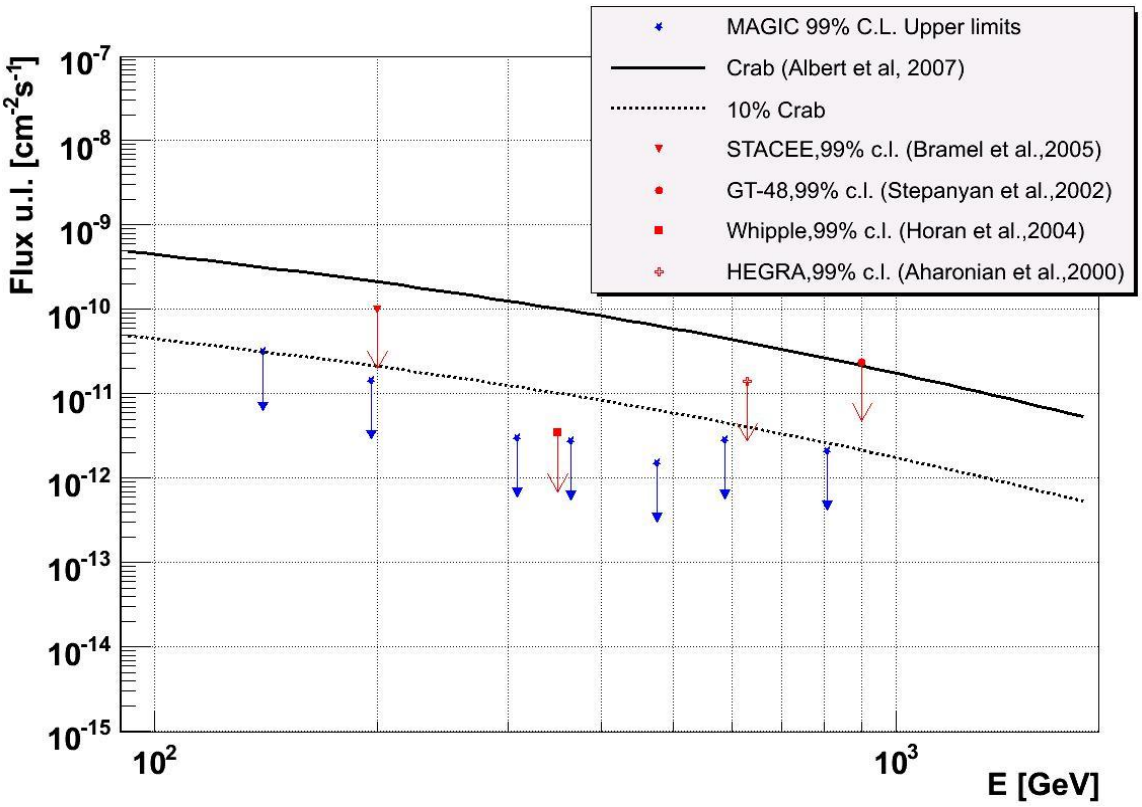

Figure 7.39: *DC Flux upper limits (99% c.l.) (table 7.4.3) for PSRJ0218+4232 (blue arrows). The black lines are the different fractions of Crab flux (10% and 100%).The red filled square corresponds to the upper limit obtained from other high-energy experiments observations.*

optimized to obtain the highest signal/$\sqrt{(background)}$ from Crab data sample. The results are shown in table 7.13.

Size (phe)	Hadr. cut	Hadr. eff. MC-γ (%)	Hadr. eff. Off (%)	Sensitivity (% Crab)
> 60	0.04	26	0.7	4.7
> 300	0.13	82	3.2	3.8
< 300	0.16	37	3.8	15.7

Table 7.13: *Hadronness cut efficiency table for Disp-analysis at the source position for Crab (∼152 min) and PSRJ0218+4232 Off data.*

Applying the hadronness cut to the θ^2-distribution for low and high energy events, figures 7.40 and 7.41 respectively are obtained.

The calculation of the sensitivity yields a relative decrease of the Disp-analysis

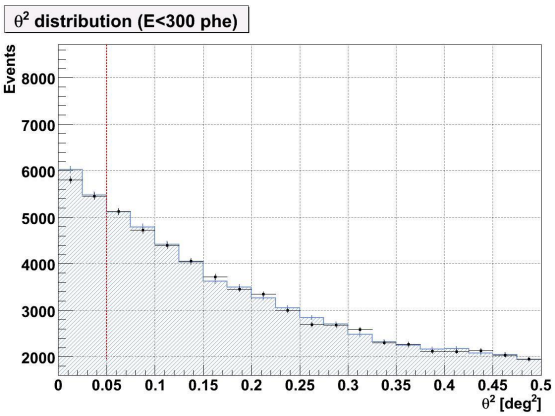

Figure 7.40: *On (black-points) and Off (blue-line) θ^2 distributions for Size < 300 phe at the source position.*

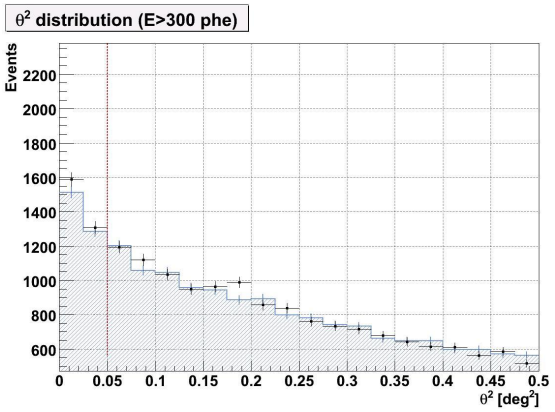

Figure 7.41: *On (black-points) and Off (blue-line) θ^2 distributions for Size > 300 phe at the source position.*

sensitivity of ∼20% for Size > 60 phe and ∼10% at high energieswith respect to the α-analysis. The values of the sensitivity have been calculated with respect to the camera center.

At a distance of ∼1° from the camera center, the telescope sensitivity decreases ∼60% with respect to the center of the camera [127]. This drop in sensitivity has to be added to the decrease already obtained from the disp-analysis compared to the α-analysis. The net effect will yield a very important loss of the disp-analysis sensitivity at 3C66A sky position, making its detection really difficult. Nevertheless it is important to check whether this blazar contributes to the background of PSR J0218+4232 analysis as it happened in other experiments. This can be seen in the source sky map (figure 7.42) up to a sky FoV of 1.2°×1.2°.

7.4.4 Search for pulsed emission: PSR J0218+4232

Timing analysis

To analyze only the pulsed component of the pulsar I have performed a timing analysis, as already explained in the previous chapter of this Thesis.

As in the PSR J0205+6449 analysis, the software used in the timing analysis of PSR J0218+4232 as the Mars executable *SearchPeriod*. The corrections to the motion of the pulsar in the binary pulsar were performed using the *Tempo* program [146].

Contrary to the canonical pulsars, the millisecond pulsars are well known as stable pulsars. Therefore their ephemeris can be extrapolated along large periods of time.

For this analysis I have used the closest ephemerides provided by the Nancay Observatory [3] (Bordeaux, France) [141]. These ephemeris are listed in table 7.14.

[3]Thanks to D. Smith (Centre d'tudes Nuclaires de Bordeaux Gradignan).

PSR	0218+42
RAJ	02:18:06.34989954
DECJ	42:32:17.4495833
F0	430.4610684699871967
F1	-1.434350498680E-14
PEPOCH	49150.610000
START	54010.071
FINISH	54114.929
DM	61.256000
EPHEM	DE200
CLK	UTC(NIST)
BINARY	ELL1
A1	1.984434500
PB	2.028846081836
TASC	49148.579983238
EPS1	0.0000004833
EPS2	0.0000039694
SINI	0.700000

Table 7.14: *Ephemeris for PSR J0218+4232 from Nancay Observatory data [141] in Tempo 1 program format. The validity period is from 2006, October 2^{sd} to 2007, January 14^{th}, covering the observations range of our sample.*

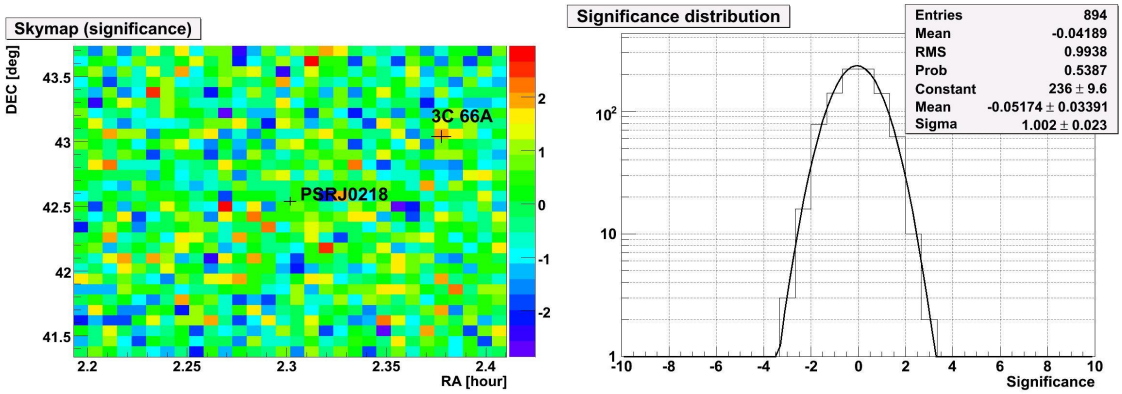

Figure 7.42: *Left: Sky map (significance) of PSR J0218+4232 for E>70 GeV. The black cross marks the pulsar position and the AGN 3C 66A (EGRET likely counterpart for E> 1 GeV). Right: Distribution of significances of the sky map.*

Due to the simultaneous of the Nancay and MAGIC observations, this analysis will not perform any scan in frequencies, improving the significance of the analysis.

Like in the analysis of PSR J0205+6449, this analysis has been also guided the two main models of pulsar magnetosphere emission (chapter 2). These models predict two different regions of emission, depending on the spectrum cutoff energy: few GeVs (for polar cap models) or hundred of GeV (for outer gap models). Therefore, the timing analysis has been carried out in two different energy bins: E < 300 GeV and E> 50 GeV. In each of these energy bins I apply different static cuts that improve the significance of the analysis. The first cuts applied are the ones described in section 7.2.4. The next cut applied to the analysis is based on the α parameter and depends on the expected width of the distribution for the different energy bins. Finally I apply a conservative hadronness cut which keeps ∼80% of the MC gammas and as many low energy events as possible, in order to increase the statistic of pulsed emission photons in the timing analysis. For E> 50 GeV I apply an hadronness cut of 0.405 which keeps ∼15% (Q = 2.1) of hadrons while for low energies (E<300 GeV) the hadronness cut is 0.445 which keeps ∼19% (Q = 1.8) of the hadron sample.

Applying the corresponding analysis cuts to each energy bin I obtained the light curves for the ephemeris frequency for low (fig. 7.44) and high (fig. 7.43) energy samples. The shadowed areas correspond to the rotational phase intervals where the X-ray pulse is emitted (fig. 7.25).

The uniformity H-test over both light curves yields a significance signal detection of 1.0σ for E> 50 GeV and 0.6σ at low energies (E< 300 GeV). Figures 7.44 and 7.43 also shown Z^2_{10} and χ^2 uniformity tests results which lead to similar results as the H-test. Therefore one concludes that no pulsed emission has been detected from MAGIC observations of PSR J0218+4232 for E> 50 GeV within the MAGIC sensitivity.

Because no signal has been detected, the last step of the analysis is to calculate

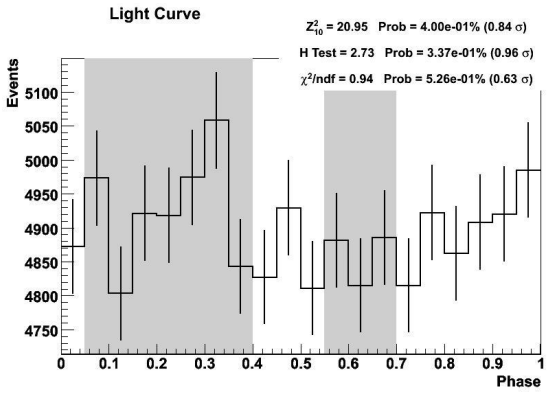

Figure 7.43: *Light curve for PSR J0218+4232 for all energies and α<10º (Hadronness<0.405 and Q∼2.1). The shadowed area corresponds to the XMM pulse peaks [150]. Signal significance ∼ 1.0 σ.*

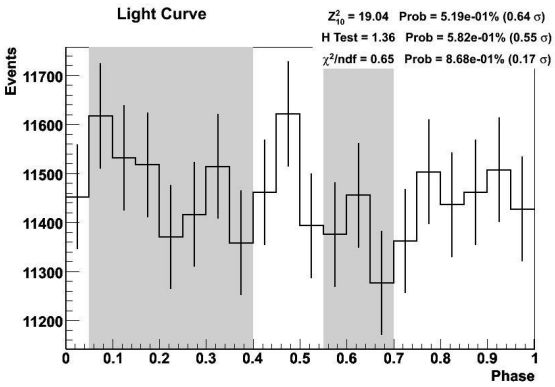

Figure 7.44: *Light curve for PSR J0218+4232 for E<300 GeV and α<20º (Hadronness<0.445 and Q∼1.8). The shadowed area corresponds to the XMM pulse peaks [150]. ∼ 0.6 σ signal significance.*

		H-Test (3σ)			On-Off (Rolke 99%)
E (GeV)	E_{th} (GeV)	H-test	p	F_{UL} $\times 10^{-6}(MeVcm^{-2}s^{-1})$	F_{UL} $\times 10^{-6}(MeVcm^{-2}s^{-1})$
48 - 119	80	2.0	0.02	34.3	20.3
119 - 300	210	1.4	0.03	9.6	4.2
300 - 754	530	0.5	0.10	3.3	2.6
754 - 1893	1320	0.5	0.31	3.5	2.7
1893 - 4755	3320	10.4	1.43	9.2	3.9
4755 - 11943	8350	0.2	1.95	4.3	3.8

Table 7.15: *Results for the PSRJ0218+4232 analysis. $T_{On}^{Eff} = 20^h$. The duty cycle is taken from the EGRET light curve [106] (ϕ = 0.1-0.4 and 0.55-0.7) and "p" is the pulsed fraction obtained.*

the upper limits of the pulsed emission for the MAGIC sensitivity at the analysis zenith angles at different energy bins. They have been computed (figure 7.45) at 3σ confidence level using the On-Off pulsed fraction (filled squares) and the H-test results (empty circles). The results are listed in detail in table 7.4.4. The total flux upper limit of the pulsed emission analysis at 3σ confidence level if $F_{ul,3\sigma}$(E>150 GeV) = 2.6×10^{-11} cm^{-2} s^{-1}.

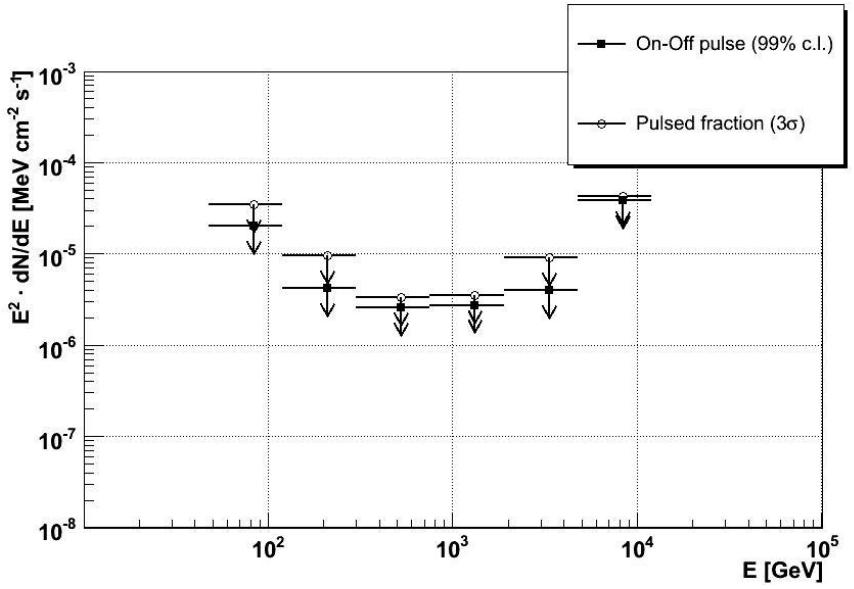

Figure 7.45: *Flux upper limits (99% c.l.) for PSRJ0218+4232 for pulsed emission ($\alpha < 10^o$). The full squares correspond to the On-Off pulse Rolke limit method and the circles to the pulsed fraction limit method (H-test). Results are shown in table 7.4.4*

7.5 Conclusions

The analysis described in this chapter has been carried out with an image cleaning which optimizes the telescope sensitivity for steady emission. Since there is no calibrating source for the pulsed emission, this image cleaning has been used also for the timing analysis, but optimizing the analysis cuts through Monte Carlo simulations.

PSR J0205+6449 is the second most powerful pulsar in the population of canonical pulsar. Its large spin-down luminosity makes it a good candidate for the detection of pulsed emission coming from the pulsar and also for the steady emission, which may come from the nebulae as a result of the injected particles in it. However, recent models of particle acceleration, through resonant scattering by heavy nuclei [23], on the pulsar wind nebulae 3C 58 have estimated a γ-ray emission significantly below the 5σ detection significance of MAGIC for 50 hr observations. The other pulsar of this analysis, PSR J0218+4232, has no nebulae associated, but has the advantage of being the only millisecond pulsar detected in γ-rays.

The double and narrow peak profile of the light curves of PSR J0205+6449 and PSR J0218+4232 (with 21% and 60% pulsed fraction respectively) makes them a good candidates for signal detection.

Despite of the optimistic predictions from previous observations, no signal has been detected from either PSR J0205+6449 or PSR J0218+4232 neither from steady or pulsed emission. The upper limits have been calculated at 99% of C.L. for steady

and pulsed emission. For PSR J0205+6449 plus 3C 58 pulsar-PWN system, the analysis yields to flux upper limits $F_{3\sigma}$ (E_{th}>280 GeV)< 7.7×10^{-12} cm^{-2} s^{-1} and $F_{3\sigma}$ (E_{th}>220 GeV) < 1.57×10^{-11} cm^{-2}s^{-1} for steady and pulsed emission respectively.

For PSR J0218+4232 the flux upper limit for the steady emission is $F_{3\sigma}$ (E_{th}>140 GeV) < 3.2×10^{-11} cm^{-2}s^{-1}. For the pulsed emission the integral upper limit resulting from this analysis is $F_{ul,3\sigma}$(E_{th} >150 GeV) < 2.6×10^{-11} cm^{-2} s^{-1}.

Concerning the search of extended emission around the pulsar position coming from the nebulae (in the case of PSR J0205+6449) or from the interaction of the pulsar wind nebulae with the interstellar medium in a binary system (like PSR J0218+4232). This possibility has been also rejected within a region of 1.2×1.2 deg^2.

The different energy thresholds for the analysis of each source are mainly due to the different zenith angle range of observation for both pulsars. As it can be seen, the trigger energy threshold (from MC simulations) can not be reached in the analysis due to a bad γ/hadron separation at low energies.

Another important conclusion from the analysis of this Thesis is the possibility of analyzing the On data with non specific Off data. The disadvantage is the unavailability of Off data to compare with MC protons to optimize better some of the analysis cuts.

The results of this analysis have been presented in the 30th International Cosmic Ray Conference (2006).

Conclusions

This Thesis presents Monte Carlo simulation studies of the MAGIC telescope's sensitivity for pulsars. These simulations predict a trigger threshold of ∼40-50 GeV for low zenith angles of observation. However, in the analysis, this trigger threshold cannot be reached due to a lack of γ/hadron separation at low energies. The simulations show a telescope effective area for gamma-rays at low zenith angles increasing quickly from 5 m^2 at 10 GeV to 5×10^4 m^2 at 100 GeV, followed by a nearly flat behaviour up to 30 TeV where the effective area is $\sim 3\times10^5$ m^2. However, for protons, the telescope effective area increases monotonously from 10 m^2 for 30 GeV protons to 10^5 m^2 for 30 TeV protons. These effective areas for protons yield an estimation of the background rate of $\sim$ 120 Hz which is in agreement with the trigger rate of background (or Off) observations. Applying an expected gamma-source spectrum to the telescope effective areas for gammas, it is possible to determine the observation time needed for a significant detection of the source over a fixed background rate.

However, due to the pulsar spectra cut-off in this energy range, the range in the observation times varies tremendously with small changes in the spectrum constants.

To complete the previous Monte Carlo studies, I have also developed in this Thesis a study about the effect of the Earth's magnetic field on Cherenkov telescopes' sensitivity. These Thesis simulations demonstrate the great importance of the Earth's magnetic field effect on EAS initiated by γ-rays of energies $\leq$ 100 GeV. In contrast, the effect on proton showers is very small in the energy range where they contribute to the observation's background. The effect on the telescope sensitivity and energy threshold cannot be corrected through software due to the spread of the far away Cherenkov photons, which may even be 1 km away from the telescope axis. This loss of light leads to an unavoidable increase of the telescope threshold for low energies and a decrease of the source rate. This effect depends strongly on the telescope site, due to the variations of the Earth's magnetic field from the dipolar assumption, and on the energy threshold achievable by the Cherenkov telescope. However, the difference in the altitude of the telescope site does not change more than 10% of the local value of the Earth's magnetic field. In the case of the site and performance of the MAGIC telescope, the minimum effect takes place at 51.2° observation zenith angle and in the North direction, while the magnetic field affects more the showers coming from the South, South-West and South-East, depending on the zenith angle. Translating the results into hour angle and declination coordinates, the simulations predict that sources with declination $\gtrsim$ 40 degrees are subjected to losses of light of nearly 70% at 10 GeV along their trajectory and lose only 10% of their Cherenkov photons for 100 GeV γ-ray showers.

In the studies of the telescope sensitivity for pulsars, the full MC simulations

were performed at the azimuth range where the effect of the Earth's magnetic field is minimum (ϕ=0° and 90°). In the case of the sources analyzed in this Thesis, PSR J0205+6449 and PSR J0218+4232, the Earth's magnetic field causes the loss of more than 30% of the light coming from the source at low energies. This may cause an increase of the energy threshold of our observations and a loss in sensitivity proportional to the light loss. Unfortunately this was not taken into account when I made the observation proposals for these two sources, underestimating the observation time needed for a significant detection.

The second part of this Thesis explains the data check and analysis programs (MAGICDC and QOSA programs) that I have developed to check the performance of MAGIC. The results of the data check program have been used to fill a daily-check report, work carried out by all the MAGIC collaboration groups during the last 2 years and coordinated mostly by the Thesis author. This report has shown long-term stability, thanks to the detection and the solution of many problems in very short time.

This long term stability is often interrupted by hardware or software updates, unexpected factors and other less important factors. As a result of these deviations from a stable behaviour, the MAGICDC program has had to be updated by changing the safety upper limits and updating part of the resulting plots. Sometimes, not only the safety limits and the plots of the program have changed but also the computing facilities in the telescope site and even the method of data-taking. However, the fast response of the subsystems experts and the telescope manager has been crucial for the recovery of the telescope's stability and the data quality.

One case of short-term instability of the telescope subsystems (such as the calibration constants) has been solved through different data-taking strategies ("interlaced" calibration events) at hardware and software level.

As I have mentioned, another important factor that has caused changes in the data check and in the on-site analysis program is the upgrade of some of the telescope subsystems, which has required study of the telescope's new performance.

The on-site analysis has detected problems with the analysis software, testing bugs of new software releases. The program results have also reported subsystems problems (with the star guider and the AMC) and have given several alerts for flaring sources (such as Mrk 501) to the MAGIC collaboration. Due to the delay of the data transfer from the telescope site to the official data centre (on the continent, PIC), the analysis performed on-site has been used for most of the MAGIC results (mainly at calibration level).

Finally, I have proposed and analyzed the data of two of the ten most powerful pulsars in the canonical and millisecond populations: PSR J0205+6449 and PSR J0218+4232, despite the intrinsic difficulties in detecting them due to their steep spectrum and the effect of the Earth's magnetic field along their trajectories. The

observations at X-rays, radio and, in the case of PSR J0218+4232, γ-rays also show them as good candidates for pulsar-PWN systems in the MAGIC energy range (above 60 GeV). In spite of the great effort in the telescope performance, the analysis reveals a clear lack of camera uniformity at low energies. The reason is still unknown. The analysis in this Thesis of PSR J0205+6449 and PSR J0218+4232 has resulted in a non-detection of the steady or the pulsed emission from these sources. This analysis sets an upper limit at 99% C.L. to the steady emission of PSR J0205+6449 plus 3C 58 of $< 7.7\times10^{-12}$ cm^{-2} s^{-1} for $E_{th}> 280$ GeV, which is lower than the upper limit reported by the Cherenkov telescope, Whipple. The upper limit to the pulsed emission of PSR J0205+6449 at 3σ CL is 1.57×10^{-11} cm^{-2}s^{-1} for $E_{th}>220$ GeV. For PSR J0218+4232 the upper limit to the steady emission only concerns the emission coming from the pulsar. The flux at 99% CL is 3.2×10^{-11} cm^{-2}s^{-1} for $E_{th}>140$ GeV. This upper limit is much better than the previous ones reported by other high energy experiments at carried out at Whipple, HEGRA, STACEE and GT-48.

It has been very important for the timing analysis, mainly for PSR J0205+6449, to have contemporaneous ephemeris to the MAGIC observations for each source. The low amount of photons at γ-ray energies make it impossible to search for the pulsed emission without the help of external ephemeris. Therefore, the pulsed emission of this Thesis has only been possible thanks to collaboration with X-ray and radio-astronomers that it is necessary to coordinate with radio and X-ray observatories to get valid ephemeris for the timing analysis of Cherenkov telescope data.

Another important conclusion from the analysis of this Thesis is the possibility to analyze the On data with non-specific Off data. Although the optimum way to analyze the data is with dedicated Off data, it is also possible to analyze the pulsar data with a set of data samples from observations of sources without signal.

Subsequent to this analysis, other image cleaning methods have been developed that increase MAGIC sensitivity at low energies and decrease the analysis energy threshold. It would be interesting to repeat the analysis with these new image-cleaning methods in the near future.

Bibliography

[1] Moralejo A., 2000, *Bsqueda de fuentes csmicas de radiacin gamma de muy alta energa con el detector AIROBICC*, PhD Thesis, UCM.

[2] Aharonian F.A. et al, 2000, A&A, 353, 847-852.

[3] Aharonian F.A., Konopelko A.K., Völk H.J., 2001, *5@5 - a 5 GeV energy threshold array of imaging atmospheric Cherenkov telescopes at 5 km altitude*, APh, 15, 4, 335-356.

[4] Aharonian F. et al, 2004, ApJ, 614, 897-913.

[5] Aharonian F. et al, 2005, A&A, 432, L9-L12.

[6] Aharonian F. et al, 2006, A&A, 448, L43-L47.

[7] Aharonian F. et al, 2007, ApJ, 661, 236-249.

[8] Alcaraz J. et al, 2000, Phys. Lett. B, 472, 215-226.

[9] Alcaraz J, et al, 2000, Phys. Lett. B, 494, 193-202.

[10] Albert et al, 2007, ApJ, 669, 1143-1149.

[11] Albert et al, 2008, ApJ, 674, 1037-1055.

[12] Amenomori M., et al, 2002, ApJ, 580, 887-895.

[13] Armada A. et al, 2006, *Telescope performance*, MAGIC internal documentation, TDAS 06-04.

[14] Arqueros F. et al, 2002, APh, 17, 3, 293-318.

[15] Arons J, 1983, ApJ, 266, 215-241.

[16] Atkins R., et al, 2000, NucIM A, 449, 478-499.

[17] Bach U., et al, 2007, A&A, 464, 175-186.

[18] Bartko H. et al, 2005, *FADC Pulse Reconstruction Using a Digital Filter for the MAGIC Telescope*, Proc. Towards a Network of Atmospheric Cherenkov Detectors VII, Palaiseau, 27-29.

[19] Bartko H. et al, 2005, *Comparison of Signal Reconstruction Algorithms for the MAGIC Telescope*, MAGIC internal documentation, TDAS 05-03.

[20] Bastieri D. et al, 2005, *The mirrors for the MAGIC telescope*, Proc. 29th ICRC, Pune, Tsukuba, 5, 283-286.

[21] Becker, R. H., et al, 1982, ApJ, 255,557.

[22] Bednarek W. & Protheroe R.J., 1997, hRvL, 79, 2616-2619.

[23] Bednarek W. and Bartosik M., 2003, A&A, 405, 689-702.

[24] Bednarek W. and Bartosik M., 2005, JPhG, 31, 1465-1474.

[25] Bietenholz M. F., 2006, ApJ, 645, 1180-1187.

[26] Biland, A., 2003, ECO meeting (Barcelona).

[27] Blanch O., 2002, *Description of the ROOT data format for the MAGIC Telescope*, MAGIC internal documentation, TDAS 02-01.

[28] Blanch O., 2001, *Trigger threshold and rates from Montecarlo studies*, MAGIC internal documentation, TDAS 01-08.

[29] Blandford, R. & Teukolsky, S.A., 1976, ApJ, 205, 580-591.

[30] Bock, R. et al, 2004, NIM, 516, 511-528.

[31] Bramel D.A. et al, 2005, ApJ, 629, 108-114.

[32] Breiman L., 2001, Machine Learning, 45, 5-32.

[33] Bretz T. et al, 2003, *The Tracking System of the MAGIC telescope*, Proc. 28th ICRC, Tsukuba, 2943-2946.

[34] Camilo, F. et al, 2002, ApJ, 571, L41-L44.

[35] Capdeville J.N. et al, 1989, JPhG,15, 909-924.

[36] Chadwick, P.M. et al, 1998, APh, 9, 131-136.

[37] Cheng A. & Ruderman M., 1977, ApJ, 214, 598.

[38] Cheng K.S. & Ruderman M. A., 1986, ApJ, 300, 500-539.

[39] Chiang J. & Romani R.W., 1994, ApJ, 436, 754-761.

[40] Coarasa J.A., 2005, *Online PC Farms for MAGIC-II and Data Transfer*, MAGIC Collaboration Meeting, Tenerife.

[41] Cooke D.J., 1983, Phy. Rev. L., 51, 4, 320-323.

[42] Commichau S., 2007, *Observation of Very High Energy Gamma-Rays from the Galactic Center with the MAGIC Telescope, considering Geomagnetic Field Effects on the Imaging Technique*, Eidgenössische Technische Hochschule, Zürich.

[43] Cortina J. et al, 2005, *The control system of the MAGIC Telescope*, MAGIC internal documentation, TDAS 00-07.

[44] Cortina J. et al, 2005, *Technical Performance of the MAGIC telescope*, Proc. 29th ICRC, Pune, 00, 101-106.

[45] Cortina J. and Gonzalez, J.C., 2001, APh, 15(2), 203-210.

[46] Corti D. et al, 2003, *The Trigger System of the MAGIC Telescope: On-line Selection Strategies for Cherenkov Telescopes*, proceedings 28th ICRC, Tsukuba, 2959-2962.

[47] de Jager, O.C. et al, 1989, ApJ, 221, 180-190.

[48] de Jager O.C. & Harding A.K., 1992, ApJ, 396, 161-172.

[49] de Jager, O.C., 1994, ApJ, 436, 239-248.

[50] de Jager O.C. et al, 1996, ApJ, 457, 253-266.

[51] de Jager O.C., 2002, private communication.

[52] de la Calle I., 1999, *A study of the polarization of Cherenkov radiation in Extensive Air Showers of energy around 1 TeV*, Diploma Thesis, UCM.

[53] delosReyes R., et al, *MAGIC data check and on-line analysis program*, MAGIC internal documentation, TDAS 06-11.

[54] delosReyes R., 2002, *Analysis and simulation of atmospheric Cherenkov telescope data*, Diploma Thesis.

[55] Daugherty J.K. & Harding A.K., 1982, ApJ, 252, 337-347.

[56] Daugherty J.K. & Harding A.K., 1996, ApJ, 458, 278-292.

[57] Dickinson J.E., et al, 2000, Nuclear Instruments & Methods A, 440:95.

[58] Doering M., 2001, *Measurement of the spectrum and polarization of Cherenkov light with the HEGRA stereoscopic IACT system*, Proc. 27th ICRC, Hamburg, 00, 2985-2988.

[59] Domingo Santamaria E., 2006, *Gamma-ray emission from regions of star formation: Theory and observations with the MAGIC telescope*, PhD Thesis, Universitat Autonoma de Barcelona.

[60] Dyks J. & Rudak B., 2002, A&A, 393, 511-521.

[61] Dyks J. & Rudak B., 2003, AdSpR, 33, 581-585.

[62] Erber T., 1966, RvMP, 38,626-659.

[63] Falcke H., Gorham P., 2003, APh, 19, 477-494.

[64] Fesefeldt Aachen H.,1985, PITHA 85102.

[65] Fierro, JM, 1995, *Observations of Spin-Powered Pulsars with the Gamma-Ray Telescope*, Ph.D. thesis, Stanford University.

[66] Firpo R., 2006, *Study of MAGIC Telescope sensitivity for Large Zenith Angle observations*, Diploma Thesis, IFAE Barcelona.

[67] Flatcher R.S. et al,1994, PhRv, D50,5710.

[68] Flix Molina J., 2006, *Observation of gamma-rays from the galactic center with the MAGIC telescope Indirect searches of supersymmetric dark matter*, PhD Thesis, Universitat Autonoma de Barcelona.

[69] Fomin V. P. et al, 1994, APh, 2, 137-150.

[70] Frackowiak M. & Ridak B., 2005, AdSpR, 35, 1152-1157.

[71] Garczarczyk M. et al, 2006, *Study of the focussing and mirror quality of the MAGIC reflector*, MAGIC internal documentation, TDAS 06-06.

[72] Gaug M. , 2006, *Calibration of the MAGIC telescope and observation of gamma-ray bursts*, PhD Thesis, Universitat Autonoma de Barcelona.

[73] Gaug M. , 2005, *Calibration of the MAGIC telescope*, Proc. 29th ICRC, Pune, 00, 101-106.

[74] Goebel F. et al, 2003, *The Data Acquistion of the MAGIC Telescope*, Proc. 28th ICRC, Tsukuba, 2939-2942.

[75] Goebel F. et al, 2005, *Absolute energy scale calibration of the MAGIC telescope using muon images*, 2005, 29th ICRC, Pune, 5, 179-182

[76] Goebel F., 2005, *Users guide and reference manual for the Data Acquisition and the FAC system of the MAGIC telescope*, MAGIC internal documentation, TDAS 04-01.

[77] Goldreich P. & Julian W.H., 1969, ApJ, 157,869-880.

[78] Gotthelf, E. V. et al, 2007, ApJ, 654, 267-272.

[79] Graisser T.K. et al, 1989, PhRvL. 62, 1425-1428.

[80] Green, R.B., 1993, *Spherical astronomy*, Cambridge University Press.

[81] Gregory P.C. & Loredo T.J., 1992, ApJ, 398, 146-168.

[82] Greisen K., 1956; Prog. Cosmic Ray Phys. 3.

[83] Greisen K., 1960, RNPS, 10, 63-108.

[84] Grieder,P.K.F. 1970, Report INS-J125, Inst. for Nuclear Studies, Univ. of Tokyo.

[85] Hall T.A., et al, 2001, *Observations of Galactic Pulsars and Shell-Type SNRs with the Whipple 10 m Imaging Atmospheric Cherenkov Telescope*, Proc. 27th ICRC, Hamburg, 2485.

[86] Harding A.K., 1981, ApJ, 245, 267-273.

[87] Harding A.K. et al, 1997, ApJ, 476, 246-260.

[88] Harding A.K., 2002, Proc. XXXVIIth Rencontres de Moriond "The Gamma-Ray Universe", Les Arcs, astro-ph/0208421.

[89] Harding A.K. & Muslimov A.G., 2002, ApJ, 568, 862-877.

[90] Hengstebeck, T, 2004, *Userguide for the Mars random forest implementation. a method for g/h separation for the MAGIC telescope*, http://magic.physik.hu-berlin.de/protected/ranforest/.

[91] Hillas A.M., 1985, *Cherenkov Images of EAS produced by primary gamma rays and by nuclei*, Proc. 19th ICRC (La Jolla), 3, 445.

[92] Hirotani K., 2000, PASJ, 52, 645-657.

[93] Horan D. et al, 2004, ApJ, 603, 51-61.

[94] Jackson M.S. & Halpern J. P., 2005, ApJ, 633, 1114-1125.

[95] Joshi B. C., et al, 2004, IAU Symposium, Sydney, 218, 319.

[96] Kalmykov N.N. et al, 1995, PAN, 58, 1728-1731.

[97] Kanbach G., 2002, Proc. 27th ICRC, Hamburg, 7, 2785.

[98] Kasztelan M., Wibig T., Sobczynska D., 2002, *Effect of the earth magnetic field on MAGIC shower images* , MAGIC internal documentation MAGIC-TDAS 02-13.

[99] Kennel C.F. & Coronoti F.V., 1984, ApJ, 283, 710-730.

[100] Knapp J., Heck D., 1995, *Extensive Air Shower Simulation with CORSIKA: A User's Guide*, Institut für Kernphysik, Forschungszentrum Karlsruhe GmbH.

[101] Konopelko A.K., 1999, APh, 11, 1-2, 263-266.

[102] Kranich D. et al, 1999, APh, 2, 65-74.

[103] Kranich D., 2002, *Temporal and spectral characteristics of the active galactic nucleus Mkn 501during a phase of high activity in the TeV range*, PhD Thesis, MPI Munich.

[104] Kuiper L., et al, 2000, A&A, 359, 615-626.

[105] Kuiper L., et al, 2002, ApJ, 577, 917-922.

[106] Kuiper L., Hermsen W., 2003, Proc. 4th AGILE Science Workshop, Roma.

[107] Li T., Ma Y., 1983, ApJ, 272, 317-324.

[108] Longair M.S.,1992, *High Energy Astrophysics*, Ed. Cambridge University Press.

[109] Lorimer, Duncan R., 2001, LRR, 4, 5L.

[110] Luo Q. et al, 2000, MNRAS, 318, 943-951.

[111] Majumdar P. et al, 2005, *Monte Carlo simulation for the MAGIc telescope*, Proc. 29th ICRC, Pune, 5, 203 - 206.

[112] Lopez, M., 2007, *Observaciones de la Nebulosa y Pulsar del Cangrejo*, PhD Thesis, UCM.

[113] Lucarelli F. et al, 2004, *The timing system of the MAGIC telescope*, Proc. 19th ECRS, 20, 29, 7012-7015.

[114] Meyer M., 2005, *Calibration of the MAGIC telescope using muon rings*, MAGIC internal documentation, TDAS 05-10.

[115] Mirzoyan R. and Lorentz E., 1994, *Measurement of the night sky background at La Palma*, Max-Planck-Institut fur Physik report PI-PhE/94-35.

[116] Murray S. et al, 2002, ApJ, 568, 226-231.

[117] Muslimov A.G. & Tsygan A.I., 1992, MNRAS, 255, 61-70.

[118] Muslimov A.G. & Harding A.K., 2003, ApJ, 588, 430-440.

[119] Navarro J. et al, 1995, ApJ, 455, L55-L58.

[120] Nel H.I. & de Jager O.C., 1996, Ap&&SS, 230, 1-2, 299-306.

[121] Nelson W.R. et al, 1985, SLAC, 265.

[122] Neyman J., 1937, Phil. Trans. Royal Soc. London, Series A, 236,333.

[123] Oya I., tesina.

[124] Paoletti R., 2003, *The MAGIC level 2 trigger. A user's manual*, MAGIC internal documentation, TDAS 03-04.

[125] Paneque D. et al, 2004, NIMPA, 518, 619-621.

[126] Paneque D., 2004, *The MAGIC Telescope: development of new technologies and first observations*, PhD Thesis, MPI Munich.

[127] Rico J., 2005, *Study of the MAGIC sensitivity for off-axis observations*, Proc. 29th ICRC, Pune, 5, 371 - 374 .

[128] Ranf J., 1995, PhRv. D51,64.

[129] Ransom S., private communication.

[130] Ransom S. et al, 2004, AIPC, 714, 350-356.

[131] Reynolds, P. et al, 1993, ApJ, 404, 206-218.

[132] Rolke W.A. et al, 2005, Nucl.Instrum.Meth. A, 551, 493-503.

[133] Romani R.W. & Yadigaroglu I.A., 1995, ApJ, 438, 314-321.

[134] Rudak B. & Dyks J., 1998, MNRAS, 295, 337-343.

[135] Rudak B. et al, 2002, Proc. 270. WE-Heraeus Seminar on Neutron Stars, Pulsars, and Supernova Remnants, 278, 142.

[136] Ruderman M.A. & Sutherland P.G., 1975, ApJ, 196, 51-72.

[137] Schremp E. J., 1938, Phy. Rev., 54, 158-162.

[138] Shoup A., 1999, *Use of Instrumented Water Tanks for the Improvement of Air Shower Detector Sensitivity*, Proc. 26th ICRC,Salt Lake City, 316.

[139] Slane P.O. et al, 2002, ApJ, 571, L45-L49.

[140] Slane P. et al, 2004, ApJ, 616, 403-413.

[141] Smith D.A., private communication.

[142] Sokolsky P., 1989, *Introduction to ultra high energy cosmic rays physics*, Ed. Addison-Wesley.

[143] Stepanyan A.A. et al 2002ARep...46..634S638 ,

[144] Stairs I.H. et al, 1999, ApJSS, 123, 627-638.

[145] Sturrock, P.A., 1971, ApJ, 164, 529-556.

[146] Taylor J.H. and Weisberg J.M., 1989, ApJ, 345, 434-450.

[147] Thompson D.J., 2004, ASSL, 304, 149.

[148] Vacanti G. et al, 1994, APh, 2, 1-11.

[149] W.-M. Yao et al., 2007, J. Phys. G 33, 1.

[150] Webb, N.A. et al, 2004, A&A, 417, 181-188.

[151] Wenger A., 2004, *The effect of the earth magnetic field on extensive air showers*, Diploma thesis, Institute for Particle Physics, ETH Zürich.

[152] Wentz J. et al, 2001, *Simulation of the geomagnetic cut-off with GEANT using the International Geomagnetic Reference Field*, Proc. 27th ICRC, Hamburg, 4213-4216.

[153] Werner K.,1993, Phys. Rep. 232, 87-299.

[154] Wiebel-Sooth B., 1998, PhD thesis, Universität Wupertal.

[155] Wittek W., 2002, *Democratic treatment of pixels in the image cleaning*, MAGIC internal document, TDAS 02-14.

[156] Wittek W., 2002, *Image parameters*, MAGIC internal documentation, TDAS 02-03.

[157] Wozna A., et al, 2002, Proc. 22nd Moriond Astrophysics Meeting, Les Arcs, astro-ph/0205224.

[158] Zavlin V. E., 2006, ApJ, 638, 951-962.

[159] Zhang L. & Cheng K.S., 1997, ApJ, 487, 370-379.

[160] *http://hea-www.harvard.edu/ slane/psr/gif/magnetosphere.gif*

[161] *http://www.ngdc.noaa.gov/cgi-bin/seg/gmag/fldsnth1.pl.*

[162] *http://gravmag.ou.edu/mag_earth/mag_earth.html*

[163] *http://en.wikipedia.org/wiki/South_Atlantic_Anomaly*

[164] *http://www.ll.mit.edu/ST/sbv/saa.html*

[165] *http://hegra1.mppmu.mpg.de/MAGICWeb/Intro.html.*

[166] *http://www.mpi-hd.mpg.de/htm/HESS/HESS.html.*

[167] *http://linmax.sao.arizona.edu/help/FLWO/whipple.html.*

[168] *http://veritas.sao.arizona.edu/old/Proposal/veritas_full/index.html.*

[169] *http://www.tuc.nrao.edu/alma/site/chajnantor/maps/coordinates.html.*

[170] *http://icrhp9.icrr.u-tokyo.ac.jp/intro.html.*

[171] *http://www.icrr.u-tokyo.ac.jp/can/presentation/beyond_03_tsuchiya.pdf.*

[172] *http://www.mpi-hd.mpg.de/hfm/HESS/HESS.html.*

[173] *http://wwwmagic.mppmu.mpg.de.*

[174] *http://www.tuc.nrao.edu/alma/site/chajnantor/maps/coordinates.html.*

[175] *http://webusers.fis.uniroma3.it/ nucleare/argo/.*

[176] *http://www-akeno.icrr.u-tokyo.ac.jp/AGASA/*

[177] *www.lngs.infn.it/lngs_infn/contents/lngs_en/research/experiments_scientific_info/experime*

[178] *http://www-ik.fzk.de/KASCADE_home.html*

[179] *Letter of intent of the Cherenkov Telescope Array (CTA internal documentation)*

[180] *http://polywww.in2p3.fr/activites/physique/glast/workbook/pages/advanced_Geant4/G4W*

[181] *http://top.gae.ucm.es/.*

[182] *http://lpnhe-auger.in2p3.fr/.*

[183] *http://www.magic.iac.es/operations/datacheck/docu_dcheck.pdf (MAGIC private URL)*

[184] *http://www.magic.iac.es/operations/datacheck/docu_calcheck.pdf (MAGIC private URL)*